PHASED ARRAY ANTENNAS

with Optimized Element Patterns

Sergei P. Skobelev

Phased Array Antennas with Optimized Element Patterns

For a list of recent related titles in the *Artech House Antennas and Propagation Series*, please turn to the back of this book.

Phased Array Antennas with Optimized Element Patterns

Sergei P. Skobelev

ARTECH
HOUSE
BOSTON | LONDON
artechhouse.com

Library of Congress Cataloging-in-Publication Data
A catalog record for this book is available from the U.S. Library of Congress.

British Library Cataloguing in Publication Data
A catalogue record for this book is available from the British Library.

ISBN-13: 978-1-60807-190-6

Cover design by Vicki Kane

685 Canton Street
Norwood, MA 02062

10 9 8 7 6 5 4 3 2 1

To my sons Sergey and Alexey

Contents

Preface

My research work on the subject of this book started in the mid-1970s while I was studying at the Moscow Institute of Physics and Technology. I studied my area of specialization at the Chair of Applied Electrodynamics, based at the Research Institute of Radio Physics in Moscow, which became the Company "Radiophyzika" after privatization in 1993. The first results based on the application of multiport networks for reducing the number of phase shifters in array designed for limited field of view were obtained in the process of performing my M.S. thesis supervised by Dr. Yu. N. Seryakov.

The results on application of modulated corrugated structures for shaping the sector flat-topped array element patterns were obtained in the frame of my Ph.D. thesis under direct supervision by Dr. V. D. Korotkov and general supervision by Professor G. G. Bubnov. As the director of the Research Institute of Radio Physics and simultaneously the head of the chair, Professor Bubnov exerted huge influence on me personally and on many other graduates of the chair and associates of the Institute.

Further results were obtained during my work as the associate of "Radiophyzika." Some papers on them were published in coauthorship with my colleagues S. A. Ganin, V. V. Denisenko, Yu. B. Dubrov, G. V. Dybtsyn, M. M. Ivanishin, A. E. Kazaryan, V. D. Korotkov, A. V. Shishlov, and A. G. Shubov. Useful bibliographic information used in the process of writing the book was received from Yu. B. Korchemkin, V. V. Denisenko, and A. V. Shishlov. A definite contribution to the research on the subject was made by my students L. L. Mukhamedov, A. S. Vyazigin, R. M. Leijon, K. V. Nikitin, and A. A. Yaparova. I always got necessary help and support from the administration of the company, in particular from V. V. Petrosov, A. A. Tolkachev, B. A. Levitan, A. N. Sheludchenko, I. V. Poplavsky, V. I. Roovinsky, and S. V. Ivanov. Assistance associated with using computer technologies could always be received from Yu. A. Bomstein. Great encouragement during work on the book was given by M. A. Kovalyova.

Of great value for me in my work was discussion of its results at the chair seminar headed by Dr. N. P. Malakshinov and Dr. V. N. Garmash, at the Joint Feld's seminar (at the Institute of Radio Engineering and Electronics, Moscow) headed by Professor V. V. Shevchenko (previously, Professors B. Ye. Kinber and D. M. Sazonov were the chairmen of the seminar), and at the seminar "Numerical Methods of Electrodynamics" headed by Professors A. G. Sveshnikov and A. S. Ilyinsky at the Moscow State University. My first review paper on arrays with flat-topped element patterns was presented in 1993 at the 10th International School Seminar on Wave Diffraction and Propagation by invitation from the program committee chairman, Professor V. A. Borovikov.

My interaction with a number of foreign specialists has exerted great influence on my work. First of all, I would like to mention Dr. R. J. Mailloux of Hanscom

AFB, Massachusetts. First, the work of R. J. Mailloux on dual-mode horn arrays gave me a good example in the beginning of my work for further development of the subject. Second, a great honor for me has been the inclusion of some my results in the second edition of his handbook (R. J. Mailloux, *Phased Array Antenna Handbook*, *Second Edition*, Artech House, 2005) and his lectures (R. J. Mailloux, *Electronically Scanned Arrays*, Morgan & Claypool, 2007). Third, due to his invitation and support, I could present and discuss my results at three international symposia on phased arrays held in the United States in 1996, 2000, and 2003, as well as at meetings in his laboratory in Hanscom. During my trip of 1996, I also made my presentations at two meetings organized by Dr. L. A. Coryell in Fort Monmouth, New Jersey, and by Mr. R. E. Welch in San Diego, California.

Due to invitation and support from the program committee headed by Dr. L. Josefsson, Ericsson Microwave Systems AB, Gothenburg, Sweden, I presented my review paper at the Nordic Antenna Symposium of 1997 in Gothenburg, Sweden. It was also very useful for me to discuss some my results at the meeting organized by Dr. P. Ingvarson in Saab Ericsson Space AB.

The initial experimental results on the application of corrugated rods for shaping flat-topped array element patterns were obtained due to support from Dr. L. E. Corey of Georgia Tech, Atlanta, Georgia. Further development of this technology was performed in cooperation with Dr. S. Y. Eom and his colleagues from the Electronics and Telecommunications Research Institute, Taejeon, R. O. Korea.

Useful bibliographical information that I included in the overview of the networks designed for shaping flat-topped subarray patterns was received from Dr. A. R. Lopez, GEC-Marconi Hazeltine, Greenlawn, New York. Dr. J. F. Johansson from Ericsson AB, Molndal, Sweden, provided me with copies of a few his papers on multiple beam antennas, which were very useful for me when working on the sections devoting to forming orthogonal beams by a planar aperture and to shaping sector patterns by dense arrays.

Of great importance and value for me was also my long-term collaboration with Professor P.-S. Kildal from Chalmers University of Technology, Gothenburg, Sweden, as well as with Dr. D. Smith from Northumbria University, Newcastle-upon-Tyne, United Kingdom, in 2006–2007. Though that collaboration was not directly related to the subject of the present book, participation in various conferences in its framework allowed me to present my results on the arrays with flat-topped patterns as well.

I am deeply grateful to all the persons listed here, as well as to many other people I was pleased to interact with during many years of everyday work.

Introduction

Rapid development of the phased array antenna area started in the 1940s after the first samples of antennas with electrical beam scanning appeared [1, 2]. As a result, large stationary radars with phased arrays, such as "Dnepr," "Daryal-U," "Neman," "Voronezh-M," "Don-2N," "Dunay-3U," "Volga" [3], "Argun" [4], and "Ruza" [5], were created in Russia during the second half of the twentieth century. Similar examples of the western radar stations are presented in [6–9], and some mobile radars of both Russian and foreign production on the basis of multi-element phased arrays are described in [8, 10].

Publications on scanning array antennas include a huge number of journal and conference papers, chapters in many textbooks and handbooks on antennas, and a few dozen books specially devoted to arrays [1, 6, 7, 11–43]. This list, having no pretensions of completeness, covers both books of general interest [1, 6, 7, 11–24] and books considering specialized issues. The latter include array synthesis [25–32] (a chapter devoted to the structural synthesis is available in [17]), active arrays [33], adaptive arrays [34–38], conformal arrays [39, 40], multifrequency integrated arrays [41], radio-optical arrays [42], and measurement of array characteristics [43]. Analytical solutions of the waveguide array problems that are of great importance both themselves and for validation of various numerical methods are given in [6, 44, 45]. Some results on statistical analysis of the array antennas are presented in [46]. Hybrid scanning reflector antennas, where arrays are used as feeds, are considered in [47].

The importance of the array antenna subject justifies permanent presence of appropriate sessions at national and international symposia and conferences on general antenna theory and technology, as well as organization of symposia and conferences devoted exclusively to the phased array antennas. Three latest such symposia were held in the United States in 1996, 2000, and 2003. Information on the earlier array conferences is available in [21].

In the process of developing one- and two-dimensional linear and planar phased array antennas, the array element spacing is conventionally determined from the well-known condition guaranteeing the absence of the array factor grating lobes in the visible space, while the main lobe scans over a specified region. Such an approach is fully justified if the main lobe is required to deflect to large angles from the broadside direction (i.e., at wide-angle scanning). However, there exist several important applications where providing high array gain is required only in a relatively narrow angle sector in one plane or in both main planes. Such arrays, also called *arrays with limited field of view* or just *limited-scan arrays*, are required and used in

Aerodrome radar stations (like AN/TPN-19 [7]) for air traffic control and instrumental landing of airplanes;

Radars for getting images of vessels on a waterway [48];
Automotive radars designed for preventing collisions and other road incidents [49, 50];
Shipboard fire-control radars [1];
Counterbattery radars like COBRA [51] designed for detecting hostile artillery positions by tracing projectile trajectories;
Systems of satellite communications [52, 53], in particular, for communication with satellites arranged on the geostationary orbit, from which the Earth is observed in the angular sector of ±9°;
Earth communications stations for tracking movement of satellites located on the geosynchronous orbit whose plane is deflected out of the equatorial plane at a small angle.

Beside these applications, fast electrical beam scanning in a narrow sector can also be combined with wide-angle mechanical rotation of the whole array, as it has been realized in the radar stations "Argun" [4] and "Ruza" [5], which are used for tracking objects in the near-Earth space.

Application of the conventional approach to selection of the element spacing in the limited-scan arrays would result in strong redundancy of the control devices, like phase shifters in passive arrays or transmit-receive (T/R) modules in active arrays [54], in comparison with the theoretical minimum of the element number equal to the number of orthogonal beams of specified gain filling in a specified sector of scan [55]. For instance, as it follows from relation (8-55) in [56] (see also Table 1 in [57]), the element number in an array designed for scanning in a conical region with flare angle of 20° using the conventional approach would exceed the theoretical minimum more than 11 times. Since the phase shifters and especially T/R modules are the most expensive phased array components, minimization of their number is always desirable. Moreover, the indicated minimization corresponds to maximization of the array element spacing that can also give some additional preferences in the array design.

Selection of the maximum element spacing corresponding to the minimum number of controlled elements in the limited-scan arrays results in the presence of the array factor grating lobes in real space. Their high level is usually undesirable, since it corresponds to lowering the array gain due to taking a part of the radiated power away from the main lobe. Besides, the presence of the high grating lobes can also result in ambiguity of the target detection finding. The simplest way of suppressing the grating lobes is to utilize large-aperture radiating elements [58, 59] or non-overlapped subarrays of simple radiators fed in phase [16, 56]. Such an approach has been realized, for instance, in an array of dual-reflector antenna elements [60–62] used in the radar "Ruza" [5]. Application of the large-aperture horn elements is considered in [63, 64]. However, more or less effective grating lobe suppression in such arrays can be provided only when the main lobe is steered in the broadside position. Deflection of the main lobe from the boresight is accompanied with fast growing of the grating lobe level and therefore fast lowering of the array gain in accordance with the shape of the radiation pattern of a large-aperture element or of a cophasal subarray. Application of the large-aperture elements in combination with their irregular arrangement in the array aperture [1, 19, 24] allows effective

destroying of the grating lobes. However, fast gain reduction with deflection of the main lobe from the boresight remains, since the power radiated earlier in the grating lobes is lost as well due to spraying into the background. Moreover, the irregular arrangement of the antenna element can result in complicating the design of both the radiating structure and the feeding system.

The theoretical minimum of the array element number is achieved not only at the maximum element spacing corresponding with the specified scan sector width, there should also be provided the maximum efficiency of the array aperture when the array gain behaves according to the $\cos\theta$ law, where θ is the angle of beam deflection from the boresight. If the gain drops faster, as takes place in arrays of the large-aperture elements or cophasal subarrays, satisfaction of the specification on the array gain in the scan region results in the necessity of enlarging the aperture area, which, in turn, leads to increasing the element number over its theoretical minimum.

Since the behavior of the grating lobes of the array and its main lobe at scanning is determined by the array element pattern shape, the ideal amplitude element pattern corresponding to the minimum number of the elements must be proportional to $\sqrt{\cos\theta}$ in the scan region and have zero level outside it thereby providing complete suppression of the grating lobes. Such patterns are referred to as *sector* or *contour patterns*. The term *flat-topped patterns* is also widely applied for them in the appropriate literature.

The shaping of the flat-topped element patterns is of interest not only from the viewpoint of minimization of the element number in the limited-scan arrays but also by other reasons considered next. In the array designed for wide-angle scanning, the element spacing must be small enough. However, the density of the array element arrangement can be restricted by the transverse dimensions of the existing phase shifters or T/R modules. For instance, application of the ferrite phase shifters [65] in the millimeter-wave band arrays [60, 66] results in element spacing exceeding the wavelength. Similar spacing may take place in some X-band phased arrays of feed-through type where their control cells are arranged nearby the phase shifters. Shaping of the sector element patterns in such cases allows the suppression of the grating lobes and the provision of maximum array gain in a maximally wide scan sector corresponding to the element spacing dictated by the phase shifter dimensions.

The sector flat-topped element patterns are of interest also in connection with the possibility of using the arrays with such elements as feeds in reflector and lens antennas. The sector element patterns in these cases allow the provision of high efficiency of the illuminated aperture with minimum loss for spillover. The use of such arrays in multiple beam antennas for radiotelescopes of a new generation and for the systems of radiovision has been considered in [67–70].

At last, some approaches to shaping the sector and contour *array element* patterns may be applied to shaping the sector and contour patterns in other antenna applications, since antennas with such patterns are required, for instance, in communications systems with contour zones of servicing [71–73] and in the systems of power transfer by means of microwave beam [74, 75].

It is known that the sector element pattern cannot be shaped by using currents or fields distributed over the aperture of only one array cell. Strictly speaking,

the appropriate distribution must occupy the entire array aperture and thereby use all the array cells. Therefore, the sector array element pattern corresponding to excitation of one controlled array input is, in fact, the pattern of the array as a whole at the indicated partial excitation. This pattern is referred to in the literature as the *subarray pattern* or the *partial array pattern*. Since the field distribution corresponding to excitation of any array input occupies the entire array aperture, the array with the sector element patterns consists of overlapped subarrays.

Publications on studying approaches to the creation of phased arrays with overlapped subarrays shaping the sector patterns started to appear in 1970s. A review of the results published on this subject over subsequent two decades in Western literature was made in Chapter 8 of [19]. The results of Russian and some foreign studies were also described in [57, 76]. The interest to the subject has not been getting weaker, and more than two dozen papers have been published since the late 1990s. Some of them have been included in the second edition of [24] and in [1].

The present book is the first separate monograph devoted to a systematic description of the theory and methods of shaping the sector and contour element patterns in linear and planar phased array antennas. The book consists of six chapters based mainly on the results obtained by the author. They are compared to the results obtained by other specialists.

Chapter 1 contains basic fundamental relations and restrictions for phased arrays obtained using the general antenna theory applied to periodic structures. Main attention is paid to the ideal array element pattern defined as a pattern corresponding to the highest achievable array gain in the widest possible scan region for specified array element spacing. We reveal and describe the properties of the ideal sector and contour element patterns. The results obtained with that connection have also allowed us to develop a technique for determining the dimensions and shape of a planar aperture providing formation of orthogonal beams arranged in a specified Cartesian regular skew lattice, as described in Appendix 1B. They have also helped to derive new expressions for evaluating the radiation efficiency of the dense arrays shaping the contour radiation patterns in general case. The material on this subject can be found in Appendix 1C.

In Chapter 2, we consider the formation of overlapped subarrays shaping the sector radiation patterns on the basis of feedthrough multiport networks. The consideration includes an overview of various technical solutions available in the previous literature, as well as a description of a proposed multicascaded beam-forming matrix, which we call the *chessboard network*. Results of its optimization together with computed and measured radiation patterns of the array on its basis are presented and discussed. We also consider the use of a linear array with the chessboard network as a feed of a parabolic-cylindrical antenna. Finally, we propose and analyze some optical analogs of the chessboard network designed for shaping very narrow sector flat-topped element patterns.

Chapter 3 is devoted to arrays of dual-mode waveguides coupled to each other through the slots in their walls. The amplitude distribution in the aperture corresponding to the sector partial pattern is formed by the first (even) and second (odd) modes propagating in the waveguides. The indicated modes are excited and phased

in the required relation obtained as a result of optimization of the array geometry. The effectiveness of such an approach is confirmed both by computed data and by measured characteristics of the appropriate array breadboard.

In Chapters 4, 5, and 6, we investigate approaches based on using the natural mutual coupling always existing between radiating elements over free space. Chapter 4 is devoted to the array of densely arranged waveguides with reactive loads realized by short circuits, forming a modulated corrugated structure. Each passive short-circuited waveguide is excited due to strong coupling both with active (controlled) elements and with other neighbor passive waveguides. The sector partial radiation pattern is formed as a result of the appropriate choice of the short-circuit positions in the waveguides. We present both a technique of analysis of such arrays and some measured results confirming the theory.

The shaping of the flat-topped element patterns in waveguide arrays with protruding dielectric elements characterized by strong mutual coupling in the forward direction is investigated in Chapter 5. The numerical analysis of the waveguide-dielectric arrays is accomplished by a hybrid projection method. This method has specially been developed for solution of both two- and three-dimensional problems and may be of independent interest.

Finally, Chapter 6 describes shaping of the flat-topped array element patterns by using multilayer strip structures, disk structures similar to the corrugated rods, and wire structures forming the Yagi-Uda antenna elements, which, similarly to the protruding dielectric elements, are also capable of supporting the traveling waves. This chapter also considers other wire structures forming semitransparent walls that provide distributed coupling between array cells with the same purpose of shaping flat-topped element patterns. We present both calculated and measured results characterizing the capabilities of such an approach. The arrays of the Yagi-Uda elements are analyzed with an efficient method developed for calculation of Green's function for dually periodic structures and described in Appendix 6A. Appendix 6B contains a modification of the Kummer's method developed for accelerating the convergence of series arising in two-dimensional problems for one-dimensional periodic structures.

This book is designed for researchers and engineers working in the array antenna area, including phased arrays, as well as to students specializing in antennas and microwave engineering.

References

[1] Mailloux, R. J., "Electronically Scanned Arrays," *Synthesis Lectures on Antennas*, No. 6, Morgan & Claypool, 2007.

[2] Vendik, O. G., and Y. V. Yegorov, "The First Phased-Array Antennas in Russia: 1955–1960," *IEEE Antennas and Propagation Magazine*, Vol. 42, No. 4, 2000, pp. 46–52.

[3] *Radiolocation in Russia* (*Biographical Encyclopedia*), Moscow: Capital Encyclopedia, 2007 (in Russian).

[4] Tolkachev, A. A., "Radar Station 'Argun' (To the Thirtieth Anniversary of the Range Tests)," *Radiotekhnika*, No. 10, 2006, pp. 9–13 (in Russian).

[5] Tolkachev, A. A., et al., "A Megawatt Power Millimeter-Wave Phased-Array Radar," *Aerospace and Electronic Systems Magazine*, Vol. 15, No. 7, 2000, pp. 25–31.

[6] Amitay, N., V. Galindo, and C. P. Wu, *Theory and Analysis of Phased Array Antennas*, New York: Wiley-Interscience, 1972.

[7] Brookner, E., (ed.), *Practical Phased Array Antenna Systems*, Norwood, MA: Artech House, 1997.

[8] Brookner, E., "Phased Arrays: Major Advances and Future Trends into the Next Millennium," *Proc. 28th Moscow Int. Conference on Antenna Theory and Techniques*, Moscow, Russia, September 22–24, 1998, pp. 24–42.

[9] Palumbo, B., "Some Examples of System Developments in Italy Based on Phased Array Technology," *IEEE Intl. Symposium on Phased Array Systems and Technology*, Boston, MA, October 15–18, 1996, pp. 444–449.

[10] Corey, L. E., "A Survey of Russian Low Cost Phased Array Technology," *IEEE Intl. Symposium on Phased Array Systems and Technology*, Boston, MA, October 15–18, 1996, pp. 255–259.

[11] Deryugin, L. N., (ed.), *Microwave Scanning Antennas*, Moscow: Mashinostroyeniye, 1964 (in Russian).

[12] Vendik, O. G., *Antennas with Non-Mechanical Movement of Beam*, Moscow: Sovetskoye Radio, 1965 (in Russian).

[13] Hansen, R. C., (ed.), *Microwave Scanning Antennas*, New York: Academic Press, 1964 (Vol. I) and 1966 (Vols. II and III).

[14] Voskresensky, D. I., (ed.), *Antennas and Microwave Devices (Calculation and Design of Antenna Arrays and Their Radiating Elements)*, Moscow: Sovetskoye Radio, 1972 (in Russian).

[15] Ma, M. T., *Theory and Application of Antenna Arrays*, New York: Wiley-Interscience, 1974.

[16] Voskresensky, D. I., (ed.), *Antennas and Microwave Devices (Design of Phases Antenna Arrays)*, Moscow: Radio & Svyaz, 1981 (in Russian).

[17] Chaplin, A. F., *Analysis and Synthesis of Antenna Arrays*, Lvov, Ukraine: Vishcha Shkola, 1987 (in Russian).

[18] Voskresensky, D. I., (ed.), *Antennas and Microwave Devices (Design of Phases Antenna Arrays)*, 2nd ed., Moscow: Radio & Svyaz, 1994 (in Russian).

[19] Mailloux, R. J., *Phased Array Antenna Handbook*, Norwood, MA: Artech House, 1994.

[20] Fourikis, N., *Phased Array-Based Systems and Applications*, New York: Wiley-Interscience, 1997.

[21] Hansen, R. C., *Phased Array Antennas*, New York: Wiley, 1998.

[22] Vendik, O. G., and M. D. Parnes, *Antennas with Electrical Scanning (Introduction to the Theory)*, Moscow: Science-Press, 2002 (in Russian).

[23] Voskresensky, D. I., (ed.), *Microwave Devices and Antennas (Design of Phases Antenna Arrays)*, 3rd ed., Moscow: Radiotekhnika, 2003 (in Russian).

[24] Mailloux, R. J., *Phased Array Antenna Handbook*, 2nd ed., Norwood, MA: Artech House, 2005.

[25] Zelkin, Ye. G., *Construction of Radiating System According to Specified Radiation Pattern*, Moscow: Gosenergoizdat, 1963 (in Russian).

[26] Dmitriyev, V. I., and A. V. Chechkin, *Methods of Solution of Antenna Synthesis Problems*, Moscow: Moscow State University Press, 1969 (in Russian).

[27] Minkovich, B. M., and V. P. Yakovlev, *Theory of Antenna Synthesis*, Moscow: Sovetskoye Radio, 1969 (in Russian).

[28] Bakhrakh, L. D., and S. D. Kremenetsky, *Synthesis of Radiating Systems (Theory and Methods of Calculation)*, Moscow: Sovetskoye Radio, 1974 (in Russian).

[29] Zelkin, Y. G., and V. G. Sokolov, *Methods of Antenna Synthesis*, Moscow: Sovetskoye Radio, 1980 (in Russian).

[30] Dmitriyev, V. I., and N. I. Berezina, *Numerical Methods of Solution of Radiating System Synthesis Problems*, Moscow: Moscow State University Press, 1986 (in Russian).

[31] Andrejchuk, M. I., et al., *Synthesis of Antennas According to Amplitude Radiation Pattern: Numerical Methods and Algorithms*, Kiev, Ukraine: Naukova Dumka, 1993 (in Russian).

[32] Zelkin, Ye. G., V. F. Kravchenko, and V. I. Gusevsky, *Constructive Methods of Approximation in the Antenna Theory*, Moscow: Science-Press, 2005 (in Russian).

[33] Voskresensky, D. I., and A. I. Kanashchenkov, (eds.), *Active Phased Antenna Arrays*, Moscow: Radiotekhnika, 2004 (in Russian).

[34] Hudson, J. E., *Adaptive Array Principles*, New York: IEE/Peregrinus, 1981.

[35] Monzingo, R. A., and T. W. Miller, *Introduction to Adaptive Arrays*, New York: Wiley-Interscience, 1980.

[36] Compton, R. T., Jr., *Adaptive Antennas*, Upper Saddle River, NJ: Prentice-Hall, 1988.

[37] Pistolkors, A. A., and O. S. Litvinov, *Introduction to the Theory of Adaptive Antennas*, Moscow: Nauka, 1991 (in Russian).

[38] Ratynsky, M. V., *Adaptation and Superresolution in Antenna Arrays*, Moscow: Radio & Svyaz, 2003 (in Russian).

[39] Voskresensky, D. I., L. I. Ponomarev, and V. S. Filippov, *Convex Scanning Antennas*, Moscow: Sovetskoye Radio, 1978 (in Russian).

[40] Josefsson, L., and P. Persson, *Conformal Array Antenna Theory and Design*, New York: Wiley-IEEE Press, 2006.

[41] Ponomarev, L. I., and V. I. Stepanenko, *Multi-Frequency Integrated Scanning Antenna Arrays*, Moscow: Radiotekhnika, 2009 (in Russian).

[42] Voskresensky, D. I., A. Y. Grinev, and E. N. Voronin, *Radio-Optical Antenna Arrays*, Moscow: Radio & Svyaz, 1986 (in Russian).

[43] Bubnov, G. G., et al., *Commutation Method of Phased Antenna Array Characteristics Measurement*, Moscow: Radio & Svyaz, 1988 (in Russian).

[44] Weinshtein, L. A., *The Theory of Diffraction and the Factorization Method*, Boulder, CO: Golem, 1969.

[45] Mittra, R., and S. W. Lee, *Analytical Techniques in the Theory of Guided Waves*, New York: Macmillian Company, 1971.

[46] Shifrin, Y. S., *Problems of Statistical Theory of Antennas*, Moscow: Sovetskoye Radio, 1970 (in Russian).

[47] Bakhrakh, L. D., and G. K. Galimov, *Reflector Scanning Antennas*, Moscow: Nauka, 1981 (in Russian).

[48] Solbach, K., "Below-Resonant-Length Slot Radiators for Traveling-Wave-Array Antennas," *IEEE Antennas and Propagation Magazine*, Vol. 38, No. 1, 1996, pp. 7–14.

[49] Sakakibara, K., T. Watanabe, K. Sato, and K. Nishikawa, "Slotted Waveguide Array Antenna for Automotive Radar Systems," *Millennium Conference on Antennas and Propagation*, Vol. I, Davos, Swizerland, April 9–14, 2000.

[50] Denisenko, V. V., et al., "Millimeter-Wave Printed Circuit Antenna System for Automotive Applications," *IEEE MTT-S 2001 Int. Microwave Symposium Digest*, Phoenix, AZ, May 20–25, 2001, Vol. III, pp. 2247–2250.

[51] Colin, J. -M., C. Renard, and C. Mangenot, "Phased Array Antennas: Status and New Developments in France," *Proc. 28th Moscow Intl. Conference on Antenna Theory and Technology*, Moscow, Russia, September 22–24, 1998, pp. 47–54.

[52] Jones, D. E., "A Limited-Scan, 20 GHz, Active Transmitting Antenna for Space Applications," *Digest of the IEEE APS International Symposium*, Vol. 2, Albuquerque, NM, May 24–28, 1982, pp. 435–438.

[53] Reudink, D. O., "Progress on the Application of Phased Arrays in Communications Satellites," *ESA/COST 204 Phased-Array Workshop*, Noordwijk, the Netherlands, June 13, 1983, pp. 45–48.

[54] Kantor, L. Y., (ed.), *Satellite Communications and Broadcasting*, 2nd ed., Moscow: Radio & Svyaz, 1988 (in Russian).

[55] Kontorovich, M. I., and V. Yu. Petrunkin, "On the Minimum Number of Elements in an Antenna with Electrical Beam Swinging," *Radiotekhnika i Elektronika*, Vol. 6, No. 12, 1961, pp. 1982–1988 (in Russian).

[56] Markov, G. T., and D. M. Sazonov, *Antennas*, Moscow: Energiya, 1975 (in Russian).

[57] Skobelev, S. P., "Design Synthesis of Antenna Arrays with Sector Partial Radiation Patterns," *Proc. 10th School-Seminar on Wave Diffraction and Propagation*, Moscow, Russia, February 7–15, 1993, pp. 369–395 (in Russian).

[58] Polukhin, G. A., "Analysis of the Radiation Pattern of a Phased Antenna Array of Large-Aperture Modules," *Radiotekhnika*, No. 2, 1989, pp. 53–55 (in Russian).

[59] Ganin, S. A., and G. A. Polukhin, "An Antenna Array of Large Modules with Circular Apertures," *Radiotekhnika*, No. 4, 1991, pp. 58–60 (in Russian).

[60] Tolkachev, A. A., et al., "High Gain Antenna Systems for Millimeter Wave Radars with Combined Electronical and Mechanical Beam Steering," *1996 IEEE Intl. Symposium on Phased Array Systems and Technology*, Boston, MA, October 15–18, 1996, pp. 266–271.

[61] Tolkachev, A. A., et al., "Large-Apertured Radar Phased Array Antenna of K_a-Band," *Proc. 28th Moscow Int. Conference on Antenna Theory and Technology*, Moscow, Russia, September 22–24, 1998, pp. 15–23.

[62] Tolkachev, A. A., et al., "A Large-Radar Phased Array Antenna of the Millimeter Wave Band," *Antenny*, No. 1, 1999, pp. 4–11 (in Russian).

[63] Amitay, N., and M. J. Gans, "Design of Rectangular Horn Arrays with Oversized Aperture Elements," *IEEE Trans. on Antennas and Propagation*, Vol. AP-29, No. 6, 1981, pp. 871–884.

[64] Egorov, E. N., et al., "New Technology in Multibeam and Scanning Antennas," *Proc. APSCC'94 Workshop*, Seoul, Korea, October 26–28, 1994, pp. 211–221.

[65] Tolkachev, A. A., et al., "Phase Shifters for Millimeter-Wave Band Multi-Element Phased Arrays," *Proc. 4th Intl. Symposium on Antennas and EM Theory*, Xi'an, China, August 1997, pp. 583–586.

[66] Denisenko, V. V., et al., "A Multi-Element Phased Antenna Array of the Ka Band," *Antenny*, No. 1, 2005, pp. 7–14 (in Russian).

[67] Ivashina, M. V., et al., "Decoupling Efficiency of a Wideband Vivaldi Focal Plane Array Feeding a Reflector Antenna," *IEEE Trans. on Antennas and Propagation*, Vol. 57, No. 2, 2009, pp. 373–382.

[68] Bankov, S. E., V. A. Kaloshin, and E. V. Frolova, "Computer Design and Experimental Study of a Cluster Feed on the Basis of an EBG Structure," *Journal of Radioelectronics*, No. 3, 2009, http://jre.cplire.ru (in Russian).

[69] Bankov, S. E., "Beamforming Network on the Basis of Unequal Couple Waveguides," *Journal of Communications Technology and Electronics*, Vol. 54, No. 7, 2009, pp. 755–764.

[70] Bankov S. E., V. A. Kaloshin, and E. V. Frolova, "Beam Forming Networks on the Base of Coupled Waveguides for Multi-Beam Hybrid Antennas," *Draft Proc. PIERS 2009*, Moscow, Russia, August 18–21, 2009, pp. 432–437.

[71] Galindo-Israel, V., S. W. Lee, and R. Mittra, "Synthesis of a Laterally Displaced Cluster Feed for a Reflector Antenna with Application to Multiple Beams and Contoured Patterns," *IEEE Trans. on Antennas and Propagation*, Vol. AP-26, No. 2, 1978, pp. 220–228.

[72] Eom, S. Y., et al., "Study of a Planar Array Antenna with Sector Radiation Pattern for Perspective Base Stations of Mobile Communications," *Antenny*, No. 1, 2005, pp. 30–38 (in Russian).

[73] Shishlov, A. V., "Theory and Design of Reflector Antennas for Radio Systems with Contour Zones of Servicing," *Radiotekhnika*, No. 4, 2007, pp. 39–49 (in Russian).

[74] Minz, M. Y., E. D. Prilepsky, and V. M. Zaslonko, "Optimization of the Coefficient of Concentration of Power Radiated by an Antenna with Circular Aperture and Maximally Flat Radiation Pattern," *Radiotekhnika i Elektronika*, Vol. 33, No. 9, 1988, pp. 1888–1894 (in Russian).

[75] Vanke, V. A., and A. A. Zaporozhets, "Synthesis of the Maximally Flat Radiation Pattern of a Transmitting Antenna for Energy Transfer by Microwave Beam," *Radiotekhnika i Elektronika*, Vol. 34, No. 12, 1989, pp. 2643–2647 (in Russian).

[76] Skobelev, S. P., "Methods of Constructing Optimum Phased-Array Antennas for Limited Field of View," *IEEE Antennas and Propagation Magazine*, Vol. 40, No. 2, 1998, pp. 39–50.

CHAPTER 1

General Concepts and Relations

1.1 Basic Characteristics

1.1.1 Element and Array Radiation Patterns

Any array antenna is a set of antenna elements referred to as *radiating elements*, or just radiators arranged some way in space. An example is presented in Figure 1.1, where the radiators are shown in the form of rectangular apertures arranged in a Cartesian rectangular system of coordinates $\{x, y, z\}$ with appropriate unit vectors $\boldsymbol{e}_x$, $\boldsymbol{e}_y$, and $\boldsymbol{e}_z$. Description of the array radiation characteristics is accepted to carry out in a system of spherical coordinates $\{r, \theta, \varphi\}$ shown in Figure 1.1 as well. The spherical coordinates relate to the Cartesian ones in such a way that the unit vector $\boldsymbol{e}_r$ directed to the observation point is determined by formula

$$\boldsymbol{e}_r = u\boldsymbol{e}_x + v\boldsymbol{e}_y + w\boldsymbol{e}_z \tag{1.1}$$

where $u = \sin\theta\cos\varphi$, $v = \sin\theta\sin\varphi$, and $w = \cos\theta$ are direction cosines, while θ and φ are the angles measured from axes z and x, respectively.

One of the fundamental concepts in the array antenna theory is the array element pattern [1, 2]. This parameter, which has actively been used since 1960s, corresponds to the case when, in the transmitting mode, the signal of excitation is supplied to the input of only one array element while all the other inputs are assumed to be terminated with matching loads. Since the electromagnetic interaction always exists between the array elements, the radiation corresponding to excitation of one input is, strictly speaking, formed by all the elements. For this reason, the array element pattern is also referred to as a *partial array pattern*.

The amplitude element pattern in general case is a complex vector function describing the angular distribution of the electric or magnetic field strength at some distance R_n from the origin of a local coordinate system related to the nth excited element. Usually, of primary interest is the element pattern in far zone where the

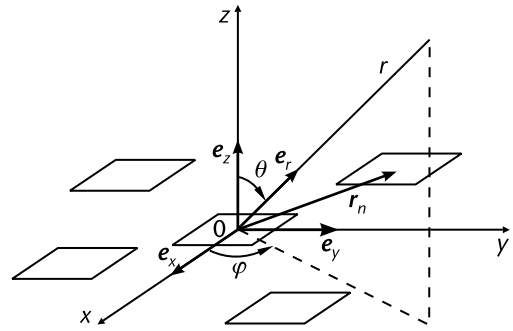

Figure 1.1 Generalized array geometry and coordinate systems.

dependence of the field strength on the distance is described by the function $\exp(ikR_n)/R_n$, where $k = 2\pi/\lambda$ is the free space wavenumber, λ is the operating wavelength, and the omitted time dependence is assumed here and later to be taken in the form $e^{-i\omega t}$.

The great importance of the element pattern not only involves accounting for interaction of any chosen element with all the other elements, but it is also the basis for determining a number of other important array characteristics. One of them is the radiation pattern of the array as a whole in its far zone (i.e., at distances $r \quad 2L^2/\lambda$, where L is the largest transverse array dimension). In this case, the directions from each element to the observation point are considered to be parallel and, therefore, their angular arguments are identical. Let $\boldsymbol{r}_n$ be a vector specifying the position of the nth array element (Figure 1.1), C_n be a complex amplitude of the signal supplied to the input of the indicated element, and $\boldsymbol{F}_n(\theta, \varphi)$ be the element pattern corresponding to the unit amplitude of the excitation. Then, according to the principle of superposition, the vector complex array pattern is determined as

$$\boldsymbol{F}_{\mathrm{A}}(\theta,\varphi) = \sum_n C_n \boldsymbol{F}_n(\theta,\varphi) e^{\,ik\boldsymbol{r}_n \times \boldsymbol{e}_r} \tag{1.2}$$

where the summation is performed over all the array elements and the exponential factor accounts for the element position in the common coordinate system shown in Figure 1.1, in which the dependence of the array far field on the distance is determined by the common factor $\exp(ikr)/r$.

1.1.2 Array Factor

Although each specific array antenna is usually composed of identical radiating elements, the radiation patterns of the latter differ from each other even in those cases when the elements have identical orientation in space and are arranged on a straight line or a plane in the nodes of a regular Cartesian lattice. This fact is explained by the effect of mutual coupling in combination with different positions of the elements with respect to the array edge. However, the mutual coupling in many cases is significant only between elements situated at a close distance from each other. For this reason, the overwhelming majority of the elements in large multi-element array antennas with regular Cartesian lattices are situated in almost equal conditions. This allows one to neglect the edge effect and believe that all the elements have identical radiation patterns. In this case, the array pattern (1.2) may be rewritten as the product

$$\boldsymbol{F}_{\mathrm{A}}(\theta,\varphi) = \boldsymbol{F}(\theta,\varphi) F_{\mathrm{AF}}(\theta,\varphi) \tag{1.3}$$

where $\boldsymbol{F}(\theta, \varphi)$ is the common element pattern replacing the patterns $\boldsymbol{F}_n(\theta, \varphi)$, and

$$F_{\mathrm{AF}}(\theta,\varphi) = \sum_n C_n e^{\,ik\boldsymbol{r}_n \times \boldsymbol{e}_r} \tag{1.4}$$

is a complex scalar function called *array factor*.

The array can provide maximum radiation in a specified direction if it is phased appropriately. Let the angles θ_0 and φ_0 determine the desired direction, and the signals of excitation come to the array inputs with complex amplitudes determined by formula

$$C_n = c_n e^{ikr_n \times e_{r0}} \tag{1.5}$$

where c_n is a complex amplitude with argument independent of n,

$$\boldsymbol{e}_{r0} = u_0 \boldsymbol{e}_x + v_0 \boldsymbol{e}_y + w_0 \boldsymbol{e}_z \tag{1.6}$$

is the unit vector corresponding to the direction of phasing, and $u_0 = \sin\theta_0 \cos\varphi_0$, $v_0 = \sin\theta_0 \sin\varphi_0$, and $w_0 = \cos\theta_0$ are its direction cosines. With accounting for (1.5), the array factor (1.4) takes the form

$$F_{\mathrm{AF}}(\theta, \varphi) = \sum_n c_n e^{ikr_n \times (e_{r0} \quad e_r)} \tag{1.7}$$

from which we see that the exponent is equal to zero in the direction of phasing, meaning that the fields from the radiating elements add in phase resulting in forming the array beam. The phases of signals (1.5) can be changed by phase shifters or other control devices for scanning the beam in the space.

The nodes of the regular lattice mentioned earlier are arranged equidistantly in the rows and columns which, in general case, may not be perpendicular to each other. Such a skew lattice is shown in Figure 1.2(a) together with a Cartesian rectangular coordinate system whose origin is placed in one of the nodes. The lattice is specified by element spacing d_x in a row, spacing d_y between the rows, and displacement d_s between adjacent rows in the row direction. The lattices usually used in practice are rectangular with $d_s = 0$ and triangular with $d_s = d_x/2$. An important special case of the triangular lattice is a hexagonal one where $d_y = d_x\sqrt{3}/2$.

If the columns and rows are numbered by two indices m and n, as shown in Figure 1.2(a), the position of each element in the array with the lattice arranged in the plane $z = 0$ can be specified by the radius-vector

$$\begin{aligned} \rho_{mn} &= x_{mn}\boldsymbol{e}_x + y_n \boldsymbol{e}_y \\ x_{mn} &= md_x + nd_s \\ y_n &= nd_y \end{aligned} \tag{1.8}$$

Accounting for (1.8) allows rewriting the array factor (1.7) as

$$F_{\mathrm{AF}}(\theta, \varphi) = \sum_{m,n} c_{mn} e^{ik[x_{mn}(u_0 \quad u) + y_n(v_0 \quad v)]} \tag{1.9}$$

where c_{mn} is the amplitude of the mnth element.

Analysis of (1.9) shows that the array factor has maxima called *grating lobes*, whose positions in the space of direction cosines u and v are determined by formulas

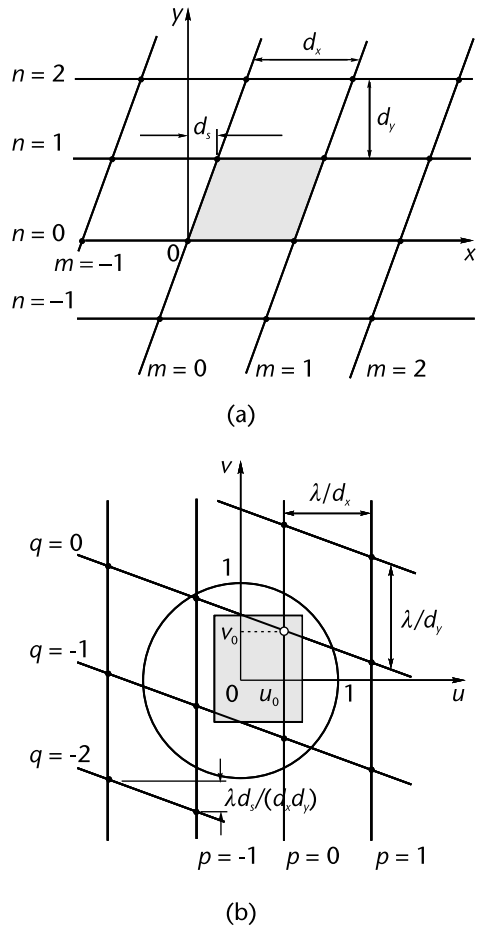

Figure 1.2 (a) Skew Cartesian array lattice, and (b) diagram of array factor grating lobes.

$$u = \frac{\alpha_p}{k} = u_0 + p\frac{\lambda}{d_x}$$
$$v = \frac{\beta_{pq}}{k} = v_0 + \quad q \quad p\frac{d_s}{d_x} \div \frac{\lambda}{d_y} \tag{1.10}$$

with $p, q = 0, \pm 1, \pm 2, \ldots$. So, the array factor grating lobes in case of array with a regular lattice are also arranged in a regular lattice in the direction cosines space as, for instance, shown in Figure 1.2(b). Note, that displacement of the rows in the array lattice at distance d_s in the horizontal direction results in displacement of the columns in the grating lobe lattice at the distance $\lambda d_s/(d_x d_y)$ in the vertical direction. The maximum corresponding to indices $p = 0$ and $q = 0$ is usually called *principal lobe*, while all the other maxima are called *secondary grating lobes* and the word "secondary" is usually omitted. Since the space of real angles (visible space) corresponds to the direction cosines satisfying the condition $u^2 + v^2 \quad 1$, only a finite number of the grating lobes can be present in the visible space, as demonstrated in

Figure 1.2(b), where the unit circle represents the visible space boundary and the main lobe position is shown by a nonfilled small circle. In practice, the presence of the main lobe only in the visible space is desirable. At sufficiently small element spacings and appropriate phasing, there exist cases when neither main nor secondary grating lobes are present in the visible space. However, such cases are not of practical value because they correspond to complete reflection of the input power from the radiating array aperture. The shadowed rectangle shown in Figure 1.2(b) represents a periodic cell of the grating lobe lattice. The issues associated with it will be discussed later in Section 1.3.2.

Apart from the grating lobes, the array factor and the array pattern as a whole have also so-called sidelobes filling in the space between the grating lobes. The level and arrangement of the sidelobes depend on the shape of the array aperture and on the distribution of the input signal amplitudes. These factors also influence on the width of the main and secondary lobes.

1.1.3 Directivity, Gain, and Efficiency

The capability of an array antenna, like any other antenna, to concentrate its radiation in some direction is characterized by a special parameter introduced in the antenna theory by A. A. Pistolkors in 1929 under the name literally translated from Russian as *coefficient of directive action*. The modern English-language antenna literature utilizes the term *directivity* for it. This parameter is defined as the ratio of the flux density of the power radiated by an antenna in a definite direction at distance r in the antenna far zone to the average radiated power flux density on a spherical surface of the same radius r surrounding the antenna. The distribution of the power flux density in far zone of an antenna fed with supplied power $P_{\mathrm{A}}^{\mathrm{in}}$ is described by function $P_A(\theta, \varphi)/r^2$, where $P_A(\theta, \varphi)$ is the power antenna radiation pattern proportional to $|\boldsymbol{F}_A(\theta, \varphi)|^2$. Using the indicated pattern in the definition given earlier, we can write the array directivity D in the direction of phasing (θ_0, φ_0) as

$$D(\theta_0,\varphi_0)=\frac{P_{\mathrm{A}}(\theta_0,\varphi_0)/r^2}{P_\Sigma/(4\pi r^2)}=\frac{4\pi P_{\mathrm{A}}(\theta_0,\varphi_0)}{P_\Sigma} \tag{1.11}$$

where

$$P_\Sigma=\int_0^{2\pi}\int_0^{\pi} P_{\mathrm{A}}(\theta,\varphi)\sin\theta\, d\theta d\varphi \tag{1.12}$$

is the total radiated power.

Although the directivity is an important energy array parameter, it does not account for inevitable losses associated with absorption of a part of the supplied power in the elements and feeding lines as well with reflection of a part of the power from the aperture back to the feeding system. The indicated features are accounted for by another parameter called the *array gain*. The array gain in the direction of phasing, $G(\theta_0, \varphi_0)$, is determined by (1.11) for the directivity, where the total radiated power (1.12) is replaced by the input power $P_{\mathrm{A}}^{\mathrm{in}}$; that is,

$$G(\theta_0, \varphi_0) = \frac{4\pi P_{\mathrm{A}}(\theta_0, \varphi_0)}{P_{\mathrm{A}}^{\mathrm{in}}} \tag{1.13}$$

Analysis of (1.13) and (1.11) shows that the array gain and directivity relate to each other as

$$G(\theta_0, \varphi_0) = \eta D(\theta_0, \varphi_0) \tag{1.14}$$

where

$$\eta = P_{\Sigma} / P_{\mathrm{A}}^{\mathrm{in}} \tag{1.15}$$

is the coefficient taking into account the losses for absorption and reflection and thereby characterizing the array radiation efficiency.

Note that (1.11) and (1.13) do not account for polarization losses, which as a rule also take place in real antennas. To account for them, one should replace the total power pattern standing in the numerators of (1.11) and (1.13) by the power pattern corresponding only to the specified operating polarization.

1.2 Infinite Array Model

As we already noted, the edge effect on the element performance in large multielement linear and planar arrays with regular lattices may be weak, and then the majority of the array elements may be considered a part of an infinite periodic structure. Such a model is of great interest, since the analysis of the fields in it can be reduced to their consideration within only one array cell. This significantly simplifies the problem and at the same time reveals some important effects that may take place in large regular arrays.

1.2.1 Quasi-Periodic Excitation

Let the inputs of an infinite planar array with the lattice shown in Figure 1.2(a) be fed by signals with identical amplitudes and progressively varying phases so that the phase difference between adjacent columns is equal to $\quad_x$ and the phase difference between adjacent rows is equal to $\quad_y$. Let $\boldsymbol{j}^e(\boldsymbol{r})$ and $\boldsymbol{j}^m(\boldsymbol{r})$ be distributions of the electric and magnetic current densities formed in a finite region $V = V_{00}$ of the central cell with indices $m = n = 0$ [Figure 1.2(a)] as a result of such an excitation, which we will call quasi-periodic. Then, due to periodicity of the structure, the current distributions in other cells will repeat the amplitude and phase relations of the input signals; that is, the current densities in the region V_{mn} situated in the mnth array cell will obey the relation

$$\boldsymbol{j}_{mn}^{e,m}(\boldsymbol{r}) = \boldsymbol{j}^{e,m}(\boldsymbol{r} \quad \rho_{mn})\, e^{im \quad x + in \quad y} \tag{1.16}$$

where ρ_{mn} is determined according to (1.8).

The vector potentials corresponding to the current distributions (1.16) are determined by

$$A^{e,m}(\boldsymbol{r}) = \int_V \boldsymbol{j}^{e,m}(\boldsymbol{r}')G_P(\boldsymbol{r},\boldsymbol{r}')dV'$$

where

$$G_P(\boldsymbol{r},\boldsymbol{r}') = \frac{1}{4\pi}\sum_{m=-\infty}^{\infty}\sum_{n=-\infty}^{\infty}\frac{e^{ikR_{mn}}}{R_{mn}}e^{im\Delta\varphi_x+in\Delta\varphi_y} \tag{1.17}$$

is the Green's function for doubly periodic structures with quasi-periodic excitation, and $R_{mn}=|\boldsymbol{r}-\boldsymbol{r}'-\boldsymbol{\rho}_{mn}|$. Since (see, for instance, [3])

$$\frac{e^{ikR_{mn}}}{4\pi R_{mn}} = \frac{i}{8\pi^2}\int_{-\infty}^{\infty}\frac{1}{\gamma}e^{i\alpha(x-x'-x_{mn})+i\beta(y-y'-y_n)+i\gamma|z-z'|}d\alpha d\beta \tag{1.18}$$

where

$$\gamma = (k^2-\alpha^2-\beta^2)^{1/2} = i(\alpha^2+\beta^2-k^2)^{1/2}$$

and x_{mn} and y_n are determined by (1.8), we can apply the Poisson's summation formula [4] to (1.17) and rewrite the superposition of spherical waves there in the form of a superposition of plane waves

$$G_P(\boldsymbol{r},\boldsymbol{r}') = \frac{i}{2d_xd_y}\sum_{p=-\infty}^{\infty}\sum_{q=-\infty}^{\infty}\frac{1}{\Gamma_{pq}}e^{i\alpha_p(x-x')+i\beta_{pq}(y-y')+i\Gamma_{pq}|z-z'|}$$

$$= \frac{i}{2}\sum_{p,q}\frac{1}{\Gamma_{pq}}\psi_{pq}(\rho)\psi_{pq}^*(\rho')e^{i\Gamma_{pq}|z-z'|} \tag{1.19}$$

where $\rho = xe_x + ye_y$ and $\rho' = x'e_x + y'e_y$ are projections of the vectors $\boldsymbol{r}$ and $\boldsymbol{r}'$ on the horizontal plane,

$$\psi_{pq}(\rho) = \frac{1}{\sqrt{d_xd_y}}e^{i\alpha_px+i\beta_{pq}y} \tag{1.20}$$

$$\Gamma_{pq} = (k^2-w_{pq}^2)^{1/2} = i(w_{pq}^2-k^2)^{1/2},\quad w_{pq} = (\alpha_p^2+\beta_{pq}^2)^{1/2} \tag{1.21}$$

and the asterisk * denotes complex conjugation.

The coefficients α_p and β_{pq}, having the meaning of the transverse propagation constants of the plane waves in (1.19) and (1.20), are determined from (1.10), where the direction cosines u_0 and v_0 relate to the phases $\Delta\varphi_x$ and $\Delta\varphi_y$ as

$$u_0 = \frac{\Delta\varphi_x}{kd_x},\qquad v_0 = \frac{1}{kd_y}\left(\Delta\varphi_y - \frac{d_s}{d_x}\Delta\varphi_x\right) \tag{1.22}$$

Using the expressions for the electric and magnetic field strengths via the vector potentials [5]

$$\begin{aligned} \boldsymbol{E} &= \frac{1}{i\omega\varepsilon_0}[\quad(\quad \times \boldsymbol{A}^e) + k^2\boldsymbol{A}^e] \qquad \boldsymbol{A}^m \\ \boldsymbol{H} &= \frac{1}{i\omega\mu_0}[\quad(\quad \times \boldsymbol{A}^m) + k^2\boldsymbol{A}^m] + \qquad \boldsymbol{A}^e \end{aligned} \tag{1.23}$$

where ε_0 and μ_0 are the electric and magnetic constants for free space, we can represent the fields above the structure (for $z \quad z_{\max}$, where $z_{\max}$ is the upper limit of the source distribution in the longitudinal direction) in the form of expansions in terms of the vector wave functions called *Floquet modes*

$$\begin{aligned} \boldsymbol{E}(\boldsymbol{r}) = \eta_0 \sum_{p,q} [& kT_{1pq}\psi_{1pq}(\rho) + \Gamma_{pq}T_{2pq}\psi_{2pq}(\rho) \\ & w_{pq}T_{2pq}\psi_{pq}(\rho)\boldsymbol{e}_z]e^{i\Gamma_{pq}z} \end{aligned} \tag{1.24}$$

$$\begin{aligned} \boldsymbol{H}(\boldsymbol{r}) = \sum_{p,q} [& \Gamma_{pq}T_{1pq}\psi_{2pq}(\rho) \quad kT_{2pq}\psi_{1pq}(\rho) \\ & w_{pq}T_{1pq}\psi_{pq}(\rho)\boldsymbol{e}_z]e^{i\Gamma_{pq}z} \end{aligned} \tag{1.25}$$

where $\eta_0 = (\mu_0/\varepsilon_0)^{1/2}$ is the free space wave resistance, and

$$\psi_{1pq}(\rho) = \frac{\beta_{pq}\boldsymbol{e}_x \quad \alpha_p\boldsymbol{e}_y}{w_{pq}}\psi_{pq}(\rho) \tag{1.26}$$

$$\psi_{2pq}(\rho) = \frac{\alpha_p\boldsymbol{e}_x + \beta_{pq}\boldsymbol{e}_y}{w_{pq}}\psi_{pq}(\rho) \tag{1.27}$$

are vector functions of the transversal electric (TE) and transversal magnetic (TM) modes, respectively. The scalar function (1.20) as well as vector functions (1.26) and (1.27) are orthonormalized [6] so that

$$\begin{aligned} &\int_0^{d_x}\int_0^{d_y} \psi_{pq}(\rho)\psi_{p\,q}(\rho)dxdy = \delta_{p\,p}\delta_{q\,q} \\ &\int_0^{d_x}\int_0^{d_y} \psi_{jpq}(\rho) \times \psi_{j\,p\,q}(\rho)dxdy = \delta_{j\,j}\delta_{p\,p}\delta_{q\,q} \end{aligned} \tag{1.28}$$

The amplitudes of the Floquet modes in (1.24) and (1.25) are determined by formulas

$$T_{1pq}(u_0, v_0) = \frac{1}{2\Gamma_{pq}} \frac{w_{pq}I^m_{zpq} \quad \Gamma_{pq}I^m_{2pq}}{\eta_0 k} \quad I^e_{1pq\div} \tag{1.29}$$

$$T_{2pq}(u_0,v_0)=\frac{1}{2\Gamma_{pq}}\left[\frac{w_{pq}I^{e}_{zpq}-\Gamma_{pq}I^{e}_{2pq}}{k}+\frac{I^{m}_{1pq}}{\eta_0}\right] \tag{1.30}$$

containing integrals over the sources

$$I^{e,m}_{jpq}=\int_V j^{e,m}_{j}(\boldsymbol{r}')\psi_{jpq}(\boldsymbol{\rho}')e^{-i\Gamma_{pq}z'}\,dV', \qquad j=1,2 \tag{1.31}$$

$$I^{e,m}_{zpq}=\int_V j^{e,m}_{z}(\boldsymbol{r}')\psi_{pq}(\boldsymbol{\rho}')e^{-i\Gamma_{pq}z'}\,dV' \tag{1.32}$$

Note that since α_p and β_{pq} determine the grating lobe coordinates in the direction cosine space [Figure 1.2(b)] and simultaneously are the transverse propagation constants of the Floquet modes (1.24) and (1.25), each Floquet mode corresponds to one grating lobe of the array factor. At that, the propagating modes correspond to the lobe arranged in the visible space while the evanescent ones correspond to the lobes situated outside the latter.

1.2.2 Aperiodic Excitation

As indicated previously, the array element pattern corresponds to the case of supplying the excitation signal to only one array input while all the other inputs are terminated with matching loads. Let such an excited input be corresponding to the central cell with $m = n = 0$ [Figure 1.2(a)] and let a distribution of the electric and magnetic currents of density $\boldsymbol{J}^{e,m}_{m,0;n,0}(\boldsymbol{r})=\boldsymbol{J}^{e,m}_{0,0;0,0}(\boldsymbol{r}-\boldsymbol{\rho}_{m,n})$ be formed in the mnth cell as a result of the indicated excitation. The relation written earlier reflects the fact that the coefficients of mutual coupling between two elements in an infinite periodic array depend only on the differences of the indices prescribed to the elements.

Using the principle of superposition and coupling coefficients introduced earlier, we can express the relation of the latter to the current distributions (1.16) corresponding to the quasi-periodic excitation. In particular, the current densities in the central cell can be represented as

$$\begin{aligned}\boldsymbol{j}^{e,m}(\boldsymbol{r},x,y)&=\sum_{m=-\infty}^{\infty}\sum_{n=-\infty}^{\infty}\boldsymbol{J}^{e,m}_{0,m;0,n}(\boldsymbol{r})e^{im\Delta_x+in\Delta_y}\\&=\sum_{m=-\infty}^{\infty}\sum_{n=-\infty}^{\infty}\boldsymbol{J}^{e,m}_{0,0;0,0}(\boldsymbol{r})e^{-im\Delta_x-in\Delta_y}\end{aligned} \tag{1.33}$$

The expression (1.33) represents a double Fourier series whose coefficients are determined by

$$\boldsymbol{J}^{e,m}_{0,m;0,n}(\boldsymbol{r})=\frac{1}{4\pi^2}\int_{-\pi}^{\pi}\int_{-\pi}^{\pi}\boldsymbol{j}^{e,m}(\boldsymbol{r},x',y')e^{-im\Delta_x-in\Delta_y}\,d\Delta_x\,d\Delta_y \tag{1.34}$$

The pair of expressions (1.33) and (1.34) determines the relation between the currents induced in an infinite periodic array at its quasi-periodic excitation and the currents corresponding to its aperiodic excitation. Using (1.8) and (1.22), we can rewrite (1.33) in the form

$$\boldsymbol{j}^{e,m}(\boldsymbol{r}, u_0, v_0) = \sum_{m=} \sum_{n=} \boldsymbol{J}^{e,m}_{0,\ m;0,\ n}(\boldsymbol{r}) e^{\ ik(x_{mn}u_0 + y_n v_0)} \tag{1.35}$$

which will be applied later.

The far zone electric and magnetic field strength components corresponding to the excitation of the central cell input can be determined by general formulas [5]

$$\begin{aligned} E_\theta &= ik(\eta_0 A^e_{\theta,\ } + A^m_{\varphi,\ }), \quad H_\varphi = E_\theta / \eta_0 \\ E_\varphi &= ik(\eta_0 A^e_{\varphi,\ } - A^m_{\theta,\ }), \quad H_\theta = -E_\varphi / \eta_0 \end{aligned} \tag{1.36}$$

where $\boldsymbol{A}^{e,m}$ are the vector potentials in the far zone. They correspond to the currents in all the cells and therefore are determined as

$$\begin{aligned} \boldsymbol{A}^{e,m}(r,\theta,\varphi) &= \frac{e^{ikr}}{4\pi r} \sum_{m=} \sum_{n=} \int_{V_{mn}} \boldsymbol{J}^{e,m}_{m,0;n,0}(\boldsymbol{r}) e^{\ ik(x\,u + y\,v + z\,w)} dV \\ &= \frac{e^{ikr}}{4\pi r} \sum_{m=} \sum_{n=} \int_{V_{mn}} \boldsymbol{J}^{e,m}_{0,\ m;0,\ n}(\boldsymbol{r} - \boldsymbol{\rho}_{mn}) e^{\ ik(x\,u + y\,v + z\,w)} dV \\ &= \frac{e^{ikr}}{4\pi r} \int_{V} \sum_{m=} \sum_{n=} \boldsymbol{J}^{e,m}_{0,\ m;0,\ n}(\boldsymbol{r}) e^{\ ik[(x + x_{mn})u + (y + y_n)v + z\,w]} dV \end{aligned} \tag{1.37}$$

where the last line is written after replacement of the integration variables $x \to x + x_{mn}$, $y \to y + y_n$, and change for integration over the central cell only.

Using (1.35), let us rewrite (1.37) in the form

$$\begin{aligned} \boldsymbol{A}^{e,m}(r,\theta,\varphi) &= \frac{e^{ikr}}{4\pi r} \int_{V} \boldsymbol{j}^{e,m}(\boldsymbol{r}, u, v) e^{\ ik(x\,u + y\,v + z\,w)} dV \\ &= \sqrt{d_x d_y}\, \frac{e^{ikr}}{4\pi r} \int_{V} \boldsymbol{j}^{e,m}(\boldsymbol{r}, u, v) \psi_{00}(\rho) e^{\ ikz\,w} dV \end{aligned} \tag{1.38}$$

where parameters u_0 and v_0 in (1.20) have been replaced by u and v, respectively.

The vector potential components in the spherical coordinates are determined via their Cartesian components as

$$\begin{aligned} A_\theta &= A_x \cos\theta \cos\varphi + A_y \cos\theta \sin\varphi - A_z \sin\theta \\ A_\varphi &= -A_x \sin\varphi + A_y \cos\varphi \end{aligned} \tag{1.39}$$

If we replace u_0 and v_0 in (1.10) by u and v, respectively, and account for (1.21), we can rewrite (1.39) as

$$\begin{aligned} A_\theta &= \frac{\Gamma_{00}}{w_{00}k}(\alpha_0 A_x + \beta_{00} A_y) \quad \frac{w_{00}}{k} A_z \\ A_\varphi &= \quad \frac{1}{w_{00}}(\beta_{00} A_x \quad \alpha_0 A_y) \end{aligned} \tag{1.40}$$

Determining the Cartesian components from (1.38) and substituting them in (1.40), we obtain

$$\begin{aligned} A_{\theta,}^{e,m} &= \sqrt{d_x d_y}\, \frac{e^{ikr}}{4\pi r} \frac{w_{00} I_{z00}^{e,m} \quad \Gamma_{00} I_{200}^{e,m}}{k} \\ A_{\varphi,}^{e,m} &= \sqrt{d_x d_y}\, \frac{e^{ikr}}{4\pi r} I_{100}^{e,m} \end{aligned} \tag{1.41}$$

where expressions (1.31) and (1.32) have also been taken into account. Finally, substituting (1.41) in (1.36), as well as accounting for (1.29) and (1.30), we obtain the following expressions

$$\begin{aligned} E_\theta &= \eta_0 H_\varphi = \frac{e^{ikr}}{r} F_\theta \\ E_\varphi &= \quad \eta_0 H_\theta = \frac{e^{ikr}}{r} F_\varphi \end{aligned} \tag{1.42}$$

where

$$F_\theta(\theta,\varphi) = \quad \frac{ik^2\eta_0}{2\pi}\sqrt{d_x d_y}\, T_{200}(u,v)\cos\theta \tag{1.43}$$

$$F_\varphi(\theta,\varphi) = \frac{ik^2\eta_0}{2\pi}\sqrt{d_x d_y}\, T_{100}(u,v)\cos\theta \tag{1.44}$$

are components of the array element pattern.

Expressions (1.43) and (1.44) determine an important relation revealed earlier in another way [6] between the array radiation characteristics at the quasi-periodic and aperiodic excitations: the array element pattern components are proportional to the amplitudes of the TE and TM Floquet modes of zero order, multiplied by cosine of the angle between the array broadside and direction to the observation point.

Let now $M \quad N$ elements in an infinite array be excited with identical amplitudes and progressive phases corresponding to scan the main beam to angles θ_0 and φ_0. Then the flux density of the power radiated in the beam direction, where contributions from all the excited elements add in phase, will be equal to

$$\frac{1}{2}\mathrm{Re}[\boldsymbol{E} \quad \boldsymbol{H}^*]\boldsymbol{e}_{r0} = \frac{M^2N^2}{2r^2\eta_0}|\boldsymbol{F}(\theta_0,\varphi_0)|^2 \tag{1.45}$$

where $\boldsymbol{e}_{r0}$ is the unit vector of the beam direction (1.6), and $\boldsymbol{F}(\theta_0, \varphi_0)$ is the vector element pattern with components (1.43) and (1.44) corresponding to input power P^{in} supplied to each excited element. Then dividing (1.45) by the flux density $MNP^{\text{in}}/4\pi r^2$ corresponding to a uniform distribution of the total input power over a sphere of radius r, we obtain the following formula for the gain of the array fragment in question:

$$G(\theta_0, \varphi_0) = MNg(\theta_0, \varphi_0) \tag{1.46}$$

where

$$g(\theta, \varphi) = \frac{2\pi}{P^{\text{in}}\eta_0} |\boldsymbol{F}(\theta, \varphi)|^2 \tag{1.47}$$

is the factor representing the array element gain.

The expressions (1.46) and (1.47) demonstrate that the dependence of the array gain on the scan angles exactly repeats the dependence of the array element pattern on the angles of observation. This property once more underlines the importance of the array element pattern concept in the array antenna theory.

1.3 Ideal Element Pattern

1.3.1 The Highest Level

In practice, it is always desirable to radiate the power supplied to the array inputs without any losses in the direction of the main array beam scanning in a specified region. In this case, the array gain achieves its maximum level, and the element pattern corresponding to such a situation is considered the ideal element pattern [1, 6, 7]. To determine the level and angular dependence of the ideal element pattern in an infinite array, let us consider a quasi-periodic excitation at which each array element is fed with power P^{in} and the radiated field is determined by superpositions of the Floquet modes (1.24) and (1.25). The power that the array radiates in the perpendicular direction through a plane surface parallel to the array aperture plane per one array cell is determined by integration of the flux density $\text{Re}[\boldsymbol{E} \times \boldsymbol{H}^*]\boldsymbol{e}_z/2$ over a rectangle of dimensions $d_x \times d_y$. Since the input power is to be radiated without losses (i.e., completely), the result of integration must be equal to P^{in}. Moreover, since all the radiated power is to be going in the main lobe corresponding to the Floquet modes of the zero order in (1.24) and (1.25), then, substituting (1.24) and (1.25) in the expression for the flux density and integrating it with account for orthogonality relations (1.28) and the fact that $\Gamma_{00}(kb\sin\theta) = k\cos\theta$, we obtain

$$\frac{1}{2}(|T_{100}|^2 + |T_{200}|^2)\eta_0 k^2 \cos\theta = P^{\text{in}} \tag{1.48}$$

Using now (1.48), (1.44), and (1.45), we finally obtain the following expression for the ideal power array element pattern:

$$P_{\mathrm{id}}(\theta,\varphi)=\frac{1}{2\eta_0}|F_{\mathrm{id}}(\theta,\varphi)|^2=P^{\mathrm{in}}\frac{d_x d_y}{\lambda^2}\cos\theta \tag{1.49}$$

Thus, the level of the ideal power element pattern is determined by the product of the power supplied to the element input, the array cell area in squared wavelengths, and the cosine of the observation angle measured from the broadside.

The ideal vector (amplitude) element pattern is determined from (1.49) as

$$\boldsymbol{F}_{\mathrm{id}}(\theta,\varphi)=\sqrt{2P^{\mathrm{in}}\eta_0\frac{d_x d_y\cos\theta}{\lambda^2}}\boldsymbol{p}(\theta,\varphi) \tag{1.50}$$

where $\boldsymbol{p}(\boldsymbol{\theta}, \boldsymbol{\varphi})$ is a factor characterizing the polarization of the radiated field—for instance,

$$\boldsymbol{p}(\theta,\varphi)=\boldsymbol{e}_\theta\sin\varphi+\boldsymbol{e}_\varphi\cos\varphi \tag{1.51}$$

for vertical polarization,

$$\boldsymbol{p}(\theta,\varphi)=\boldsymbol{e}_\theta\cos\varphi\quad\boldsymbol{e}_\varphi\sin\varphi \tag{1.52}$$

for horizontal polarization, and

$$\boldsymbol{p}(\theta,\varphi)=\frac{\boldsymbol{e}_\theta\mp i\boldsymbol{e}_\varphi}{\sqrt{2}}e^{\pm i\varphi} \tag{1.53}$$

for circular polarization of that or another rotation, while $\boldsymbol{e}_\theta$ and $\boldsymbol{e}_\varphi$ are unit vectors of the corresponding spherical coordinates.

Note that the highest possible level of the power and amplitude element patterns determined by (1.49) and (1.50) corresponds to the far field components written in the form (1.42). Therefore, appearance of any factors in the expression for the far field should be appropriately accounted for in the expressions for the ideal element patterns.

Substitution of (1.50) in (1.47) yields the well-known expression for the ideal array element gain [7]

$$g_{\mathrm{id}}(\theta,\varphi)=\frac{4\pi d_x d_y}{\lambda^2}\cos\theta \tag{1.54}$$

The expression (1.54) allows for a simple interpretation [7] resulting from the expression $4\pi A/\lambda^2$ for the gain of a planar uniformly excited aperture of large area A. Since the array gain equals to the product of the element gain by the number of the elements (1.46), the element gain is derived from the gain of the array aperture

with replacement of area A by the area of the cell allotted to one array input, and the multiplication by $\cos\theta$ corresponds to projecting of the cell area onto the plane perpendicular to the observation point direction. This simple reasoning was put in the basis of the work [7], while (1.54) here is the result of a rigorous derivation published initially in [8, 9].

1.3.2 Contours of the Ideal Element Pattern

At sufficiently small interelement spacings (e.g., at $d_x = d_y < \lambda/2$ in a square lattice or at $d_x < \lambda/\sqrt{3}$ in a hexagonal lattice), the secondary grating lobes of the array factor (1.9) cannot appear in the visible space at any position of the main lobe in that space. Therefore, the expressions for the ideal power and amplitude element patterns (1.49) and (1.50) corresponding to radiation of the whole input power in the main lobe are valid for any angles in the visible space. If, on the contrary, the element spacings are sufficiently large (e.g., $d_x = d_y > \lambda/\sqrt{2}$ in the square lattice or $d_x > 2\lambda/3$ in the hexagonal lattice), at least one secondary grating lobe can enter the visible space when steering the main lobe to some positions. Such a situation considered in [10, 11] in the context of the ideal element pattern is typical for practice since the beam scanning in planar arrays is required as a rule only in some part of the visible space rather than in the whole space, and the array designers try to meet that requirement at maximum admissible element spacings. In this case, the radiation of the whole input power in the main lobe can be provided if the array element pattern suppresses the grating lobes appearing in the visible space when scanning the main lobe. In other words, the ideal element pattern must be equal to zero in the region of the grating lobe movement and have the highest level (1.49) or (1.50) in the region of the main lobe scanning. At the same time, the scan region of the main lobe must be as wide as possible.

Thus, together with the highest level (1.49) or (1.50), the definition of the ideal array element pattern includes the concept of the maximum single-beam scan region, which we denote as . The area of the region under the condition that it is completely arranged inside the unit circle in the direction cosine space is evidently equal to $S = \lambda^2/(d_x d_y)$ because just that area is allotted to each grating lobe, as shown in Figure 1.2(b). Therefore, the simplest maximum scan region and correspondingly ideal contour element pattern is the gray rectangle in Figure 1.2(b). Each position of the beam in this rectangle is determined by a single pair of control phase values lying in an interval of 2π. However, the contour shape satisfying the requirements of the area and one-to-one correspondence between the control phases and beam position may vary. Some examples of possible ideal element pattern contours for rectangular lattices are given in Figure 1.3. The scan region shown in Figure 1.3(a) consists of two adjacent parallelograms with base λ/d_x and height $\lambda/(2d_y)$. The contour shown in Figure 1.3(b) is formed by two shifted 120° arcs of radius $\lambda\sqrt{3}/(2d_y)$ and two straight horizontal segments of length λ/d_x. Apart from the singly connected contours like those just considered, the ideal scan region can be a multiply connected one and the ideal contour element patterns can correspondingly be multibeam pattern. For instance, the contour presented in Figure 1.3(c) consists of two rectangles of width $\lambda/(2d_x)$ and height λ/d_y arranged with a gap of λ/d_x. In this case, the beam scanning in one subregion corresponds to negative phase differ-

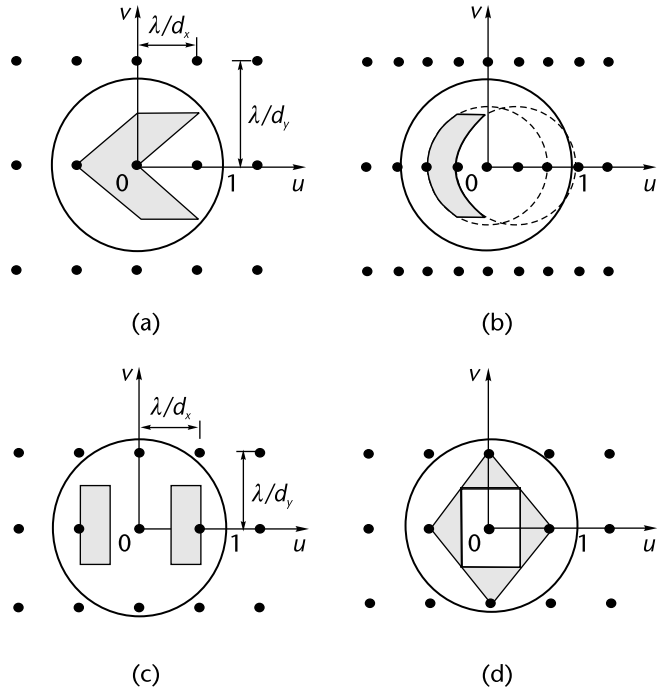

Figure 1.3 (a–d) Contours of the ideal element pattern of array with rectangular lattice.

ence between the adjacent array columns, while the scanning in another subregion is performed with positive phase difference. The scan region in Figure 1.3(d) consists of four isosceles triangles with bases equal to λ/d_x for the upper and lower triangles and λ/d_y for the left-hand and right-hand ones. All their lateral sides are identical and equal to $\lambda\sqrt{d_x{}^2 + d_y{}^2}\,/2$. Note that the areas of subregions in a multiply connected scan region may, in principle, be nonidentical. For instance, instead of the identical rectangles in Figure 1.3(c), one may have width $\quad, 0 < \quad < \lambda/d_x$, while the width of the other will then be $\lambda/d_x \quad$, and the left side of the left-hand rectangle must be at the distance $2\lambda/d_x$ from the right side of the right-hand rectangle.

Some examples of the ideal contours for a hexagonal lattice are presented in Figure 1.4. They can be an ordinary equilateral hexagon of side $2\lambda/(3d_x)$ [Figure 1.4(a)] and a parallelogram of width λ/d_x and lateral side length λ/d_y [Figure 1.4(b)]. The angle α in the parallelogram must obey only the condition that the parallelogram is completely situated within the unit circle corresponding to the visible space. Two starlike multiply connected ideal contours are presented in Figure 1.4(c, d). One consists of six identical equilateral triangles with side length $2\lambda/(3d_x)$, while the other comprises six isosceles triangles with base length $2\lambda\sqrt{3}\,/d_x$ and lateral side length $2\lambda/(3d_x)$.

Although exotic, some of the contours considered here may be of practical interest. For instance, using two hexagonal arrays with the element patterns shown in Figures 1.4(c, d), one can cover a biconical (annular in the direction cosine space) scan region as demonstrated in Figure 1.5(a) that is required in some modern applications of satellite communications and telecasting [12, 13]. The same region may also be covered by three arrays with the element patterns shown in Figure 1.3(b)

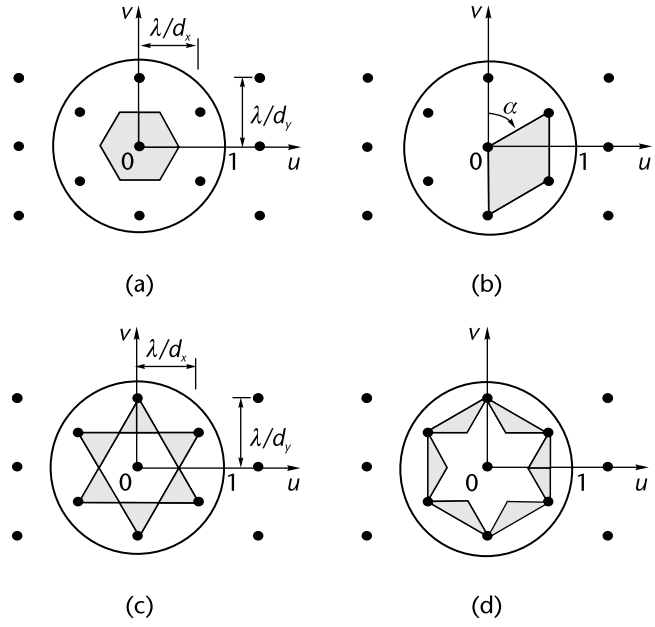

Figure 1.4 (a–d) Contours of the ideal element pattern of array with hexagonal lattice.

by arranging these arrays in one plane at an angle of 120° to each other, as shown in Figure 1.5(b).

1.3.3 Element Gain on Ideal Contour

One of the properties of the ideal element pattern contour is that if the main lobe gets to the contour, at least one grating lobe must appear in another place on the contour. Such a situation can be seen in Figures 1.3 and 1.4. In these cases, the radiated power is distributed among the main and secondary grating lobes, and the expression (1.54) for the element gain should be corrected. This can be done by multiplying (1.54) by correction factor $\xi = P_0/P$ equal to the power concentrated in the main lobe divided by the total radiated power.

Let us first consider the simplest cases. Assume that one of the lobes arranged on the contour depicted in Figure 1.3(c) is the main one. Then we have $\xi = 1/2$ for

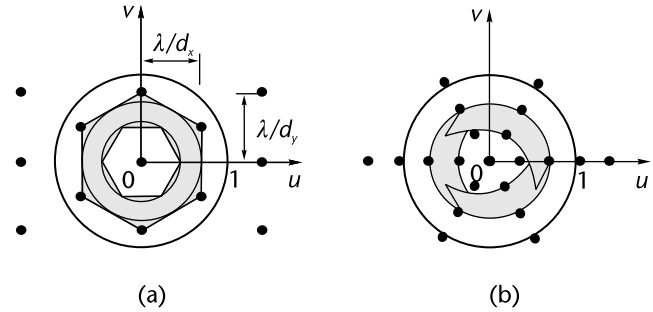

Figure 1.5 (a, b) Application of the element patterns shown in Figure 1.4(c, d), as well as in Figure 1.3(a) for covering annular scan region.

the symmetry. If the main lobe falls upon the ideal scan region boundary, as shown in Figure 1.4(c, d), then $\xi = 1/6$ also for the symmetry. If the main lobe scans from the center of the scan region in Figure 1.4(a) to the right-hand corner, then two grating lobes will occupy the left-hand upper and lower corners of the equilateral hexagon. A symmetric configuration of the three lobes will be formed in this case, and, therefore, $\xi = 1/3$.

In general case, as shown in Appendix 1A, the correction factor is determined by

$$\xi = \frac{\alpha}{2\pi} \tag{1.55}$$

where α is the angle at which the scan region (or its part) is seen from the point of the main lobe position. Let us consider the contour shown in Figure 1.4(b). If the main lobe is arranged in the upper corner of the contour, the correction factor is determined by (1.55). If the main lobe is placed on the left side or in the right lower corner, then $\xi = 1/2$ or $\xi = (1 \quad \alpha/\pi)/2$, respectively. The value $\xi = 1/2$ is valid for beam arrangement not only on straight sections, but also on any smooth curvilinear sections of an ideal contour, such as, for instance, the contour shown in Figure 1.3(b). For the contour shown in Figure 1.3(a), $\xi = \arctan(d_x/2d_y)/\pi$ when the beam is placed in the left corner, and $\xi = 1 \quad \arctan(d_x/2d_y)/\pi$ when it is placed in the right corner point (in the coordinate system origin). If the beam is arranged in the upper or lower corners of the contour shown in Figure 1.3(d), then $\xi = \arctan(d_y/d_x)/\pi$, while the beam arrangement in the right or left corners gives $\xi = \arctan(d_x/d_y)/\pi$.

Note that the sum of the angles at which an ideal scan region is seen from the points of all the lobes situated on scan region contour is constant and equal to 2π. The factor (1.55) can be used not only when the main lobe is situated on the ideal contour but also when it is arranged inside the scan region since $\alpha = 2\pi$ in this case and hence $\xi = 1$.

1.3.4 Ideal Element Efficiency and Mutual Coupling

To reveal some other properties of the array element having the ideal radiation pattern (1.49), let us consider the array element efficiency η_e. This parameter was introduced in [7] and additionally studied in [14]. The ideal element efficiency can be calculated by formula (1.15) where power P_{A}^{in} should be replaced by power P^{in} supplied to the input of one element only. Furthermore, one should substitute the ideal element pattern (1.49) in the total radiated power (1.12) instead of $P_{\text{A}}(\theta,\varphi)$ and perform the integration only over the ideal single-beam scan region outside of which the pattern element pattern is equal to zero. Taking into account that the angular variables in the integral can be replaced by the direction cosines as

$$\sin\theta d\theta d\varphi = \frac{dudv}{\sqrt{1 \quad u^2 \quad v^2}} \tag{1.56}$$

as well as that $\cos\theta = \sqrt{1 \quad u^2 \quad v^2}$, we obtain

$$\eta_e = \frac{S}{\lambda^2/(d_x d_y)} \tag{1.57}$$

Thus, the ideal element efficiency is determined by the ratio of maximum scan region area and the area of a periodic cell in the grating lobe lattice on the direction cosine plane.

In case of sufficiently large element spacings when the periodic cell is totally situated inside the unit circle representing the visible space, this cell itself is the maximum scan region of area $\lambda^2/(d_x d_y)$, and the ideal element efficiency (1.57) is equal to unity or 100%. As already noted, such a situation takes place at $d_x = d_y \quad \lambda/\sqrt{2}$ for a square lattice and at $d_x \quad 2\lambda/3$ for a hexagonal one.

In the opposite case (i.e., when the element spacings are small enough), the maximum single-beam scan region occupies the whole visible space. Its area equals the area of the unit circle $S \quad = \pi$, and the ideal element efficiency (1.57) takes the form [7, 14]

$$\eta_e = \frac{\pi d_x d_y}{\lambda^2} \tag{1.58}$$

valid at $d_x \quad \lambda/2$ for a square lattice and at $d_x \quad \lambda/\sqrt{3}$ for a hexagonal lattice.

In the intermediate case, the periodic cell covers a part of the visible space and partially goes out of the boundary of the latter. The maximum scan region therefore represents a figure formed by interception of the cell with the unit circle as shown in grey in the insets of Figure 1.6. One of the examples here is the square lattice with square unit cell. Calculating the area of interception of the square with the unit circle $S \quad$ and substituting it in (1.57), we obtain

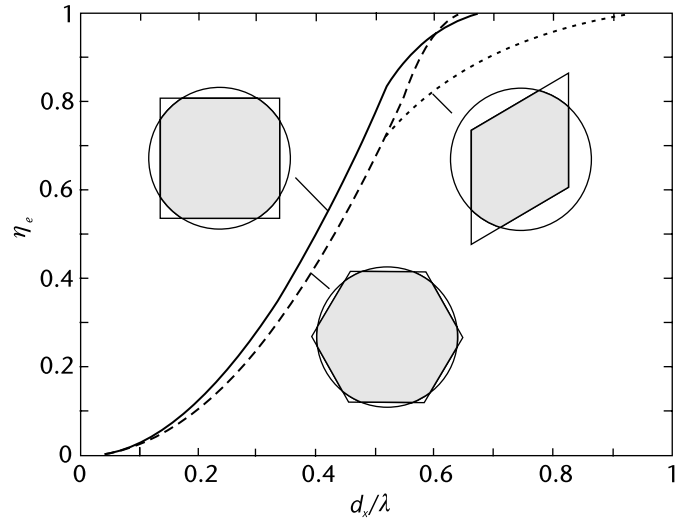

Figure 1.6 Ideal array element efficiency versus element spacing in square and hexagonal lattices.

$$\eta_e = \sqrt{\frac{4d_x^2}{\lambda^2} \quad 1} + \frac{4d_x^2}{\lambda^2} \quad \frac{\pi}{4} \quad \arcsin\sqrt{1 \quad \frac{\lambda^2}{4d_x^2}} \div \div \tag{1.59}$$

for element spacing $\lambda/2 \quad d_x \quad \lambda/\sqrt{2}$.

Similar calculations for a hexagonal array with element spacing $\lambda/\sqrt{3} \quad d_x \quad 2\lambda/3$ and when the periodic cell in the direction cosines space is taken in the form of equilateral hexagon give

$$\eta_e = \sqrt{3} \quad \sqrt{\frac{3d_x^2}{\lambda^2} \quad 1} + \frac{3d_x^2}{\lambda^2} \quad \frac{\pi}{6} \quad \arcsin\sqrt{1 \quad \frac{\lambda^2}{3d_x^2}} \div \div \tag{1.60}$$

Variations of the ideal element efficiency with element spacing for the cases of the square and hexagonal arrays considered earlier are shown in Figure 1.6 by a solid curve and a curve with large dashes, respectively. As we see, the initial section of the curve corresponding to formula (1.58) for the hexagonal array goes below the curve for the square array. This takes place because of a denser arrangement of the elements in the hexagonal array compared to the square one at identical element spacing d_x in the rows.

Note the ideal array element efficiency can depend not only on the type of the lattice as demonstrated and shown earlier in [14] but also on the shape of the scan region ideal for the specified lattice. For example, instead of the equilateral hexagon, we take a rhomb of the same area and with smaller angle of 60°, as shown in Figure 1.6, and the 100% element efficiency is realized at $d_x \quad \lambda$ (i.e., at the greater minimum value of spacing), while formula (1.58) is valid only for $d_x \quad \lambda/2$ (i.e., for the smaller maximum value for spacing). The element efficiency for the intermediate values of the element spacing is determined in this case as

$$\eta_e = \begin{array}{c} \sqrt{\frac{3d_x^2}{\lambda^2} \quad \frac{3}{4}} + \frac{d_x^2\sqrt{3}}{\lambda^2} \quad \frac{\pi}{2} \quad 2\arcsin\sqrt{1 \quad \frac{\lambda^2}{4d_x^2}} \div \div \\ \lambda/2 \quad d_x \quad \lambda/\sqrt{3} \\ \frac{1}{2} \quad \frac{1}{2} + \sqrt{\frac{3d_x^2}{\lambda^2} \quad \frac{3}{4}} \div + \frac{d_x^2\sqrt{3}}{\lambda^2} \quad \frac{\pi}{3} \quad \arcsin\sqrt{1 \quad \frac{\lambda^2}{4d_x^2}} \div \\ \lambda/\sqrt{3} \quad d_x \quad \lambda \end{array} \tag{1.61}$$

and the curve calculated according to (1.61) is shown in Figure 1.6 with small dashes.

The concept of the element efficiency is closely associated with important phenomena, such as interaction or coupling between array elements. This interaction has a few components [7]. In particular, it can act as coupling between the array inputs (coupling in the backward direction) and as coupling between

the array inputs and the radiators in the array aperture (coupling in the forward direction). The 100% element efficiency corresponds to the complete absence of coupling between the inputs (i.e., the backward coupling coefficients are equal to zero). From this fact and formula (1.33), we can conclude that the amplitudes of reflected waves at the quasi-periodical excitation of an array with such ideal elements are also equal to zero, and this takes place at any values of control phases. The array in this case is called ideally matched [7] or unconditionally matched [6, 15].

As already noted, for sufficiently small element spacing, the periodic cell on the direction cosine plane completely or partially covers the unit circle corresponding to the visible space (the examples for the latter case are given in Figure 1.6). At quasi-periodic excitation of an array with such ideal elements, the power supplied to the inputs is completely radiated in the main lobe while it is situated in the ideal scan region. Theoretical possibility of such an ideal match has been proven in [16]. However, there exist some values of the control phases at which the main lobe is steered in the sections of the periodic cell situated beyond the unit cell and, at the same time, the grating lobes are situated outside the ideal scan region. Since the main lobe is not present in the visible space and those grating lobes that have entered there are suppressed by the ideal element pattern, there is no power radiated in the visible space. That means that the power supplied to the array is totally reflected back to the feeding system. So, the reflections in the array of ideal elements are not absent for all values of the control phases, and for this reason such an array has been called *conditionally matched* in [6, 15]. Since the amplitudes of the reflected modes at the quasi-periodic excitation are not equal to zero in some range of the control phase values, the backward mutual coupling coefficients determined by formula similar to (1.34) are already not equal to zero, and as a result, the ideal element efficiency is below 100%.

1.3.5 On Realizability of the Ideal Contour Element Pattern

It is well known (e.g., [5]) that field distribution over an aperture and its radiation pattern relate to each other via Fourier transform. As described earlier, the ideal element pattern corresponding to the 100% element efficiency is a contour one (i.e., is a function of observation angles having a jump from nonzero values in the scan region down to zero outside). Nonzero values of the Fourier transform of such a function determining the amplitude of excitation are distributed over the whole infinite aperture. That means that each array input must be coupled with all the radiators in the aperture, and therefore the forward mutual coupling must be realized in the array in the absence of backward coupling. Excitation of all the array inputs results in forming of overlapped aperture distributions, and for this reason the array may be considered an antenna consisting of controlled elements in the form of overlapped subarrays.

The amplitude distribution over the subarray aperture corresponding to the ideal contour element pattern may vary considerably even within one array cell. For instance, the distribution $\sin(\pi x/d)/(\pi x/d)$ corresponding to a sector pattern of width $2\arcsin(0.5\lambda/d)$, where d is the array cell dimension, changes the sign in the limits of each lateral cell. One of the possible approaches to forming similar

aperture distributions consists of making use of radiators of sufficiently small transverse dimensions densely arranged in the array aperture. However, as described in the previous section, the radiators arranged in a dense lattice have low radiation efficiency because of the backward mutual coupling. For this reason, the question about the fundamental possibility of forming the ideal contour element pattern corresponding to the 100% element efficiency by means of a subarray of closely spaced low efficient radiators requires a special analysis. Such analysis reported earlier in [17, 18] is reproduced next.

Let us consider an infinite array whose inputs are arranged in the nodes of the skew lattice shown in Figure 1.2(a). Each array cell of dimensions d_x d_y is filled in by radiators forming a dense lattice with spacing $a = d_x/M$ in the horizontal rows and distance $b = d_y/N$ between adjacent rows shifted at $= d_s/M$ in the horizontal direction, where M and N are some positive integer numbers. The radiators are assumed to be ideal (i.e., conditionally matched). The aperture geometry of such an array is shown in Figure 1.7(a).

Let the central array input be fed by a signal of power P^{in}, and this power is further distributed without losses and reflections through a hypothetical beam-forming network over the subarray radiators as shown in Figure 1.7(b). All the other array

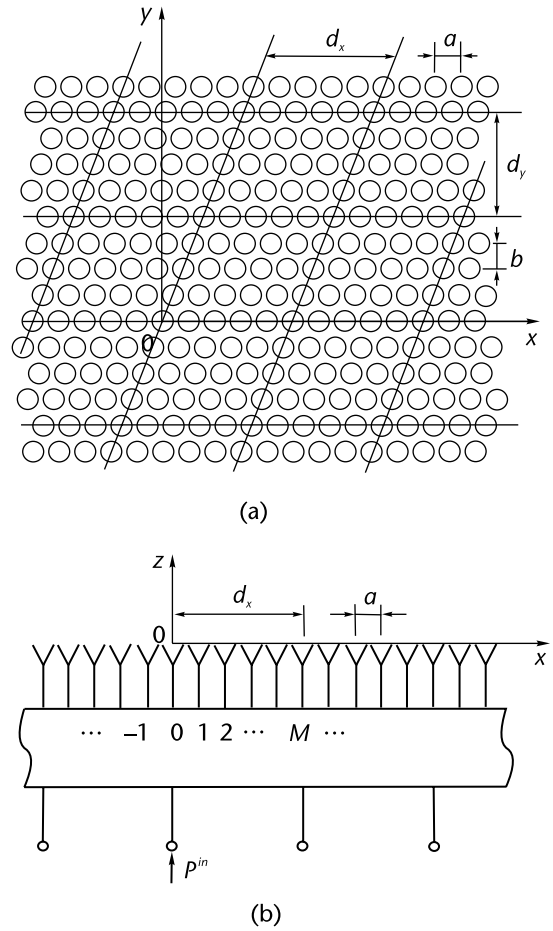

Figure 1.7 Dense array geometry (a) in the aperture plane and (b) in the 0*xz* plane.

inputs are assumed to be terminated with matching loads. We represent the power coming to the pqth radiator as a product $P|A_{pq}|^2$, where A_{pq} is a dimensionless amplitude coefficient and P is a common factor having dimension of power and determined from the condition

$$P \sum_{p=} \sum_{q=} |A_{pq}|^2 = P^{\text{in}} \tag{1.62}$$

resulting from the energy conservation law. Then, noting that the radiators filling in the aperture with spacings a and b are ideal as assumed earlier, we can write the subarray radiation pattern in the form

$$\boldsymbol{F}(\theta,\varphi) = \sqrt{2P\eta_0 \frac{ab\cos\theta}{\lambda^2}}\boldsymbol{p}(\theta,\varphi)F_{\text{AF}}(u,v) \tag{1.63}$$

where the product of the first two factors represents the ideal radiator pattern (1.50) where all the mutual couplings are taken into account and

$$F_{\text{AF}}(u,v) = \sum_{p=} \sum_{q=} A_{pq} e^{\,ik(x_{pq}u+y_q v)} \tag{1.64}$$

is the subarray factor where $x_{pq} = pa + q\ /M$ and $y_q = qb$ are coordinates of the pqth radiator and (u, v) are direction cosines of the observation point.

The cosine behavior of the subarray pattern has already been accounted for in the first factor of (1.63). So, it is appropriate to determine the amplitude distribution over the subarray aperture as the Fourier transform of the function equal to unity inside the ideal scan region and zero outside it (i.e., of the window function corresponding to the ideal contour element pattern). Choosing the samples of that transform in the points corresponding to the radiator coordinates, we write the amplitudes of the radiator excitation as

$$A_{pq} = \int\int e^{ik(x_{pq}u + y_q v)}\,du\,dv \tag{1.65}$$

Substituting (1.65) in (1.64) and taking into account the well-known properties of the delta function, in particular,

$$\sum_{p=} e^{ipx} = 2\pi \sum_{p=} \delta(x + 2\pi p) \tag{1.66}$$

$$\delta(\alpha x) = \frac{1}{|\alpha|}\delta(x) \tag{1.67}$$

we obtain

$$F_{\text{AF}}(u,v) = \frac{\lambda^2}{ab} \tag{1.68}$$

for (u, v) inside and $F_{AF}(u,v) = 0$ for (u, v) outside . Note that being a periodic function, the subarray factor (1.64) has other regions in the (u, v) space where it is not equal to zero either. However, those regions for sufficiently small spacings a and b are situated beyond the visible space and therefore they give no contribution.

Let us now consider the condition (1.62). Taking the distribution (1.65) into account, we can write

$$|A_{pq}|^2 = \quad du\, dv \qquad e^{ikx_{pq}(u \quad u)+iky_q(v \quad v)} du dv \qquad (1.69)$$
$$p= \quad q= \qquad\qquad p= \quad q=$$

Using the properties (1.68) and (1.69) again, we will see that the integration over u and v gives the value (1.68) in the scan region , and the integration over u and u gives just the ideal scan region area $\lambda^2/(d_x d_y)$. Therefore,

$$|A_{pq}|^2 = \frac{\lambda^2}{ab}\frac{\lambda^2}{d_x d_y}$$
$$p= \quad q=$$

and we determine from (1.62) that

$$P = P^{\text{in}}\frac{ab}{\lambda^2}\frac{d_x d_y}{\lambda^2} \qquad (1.70)$$

Finally, substituting (1.68) and (1.70) in (1.63) and comparing the result to (1.50) we will see that $F(\theta,\varphi) \quad F_{\text{id}}(\theta,\varphi)$.

Thus, the ideal contour array element pattern corresponding to the 100% element efficiency and absence of the backward mutual coupling can in principle be formed by an infinite subarray of closely spaced ideal radiators despite that each such radiator excited in the subarray individually has low efficiency corresponding to the presence of backward mutual coupling. The appropriate amplitude distribution over the subarray aperture is determined by Fourier transform (1.65) of the ideal contour element pattern divided by $\sqrt{\cos\theta}$ (i.e., of the corresponding window function). The reflected modes in this case are completely compensated for just as it takes place at a quasi-periodic array excitation, while the main lobe remains in the visible space.

1.3.6 Properties of Orthogonality

General formulas (1.42) determine the far field corresponding to excitation of the central array element by a signal of power P^{in}. If this power is supplied to the input of the mnth element forming the ideal radiation pattern, the far field can be written as

$$\boldsymbol{E}^{mn}(r,\theta,\varphi) = \frac{e^{ikr}}{r}\boldsymbol{F}_{\text{id}}(\theta,\varphi)e^{\ ik(x_{mn}u+y_n v)}$$
$$\boldsymbol{H}^{mn}(r,\theta,\varphi) = \frac{1}{\eta_0}[\boldsymbol{e}_r \quad \boldsymbol{E}^{mn}(r,\theta,\varphi)] \qquad (1.71)$$

where the exponential factor accounts for the *mn*th element position, whose coordinates x_{mn} and y_n are determined in (1.8). The product of the second and third factors in the upper line of (1.71) represents the ideal *mn*th element pattern $\boldsymbol{F}_{\mathrm{id}}^{mn}(\theta,\varphi)$ in the general coordinate system shown in Figures 1.2(a) or 1.7(a).

Let us consider the product of the far fields of the *mn*th and *m n* th elements in the form

$$\left\langle \boldsymbol{E}^{mn}, \boldsymbol{H}^{m\,n} \right\rangle = \frac{1}{2} \int_0^{2\pi} \int_0^{\pi} [\boldsymbol{E}^{mn} \quad \boldsymbol{H}^{m\,n}\ ] \times \boldsymbol{e}_r r^2 \sin\theta d\theta d\varphi$$
$$= \frac{1}{2\eta_0} \int_0^{2\pi} \int_0^{\pi} \boldsymbol{F}_{\mathrm{id}}^{mn}(\theta,\varphi) \times \boldsymbol{F}_{\mathrm{id}}^{m\,n}\ (\theta,\varphi) \sin\theta d\theta d\varphi \tag{1.72}$$

where the lower line obtained from the upper one using (1.71) is a scalar product of the ideal *mn*th and *m n* th element patterns $\left\langle \mathbf{F}_{\mathrm{id}}^{mn}, \mathbf{F}_{\mathrm{id}}^{m\,n} \right\rangle$. The asterisk in (1.72) denotes complex conjugation. Replacing the angular coordinates in (1.72) by the direction cosines according to (1.56) and assuming that ideal element pattern is the contour one, we can rewrite (1.72) as

$$\left\langle \boldsymbol{F}_{\mathrm{id}}^{mn}, \boldsymbol{F}_{\mathrm{id}}^{m\,n} \right\rangle = P^{\mathrm{in}} \frac{d_x d_y}{\lambda^2} \int_{\Omega} e^{ik[(x_{m\,n} \quad x_{mn})u + (y_n \quad y_n)v]} du dv \tag{1.73}$$

The integral similar to that standing in (1.73) has been considered in [6, Chapter 7, Appendix 2] to prove the orthogonality of the transverse wave functions (1.20), (1.26) and (1.27) of the Floquet modes. At $m = m$ and $n = n$, this integral is just equal to the area $S = \lambda^2/(d_x d_y)$ that the ideal contour element pattern occupies on the direction cosines plane. If the inputs are different, the integral in (1.73) is equal to zero. This fact is easy to prove using the periodicity of the integrand along the rows and columns. If the ideal region is not rectangular, the indicated periodicity allows us to transform it into a rectangle of dimensions $(\lambda/(d_x) \quad (\lambda/(d_y)$, and the equality of the integral to zero can be inspected directly. Thus,

$$\left\langle \boldsymbol{F}_{\mathrm{id}}^{mn}, \boldsymbol{F}_{\mathrm{id}}^{m\,n} \right\rangle = P^{\mathrm{in}} \delta_{m\,m} \delta_{n\,n} \tag{1.74}$$

and therefore the ideal contour patterns of different array elements are orthogonal. At $m = m$ and $n = n$, the expression (1.72) determines the total power that is radiated by the element and that, according to (1.74), is equal to the input power so that the element efficiency is equal to 100%, as noted in Section 1.3.4.

Let us now consider the aperture distributions corresponding to the ideal contour element patterns. The array aperture is assumed to be densely filled in with radiators, as shown in Figure 1.7(a). Let $\boldsymbol{f}_{pq}(x,y)$ be a distribution of the transverse vector field in the aperture S_{pq} of the *pq*th radiator or in the cross section of the corresponding closed feed line if the radiators are not the aperture-type ones. The function $\boldsymbol{f}_{pq}(x,y)$ is also assumed to be corresponding to the undisturbed incident

operating mode of unit amplitude and to be equal to zero outside S_{pq}. Then the incident field distribution over the radiator apertures (or over the cross sections of the feeding lines) can be written as

$$A^{mn}(x,y) = \sum_{p=} \sum_{q=} f_{pq}(x,y) \quad e^{ik[(x_{pq} \quad x_{mn})u+(y_q \quad y_n)v]} du dv \tag{1.75}$$

where the integral over determines the amplitude for the pqth radiator corresponding to excitation of the mnth input. The indicated amplitude coincides with (1.65) at $m = n = 0$.

The scalar product of the distributions corresponding to excitation of the mnth and $m\,n$ th inputs is

$$\left\langle A^{mn}, A^{m\,n} \right\rangle = \int_{\Omega} A^{mn}(x,y) \chi A^{m\,n} \quad (x,y) dx dy \tag{1.76}$$

Substitution of the appropriate expressions resulting from (1.75) in (1.76) yields

$$\left\langle A^{mn}, A^{m\,n} \right\rangle = Q \int_{\Omega} du dv e^{\ ik(x_{mn}u+y_n v)} \tag{1.77}$$

$$du\ dv\ e^{ik(x_{m\,n}\,u\,+y_n\,v\,)} \sum_{p=} \sum_{q=} e^{ik[x_{pq}(u \quad u)+y_q(v \quad v)]}$$

where

$$Q = \int_{S_{pq}} |f_{pq}(x,y)|^2 dx dy \tag{1.78}$$

is the value identical for all the radiators. Taking into account that $x_{pq} = pa + q \quad /M$ and $y_q = qb$ as well as using the properties (1.66) and (1.67), we reduce (1.77) to

$$\left\langle A^{mn}, A^{m\,n} \right\rangle = Q \frac{\lambda^2}{ab} \quad e^{ik[(x_{m\,n} \quad x_{mn})u+(y_n \quad y_n)v]} du dv \tag{1.79}$$

where we see the same integral as that standing in (1.73), proving the orthogonality of the ideal contour element patterns.

Thus, the aperture distributions corresponding to the window functions of the ideal contour element patterns are also orthogonal. The orthogonality of the element patterns and appropriate aperture distributions is one more property characterizing the absence of the mutual coupling between the array input ports.

A similar situation takes place in multibeam antennas, where the orthogonality of the beams corresponds to the absence of coupling between the input ports and therefore the absence of losses in beam-forming circuits [19–23]. Moreover, the relations between the ideal contour element patterns as well as between the appropriate

amplitude distributions over the array aperture allow us to develop a technique for determining dimensions and shape of a planar aperture providing formation of orthogonal beams arranged in a specified regular lattice. That technique was first presented in [24]. Its description in more detail is given in [25, 26] and Appendix 1B.

1.4 Element Pattern with Nonideal Contour

As described in Section 1.3.2, the ideal element pattern contour corresponding to the scan region occupying only an internal part of the visible space consists of a few pairs of shifted straight or curved lines and always has angular points. As a rule, these features are absent in the scan region contours specified in practice. The simplest example of that is a conical scan region having a circular contour. Such a scan region has been considered in [5] and [24] in connection with determining the minimum number of controlled elements necessary for providing beam scanning with a specified gain in a specified region. The element power pattern level in this case varies as $\cos\theta$ within the cone where only the main lobe is present. The pattern level outside the cone is zero providing complete suppression of the grating lobes. Let θ_m be the semiflare angle of the cone corresponding to the maximum scan angle. Such a circular scan region is shown in gray in Figure 1.8.

The array element directivity determined according to (1.11) and (1.12) is in this case [5]:

$$D_e(\theta,\varphi)=\frac{4\cos\theta}{\sin^2\theta_m} \tag{1.80}$$

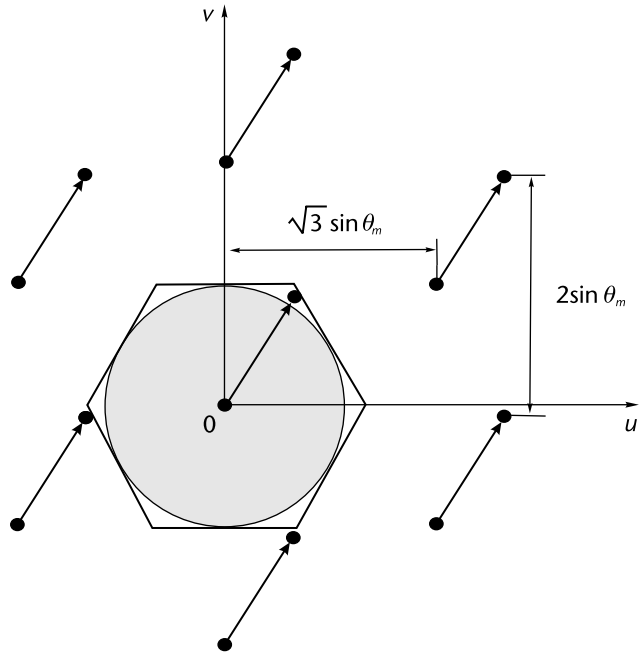

Figure 1.8 Circular scan region and arrangement of grating lobes for a hexagonal array with maximum element spacing.

If such a circular scan region is realized by an array with hexagonal lattice, the maximum element spacing in a horizon row at which the secondary grating lobes do not enter the circle is determined by

$$d_{x,\max} = \frac{\lambda}{\sqrt{3}\sin\theta_m} \tag{1.81}$$

Taking into account that the maximum spacing between adjacent rows in the hexagon lattice is $d_{y,\max} = d_{x,\max}\sqrt{3}/2$, and using (1.54), we obtain the maximum element gain

$$g_e(\theta,\varphi) = \frac{2\pi\cos\theta}{\sqrt{3}\sin^2\theta_m} \tag{1.82}$$

Since the element gain is equal to the element directivity multiplied by the element efficiency η_e, then dividing (1.82) by (1.80), we obtain

$$\eta_e = \frac{\pi}{2\sqrt{3}} \tag{1.83}$$

that amounts about 90.69%. Note, that the element efficiency (1.83) is exactly equal to the area of the circular scan region divided by the area of the maximum (ideal) scan region. The latter is also shown in Figure 1.8 in the form of an equilateral hexagon surrounding the circular region.

If the conical element pattern is formed by an array with square lattice, the maximum element spacings providing the single-beam scanning in the region covered by the element pattern are $d_{x,\max} = d_{y,\max} = \lambda/(2\sin\theta_m)$. The ideal scan region area in this case is equal to $(\lambda/d_{x,\max})^2 = 2\sin^2\theta_m$. Dividing the circular region area $\pi\sin^2\theta_m$ by the ideal scan region area, we obtain

$$\eta_e = \frac{\pi}{4} \tag{1.84}$$

or about 78.54% (i.e., the efficiency of shaping the conical element pattern in the array with square lattice is still lower than that in the hexagonal array).

It is interesting to note that the highest achievable element efficiency (1.83) for array with hexagonal lattice and (1.84) for array with square lattice coincide with the maximum efficiency determined in [27] for a multibeam antenna with circular aperture and arrangement of the beams in the nodes of hexagonal and square lattices, respectively.

The element efficiency reduction caused by nonideality of the element pattern contour in the array with maximum element gain can be explained as follows. Since the element gain is maximal, the nonideal contour must situate inside the ideal one. In this case, there exist some values of the control phases at which the main lobe falls into the gap between the two contours. An example of such a situation is presented in Figure 1.8, where the main lobe displacement from the central position to the gap between the nonideal circular contour and ideal hexagonal contour is shown by an arrow. Since both the main lobe and the secondary grating lobes are arranged in the region where the element pattern has zero level completely suppressing them,

the power supplied to the array is completely reflected from the array aperture back to the feeding system. This situation in some sense is similar to the regime of conditional match introduced in [6, 15] and mentioned in Section 1.3.4. The only difference is that the main and grating lobes there are arranged outside the visible space, while here they all are situated outside the region covered by the contour element pattern. In both cases, there exist some regions of the control phase values where the array reflection coefficient is not equal to zero when scanning. And since the coefficients of coupling between the array inputs are Fourier coefficients of the reflection coefficient [6, 7], similar to (1.34), the coupling coefficients are already not equal to zero, unlike those corresponding to the element pattern (1.50) having an ideal contour.

Thus, if the contour element pattern has the ultimate level (1.50) but its contour differs from an ideal one for a specified lattice, then such element patterns do not possess the property of orthogonality any more, and the element efficiency cannot in principle achieve the 100% level because of the presence of mutual coupling between the input ports.

However, note that if a contour radiation pattern is formed in an infinite array not as the element pattern corresponding to excitation of only one input port, the conclusion concerning the efficiency of such a shaping drawn earlier is not valid. If, for instance, the contour pattern is formed by an infinite array of closely spaced radiators at independent excitation of all the inputs of the latter, then, as shown in [17, 28, 29] and in Appendix 1C, the array efficiency can achieve the theoretical maximum of 100% at any specified shape of the contour.

1.5 Minimum Number of Controlled Elements

As noted in the Introduction, array antennas having large aperture for providing high gain in a specified scan region may comprise thousands and even tens of thousands of controlled elements. Since the control devices are the most complex and expensive components in an array antenna, minimization of their number has always been a problem of great importance. The first fundamental results of its solution were obtained in [1], where the minimum number of controlled elements in a linear array was determined by the scan sector width divided by the beam width. In the subsequent paper [30], the minimum number of controlled array elements was determined in the form

$$N_{\min} = \frac{1}{4\pi} \quad Dd \tag{1.85}$$

where is a specified scan region, $d = \sin\theta d\theta d\varphi$, and $D(\theta,\varphi)$ is a specified function of directivity. The result similar to (1.85) was later reported in [31] (see also formula (8.80) in [21]). Some other expressions for the minimum number of controlled elements can be found in [21, 32–34]. The reasoning used for derivation of the expression for the minimum number of controls is presented next.

1.5.1 Formulation

Since the edge effect on the characteristics of a multi-element array antenna is weak, we can assume that the array element characteristics are identical. In this case, we can consider a large finite array as a fragment in an infinite array, as has been done in the end of Section 1.2.2. According to (1.46), the gain of such an array equals the element gain multiplied by the number of the array elements. If the array gain has been specified, it is clear that the minimum number of its elements is achieved at the highest achievable element gain [i.e., at the ideal element gain that is determined by formula (1.54)]. Taking into account the angular dependence of the ideal element gain (1.54), we can write the array gain as

$$G(\theta,\varphi) = G_0 \cos\theta \tag{1.86}$$

where G_0 is the array gain in the broadside direction, which is assumed to be specified. Since this gain is related with the aperture area A according to the well-known formula $G_0 = 4\pi A/\lambda^2$, then

$$A = \frac{\lambda^2}{4\pi} G_0 \tag{1.87}$$

As described in Section 1.3.2, the area S of the scan region corresponding to the ideal element pattern and completely lying inside the visible space is related to the element spacings d_x and d_y by formula $S = \lambda^2/(d_x d_y)$. Assuming that the scan region area is specified, we can express the cell area allotted to one array element as

$$A_{\text{cell}} = d_x d_y = \frac{\lambda^2}{S} \tag{1.88}$$

Dividing now the array aperture area (1.87) by the cell area (1.88), we obtain the minimum number of the elements

$$N_{\min} = \frac{S}{4\pi} G_0 \tag{1.89}$$

expressed via the specified array gain in broadside and the specified area of the ideal scan region in the plane of direction cosines.

Note that formula (1.89) can be obtained directly from (1.85) if one substitutes the gain (1.86) in (1.85) instead of the directivity because the gain and directivity for the array with ideal contour element pattern are identical and therefore the indicated substitution is valid. Note also that if formula (1.89) gives a number having a fractional part, one should throw off the latter and add unity.

Another approach to determining the minimum number of controlled elements is based on the concept of orthogonal beams filling the specified scan region [21]. If each array input port corresponds to one such a beam, as, for instance, takes place in an array utilizing a Butler matrix [5, 23, 35], then the scanning in the specified region by switching N beams requires N 1 switches [21]. The minimum number

of the beams and therefore the number of the input ports in this case will be determined by formula

$$N_{\min} = \frac{S}{S_{\text{beam}}} \tag{1.90}$$

where $S_{\text{beam}} = \quad_u \quad_v$ is the area allotted to one node in the lattice of the orthogonal beam arrangement in the direction cosine plane, with $\quad_u$ and $\quad_v$ being the lattice periods shown in Figure 1B.1 in Appendix 1B. Using (1B.1), we obtain $S_{\text{beam}} = \quad_u \quad_v = \lambda^2/A$. Substituting this expression in (1.90) and taking into account (1.87), we again come to (1.89).

Thus, both approaches considered here give the same expression for the minimum number of controlled elements. However, unlike the former one, the latter approach uses no suggestions on the contour shape bounding the specified scan region. If the scan region has a nonideal shape, like, for instance, a circle considered in Section 1.4, the minimum number in the first approach is determined by the area of an ideal scan region covering the specified nonideal scan region rather than the area of the specified region itself. This situation is illustrated in Figure 1.8, where the circle represents the nonideal region while the hexagon embracing it corresponds to the ideal one. Since the area of the nonideal region is smaller than that of the ideal one, the second approach provides a smaller minimum number of controls compared to the minimum number obtained when using the first approach.

1.5.2 Element Use Factor

Antenna elements and matrices designed for forming orthogonal beams cannot be ideal in practical array antennas, and therefore the number of controlled elements in them always exceeds the theoretical minimum. One of the parameters characterizing the indicated exceeding is the element use efficiency introduced in [36, p. 159] (see also [34, pp. 77–78]). It has been determined as the ratio of the minimum number of controlled elements and their actual number N (i.e., $N_{\min}/N$). There also exists the inverse parameter

$$\zeta = \frac{N}{N_{\min}} \tag{1.91}$$

which was introduced in [37] (see also [21], p. 447) and called the *element use factor*.

The exceeding of the element number above the theoretical minimum (1.89) when satisfying specifications on the array gain and scan region may be caused by the necessity of decreasing the element spacings or increasing the aperture area or both. The former case can be illustrated by the arrays where the element spacings are determined from the condition that the grating lobes do not appear in the visible space as the main lobe scans over a specified region. If the latter is a circle of radius $\sin\theta_m$ considered in Section 1.4, the maximum spacing between adjacent

elements arranged in hexagonal lattice is determined by the well-known formula $d_x = 2\lambda/[\sqrt{3}(1+\sin\theta_m)]$. Dividing the aperture area (1.87) by the cell area of $d_x^2\sqrt{3}/2$, we obtain the number of elements $N = \sqrt{3}(1+\sin\theta_m)G_0/(8\pi)$. Substituting this number and minimum number (1.89) in (1.91) and taking into account that $S = \pi\sin^2\theta_m$, we obtain [5, 38]

$$\frac{N}{N_{\min}} = \frac{\sqrt{3}(1+\sin\theta_m)^2}{2\pi\sin^2\theta_m} \tag{1.92}$$

The plot of the element use factor (1.92) versus maximum scan angle θ_m is presented in Figure 1.9. As we can see, the superfluity of the controlled elements in the arrays based on keeping the grating lobes outside of the visible space are very high for narrow scan regions, and the use of the elements shaping contour radiation patterns in such cases may be preferable.

The necessity of using the number of controlled elements exceeding the theoretical minimum (1.89) due to increasing the array aperture area may be illustrated by the example of the phased arrays consisting of uniformly excited nonoverlapped subarrays [5, 38]. Let the period of arrangement of such subarrays in a hexagonal lattice be maximum determined according (1.81) for a specified maximum scan angle θ_m. Let also the subarray aperture be an equilateral hexagon uniformly filled with closely spaced radiators. Then, the radiation pattern of such a subarray in the region of its main lobe and a few nearest sidelobes will be close to the radiation pattern of an appropriate continuous hexagonal aperture. The level of the indicated pattern in the main planes of the aperture is determined by formulas (1B.8) and (1B.9). Substitution of the hexagon side $a = d_{x,\max}/\sqrt{3} = \lambda/(3\sin\theta_m)$ in (1B.7) gives the level in the horizontal plane $F^H(\sin\theta_m) = 6/\pi^2$. The level of the pattern at the

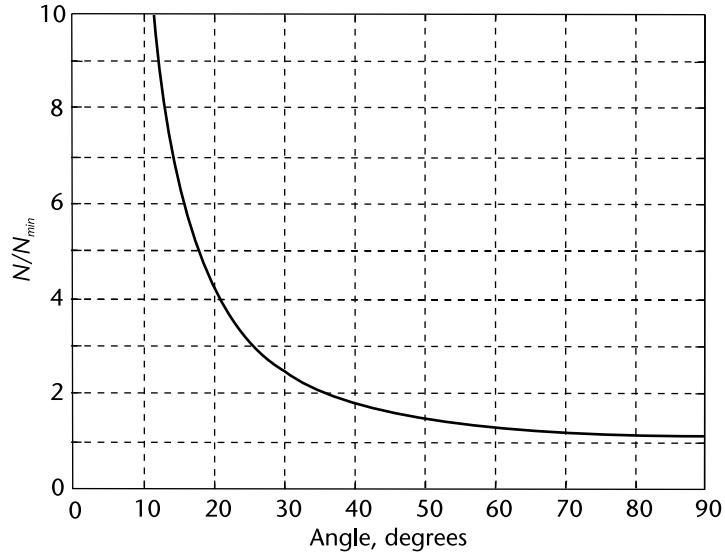

Figure 1.9 Element use factor versus maximum scan angle for a hexagonal array scanning without grating lobes in visible space.

scan region edge in the vertical plane is practically the same. Assuming that the cosine behavior of the subarray gain is accounted for by the radiator pattern, we find that the array gain at the scan region edge turns out to be $\pi^4/36$ 2.7 times lower than the ideal level. To compensate this reduction, one should increase the array aperture area by the same factor 2.7, and this corresponds to the same increase of the number of controlled elements compared to the theoretical minimum.

Note that the factor (1.92) as well as the array gain reduction when using the uniformly excited nonoverlapping subarrays presented earlier corresponds to the ideal match of the elements to free space. If there are mismatch losses, the exceeding of the element number will be even higher. The number of elements may be increased compared to the theoretical minimum for some other reasons as well (e.g., because of the tapered amplitude distributions required for reduction of the level of sidelobe radiation).

1.6 Two-Dimensional Problems for One-Dimensional Periodic Structures

1.6.1 Fields at Quasi-Periodic Excitation

As noted in Section 1.2, a doubly periodic structure is a convenient model for analysis of real large multi-element planar phased arrays, since it allows one to reduce the problem to consideration of the electromagnetic fields within only one period. However, in spite of such simplification, the problem is still three dimensional and vector, and therefore its solution still requires large computational costs. One may consider such costs defensible for analysis of the arrays for which the principles of construction and basic design have already been determined. However, it is often useful to study novel approaches to array construction including novel methods of shaping sector and contour array element patterns by making use of an even simpler model. Such a model is a one-dimensional (1D) periodic structure, the geometry and excitation of which do not depend on one of the coordinates. The geometry of such a two-dimensional (2D) problem is sketched in Figure 1.10. The array is periodic with period (element spacing) b. Its geometry and functions representing excitation of the array inputs are assumed to be independent of y. Therefore, all the fields in the structure depend only on two Cartesian coordinates x and z or two cylindrical coordinates ρ and θ related to the Cartesian ones by formulas $x = \rho\sin\theta$ and $z = \rho\cos\theta$.

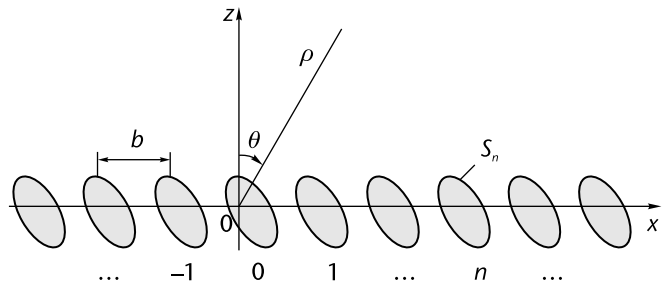

Figure 1.10 Geometry of two-dimensional problem for one-dimensional periodic structure.

Analysis of this 1D periodic structure can be performed similarly to that described in Section 1.2 for a 2D periodic structure. Consider first the quasi-periodic excitation at which the signal coming to the inputs have identical amplitudes and linearly progressing phases with increment . Let such an excitation result in forming a distribution of electric and magnetic currents of density $\boldsymbol{j}^e(x,z)$ and $\boldsymbol{j}^m(x,z)$, respectively, over finite region $S = S_0$ corresponding to the central array cell with index $n = 0$, as shown in Figure 1.10. Then the current distributions in other cells will repeat the amplitude and phase relations of the excitation signals, and therefore we can write the following relation for the currents formed in region S_n

$$\boldsymbol{j}_n^{e,m}(x,z) = \boldsymbol{j}^{e,m}(x \quad nb, z)e^{in} \tag{1.93}$$

where (x,y) S_n. Note that the currents $\boldsymbol{j}^{e,m}(x,z)$ depend also on the controlling phase .

Vector potentials corresponding to the currents (1.93) are determined by formula

$$\boldsymbol{A}^{e,m}(\rho) = \int_S \boldsymbol{j}^{e,m}(\rho\ )G_{\mathrm{P}}^{(2)}(\rho, \rho\ )dS \tag{1.94}$$

where $\rho = x\boldsymbol{e}_x + z\boldsymbol{e}_z$, $\rho\ = x\ \boldsymbol{e}_x + z\ \boldsymbol{e}_z$,

$$G_{\mathrm{P}}^{(2)}(\rho, \rho\ ) = \frac{i}{4}\sum_{n=} e^{in}\ H_0^{(1)}(k\sqrt{(x \quad x \quad nb)^2 + (z \quad z\ )^2}) \tag{1.95}$$

is the quasi-periodic Green's function for the 1D periodic structure under consideration, and $H_0^{(1)}(...)$ is the Hankel function of the first kind and zero order arising after integration of the corresponding three-dimensional scalar Green's function (1.18) over y' using formula 8.421.11 from [39]

$$H_0^{(1)}(x) = \frac{i}{\pi}\int \frac{e^{i\sqrt{x^2+t^2}}}{\sqrt{x^2+t^2}}dt, \quad x>0 \tag{1.96}$$

Using the spectral representation for the Hankel function (see, for instance, [3]),

$$H_0^{(1)}\left(k\sqrt{x^2+z^2}\right) = \frac{1}{\pi}\int \frac{e^{i\alpha x + i\gamma|z|}}{\gamma}d\alpha \tag{1.97}$$

where $\gamma = \sqrt{k^2 \quad \alpha^2} = i\sqrt{\alpha^2 \quad k^2}$, as well as the Poisson's summation formula [4], we can rewrite the superposition of cylindrical waves (1.95) in the form of a superposition of plane waves (Floquet modes)

$$G_{\mathrm{P}}^{(2)}(\rho, \rho\ ) = \frac{i}{2b}\sum_{q=} \frac{e^{i\alpha_q(x \quad x\ ) + i\Gamma_q|z \quad z\ |}}{\Gamma_q} \tag{1.98}$$

with transverse and longitudinal propagation constants

$$\alpha_q = \frac{+2\pi q}{b}$$
$$\Gamma_q = \sqrt{k^2 \quad \alpha_q^2} = i\sqrt{\alpha_q^2 \quad k^2} \tag{1.99}$$

It is well known that if the fields and sources do not depend on one of the Cartesian coordinates, the system of Maxwell's equations contains two independent subsystems. In our case, when there is no dependence of y, one of the subsystems comprises field components E_y, H_x, H_z and current components j_y^e, j_x^m, j_z^m, while the components H_y, E_x, E_z of the fields and components j_y^m, j_x^e, j_z^e, of the currents compose the other subsystem. Using expressions of the fields via vector potentials (1.23) and taking into account formulas (1.94) and (1.98), the fields over the structure (at $z \quad z_{\max}$) corresponding to the first subsystem may be expressed as follows:

$$E_y(x,z) = \underset{q=}{} T_{1q} e^{i\alpha_q x + i\Gamma_q z} \tag{1.100}$$

$$H_x = \frac{1}{i\omega\mu_0}\frac{E_y}{z}$$
$$H_z = \frac{1}{i\omega\mu_0}\frac{E_y}{x} \tag{1.101}$$

where

$$T_{1q}(\quad) = \frac{1}{2\Gamma_q b}\int_S (\omega\mu_0 j_y^e \quad \Gamma_q j_x^m + \alpha_q j_z^m) e^{\ i\alpha_q x \quad i\Gamma_q z} dx\, dz \tag{1.102}$$

The fields with components (1.100) and (1.101) represent TE modes of amplitudes (1.102) determined by the currents distributed in the array. Since the magnetic field strength components (1.101) are determined via the only electric field strength component, the presented solution corresponds to the so-called case of E-polarization. The solution of the second subsystem corresponding to the case of H-polarization represents the TM mode fields

$$H_y(x,z) = \underset{q=}{} T_{2q} e^{i\alpha_q x + i\Gamma_q z} \tag{1.103}$$

$$E_x = \frac{1}{i\omega\varepsilon_0}\frac{\partial H_y}{z}$$
$$E_z = \frac{1}{i\omega\varepsilon_0}\frac{\partial H_y}{\partial x} \tag{1.104}$$

above the structure, and

$$T_{2q}(\quad) = \frac{1}{2\Gamma_q b}\int_S (\Gamma_q j_x^e \quad \alpha_q j_z^e + \omega\varepsilon_0 j_y^m) e^{\ i\alpha_q x \quad i\ \gamma_q z}\, dx\, dz \tag{1.105}$$

are their amplitudes.

Note that the terms S-polarization an P-polarization are often used in the appropriate literature instead of the terms E-polarization and H-polarization, respectively, used in this book.

1.6.2 Excitation of One Array Input

Let $\boldsymbol{J}_{n,0}^{e,m}(x,z)$ be distributions of the electric and magnetic current density formed in the nth cell (i.e., for $(x,z) \quad S_n$) as a result of excitation of the central cell input with the inputs of all the other cells being terminated with matching loads. Since the mutual coupling coefficients depend only on the difference of the indices prescribed to the cells, we may write $\boldsymbol{J}_{n,0}^{e,m}(x,z) = \boldsymbol{J}_{0,\ n}^{e,m}(x \quad nb, z)$. The indicated distributions may be used for representation of the current density distributions (1.93) corresponding to the quasi-periodic excitation. In particular, for the currents in the central cell, there will be valid the expression

$$\boldsymbol{j}^{e,m}(x,z,\quad) = \sum_{n=} \boldsymbol{J}_{0,n}^{e,m}(x,z) e^{in} \quad = \sum_{n=} \boldsymbol{J}_{0,\ n}^{e,m}(x,z) e^{\ in} \tag{1.106}$$

Using the asymptotic expression for the Hankel function as $k\rho = k\sqrt{x^2+z^2}$

$$H_0^{(1)}(k\sqrt{(x \quad x)^2 + (z \quad z)^2} \quad \sqrt{\frac{2}{\pi k\rho}} e^{i(k\rho \quad \pi/4)} e^{\ ik(x\sin\theta + z\cos\theta)} \tag{1.107}$$

we may represent the far zone vector potentials corresponding to excitation of the central array input as

$$\begin{aligned} \boldsymbol{A}^{e,m}(\rho,\theta) &= \frac{ie^{i(k\rho \quad \pi/4)}}{2\sqrt{2\pi k\rho}} \sum_{n=} \int_{S_n} \boldsymbol{J}_{n,0}^{e,m}(x\ ,z\ ) e^{\ ik(x\sin\theta + z\cos\theta)} dx\, dz \\ &= \frac{ie^{i(k\rho \quad \pi/4)}}{2\sqrt{2\pi k\rho}} \sum_{n=} \int_{S_n} \boldsymbol{J}_{0,\ n}^{e,m}(x \quad nb, z\ ) e^{\ ik(x\sin\theta + z\cos\theta)} dx\, dz \end{aligned} \tag{1.108}$$

Replacing the variable $x \quad x + nb$, changing for integration over the central region S, and accounting for (1.106), we rewrite (1.108) as

$$\boldsymbol{A}^{e,m}(\rho,\theta) = \frac{ie^{i(k\rho \quad \pi/4)}}{2\sqrt{2\pi k\rho}} \int_S \boldsymbol{j}^{e,m}(x\ ,z\ , kb\sin\theta) e^{\ ik(x\sin\theta + z\cos\theta)} dx\, dz \tag{1.109}$$

Substituting (1.109) into (1.23) and keeping only the terms containing $\rho^{-1/2}$, we represent the electric and magnetic field strengths in far zone in the form

$$\begin{aligned} E_y(\rho,\theta) &= \sqrt{\frac{k}{\rho}} e^{i(k\rho - \pi/4)} F_1(\theta) \\ H_\theta(\rho,\theta) &= \frac{1}{\eta_0} E_y(\rho,\theta) \end{aligned} \tag{1.110}$$

where

$$F_1(\theta) = \frac{1}{2\sqrt{2\pi}} \int_S (\eta_0 j_y^e - j_x^m \cos\theta + j_z^m \sin\theta) e^{ik(x \sin\theta + z \cos\theta)} dx\, dz \tag{1.111}$$

is the nonnormalized array element pattern having the same dimension (volts) as that in (1.42) and (1.43). Comparing (1.111) to (1.102), we have

$$F_1(\theta) = \frac{1}{\sqrt{2\pi}} T_{10}(kb \sin\theta) b \cos\theta \tag{1.112}$$

that is, just as for the doubly periodic structures considered in Section 1.2, the element pattern in a one-dimensional periodic structure is proportional to the amplitude of the Floquet mode of zero order multiplied by cosine of the observation angle measured from the array broadside.

Excitation of one array input by an H-polarized signal can be considered in a similar way. As a result, the electric and magnetic field strengths in far zone are represented as follows:

$$\begin{aligned} E_\theta(\rho,\theta) &= \sqrt{\frac{k}{\rho}} e^{i(k\rho - \pi/4)} F_2(\theta) \\ H_y(\rho,\theta) &= \frac{1}{\eta_0} E_\theta(\rho,\theta) \end{aligned} \tag{1.113}$$

where

$$F_2(\theta) = \frac{\eta_0}{\sqrt{2\pi}} T_{20}(kb \sin\theta) b \cos\theta \tag{1.114}$$

is the nonnormalized array element pattern (also in volts) determined by the amplitude of the zero-order Floquet mode resulting from (1.105).

1.6.3 Ideal Array Element Characteristics

Similarly to those in a doubly periodic array, the ideal element characteristics (pattern, gain, and efficiency) in one-dimensional periodic array correspond to

the case when the total power supplied to the array inputs at quasi-periodic excitation is radiated only in the main lobe corresponding to one propagating Floquet mode of zero order in expressions (1.100) and (1.103). Let $\overline{P}_{\text{in}}$ be power supplied to each array input per unit length along the y-axis. The power that the array radiates through a planar surface arranged parallel to the aperture per one period and unit length along y is determined by the corresponding integral of the flux density $\text{Re}[\boldsymbol{E} \quad \boldsymbol{H}^*] \times \boldsymbol{e}_z/2$. Since the input power is completely radiated, the indicated integral must be equal to $\overline{P}_{\text{in}}$. Furthermore, since the power is radiated in the zero-order Floquet mode only, then, substituting (1.100) and (1.101) for the E-polarization as well as (1.103) and (1.104) for the H-polarization in the expression for the flux density indicated earlier, we obtain relations

$$\frac{1}{2\omega\mu_0}|T_{10}(\quad)|^2\Gamma_0 b = \overline{P}_{\text{in}} \tag{1.115}$$

$$\frac{1}{2\omega\varepsilon_0}|T_{20}(\quad)|^2\Gamma_0 b = \overline{P}_{\text{in}} \tag{1.116}$$

Substituting the magnitudes of the Floquet mode complex amplitudes resulted from (1.115) and (1.116) in (1.112) and (1.114), respectively, and replacing by $kb\sin\theta$, we obtain the expression for the ideal amplitude element pattern

$$F_{\text{id}}(\theta) = \sqrt{\frac{\eta_0 \overline{P}_{\text{in}} b\cos\theta}{\pi}} \tag{1.117}$$

valid both for E- and for H-polarization.

If the array period b exceeds half the wavelength, the secondary grating lobes may appear in the visible space when scanning of the main beam. The highest possible element pattern level (1.117) in this case is achieved if the element pattern is zero in the region of the grating lobes. Therefore, the ideal element pattern must have a sector shape, and its width in the $\sin\theta$ space is equal to λ/b (i.e., to the distance between the adjacent grating lobes). An example of a symmetrical ideal sector element pattern normalized to the maximum of (1.117) is given in Figure 1.11(a), where the gating lobe positions in the visible space are shown by vertical arrows. The ideal sector element pattern of width λ/b may also be nonsymmetrical with respect to the array broadside as shown in Figure 1.11(b). Just as for doubly periodic arrays, the ideal region (sector) of scan of a one-dimensional periodic array may be multiply connected one. If, for instance, the scan sector is symmetrical and doubly connected, the corresponding ideal dual-sector element pattern is shown in Figure 1.12(a), where the width of each sector is equal to half the total ideal width of the scan region. Figure 1.12(b) gives an example of a nonsymmetrical dual-sector element pattern with sectors of different widths. If in this case the width of the left-hand sector is $0 < \quad < \lambda/b$, then the width of the right-hand sector will be λ/b . The outer boundaries of these sectors must be spaced at $2\lambda/b$ apart.

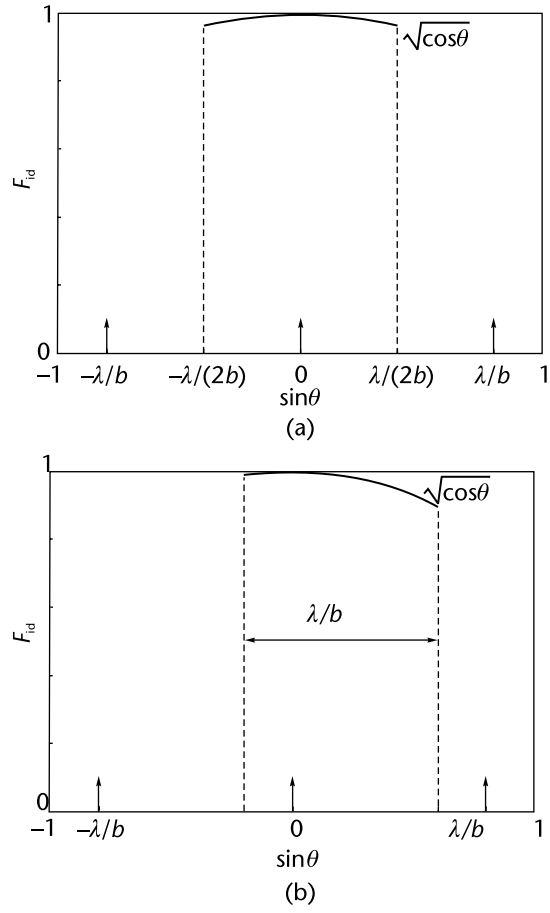

Figure 1.11 (a) Symmetrical and (b) nonsymmetrical normalized ideal sector element patterns.

If the main lobe is arranged at one edge of the ideal scan region (or its part in case of a multiply connected region), then a grating lobe of the array factor will appear at another edge. The radiated power in this case is divided in two parts, and therefore the element pattern level (1.117) for the edge angles must be multiplied by $1/\sqrt{2}$.

At last, the ideal one-sector and multisector element patterns with level (1.117) and total width λ/b at $b \quad \lambda/2$ corresponding to excitation of different array inputs are orthogonal to each other. The way of proving this property is similar to that described in Section 1.3.6.

The reasoning concerning the determination of the amplitude distributions corresponding to the ideal element patterns is presented in Sections 1.3.5 and 1.3.6. Similarly to (1.65), the continuous amplitude distribution corresponding to the ideal sector pattern of the nth element in a one-dimensionally periodic array is determined by

$$A^n(x) = A_0 \quad e^{ik(x \quad nb)u} du \tag{1.118}$$

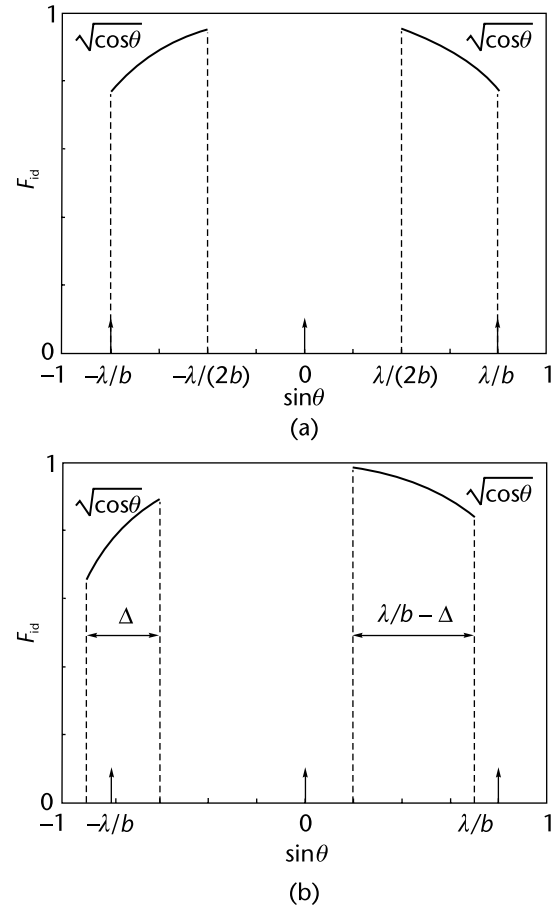

Figure 1.12 (a) Symmetrical and (b) nonsymmetrical normalized ideal dual-sector element patterns.

where $u = \sin\theta$ and A_0 is some normalizing coefficient. For the pattern shown in Figure 11(b), the expression (1.118) is reduced to

$$A^n(x) = \frac{A_0\lambda}{b}\frac{\sin[\pi(x/b \quad n)]}{\pi(x/b \quad n)}e^{ik(x \quad nb)(u_1+u_2)/2} \tag{1.119}$$

where $u_1 = \sin\theta_1$ specifies the position of the sector pattern left-hand edge, while $u_2 = u_1 + \lambda/b$. The normalized distributions (1.119) for the symmetrical sector pattern, when $u_1 = \quad \lambda/(2b)$, as shown Figure 1.11(a), corresponding to excitation of the central ($n = 0$) and adjacent inputs are shown in Figure 1.13. The distribution resulting from (1.118) for the symmetrical dual-sector element pattern presented in Figure 1.12(a) is determined by formula

$$A^n(x) = \frac{A_0\lambda}{b}\frac{\sin[\pi(x/b \quad n)/2]}{\pi(x/b \quad n)/2}\cos[3\pi(x/b \quad n)/2] \tag{1.120}$$

The normalized distributions (1.120) for the central and adjacent elements are depicted in Figure 1.14. As we see, these distributions are more complex than those

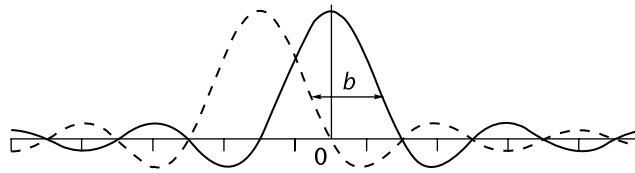

Figure 1.13 Normalized amplitude distributions corresponding to shaping symmetrical single-sector patterns of the central and adjacent elements.

corresponding to the one-sector pattern and require four or more radiators in each array cell for their realization.

The orthogonality of the distributions (1.119) is well known. The orthogonality of (1.118) in a general case can be proven in the same way as in Section 1.3.6 for the case of dual-periodic arrays.

The array element gain in the two-dimensional case is determined by expression

$$g(\theta) = \frac{\frac{1}{2}\mathrm{Re}[\boldsymbol{E} \quad \boldsymbol{H}\ ]\times \boldsymbol{e}_\rho}{\frac{\bar{P}^{\mathrm{in}}}{2\pi\rho}} \tag{1.121}$$

where the average flux density standing in the denominator is taken over a cylindrical surface instead of a spherical one in the three-dimensional case. Substitution of the fields (1.110) or (1.113) in (1.121) gives

$$g(\theta) = \frac{\pi k}{\bar{P}^{\mathrm{in}}\eta_0}|F_{1,2}(\theta)|^2 \tag{1.122}$$

that is, the element gain is determined by the element pattern. If (1.117) for the ideal element pattern is substituted in (1.122) instead of $F_{1,2}$, we will obtain the ideal array element gain in the two-dimensional case

$$g_{\mathrm{id}}(\theta) = kb\cos\theta \tag{1.123}$$

and if the ideal element pattern is a sector one, the ideal element gain is zero outside the sector of scanning.

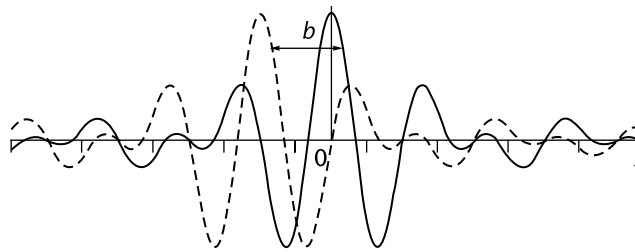

Figure 1.14 Normalized amplitude distributions corresponding to shaping symmetrical dual-sector patterns of the central and adjacent elements.

The power radiated by the array element per unit length along y is determined by integrating the flux density

$$\bar{P} = \frac{1}{2}\int_{-\pi/2}^{\pi/2} \mathrm{Re}[\boldsymbol{E} \quad \boldsymbol{H}^{*}] \times \boldsymbol{e}_{\rho}\, \rho d\theta \tag{1.124}$$

Substitution of (1.110) or (1.113) in (1.124) and use of the ideal element pattern (1.117) reduce (1.124) to

$$\bar{P} = \frac{\bar{P}^{\mathrm{in}} b}{\lambda} \quad d\sin\theta \tag{1.125}$$

If $b > \lambda/2$, then the total width of the single beam scanning region in the $\sin\theta$ units is equal to λ/b so that (1.125) gives $\bar{P} = \bar{P}^{\mathrm{in}}$. The width of for $b < \lambda/2$ is equal to 2, and then $\bar{P} = 2\bar{P}^{\mathrm{in}} b/\lambda$. These results and definition (1.15) allow us to calculate the ideal array element efficiency in the two-dimensional case by formula

$$\eta_e = \frac{\bar{P}}{\bar{P}^{\mathrm{in}}} = \begin{array}{ll} \dfrac{2b}{\lambda}, & b < \lambda/2 \\ 1, & b \quad \lambda/2 \end{array} \tag{1.126}$$

derived first in [14] (see also [40]).

The element efficiency lower than 100% at small element spacing corresponds to the presence of mutual coupling between the elements. Reduction of the element efficiency can also take place at large element spacing when the sector element pattern width is smaller than the ideal width λ/b in the units of $\sin\theta$. The reasons of such reduction are discussed in Section 1.4.

References

[1] Vendik, O. G., "Synthesis of a Linear Array of Radiators with Non-Mechanical Beam Swinging," *Izvestiya Vuzov—Radiotekhnika*, Vol. 3, No. 1, 1960, pp. 77–86 (in Russian).

[2] Allen J. L., "Gain and Impedance Variation in Scanned Dipole Arrays," *IRE Trans. on Antennas and Propagation,* Vol. 10, No. 5, 1962, pp. 566–572.

[3] Markov, G. T., and A. F. Chaplin, *Excitation of Electromagnetic Waves*, Moscow: Radio i svyaz', 1967 (in Russian).

[4] Korn, G. A., and T. M. Korn, *Mathematical Handbook*, 2nd ed., New York: McGraw Hill, 1968.

[5] Markov, G. T., and D. M. Sazonov, *Antennas*, Moscow: Energiya, 1975 (in Russian).

[6] Amitay, N., V. Galindo, and C. P. Wu, *Theory and Analysis of Phased Array Antennas*, New York: Wiley-Interscience, 1972.

[7] Hannan P. W., "The Element-Gain Paradox for a Phased-Array Antenna," *IEEE Trans. on Antennas and Propagation*, Vol. 12, No. 4, 1964, pp. 423–433.

[8] Skobelev, S. P., "On the Ideal Gain of a Radiating Element in a Planar Array," *Proc. of the 12th Intl. Conf. on Mathematical Methods in Electromagnetic Theory (MMET'08)*, Odessa, Ukraine, June 29–July 2, 2008, pp. 305–307.

[9] Skobelev, S. P., "Radiation Pattern and Gain of an Ideal Element in a Planar Phased Array Antenna," *Antennas*, No. 2, 2009, pp. 28–32 (in Russian).

[10] Skobelev, S. P., "On the Ideal Element Pattern in Planar Phased Array Antennas," *2003 IEEE AP-S Int. Symp. Digest*, Columbus, OH, June 22–27, 2003, Vol. 2, pp. 444–447.

[11] Skobelev, S. P., "Some Properties of the Ideal Element Pattern in Planar Phased Array Antennas," *Radiotekhnika*, No. 4, 2007, pp. 76–81 (in Russian).

[12] Kawakami, H., G. Sato, and R. Wakabayashi, "Research on Circularly Polarized Conical-Beam Antennas," *IEEE Antennas and Propagation Magazine*, Vol. 39, No. 3, June 1997, pp. 27–39.

[13] Jeon, S. I., et al. "Vehicular Active Antenna System with Combined Electronical and Mechanical Beam Steering for Reception from DBS in Ku-Band," *Proc. 28th Moscow Intl. Conf. on Antenna Theory and Technology*, Moscow, Russia, September 22–24, 1998, pp. 72–77.

[14] Kahn, W. K., "Ideal Efficiency of a Radiating Element in an Infinite Array," *IEEE Trans. on Antennas and Propagation,* Vol. 15, No. 4, 1967, pp. 534–538.

[15] Amitay, N., et al., "On Mutual Coupling and Matching Conditions in Large Planar Phased Arrays," *IEEE AP-S Intl. Symp. Digest*, September 1964, Vol. 2, pp. 150–156.

[16] Hannan, P. W., "Proof that a Phased-Array Antenna Can Be Impedance Matched for All Scan Angles," *Radio Science*, Vol. 3, No. 3, 1967, pp. 361–369.

[17] Skobelev, S. P., "On One More Property of the Ideal Array Element Pattern," *IEEE Trans. on Antennas and Propagation*, Vol. 57, No. 3, March 2009, pp. 631–637.

[18] Skobelev, S. P., "Realizability and Other Features of the Ideal Contour Element Pattern in Planar Phased Array Antennas," *Radiotekhnika*, No. 4, 2009, pp. 71–76 (in Russian).

[19] Allen, J. L., "A Theoretical Limitation on the Formation of Lossless Multiple Beams in Linear Arrays," *IRE Trans. on Antennas and Propagation*, Vol. AP-9, No. 4, 1961, pp. 350–352.

[20] Stein, S., "On Cross Coupling in Multiple-Beam Antennas," *IRE Trans. on Antennas and Propagation*, Vol. AP-10, No. 5, 1962, pp. 548–557.

[21] Mailloux, R. J., *Phased Array Antenna Handbook*, Norwood, MA: Artech House, 1994.

[22] Benenson, L. S., "Multibeam Antennas," *Journal of Communication Technology and Electronics*, Vol. 41, No. 9, 1996, pp. 749–754.

[23] Hansen, R. C., *Phased Array Antennas*, New York: Wiley, 1998.

[24] Skobelev, S. P., "On the Forming of Orthogonal Beams by Planar Apertures," *Proc. 50th Scientific Conf. of the Moscow Institute of Physics and Technology*, Dolgoprudny, Moscow Reg., November 24–25, 2007, Pt. 1, pp. 147–150 (in Russian).

[25] Skobelev, S. P., "Forming of Orthogonal Beams by Planar Apertures," *Radiotekhnika*, No. 4, 2008, pp. 37–40 (in Russian).

[26] Skobelev, S. P., "Determination of Dimensions and Shape of a Planar Aperture for Forming of Orthogonal Beams," *IEEE Trans. on Antennas and Propagation*, Vol. 56, No. 8, Pt. 2, August 2008, pp. 2755–2757.

[27] Johansson, J. F., "Fundamental Limits for Focal Plane Array Efficiency," *Multi-Feed Systems for Radio Telescopes. ASP Conference Series*, Vol. 75, 1995, pp. 34–41.

[28] Skobelev, S. P., "On the Radiation Efficiency of a Dense Array Antenna Shaping a Sector Radiation Pattern," *Proc. 12th Intl. Conf. on Mathematical Methods in Electromagnetic Theory (MMET'08)*, Odessa, Ukraine, June 29–July 2, 2008, pp. 320–322.

[29] Skobelev, S. P., "Radiation Efficiency of Dense Antenna Arrays Forming Flat-Top and Contour Radiation Patterns," *Journal of Communication Technology and Electronics*, Vol. 54, No. 7, 2009, pp. 797–799.

[30] Kontorovich, M. I., and V. Y. Petrun'kin, "On the Minimum Number of Elements in an Antenna with Electrical Beam Swinging," *Radiotekhnika i Elektronika*, Vol. 6, No. 12, 1961, pp. 1982–1988 (in Russian).

[31] Stangel, J., "A Basic Theorem Concerning the Electronic Scanning Capabilities of Antennas," *URSI Commission VI*, Spring Meeting, June 11, 1974.

[32] Mikheyev, S. M., "Minimum Quantity of Amplitude Commutators in Switching Scanning Antennas and Their Elements," *Izvestiya Vuzov—Radioelektronika*, Vol. 11, No. 5, 1968, pp. 520–528 (in Russian).

[33] Vendik, O. G., and Y. V. Yegorov, "The First Phased-Array Antennas in Russia: 1955–1960," *IEEE Antennas and Propagation Magazine*, Vol. 42, No. 4, 2000, pp. 46–52.

[34] Vendik, O. G., and M. D. Parnes, *Antennas with Electrical Scanning (Introduction to the Theory)*, Moscow: Science-Press, 2002 (in Russian).

[35] Butler, J., and R. Love, "Beam Forming Matrix Simplifies Design of Electronically Scanned Antennas," *Electronic Design*, Vol. 9, April 12, 1961, pp. 170–173.

[36] Vendik, O. G., *Antennas with Non-Mechanical Movement of Beam*, Moscow: Sovetskoye Radio, 1965 (in Russian).

[37] Patton, W., "Limited Scan Arrays," in *Phased Array Antennas: Proc. 1970 Phased Array Symp.*, A. A. Oliner and G. A. Knittel, (eds.), Dedham, MA, 1972, pp. 254–270.

[38] Voskresensky, D. I., (ed.), *Antennas and Microwave Devices (Design of Phases Antenna Arrays)*, Moscow: Radio i Svyaz', 1981 (in Russian).

[39] Gradstein, I. S., and I. M. Ryzhik, *Tables of Integrals, Series, and Products*, New York: Academic, 1980.

[40] Kahn, W. K., "Element Efficiency: A Unifying Concept for Array Antennas," *IEEE Antennas and Propagation Magazine*, Vol. 49, No. 4, August 2007, pp. 48–56.

[41] Madelung, E., *Die Mathematischen Hilfsmittel des Physikers*, Berlin, Germany: Springer-Verlag, 1957.

[42] Jahnke, E., F. Emde, and F. Losch, *Tables of Higher Functions*, New York: McGraw-Hill, 1960.

[43] Galindo-Israel, V., S.-W. Lee, and R. Mittra, "Synthesis of a Laterally Displaced Cluster Feed for a Reflector Antenna with Application to Multiple Beams and Contoured Patterns," *IEEE Trans. on Antennas and Propagation*, Vol. AP-26, No. 2, 1978, pp. 220–228.

[44] Shishlov, A. V., "Theory and Design of Reflector Antennas for Radio Systems with Contour Zones of Servicing," *Radiotekhnika*, No. 4, 2007, pp. 39–49 (in Russian).

[45] Woodward, P. M., and J. D. Lawson, "The Theoretical Precision with Which an Arbitrary Radiation Pattern May Be Obtained from a Source of Finite Size," *J. AIEE*, Vol. 95, Pt. 3, September 1948, pp. 362–370.

[46] Garmash, V. N., *Theory and Methods of Processing Information in Radio Systems*, School-Book of the Moscow Institute of Physics and Technology (MIPT), Moscow: MIPT Press, 1987 (in Russian).

[47] Johansson, J. F., "Theoretical Limits for Aperture Efficiency in Multi-Beam Antenna Systems," *Research Report No. 161*, Dept. of Radio and Space Systems, Chalmers University of Technology, Gothenburg, Sweden, August 1988.

[48] Johansson, J. F., "Stein's Limit for Finite and Infinite Multi-Beam Arrays," *1989 IEEE AP-S Int. Symp. Digest*, Vol. 27, June 1989, pp. 713–716.

[49] Skobelev, S. P., "Methods of Constructing Optimum Phased-Array Antennas for Limited Field of View," *IEEE Antennas and Propagation Magazine*, Vol. 40, No. 2, April 1998, pp. 39–50.

[50] Eom, S. Y., et al., "Study of a Planar Array Antenna with Sector Radiation Pattern for Perspective Base Stations of Mobile Communications," *Antennas*, No. 1, 2005, pp. 30–38 (in Russian).

[51] Minz, M. Y., E. D. Prilepsky, and V. M. Zaslonko, "Optimization of the Coefficient of Concentration of Power Radiated by an Antenna with Circular Aperture and Maximally Flat Radiation Pattern," *Radiotekhnika i Elektronika*, Vol. 33, No. 9, 1988, pp. 1888–1894 (in Russian).

[52] Vanke, V. A., and A. A. Zaporozhets, "Synthesis of the Maximally Flat Radiation Pattern of a Transmitting Antenna for Energy Transfer by Microwave Beam," *Radiotekhnika i Elektronika*, Vol. 34, No. 12, 1989, pp. 2643–2647 (in Russian).

[53] Hall, P., (ed.), *The Square Kilometre Array: An Engineering Perspective*, New York: Springer, 2005.

[54] Alimova, L. I., et al., "The Possibility of Wide-Angle Scanning in Hybrid Reflector Antennas," *Radiotekhnika i Elektronika*, Vol. 26, No. 12, 1981, pp. 2500–2510 (in Russian).

[55] Kinber, B. Ye, et al., "Experimental Verification of the Hybrid Reflector Antenna Beam Deflection in a Wide Angular Sector," *Radiotekhnika i Elektronika*, Vol. 29, No. 8, 1984, pp. 1462–1471 (in Russian).

[56] Holter, H., T.-H. Chio, and D. H. Schaubert, "Experimental Results of 144-Element Dual-Polarized Endfire Tapered-Slot Phased Arrays," *IEEE Trans. on Antennas and Propagation*, Vol. 48, No. 11, 2000, pp. 1707–1718.

[57] Ng Mou Kehn, M., and P. -S. Kildal, "Fundamental Limitations of Focal Plane Arrays Characterized in Terms of Radiation Efficiencies of their Embedded Element Patterns," *Proc. 2006 IEEE AP-S Int. Symp.*, Albuquerque, NM, July 2006, pp. 4319–4322.

[58] Ivashina, M. V., et al., "Control of Reflection and Mutual Coupling Losses in Maximizing Efficiency of Dense Focal Plane Arrays," *Proc. 1st European Conference on Antennas and Propagation (EuCAP 2006)*, Nice, France, November 6–10, 2006.

[59] Ivashina, M. V., et al., "Radiation Efficiency as a Fundamental Limitation of Wideband Dense Arrays for Multi-Beam Applications," *Proc. 29th ESA Antenna Workshop on Multiple Beams and Reconfigurable Antennas, ESTEC*, Noordwijk, the Netherlands, April 18–20, 2007, pp. 118–121.

[60] Kildal, P. -S., et al., "Measurement of Embedded Element Efficiencies of Wideband Dense Arrays in Reverberation Chamber," *Proc. 2nd European Conference on Antennas and Propagation (EuCAP 2007)*, Edinburgh, U.K., November 11–16, 2007.

[61] Ivashina, M. V., et al., "Decoupling Efficiency of a Wideband Vivaldi Focal Plane Array Feeding a Reflector Antenna," *IEEE Trans. on Antennas and Propagation*, Vol. 57, No. 2, 2009, pp. 373–382.

[62] Ng Mou Kehn, M., et al., "Definition of Unifying Decoupling Efficiency of Different Array Antennas: Case Study of Dense Focal Plane Array Feed for Parabolic Reflector," *International Journal of Electronics and Communications (AEU)*, 2009, doi: 10.1016/j.aeue.2009.02.011.

[63] Korotkov, V. D., and S. P. Skobelev, "Shaping of Sector Partial Radiation Patterns in Array Antennas with Corrugated Structures," *Radiotekhnika i Elektronika*, Vol. 39, No. 5, 1994, pp. 767–772 (in Russian).

Appendix 1A Array Element Gain on the Ideal Contour

To derive the expression (1.55) for the correcting factor to the element gain on the ideal contour (or to the array gain when the array beam is placed on the boundary of the ideal scan region), let us consider an infinite array with rectangular lattice and ideal contour element pattern occupying region on the plane of direction cosines u and v. Assume that M N elements forming a rectangular fragment of this array are excited with identical amplitudes and progressing phases corresponding to the beam position characterized by direction cosines (u_0, v_0). Then, the total radiated power per one element may be determined by formula

$$P = \frac{1}{MN} \frac{P(u,v)dudv}{\sqrt{1 u^2 v^2}} \tag{1A.1}$$

where

$$P(u,v) = \sqrt{1 u^2 v^2} \frac{\sin^2(MU)}{\sin^2 U} \frac{\sin^2(NV)}{\sin^2 V} \tag{1A.2}$$

is the power fragment pattern where the first factor is the ideal element pattern (1.49) normalized to its maximum, and the two other ones represent the finite array factor with $U = kd_x(u u_0)/2$ and $V = kd_y(v v_0)/2$.

Let us consider the limit of (1A.2) as M and N . Taking into account that

$$\frac{\sin^2(Mx)}{\sin^2 x} \frac{\sin^2[M(x n\pi)]}{(x n\pi)^2}$$

for large M and x $n\pi$, $n = 0, \pm 1, ...$, and using the delta function representation in the form (see, for instance, [41, p. 36]):

$$\delta(x) = \frac{1}{\pi} \lim_M \frac{\sin^2(Mx)}{Mx^2}$$

in (1A.1) and (1A.2), we obtain the following expression:

$$P = \frac{\lambda^2}{d_x d_y} {}_n I_n \tag{1A.3}$$

where

$$I_n = \delta(u u_n)\delta(v v_n)dudv \tag{1A.4}$$

and $u_n = u_0 + p(n)\lambda/d_x$, $v_n = v_0 + q(n)\lambda/d_y$ are direction cosines of the nth grating lobe (it may be the main lobe as well), with n being an ordinal number prescribed by the lobe characterized by pair of indices $p, q = 0, \pm 1, \ldots$. Note that (1A.4) will also be valid for a triangular lattice if the grating lobe direction cosines u_n and v_n account for the grating lobe arrangement in the corresponding triangular lattice.

To determine the value of integral (1A.4) when the main lobe and at least one secondary grating lobe are placed on the contour of the ideal element pattern, let us consider Figure 1A.1 as an example where the ideal scan region is depicted in the form of a parallelogram with angles α_1 and $\alpha_2 = \pi \quad \alpha_1$ at the base. The positions of the three lobes are shown by the dots.

The contribution of the lobe arranged in the left-hand bottom corner to the radiated power (1A.3) is determined by integral I_1 for which $u_1 = v_1 = 0$ in (1A.4). Using the spectral representation for the delta function

$$\delta(u)\delta(v) = \frac{1}{4\pi^2} \qquad e^{iux+ivy}\,dxdy$$

and changing for polar coordinates (ρ,φ) and (w,ψ) related to the Cartesian coordinates by formulas $x = \rho\cos\varphi$, $y = \rho\sin\varphi$, $u = w\cos\psi$, and $v = w\sin\psi$, we may rewrite (1A.4) for $n = 1$ as

$$I_1 = \int_{0\ 0}^{\alpha_1\ \bar{w}} w dw d\psi \frac{1}{4\pi^2} \int_{0\ 0}^{2\pi} e^{iw\rho\cos(\varphi\ \ \psi)}\,\rho d\rho d\varphi \tag{1A.5}$$

where $\bar{w} = \bar{w}(\psi)$ is the equation of contour fragment ABC in Figure 1A.1. Representing the exponential function by a Fourier series of argument $\varphi \quad \psi$ (see, for instance, [3, p. 45]) and calculating the integral over φ, we reduce (1A.5) to the expression

$$I_1 = \frac{1}{2\pi} \int_0^{\alpha_1} d\psi \int_0^{\bar{w}} w dw \int_0 J_0(w\rho)\rho d\rho \tag{1A.6}$$

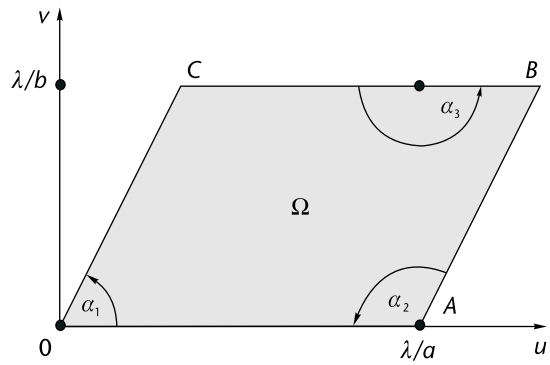

Figure 1A.1 Positions of the main and grating lobes on the contour of the ideal element pattern.

where $J_0(x)$ is the Bessel function of the zero order. Since [42] $xJ_0(x)dx = d[xJ_1(x)]$, where $J_1(x)$ is the Bessel function of the first order, the integral over w in (1A.6) is equal to $\bar{w}J_1(\bar{w}\rho)/\rho$. Since $J_1(x)dx = dJ_0(x)$, the subsequent integral over ρ is equal to $J_0(0) = 1$. Performing further integration over ψ, we finally obtain $I_1 = \alpha_1/(2\pi)$. The contributions of the other lobes in the radiated power calculated in a similar way are equal to $I_n = \alpha_n/(2\pi)$ where $n = 2$ or 3. As already noted in Section 1.3.3, the sum of angles α_n is always equal to 2π, and therefore the relative contribution of each lobe arranged on the ideal contour in the radiated power is determined by formula (1.55).

Appendix 1B On the Forming of Orthogonal Beams by a Planar Aperture

The concept of orthogonal beams is of importance in antenna theory. First of all, it is associated with designing multiple beam antennas for applications in communication and radar systems. Such antennas can also serve as a basis for designing the limited-scan phased arrays (see, for instance, Chapter 8 in [21]) mentioned in the Introduction, as well as antennas with contour zones of service [43, 44]. It is well known [19, 20, 22] that providing 100% efficiency of channels in a multiple beam antenna implies that its beams formed via a feedthrough network by the common antenna aperture must be orthogonal. Furthermore, the orthogonal beams are a convenient tool for synthesis of the antenna radiation pattern in the Woodward-Lawson method [45].

The issues of forming the orthogonal beams by linear antennas have been described in detail in the literature, in particular, in [21, 23]. As for the planar apertures, the situation is not so clear except for the simplest case of the orthogonal beams arranged in a rectangular lattice in the direction cosine space [21]. A possibility of generalizing the two-dimensional sampling theorem to a skew lattice has been mentioned in [46]; however, no references to the realization of that possibility have been made there.

The technique described next allows the determination of the dimensions and shape of a planar aperture capable of forming orthogonal beams arranged in a general skew Cartesian periodic lattice with arbitrary angle between its rows and columns in the plane of direction cosines.

Let the antenna aperture be arranged in the plane $z = 0$ of a rectangular Cartesian coordinate system $0xyz$, and let the beam directions be determined by coordinates of nodes in skew Cartesian periodic lattice specified as shown in Figure 1B.1 in the plane of direction cosines $u = w\cos\varphi$ and $v = w\sin\varphi$, where $w = \sin\theta$. The nodes are arranged in horizontal rows with spacing $\quad_u$, while the rows are arranged with spacing $\quad_v$. The adjacent rows may be shifted with respect to each other along the axis u at a specified distance $\quad$. In particular, $\quad = 0$ corresponds to a rectangular lattice, while $\quad = \quad_u/2$ corresponds to a triangular lattice, including an important special case of hexagonal lattice with $\quad_v = \quad_u\sqrt{3}/2$.

The first step of the technique is construction, in the plane $z = 0$, of a lattice reciprocal with respect to the beam lattice. The reciprocal lattice geometry is shown in Figure 1B.2. The columns of the lattice nodes are arranged with spacing $d_x = \lambda/\quad_u$, where λ is the operating wavelength. The spacing of nodes in a column is $d_y = \lambda/\quad_v$.

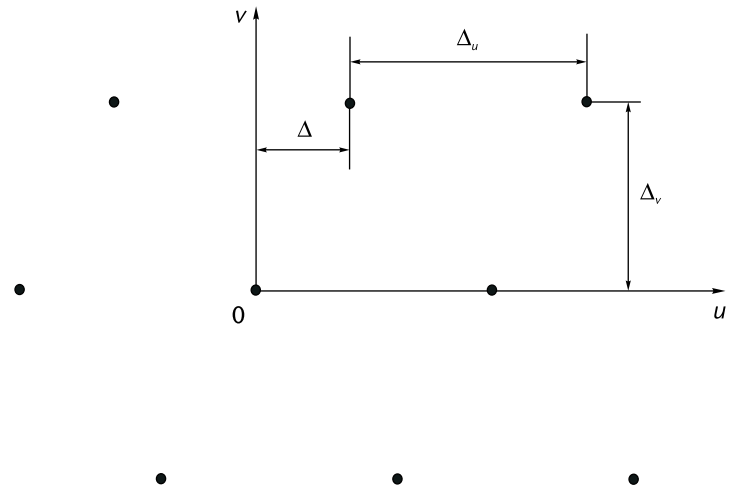

Figure 1B.1 Skew periodic lattice of arrangement of beams.

The adjacent columns are shifted with respect to each other along the *y*-axis at $d_s = \lambda \quad /(\quad _u \quad _v)$ so that the angle between the columns and rows remains the same as that in the beam lattice. The properties of the original and reciprocal lattices are such that if some radiators were arranged in the reciprocal lattice and excited with identical amplitudes and phases, then the grating lobes of the array factor would just be arranged in the nodes of the original lattice in the direction cosine space.

The next step is determination of the aperture dimensions and shape. The aperture area is determined as the area of the reciprocal lattice cell (Figure 1B.2) allotted to one node; that is,

$$A = d_x d_y = \frac{\lambda^2}{u \quad v} \tag{1B.1}$$

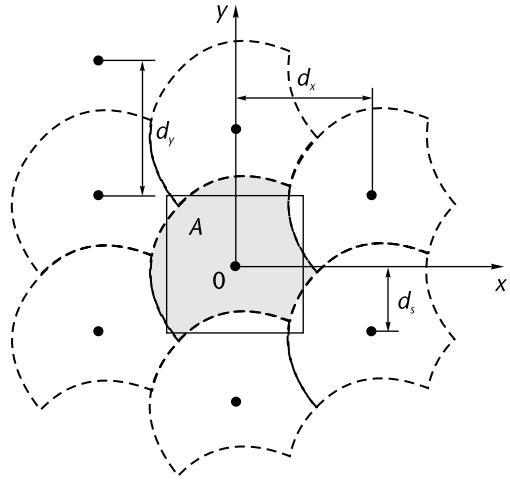

Figure 1B.2 Reciprocal lattice in the aperture plane and example of periodic cells.

The aperture shape may be rather arbitrary, and the aperture may even be a multiply connected region. However, the following condition must be met. The apertures of the chosen shape, when arranging them in the reciprocal lattice nodes, must cover the plane $z = 0$ with neither gaps nor overlapping. This requirement is illustrated by Figure 1B.2, where the chosen aperture of area A is shown in gray. Similarly to the ideal area of single-beam scanning considered in Section 1.3.2, the contour of such an aperture should consist of a few pairs of shifted straight or curved lines and should always have angular points.

Let us now prove that the beams formed by a uniformly excited and appropriately phased aperture constructed according to the technique described earlier are orthogonal. The nonnormalized radiation pattern phased in the node with coordinates $u_{mn} = m \quad_u + n \quad$ and $v_n = n \quad_v$ corresponding to the mnth beam is determined by formula

$$F_{mn}(\theta,\varphi) = \sqrt{\cos\theta} \int_A e^{ik[x(u \quad u_{mn})+y(v \quad v_n)]} dxdy \tag{1B.2}$$

where the square root of the cosine accounting for the gain reduction when deflecting the beam from the broadside may be considered as a normalized ideal radiation pattern of an aperture element resulting from (1.50). Consider the integral

$$C_{mn,pq} = \int_0^{2\pi} \int_0^{\pi/2} F_{mn}(\theta,\varphi) F_{pq}(\theta,\varphi) \sin\theta d\theta d\varphi \tag{1B.3}$$

determining the coefficient of coupling between the mnth and pqth beams. The asterisk in (1B.3) means complex conjugation while the radiation pattern $F_{pq}(u,v)$ for the pqth beam is determined by (1B.2) by replacing the indices mn by pq and by using other variables of integration (e.g., x and y instead of x and y). Replacing the angles θ and φ by direction cosines u and v, as well as accounting for (1.56), we may rewrite (1B.3) as

$$C_{mn,pq} = \int_{u^2+v^2 \quad 1} \frac{F_{mn}(u,v) F_{pq}(u,v)}{\cos\theta} dudv \tag{1B.4}$$

For large apertures forming narrow beams and for the cases when such beams are arranged sufficiently far from the grazing direction, the finite limits of integration in (1B.4) may be replaced by the infinite ones. Then substitution of the expressions for radiation patterns (1B.2) in (1B.4) and integration over u and v give the product of delta functions $\lambda^2 \delta(x \quad x)\delta(y \quad y)$. The subsequent integration over x and y reduces (1B.4) to the expression

$$C_{mn,pq} = \lambda^2 \int_A e^{ik[x(u_{mn} \quad u_{pq})+y(v_n \quad v_q)]} dxdy \tag{1B.5}$$

representing the coefficient of coupling between the amplitude-phase distributions corresponding to formation of the *mn*th and *pq*th beams. The integral in (1B.5) is similar to that in (1.73) for the scalar product of the ideal array element patterns. In the case under consideration, it is equal to the aperture area at $m = p$ and $n = q$, and to zero otherwise; that is,

$$C_{mn,pq} = \frac{\lambda^4}{u\ v}\delta_{mp}\delta_{nq} \tag{1B.6}$$

This result proves the exact orthogonality of the amplitude distributions corresponding to different beams. As for the beams themselves, they are orthogonal only asymptotically when the aperture dimensions tend to infinity.

Consider some illustrative examples. A square aperture can provide equal-width orthogonal beams arranged in a square lattice. The crossover level of two adjacent beams in the principal planes is, as is well known, equal to –3.92 dB with respect to the beam peak, while the crossover point of four adjacent beams (equally distant from their peaks) is placed at the level of –7.84 dB. To enhance the crossover level, one should arrange the beams in a hexagonal lattice. In this case, the crossover level of three adjacent beams in the point of their symmetry is approximately equal to –5.43 dB. However, as has been noted in [21], such beams from the square are not orthogonal any more. Therefore, when forming them, a part of the supplied power will inevitably be lost in the beam-forming network.

To form the orthogonal beams arranged in a hexagonal lattice, one may take a rectangular aperture with ratio of its sides $d_x/d_y = \sqrt{3}/2$ obtained according to the technique presented earlier. The beams in this case have different widths in the principal planes and a conventional level of –13.46 dB for the first sidelobes. Because of the beam nonsymmetry, the beam crossover level is lower than that for the symmetrical beams. If it is required to form more symmetric beams, one can choose

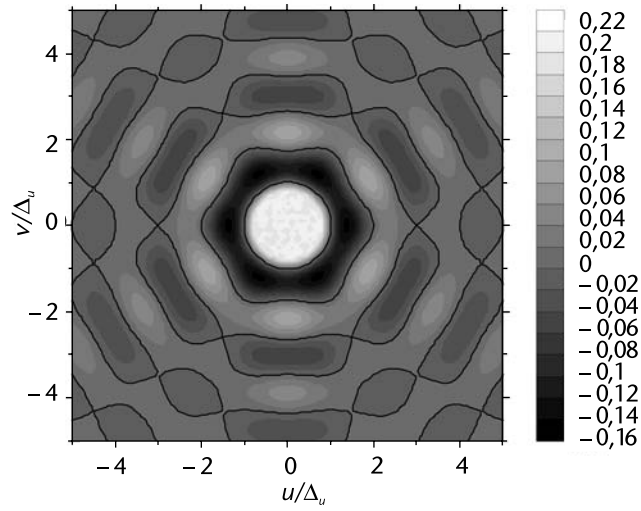

Figure 1B.3 Contour map of the radiation pattern formed by an equilateral hexagonal aperture.

an aperture in the form of an equilateral hexagon. The possibility of obtaining orthogonal beams arranged in a hexagonal lattice from a hexagonal aperture has been noted in [27; private communication with D. B. Rutledge]. The contour map of the radiation pattern (1B.2) phased in the broadside, normalized to its maximum, and divided by $\sqrt{\cos\theta}$, for such a hexagon aperture with its side length

$$a = \frac{2}{3} d_x = \frac{2\lambda}{3 \quad u} \tag{1B.7}$$

is presented in Figure 1B.3, where the contours of the zero level are specially shown. The central part of the beam is truncated at the level 0.2 for better visualization of the sidelobe structure. The plots of the radiation pattern magnitude (divided by $\sqrt{\cos\theta}$) in decibels in the horizontal ($u = w$, $v = 0$) and vertical ($u = 0$, $v = w$) planes are calculated using the expressions

$$F^H(w) = \frac{2}{3} \frac{\cos U \quad \cos 2U}{U^2} \tag{1B.8}$$

$$F^V(w) = \frac{1}{3} \quad 2\cos V + \frac{\sin V}{V} \div \frac{\sin V}{V} \tag{1B.9}$$

where $V = U\sqrt{3}/2$ and $U = kaw/2 = 2\pi w/(3 \quad u)$ are shown in Figure 1B.4 by solid and dashed lines, respectively. As we see, the hexagonal aperture forms an almost symmetrical beam, and the first sidelobe level, unlike that of –13.46 dB for a rectangular aperture, is equal –16.64 dB in the horizontal plane and –19.02 dB in the vertical plane. The crossover level of a pair of adjacent beams obtained from (1B.8) at $w = \quad u/2$ is equal to $6/\pi^2$ or –4.32 dB, which is slightly lower than that

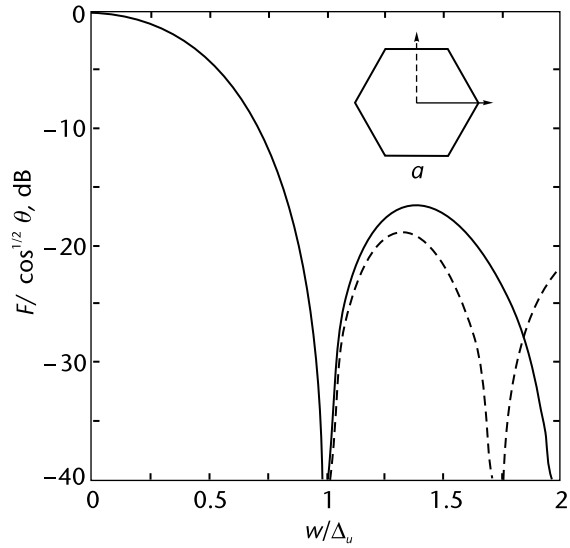

Figure 1B.4 Radiation pattern in the principal planes of a hexagonal aperture.

for a rectangular aperture. The crossover level in the center of symmetry of three adjacent beams, determined from (1B.9) at $w = \quad_u/\sqrt{3}$, is –5.96 dB.

Finally, note that the circular aperture does not meet the requirements listed earlier for the periodic cell shape, and therefore it is impossible in principle to form orthogonal beams by such an aperture. This explains the results obtained earlier in [27, 47, 48] when calculating the Stein efficiency of the beams formed by a circular aperture and arranged in the square and hexagonal lattices.

Appendix 1C On the Efficiency of a Dense Array Shaping a Contour Radiation Pattern

The problem of shaping contour radiation patterns is of great interest in the antenna theory and technology fields, and not only from the viewpoint of creation of the limited-scan array antennas [21, 49], as mentioned in the Introduction. Antennas with the contour beams are also used in communication systems [44, 50] and power-transmitting systems [51, 52]. Great attention to this problem has in recent years been paid in connection with research and development of large arrays for radiotelescopes of new generation [53]. One of the possible modifications of the array element is a short-focus multibeam reflector antenna. This antenna is required to provide high aperture efficiency even for the beams steered at large angles from the broadside in a wide frequency band. The possibility of keeping high aperture efficiency of a reflector antenna when deflecting the beams at large angles from the broadside has been proved theoretically in [54] and confirmed by measured results in [55]. This possibility is based on making use of an array of radiators arranged in the focal zone (in particular, in the focal plane) of the reflector. The amplitude distribution over the focal plane array aperture is chosen so as to remove the aberrations and to shape a contour radiation pattern for minimization of the loss for spillover. The operation of the focal array in a wide frequency band can be provided by application of Vivaldi antennas [56] as radiating elements.

Extensive numerical and experimental studies of the focal plane arrays shaping the flat-topped radiation patterns have been described in [57–62]. According to the indicated papers, the feature of such arrays is that the array element spacings at lower operating frequencies become considerably smaller than half the wavelength. The element efficiency in such dense arrays is very low, even for ideally matched elements, for which it is determined by formulas (1.58) and (1.126) in case of doubly periodic arrays and singly periodic arrays, respectively. The low radiation efficiency of the element in the dense arrays is explained by the presence of strong backward mutual coupling. The authors of [57–62] believe that the combination of the strong mutual coupling and strong nonuniformity of the amplitude distribution corresponding to shaping of the necessary contour radiation pattern results in fundamental limitations in the radiation efficiency of the dense array as a whole.

To draw a general conclusion on the highest achievable level of the radiation efficiency of dense arrays shaping the contour radiation patterns, let us consider a model in the form of an infinite two-dimensionally periodic array. This model is convenient for two reasons. First, a contour pattern is formed at an amplitude distribution tapered to the array aperture edges. The edge effect in this case is weaker

than that in the case of a uniform distribution, and therefore the infinite array model will be more accurate. Second, as will be shown next, such a model allows us to obtain results in the explicit form that makes them more attractive for the subsequent analysis.

Let the radiators arranged in the infinite two-dimensionally periodic array with small spacings a and b along the axes x and y, respectively (Figure 1.7), be excited by the signals having nonidentical amplitudes A_{mn}. Assuming that the radiators are fed through single-mode lines, we can determine the amplitude of the wave reflected from the pqth radiator input as

$$R_{pq} = \sum_{m=} \sum_{n=} A_{mn} C_{p\ m,q\ n} \tag{1C.1}$$

where

$$C_{p\ m,q\ n} = \frac{1}{4\pi^2} \int_{\pi}^{\pi} \int_{\pi}^{\pi} R(U,V) e^{i(p\ m)U + i(q\ n)V} dU dV \tag{1C.2}$$

is the coefficient of coupling between the pqth and mnth radiators determined by the reflection coefficient $R(U,V)$ depending on controlling phases U and V in the array excited with uniform amplitude distribution [6, 7]. Let the amplitudes A_{mn} of the array excitation be determined by formula (1.65), where the shape of the region

arranged inside the visible space is assumed to be arbitrary and the array lattice is assumed to be rectangular for simplicity. Then, substituting (1.65) and (1C.2) in (1C.1), using the properties (1.66) and (1.67), and integrating over U and V, we obtain

$$R_{pq} = \int\int R(kau, kbv) e^{ik(apu + bqv)} du dv \tag{1C.3}$$

Since $u^2 + v^2 < 1$ for (u,v) , the controlling phase values $U = kau$ and $V = kbv$ correspond to the presence of the main lobe in the visible space. If the radiators in this case are ideally matched at the uniform amplitude distribution [6, 7, 16] (i.e., $R(U, V) = 0$), the expression (1C.3) gives zero amplitudes of the reflected waves that already corresponds to the 100% array efficiency.

In general case, if the radiators are not matched ideally at the uniform amplitude distribution, the array efficiency at the nonuniform excitation can be calculated by [7, 63]:

$$\eta = 1 \quad \frac{P_{\text{A}}^{\text{ref}}}{P_{\text{A}}^{\text{in}}} = 1 \quad \frac{\sum_{p=} \sum_{q=} |R_{pq}|^2}{\sum_{m=} \sum_{n=} |A_{mn}|^2} \tag{1C.4}$$

Evaluation of the sum standing in the denominator in (1C.4) has already been considered in Section 1.3.5 when deriving (1.70). Evaluation of the numerator of fraction in (1C.4) is carried our similarly. As a result, (1C.4) is reduced to

$$\eta = \frac{1}{S} \quad [1 \quad |R(kau, kbv)|^2]dudv \tag{1C.5}$$

It is well known that the mismatch efficiency of an infinite array with uniform amplitude and linear phase distributions is determined by the expression standing in square brackets in (1C.5). Therefore, the expression (1C.5) shows that the efficiency of the same array but with the nonuniform excitation corresponding to shaping the contour radiation pattern with an arbitrary contour shape is determined by averaging the mismatch efficiency of the uniformly excited scanning array over the scan region bounded by the pattern contour.

The results presented here allow us to conclude that if a dense array is well matched and therefore has high mismatch efficiency at the uniform amplitude and linear phase distribution corresponding to scanning in the region coinciding with the region covered by a sector or contour radiation pattern, then the array radiation efficiency will remain high also at the nonuniform excitation corresponding to shaping the indicated sector or contour patterns. So, the strong mutual coupling in a dense array shaping a contour pattern brings nothing exclusive compared to the case of scanning array with uniform excitation.

The expressions (1C.3) and (1C.5) also allow us to draw a conclusion about the highest possible level of the array efficiency. As proved in [16], an infinite dense phased array antenna with uniform excitation can theoretically be ideally matched for all scan angles (i.e., the reflection coefficient will be equal to zero when scanning in the whole visible space). That means that a contour radiation pattern in such an array of ideally matched radiators can be shaped with 100% efficiency, and therefore the presence of the mutual coupling itself is not an obstacle for that.

Similar results for dense one-dimensionally periodic arrays shaping sector radiation patterns have been obtained in [28, 29].

CHAPTER 2

Arrays with Beam-Forming Networks

2.1 Overview of Technical Solutions

The most general approach to forming overlapped subarrays with sector radiation patterns has been formulated in [1]. This approach applies passive multiport beam-forming networks arranged between control devices (e.g., phase shifters) and radiating elements as schematically shown in Figure 2.1. The controlled array inputs in this variant are arranged with spacing close to its maximum value corresponding to a specified scan sector and connected to the radiators via a network to form overlapped subarrays. Each array cell corresponding to one controlled input in this case can contain either a few single-mode radiators, as shown in Figure 2.1, or one multimode radiator, while the network itself forms amplitude distributions over the subarrays corresponding to the sector radiation patterns.

At present, there exist a lot of various technical solutions proposed in the framework of the beam-forming network approach. The most demonstrative versions of them are briefly described next, and some other are mentioned in the references.

2.1.1 Arrays Based on Butler Matrices

An example of the network forming completely overlapped subarrays with aperture dimension equal to that of the whole array aperture is the Shelton's network [2] consisting of two cascaded Butler matrices, as shown in Figure 2.2. The lower matrix with controlled inputs has dimension $M \quad M$, where M is the number of controls coinciding with the number of subarrays. All the M output ports of this matrix are connected to the M inputs of the upper matrix of dimension $N \quad N$, where N is the number of radiating elements exceeding M. All the other $N \quad M$ inputs of the upper matrix are not used.

When the signal comes to one of the array inputs (solid arrow in Figure 2.2), it is distributed over outputs of the lower matrix with uniform amplitude and linear

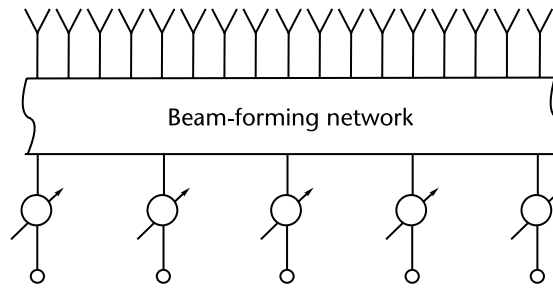

Figure 2.1 General block-diagram of array with a beam-forming network.

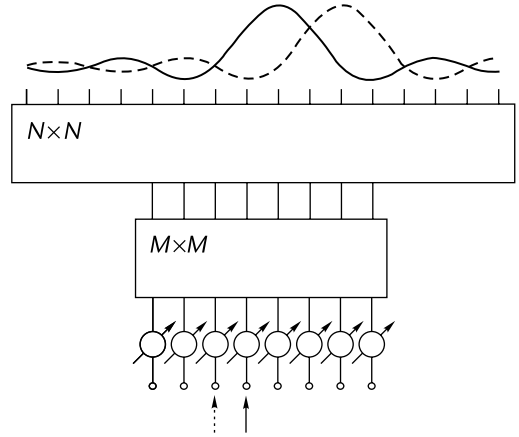

Figure 2.2 Network on the basis of two Butler matrices for forming totally overlapped subarrays.

phase distributions. The arrival of the signal to one input of the upper matrix results in the formation of an array beam definitely arranged in the space with respect to the array broadside. The excitation of the M inputs in the upper matrix results in the formation of a fan of the beams filling in the specified sector, thereby shaping the required sector subarray radiation pattern. The amplitude distribution over the subarray aperture of $\sin x/x$ type is shown in Figure 2.2 by a solid line. Excitation of an adjacent array input (dashed arrow in Figure 2.2) results in the formation of a similar amplitude distribution over the aperture but shifted at one period, with which the subarrays are formed, as shown in Figure 2.2 by a dashed line.

Since each Butler matrix accomplishes the discrete Fourier transform of the input signals, such networks are called *dual-transform* ones. The multi-element Butler matrices and similar matrices are very bulky, even for linear array antennas. For this reason, an alternative approach to the realization of the networks providing dual transformation of the input signals is the replacement of the upper matrix by a lens or a reflector illuminated via the free space by radiators connected to the output ports of the lower matrix. Design of such a hybrid antenna has been considered in [3]. References to other works where such an approach are applied can be found in [4].

2.1.2 Network of J. T. Nemit

One of the first simple approaches to reduction of the number of phase shifters in the arrays designed for scanning in a small sector is development and application of the network providing interpolation of the phase distributions over the array aperture [4–6]. As a demonstrative example, let us consider the network proposed by J. T. Nemit in [6]. A linear array utilizing Nemit's network is shown in Figure 2.3. The array comprises main radiators controlled directly by their phase shifters and intermediate radiators excited by the sum signals coming from the neighbor phase shifters via power dividers and hybrid devices. Each subarray with such a network overlaps one array period and a half. The network provides exact linear interpolation of the phase of the signal in the intermediate radiators. As shown in [7] for linear arrays and in [8] for planar arrays, an appropriate choice of the power divider parameters in the network allows suppression of the array factor grating lobes to a sufficiently low level when

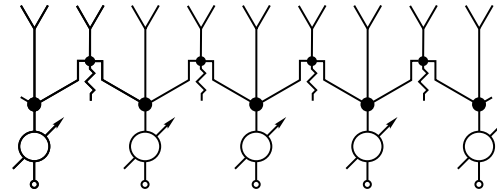

Figure 2.3 Network of J. T. Nemit.

scanning the main lobe in the specified sector. This provides almost constant array directivity in the scan sector. However, the amplitudes of the signals in the intermediate radiators decrease with deflection of the main lobe from the broadside because a part of the power coming to the hybrid devices is dissipated in the loads connected to the difference ports of the hybrids. The loss of the power in the hybrids results in rapid reduction of the array gain with deflecting the main lobe from the broadside, and therefore the subarray radiation pattern does not have the sector shape.

A modification of Nemit's network has been proposed in [9], where the signals from the different ports of the hybrids pass through π-manipulators introduced in the network and come to additional radiators. This solution improves the array performance at the expense of using additional controlled devices, though they are the simplest ones.

One more technical solution providing similar subarray overlap and therefore similar radiation characteristics has been proposed in [10] and considered in some detail in [11].

2.1.3 Network of R. J. Mailloux and P. R. Franchi

One of the successful technical solutions obtained in the area of arrays with beamforming networks is the array network proposed in [12]. This network, whose capabilities have been studied in [13, 14], is shown in Figure 2.4. The array consists of horn elements with dual-mode sections excited through power dividers and directional couplers. The subarray corresponding to one controlled array input consists here of three horns. Excitation of the subarray input results in excitation of the even

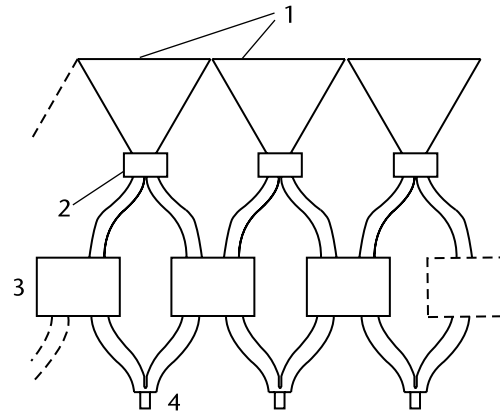

Figure 2.4 Network of R. J. Mailloux and P. R. Franchi: (1) horn radiators, (2) dual-mode sections, (3) directional couplers, and (4) power dividers.

dominant mode in the central subarray horn, as well as of both even and odd modes in the two lateral subarray horns. The optimum amplitude relation of the even and odd modes is determined by the directional coupler parameters, while the optimum phase difference with which the two modes come to the horn aperture is provided by the appropriate horn length.

This relatively simple network provides suppression of grating lobes down to –15 dB when scanning the main lobe in the sector of width equal approximately to 0.8 of the width corresponding to the appropriate ideal sector element pattern. Since the subarray includes only three array cells, its capabilities of shaping the sector patterns of higher quality are limited. For this reason, additional means for stronger suppression of the grating lobes have been proposed in [15] in the form of spatial filters studied in [16, 17]. The spatial filters make the array more bulky. Application of the network is also limited by the radiator type since the network has been developed only for waveguide-horn elements.

2.1.4 Network of R. F. Frazita, A. R. Lopez, and R. J. Giannini

One of the modifications of the technical solution proposed by R. F. Frazita, A. R. Lopez, and R. J. Giannini in [18] is shown Figure 2.5(a). The advantage of the

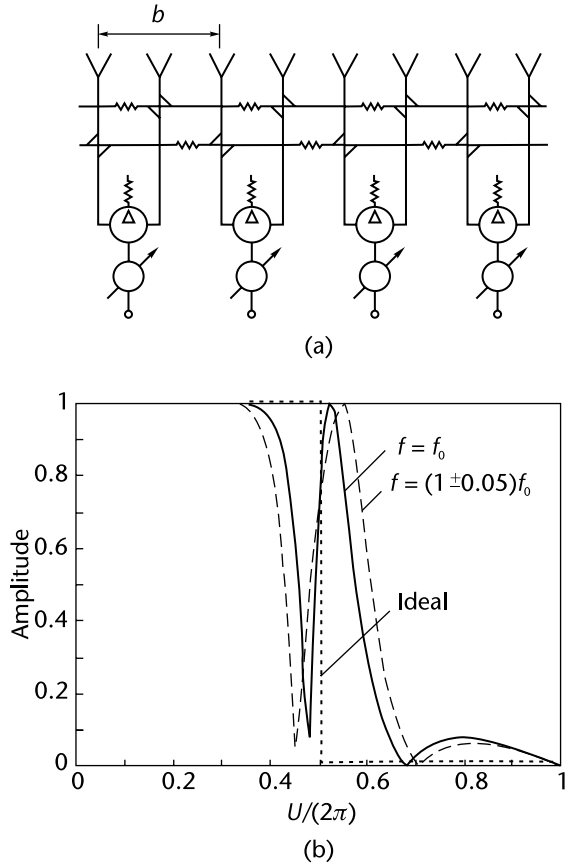

Figure 2.5 (a) Network of R. F. Frazita, A. R. Lopez, and R. J. Giannini, and (b) its subarray factor magnitude for $b = 2.25\lambda$.

network is the simplicity with which the overlapped subarrays are realized with the apertures equal to the aperture of the array as a whole. In other words, the network allows forming completely overlapped subarrays. Due to that feature, very steep slopes of the sector subarray pattern can be provided. This, as the authors underline, is especially important for the aerodrome landing systems, where the radar beam must be driven very close to the Earth's surface without any influence of the latter. However, the network has some limitations. It can be shown that its subarray factor is determined by formula

$$F_a(U) = \frac{iq + te^{iU}}{1 \quad iqte^{iU}} e^{iU/4} + \frac{iq + te^{iU}}{1 \quad iqte^{iU}} e^{iU/4} \tag{2.1}$$

where $U = kb\sin\theta$, b is the array period (subarray spacing), θ is the angle measured from the broadside, q is the coefficient of coupling between the cross ports in the directional couplers, and $t = \exp[(\alpha + i\gamma)b]$ is the transmission coefficient between the adjacent cells over the transmission line having attenuation coefficient α and propagation constant γ. The electric length of the line between adjacent cells must be such that $\gamma b = 2\pi n + \pi/2$, where n is a natural number.

The shape of the normalized magnitude of the subarray factor (2.1) corresponding to the condition indicated earlier at $\alpha = 0$ and $q = 0.75$ is presented in Figure 2.5(b) by solid curve. As we see, the subarray factor (2.1) has a dip near the ideal scan sector edge, and this feature reduces the useful sector width by about 20% with respect to its theoretical maximum.

Furthermore, since the subarray radiators are excited in series (like in frequency-scanning array antennas), the subarray pattern shape strongly depends on frequency [19], and larger array periods cause stronger dependence. An example characterizing the subarray factor shape distortion due to changing the frequency is shown in Figure 2.5(b) by the dashed curve obtained for $b = 2.25\lambda$, $\gamma = k$, and 5% frequency shift.

To widen the operating frequency band of the arrays utilizing the networks [18], Wheeler [20] and Lopez [21] have proposed their solutions, shown in Figure 2.6(a, b), respectively. These networks, however, are more complex and bulky. According to the proposed solutions, the SU Author's Certificates [22, 23] were offered.

2.1.5 Network of E. C. DuFort

One more approach to designing the networks for forming the overlapped subarrays has been proposed by E. C. DuFort in [24] and considered in more detail in [25]. In a general case, this approach allows the construction of subarrays with an arbitrary degree of overlapping and therefore possesses good capability on controlling the quality of the sector subarray pattern shape. However, that capability is provided at the expense of using a large number of directional couplers and a rather complicated network configuration. The simplest of the proposed networks where, like in [12], each subarray comprises three array cells, is shown in Figure 2.7(a). Each module corresponding to one phase shifter in this network contains a three-channel power divider using two directional couplers, a crossover providing

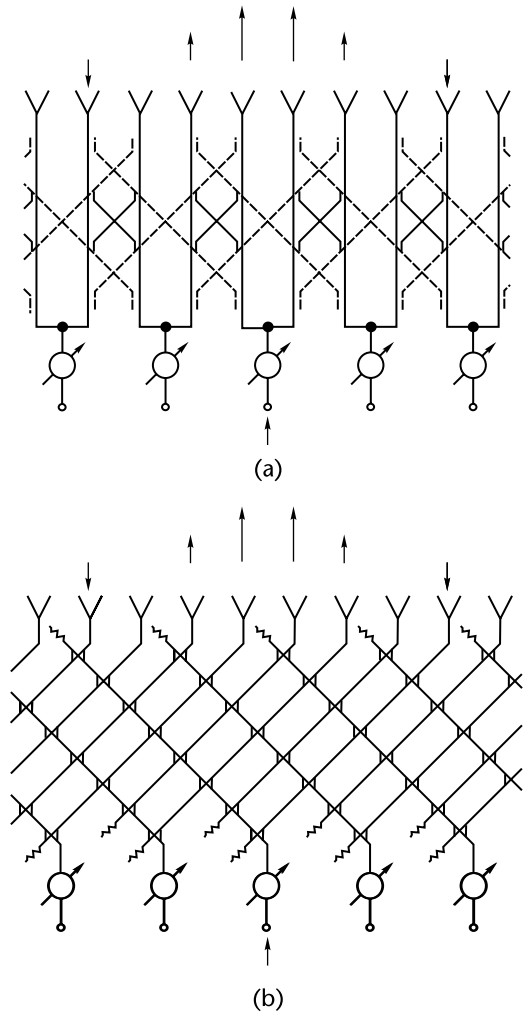

Figure 2.6 Networks of (a) H. A. Wheeler and (b) A. R. Lopez.

connection with adjacent modules, and three directional couplers connected to three radiators, with the central one being provided with a fixed phase shifter. The realization of such a network on the basis of microstrip technology has been considered in [25]. The subarray factor corresponding to optimum parameters of the network determined in [26] is shown in Figure 2.7(b). One more subarray network also comprising three array cells, but with four radiators within one cell, has recently been proposed and studied in [27, 28].

2.2 Multicascaded Chessboard Network

An array network, which to a definite degree is free of the restrictions inherent to the technical solutions considered earlier, has been proposed in [29]. This array, shown in Figure 2.8, is a periodic modular structure with period a. Each module (or cell) comprises two radiators arranged with spacing $a/2$ apart. The type of the radiators that are assumed to be identical can be arbitrary. The radiators are excited

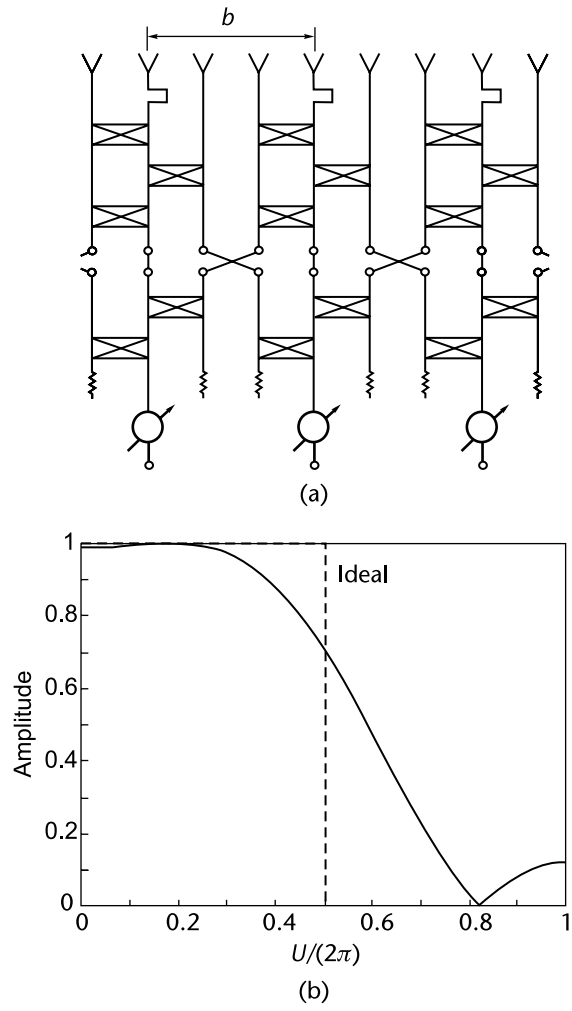

Figure 2.7 (a) Simplest networks of E. C. Dufort and (b) its subarray factor where $U = kb\sin\theta$.

through symmetrical two-channel power dividers and, in general case, N 1 cascades of directional couplers. Each cascade contains one row of couplers arranged between the modules and one more row of couplers arranged in the modules themselves. The arrangement of the directional couplers resembles a chessboard, and for this reason, the network is called chessboard one for brevity. The lengths of the transmitting lines situated at the same level are assumed to be identical. Excitation of each array input results in forming amplitude distributions (subarrays) embracing $2N + 1$ cells.

2.2.1 Analysis of the Radiation Characteristics

The analysis of the array radiation characteristics is carried out next in the assumption that all the power dividers and directional couplers included in the chessboard network are ideal. The radiation pattern of the subarray corresponding to excitation of the central array input can be written in the form

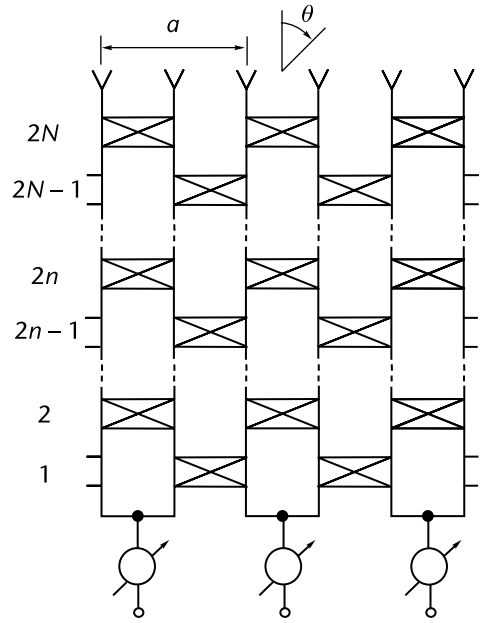

Figure 2.8 Multicascaded chessboard network.

$$F(\boldsymbol{q},U) = f(U)M(\boldsymbol{q},U) \tag{2.2}$$

where $f(U)$ is the radiation pattern of the array radiator,

$$M(\boldsymbol{q},U) = 2\sum_{n=1}^{2N+1} A_n \cos\frac{(2n \quad 1)U}{4} \tag{2.3}$$

is the subarray factor written to account for the symmetry of the network and amplitude distribution with respect to the excited input, $U = ka\sin\theta$, θ is the observation angle measured from the aperture broadside, A_n is the complex amplitude of the signal at the input of the nth array radiator, and $\boldsymbol{q} = (q_1, \ldots, q_{2N})$ is the vector of the coefficients of coupling between the cross ports of the directional couplers numbered from the power dividers to the radiators.

In the simplest case of one cascade (when $N = 1$), the amplitudes of the signals in the subarray radiators are determined by formulas

$$\begin{aligned} A_1 &= A^i \frac{p_1(p_2 + iq_2)}{\sqrt{2}} \\ A_2 &= A^i \frac{iq_1p_2}{\sqrt{2}} \\ A_3 &= \quad A^i \frac{q_1q_2}{\sqrt{2}} \end{aligned} \tag{2.4}$$

where A^i is the amplitude of the signal at the subarray input, while $q_{1,2}$ are coefficients of coupling between the cross ports in the directional couplers of the first and second rows, and $p_{1,2} = \sqrt{1 \quad q_{1,2}^2}$.

For the case of $N > 1$, formulas for the amplitudes A_n become too bulky, and, for this reason, we will merely present the algorithm for their calculation. Let $A_n^{(m-1)}$ be the amplitude of the signal at the nth output of the $(m-1)$th cascade (Figure 2.8), with $A_n^{(m-1)} = 0$ for $n \quad 2m$. Then the amplitudes of the signals at the outputs of the $(2m-1)$ couplers will be determined by formulas

$$\begin{aligned}
&B_{2n\ \ 1} = p_{2m\ \ 1}A_{2n\ \ 1}^{(m\ \ 1)} + iq_{2m\ \ 1}A_{2n}^{(m\ \ 1)}\\
&B_{2n} = iq_{2m\ \ 1}A_{2n\ \ 1}^{(m\ \ 1)} + p_{2m\ \ 1}A_{2n}^{(m\ \ 1)}, \quad n = 1,2,\ldots,m,\\
&B_n = 0, \quad n > 2m
\end{aligned} \tag{2.5}$$

and the amplitudes of the signals at the outputs of the $2m$th couplers and therefore at the outputs of the mth cascade are

$$\begin{aligned}
&A_1^{(m)} = \left(p_{2m} + iq_{2m}\right)B_1\\
&A_{2n}^{(m)} = p_{2m}B_{2n} + iq_{2m}B_{2n+1}\\
&A_{2n+1}^{(m)} = iq_{2m}B_{2n} + p_{2m}B_{2n+1}, \quad n = 1,2,\ldots,m
\end{aligned} \tag{2.6}$$

So, supposing that $A_0^{(1)} = A^i/\sqrt{2}$ and using the recurring relations (2.5) and (2.6), one can easily calculate the amplitudes $A_n = A_n^{(N)}$ of the signals at the radiators to use them subsequently for calculating the subarray factor (2.3).

To reveal some properties of the subarray factor that will be taken into account when formulating the problem of synthesis, let us derive one more representation for it. Let us consider the quasi-periodic excitation at which the signals come to the array inputs with complex amplitudes $A^i\exp(im\quad)$, where $m = 0$, ±1, ... is the number of the input and is the phase difference for the signals at adjacent inputs. The array factor corresponding to the indicated excitation is determined by

$$\begin{aligned}
M_p(q,U,\ ) &= [A_l(\ )e^{iU/4} + A_r(\ )e^{\ \ iU/4}] \underset{m=}{\quad} e^{im(\ \ \ U)}\\
&= 2\pi[A_l(\ )e^{iU/4} + A_r(\ )e^{\ \ iU/4}] \underset{m=}{\quad} \delta(\quad U \quad 2\pi m)
\end{aligned} \tag{2.7}$$

where A_l and A_r are complex amplitudes of the signals at the left and right radiators, respectively, in the central cell of number 0, and $\delta(x)$ is the delta function.

Since the subarray factor relates to the factor of the infinite periodic array in the same manner as the currents in the central cell at the aperiodic excitation relate by formula (1.33) to the currents in the same cell corresponding to the quasi-periodic excitation, then

$$M(q,U) = \frac{1}{2\pi}\overset{2\pi}{\underset{0}{\quad}} M_p(q,U,\ )d$$

Substituting (2.7) in this formula, we obtain

$$M(\boldsymbol{q},U) = A_l(U)e^{iU/4} + A_r(U)e^{\ iU/4} \tag{2.8}$$

Using (2.8) and taking into account relations

$$\begin{aligned} &|A_l(U)|^2 + |A_r(U)|^2 = (A^i)^2 \\ &A_l(2\pi \quad U) = A_l(\ \ U) = A_r(U) \\ &A_r(2\pi \quad U) = A_r(\ \ U) = A_l(U) \end{aligned}$$

resulting from the energy conservation law as well as from the array periodicity and symmetry, we can obtain that

$$|M(\boldsymbol{q},U)|^2 + |M(\boldsymbol{q},2\pi \quad U)|^2 = 2(A^i)^2 \tag{2.9}$$

The relation (2.9) shows that the radiated power from each point of the region $\pi < |U| < 2\pi$ will change for the corresponding point of the region $0 < |U| < \pi$ and back with changing the parameters of the directional couplers so that the total radiated power in the indicated regions will remain constant.

2.2.2 Statement and Solution of the Synthesis Problem

The properties of the subarray factor revealed earlier allow us to set the problem of synthesis of the sector subarray radiation patterns as a problem of searching for such values of the coupler parameters q_n, at which the objective function

$$P(\boldsymbol{q}) = \frac{1}{\pi}\int_0^{\pi} |M(\boldsymbol{q},U)|^2\, dU \tag{2.10}$$

achieves its maximum value.

Solution of the previous problem set will automatically provide minimization of the power radiated in the region $\pi < |U| < 2\pi$. Substituting (2.3) in (2.10) and accomplishing a simple operation, we obtain the following expression for calculation of the objective function

$$P(\boldsymbol{q}) = 2\sum_{m=1\ \ n=1}^{2N+1\,2N+1} (X_m X_n + Y_m Y_n)\ \frac{\sin(m \quad n)\pi/2}{(m \quad n)\pi/2} + \frac{\sin(m+n \quad 1)\pi/2}{(m+n \quad 1)\pi/2} \tag{2.11}$$

where X_n and Y_n are respectively real and imaginary parts of the complex amplitudes A_n calculated according to the algorithm given earlier including formulas (2.5) and (2.6).

The results of maximization of function (2.11) for $N = 1, 2, 3$, and 4 obtained at $A^i = 1/\sqrt{2}$ using the method of deformable polyhedron [30] are presented in Table 2.1, while the plots of the subarray factor magnitude corresponding to the optimum values for the coupler parameters q_n are shown in Figure 2.9(a). For convenience of their distinction, the curves are successively shifted downward with step 0.2. The

Table 2.1 Values of the Directional Coupler Parameters Providing Maximum of Objective Function (2.10) for $N = 1, 2, 3$, and 4

N	P	q_1	q_2	q_3	q_4	q_5	q_6	q_7	q_8
1	0.921	0.438	0.740	—	—	—	—	—	—
2	0.950	0.455	0.971	0.714	0.631	—	—	—	—
3	0.963	0.440	0.989	0.789	0.952	0.767	0.569	—	—
4	0.971	0.428	0.994	0.802	0.982	0.872	0.942	0.783	0.531

values of q_n indicated in the table provide radiation of 92.1%, 95.0%, 96.3%, and 97.1% of power in the ideal sector for the indicated numbers of the cascades, respectively. The sidelobe level of the subarray factor does not exceed –15.4 dB, –17.1 dB, –18.8 dB, and –19.8 dB, respectively. As noted in [29], the sidelobe level at another statement of the synthesis problem can be made even lower at the expense of slight

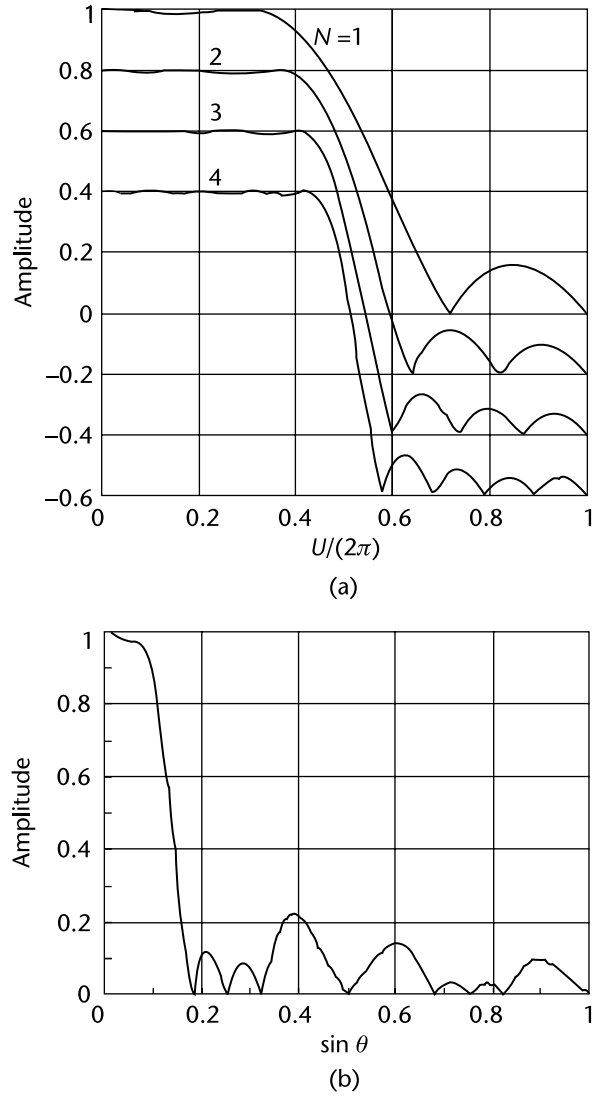

Figure 2.9 (a) Subarray factor for optimized 1-, 2-, 3-, and 4-cascaded chessboard network and (b) single-cascaded subarray pattern (2.2) with $f(U) = 4\sin(U/4)/U$ for $a = 4\lambda$.

worsening of the sector beam shape. Such an option has been realized in [31] for $N = 1$ and 3, as well as in [32] for $N = 2$ and 4. Furthermore, the sidelobe level is additionally reduced because of the slope of the radiator pattern itself.

Note that the subarray factor (2.3) is a periodic function of $\sin\theta$ with period $2\lambda/a$. Therefore, the secondary sector lobes can be present in the visible space together with the main sector beam at sufficiently large values of the array period a. However, the secondary lobes are suppressed to some degree by the radiation pattern $f(U)$ of the array radiator. An example of this is shown in Figure 2.9(b), where the subarray pattern (2.2) corresponding to optimum parameters q_n for $N = 1$ and $f(U) = 4\sin(U/4)/U$, which corresponds to a uniformly excited aperture of width 2λ. Even more efficient suppression of the secondary sector lobes can be provided by means of repeated application of the chessboard network but with period equal to half the initial one. Such a doubled single-cascaded chessboard network is shown in Figure 2.10. The secondary sector lobes nearest to the main beam in this case are situated just in the low sidelobe region of the upper level subarray radiation pattern.

As it was mentioned in [33], the chessboard network was realized using the microstrip elements for scanning in a limited sector in one plane. This technology seems to be most convenient for realization of the network for limited scan in both principal planes. An example of such array architecture is shown in Figure 2.11.

The results of the chessboard network parameter optimization demonstrate good capabilities of the chessboard network for shaping sector subarray radiation patterns. Comparing this network to the other technical solutions described earlier, we can note the following features. Application of N coupler cascades in the chessboard network allows the formation of overlapped subarrays, including $2N + 1$ array cells. The single-cascaded chessboard network resembles the network [12] shown in Figure 2.4. However, it possesses greater capabilities than [12] does because it allows using radiators of arbitrary type, not only the horns used in [12]. Furthermore, it is more capable than [12] of improving the quality of the sector patterns, since it allows the use of a greater number of cascades for forming subarrays of larger aperture, thereby with steeper slopes of the sector patterns.

Unlike the network [18] [Figure 2.5(a)] with excitation of the array radiators in series, the subarray radiators in the chessboard network are fed in parallel, which makes it more wideband than the network [18]. The subarrays formed in the networks [20, 21] involve radiators of five modules. This is done with using eight directional couplers and one divider per one module in the former network and eight couplers per one module in the latter one. The subarrays involving radiators of five

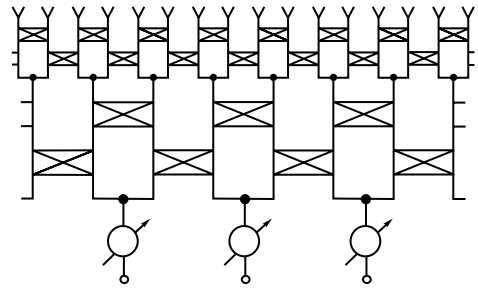

Figure 2.10 A doubled single-cascaded chessboard network.

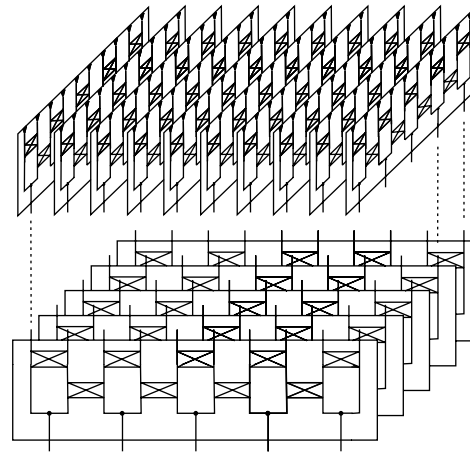

Figure 2.11 Architecture of an array with single-cascaded chessboard network for limited-scan in both principal planes.

modules in the chessboard network are formed using two cascades of directional couplers. Such a dual-cascaded chessboard network has been separately proposed in [34]. The network uses four couplers and one divider per one module (i.e., it is considerably simpler than the networks shown in Figure 2.6). Moreover, all the subarray radiators are excited in the chessboard network, while only 6 radiators of 10 are excited in the networks [20, 21].

All other things being equal, the chessboard network is also simpler than the network proposed in [24]. For instance, the simplest modification of the latter contains one three-channel divider, one crossover, and three couplers per one array module. The single-cascaded chessboard network uses only two couplers and a simpler power divider per one module. In the general case of forming overlapped subarrays involving radiators of $2N + 1$ modules, the chessboard network uses $N + 1/2$ times less directional couplers than those used in the modules of network [24].

2.3 Experimental Study of the Chessboard Network

The single-cascaded chessboard network has been realized in an experimental breadboard of a K_a-band array of rectangular waveguides arranged in the nodes of a rectangular lattice, as shown in Figure 2.12(a). The array has been designed (see [35, 36]) for providing wide-angle scanning in the E-plane, where the waveguide width can be chosen to be sufficiently small, and for scanning in a limited sector of ±17° in the H-plane using the single-cascaded chessboard network.

The directional couplers in the breadboard are performed in the form of doubled slots, as shown in Figure 2.12(b). The widths of the slots and spacing between them have been chosen as a result of a numerical experiment to provide the necessary values for the cross coupling coefficients in the directional couplers at their almost ideal match at a specified frequency. The slots in the waveguide walls are also used for matching the power dividers as well as the waveguide array aperture to free space. Determination of the geometrical parameters for structure elements

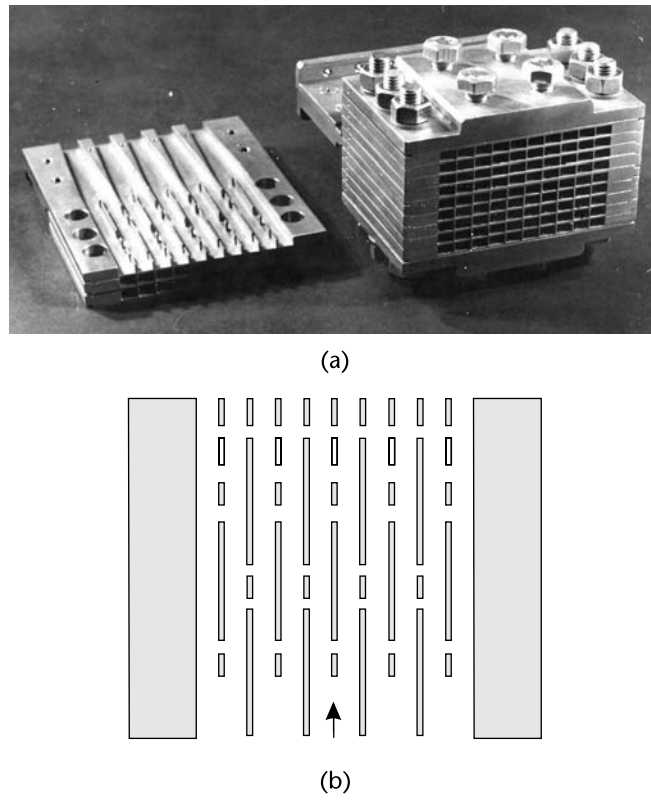

Figure 2.12 (a) The waveguide array breadboard and (b) cross-section of its central plate in the H-plane.

has been performed with using the method of mode-matching at the boundaries of the partial regions [37]. Since the dividers and couplers have been assumed to be separately well matched, the distances between them are chosen from the condition of providing their negligible interaction over evanescent higher-order modes.

The design of the array shown in Figure 2.12(a) is an assemblage of H-plane corrugated plates made of brass by the method of milling. The geometry corresponding to the chessboard network shown in Figure 2.12(b) has been realized only in the central plate. All the other plates serving for imitation of operating the excited elements in the array surrounding only have slots matching the array aperture to free space. The corrugated plates of 1-mm thickness with fins of 0.4-mm thickness forming an aggregate of waveguide channels of cross-section 6.1 3.4 mm^2 are added with two outer steel plates. All the plates are tightened by six screws arranged at the side edges. Each outer plate is provided with four screws used for pressing the assemblage in the central region and thereby for providing good contacts between the adjoining surfaces of the inner plates. The central plate together with its cover is terminated at the rear side by a flange with five waveguide inputs of standard cross-section 7.2 3.4 mm^2.

When measuring the radiation pattern, the array was installed on a rotating table so that the rotation axis passed in the array aperture plane to exclude the parallax. The signal from a generator also installed on the table came to one of the

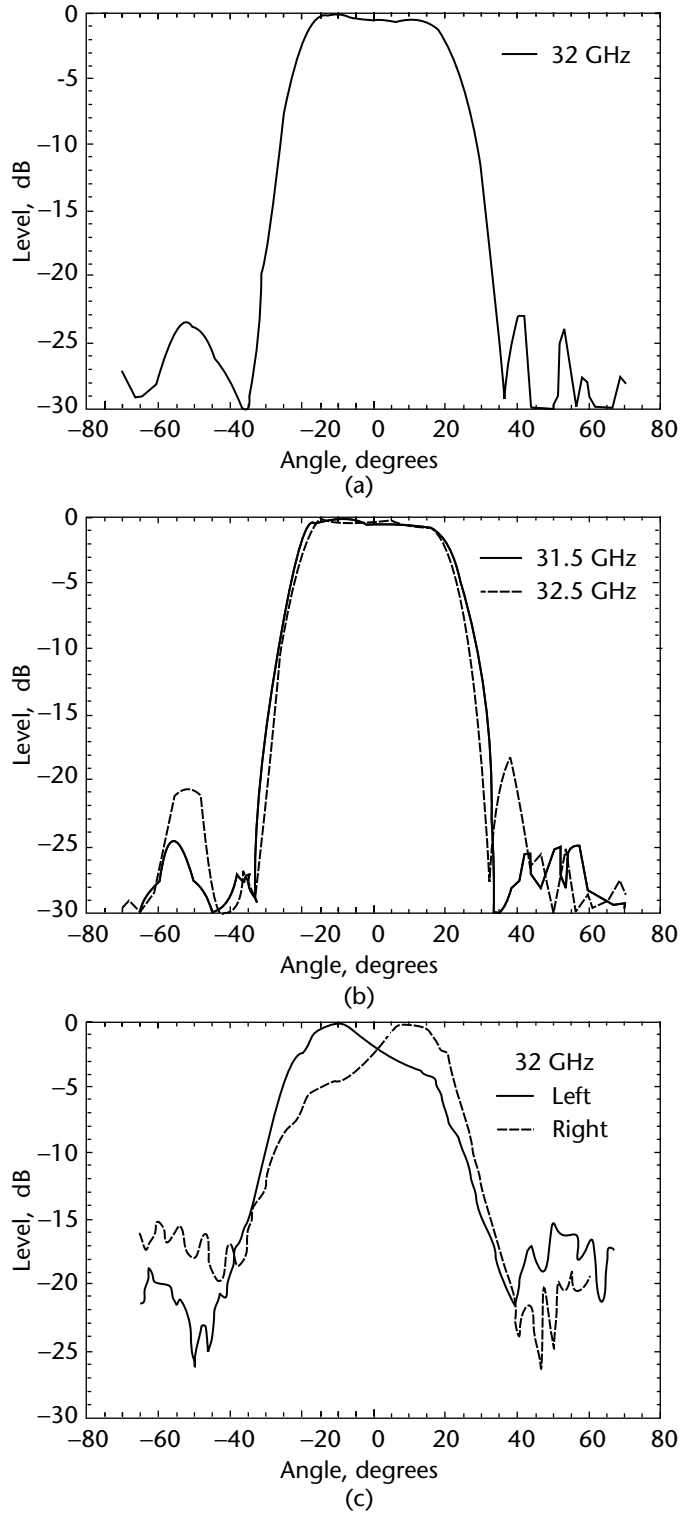

Figure 2.13 Measured array radiation patterns in the H-plane at excitation of the central input at (a) 32 GHz, (b) central input at 31.5 and 32.5 GHz, and (c) left and right outer inputs at 32 GHz.

array inputs. All the other inputs and all the waveguide channels formed in the lateral corrugated plates were terminated with matching loads. The radiated field was received by a horn antenna arranged in the far zone of the array. The signal from the horn came to a receiver via an attenuator and further to a plotter. The angle of rotation was measured by the rotating table scale, while the received signal level was measured by the attenuator table.

The measured array radiation pattern at the frequency 32 GHz corresponding to the excitation of the central input is presented in Figure 2.13(a). The sinus of its half-width at the levels of –1.5 dB and –10 dB is equal to 0.326 and 0.46, respectively, or 0.904 and 1.3 of the half-width $\lambda/(2a)$ corresponding to the ideal sector element pattern. The appropriate data 0.9 and 1.26 resulting from Figure 2.9(a) are close to the measured results indicated earlier.

Figure 2.13(b) represents the radiation patterns, corresponding to the central input, measured at the frequencies 31.5 and 32.5 GHz (i.e., at deviation of frequency by ±1.56% from the central value of 32 GHz). The results show that the sector shape of the pattern is kept well in the indicated frequency band.

The study of how the array edges influence the subarray pattern shape was performed by measurement of the array radiation pattern at successive excitation of the lateral array inputs. The pattern measurements corresponding to excitation of the left and right inputs nearest to the central one have shown that the patterns differ from the pattern corresponding to the central input [Figure 2.13(a)] very weakly. This is explained by the fact that the three-cell subarrays have not been truncated by the array edges. Though the edges are closer for them than for the central subarray, their influence on the subarray pattern shape is still weak due to the tapered subarray amplitude distributions. The subarrays corresponding to the edge array inputs become nonsymmetrical and include only two cells each. As we can see from Figure 2.13(c), this feature results in significant distortion of the pattern shape compared to the cases of excitation of the inner inputs.

Together with the radiation pattern, the measurements of the voltage standing wave ratio (VSWR) corresponding to excitation of different array inputs were performed. The measurements have shown that the VSWR varies in the limits from 1.07 to 1.8 in the frequency band from 31.5 to 32.5 GHz. The measured values have turned out to be slightly higher than the calculated data. This seems to be explained by some inaccurateness in fabrication of the breadboard.

2.4 A Linear Array with Chessboard Network as a Feed of a Parabolic Cylindrical Antenna

Some radio systems, such as, for instance, aerodrome and sea port radars [38], as well as automotive radars [39, 40] require application of antennas performing electrical scanning of narrow beam in a limited sector in one plane only. The indicated systems can be constructed on the basis of hybrid antennas, where the beam steering is provided by a linear or arc array, while the required narrow beam is formed by a reflector or a lens. One of the possible reflector types used in the hybrid antennas is a focuser [41] capable of transforming a plane wave into a line of finite size. The indicated focal line serves as a place for arranging an array of feeds. However,

the studies of such antennas in [42, 43] have shown that they are considerably inferior to the parabolic cylindrical antennas of the same aperture dimension in scanning performance because of arising and increasing phase errors when deflecting the beam from the broadside. A way of eliminating the indicated flaw has been proposed in [44]. This way uses a reflector-focuser of increased dimensions where a region of effective illumination corresponding to a definite beam position moves over the reflector to scan the beam.

The suggestion of using the focusers in [42–44] has been motivated by the fact that they allow a reduction of the size of the array feed and the number of radiating elements in the latter in comparison to those in the parabolic cylindrical antennas. Actually, the array dimension in the parabolic cylindrical antennas (e.g., described in [45–47]) is close to the dimension of the reflector itself, and the array element spacing is chosen to prevent arising of the array factor grating lobes in the visible space when scanning the main lobe in the specified sector. In [47], where the design of a cylindrical antenna for investigation of the space radio sources is described in detail, the array element spacing is $d = 0.7\lambda$, while the maximum angle of beam deflection from the broadside is $\theta_m = 21.3°$. The maximum admissible spacing for such a scan sector is $d_m = 0.5\lambda/\sin\theta_m \quad 1.376\lambda$, and therefore the array element use factor in the antenna of [47] is $d_m/d \quad 1.97$.

The example presented earlier together with other examples given in [42–44] justify the motivation of the indicated works on the creation of hybrid antennas with a compact feed array containing a smaller number of the elements compared to those in the arrays usually used for illumination of the parabolic cylindrical reflector. However, neither indicated works nor other publications mentioning the parabolic cylindrical antennas consider the situation when the ordinary feed array is replaced by an array with minimum number of elements shaping sector radiation patterns of width equal to the width of the scan sector. Such an antenna is considered next from the viewpoint of its achievable radiation characteristics, since the parabolic cylinder has a simpler shape and smaller dimensions compared to a reflector of double curvature in [44] (i.e., the parabolic cylindrical antenna remains attractive from the viewpoint of its simple design).

2.4.1 Formulation of the Problem

Let us consider a parabolic cylindrical reflector antenna shown in Figure 2.14. The reflector surface in the Cartesian coordinate system $0xyz$ is given by formulas

$$\begin{aligned} & L_x/2 \quad x \quad L_x/2 \\ & \rho(\psi) = \sqrt{y^2 + z^2} = \frac{2f}{1+\cos\psi} \end{aligned} \tag{2.12}$$

where L_x is the horizontal reflector dimension, f is the focal distance, and $\psi_1 \quad \psi \quad \psi_2$ is the angle measured from the negative hemi-axis z. The antenna aperture height is determined by

$$L_y = \rho(\psi_2)\sin\psi_2 \quad \rho(\psi_1)\sin\psi_1 \tag{2.13}$$

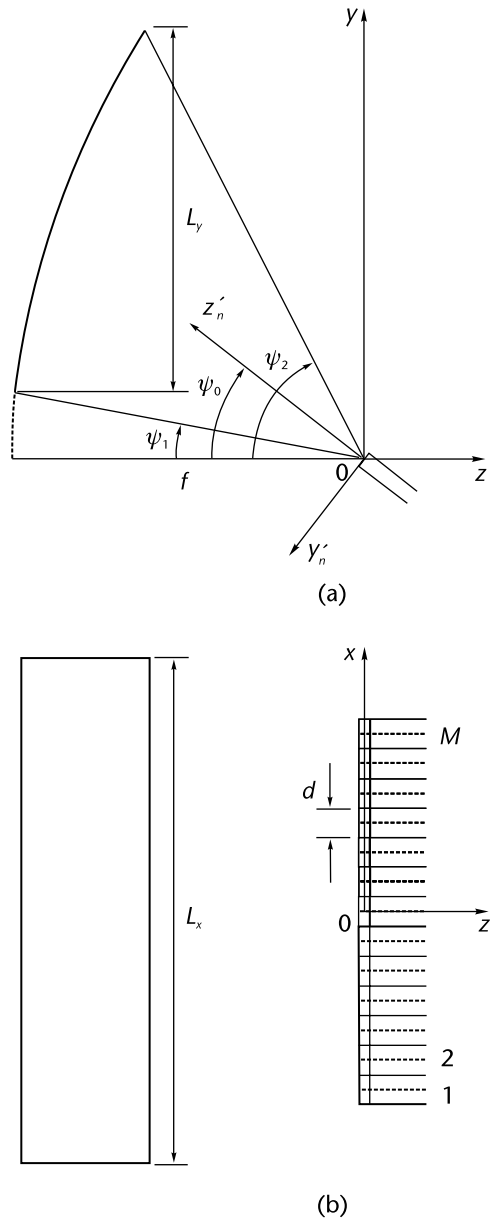

Figure 2.14 Geometry of the parabolic cylindrical antenna: (a) side view and (b) view from the top.

The reflector is illuminated by a linear array arranged over the focal line coinciding with the x-axis. Radiators of various types may be used as the array elements. Thus, for example, the reflector in [38] is illuminated from the slots cut through in the narrow wall of a meander waveguide of rectangular cross-section. Electric dipoles have been used in antenna [47]. In our model, we will assume that the array of element spacing d is formed by the open-ended rectangular waveguides of width $a \quad d/2$ (along the x-axis) and height b. The array aperture broadside is directed at angle ψ_0 from the negative semi-axis z.

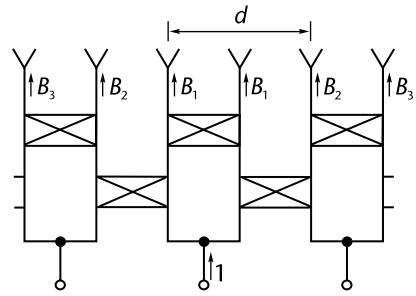

Figure 2.15 Linear array with single-cascaded chessboard network.

We will assume further that the waveguides are excited through a single-cascaded chessboard network shown in Figure 2.15. Excitation of one controlled array input by a signal of unit amplitude results in forming a subarray of six radiators with a symmetrical distribution of amplitudes, which, instead of (2.4) for convenience of the further actions, we write as

$$\begin{aligned} B_1 &= \frac{p_1(p_2 + iq_2)}{\sqrt{2}} \\ B_2 &= \frac{iq_1p_2}{\sqrt{2}} \\ B_3 &= \frac{q_1q_2}{\sqrt{2}} \end{aligned} \tag{2.14}$$

where the optimum values of the coupler parameters $q_1 = 0.438$ and $q_2 = 0.74$ are taken from Table 2.1.

Let the array consist of M subarrays, and their inputs be excited by signals with amplitudes A^i_m and phases $(m \quad 1)U$, where $1 \quad m \quad M$, $U = kd\sin\theta_0$, $k = 2\pi/\lambda$, and θ_0 is the angle of the beam deflection from the broadside. Then the distribution of the amplitudes over the waveguides, the total number of which is $N = 2M + 4$, will be determined by formulas

$$\begin{aligned} A_1 &= A^i_1 B_3 \\ A_2 &= A^i_1 B_2 \\ A_{2m+1} &= (A^i_{m\ 1}e^{\ 2iU}B_2 + A^i_m e^{\ iU}B_1 + A^i_{m+1}B_3)e^{imU} \\ A_{2m+2} &= (A^i_{m\ 1}e^{\ 2iU}B_3 + A^i_m e^{\ iU}B_1 + A^i_{m+1}B_2)e^{imU} \\ A_{N\ 1} &= A^i_M e^{i(M\ 1)U}B_2 \\ A_N &= A^i_M e^{i(M\ 1)U}B_3 \end{aligned} \tag{2.15}$$

where the amplitudes A^i_0 and A^i_{M+1} at the inputs are assumed to be zero.

The electric field strength in the far zone of the antenna can be determined by the well-known formula (see, for instance, [45]):

$$\boldsymbol{E}(r,\theta,\varphi) = \frac{ik\eta_0 e^{ikr}}{4\pi r}\boldsymbol{F}(\theta,\varphi) \tag{2.16}$$

where

$$\boldsymbol{F}(\theta,\varphi) = \sum_{n=1}^{N} A_n[\boldsymbol{I}_n \quad (\boldsymbol{I}_n \times \boldsymbol{e}_r)\boldsymbol{e}_r] \tag{2.17}$$

is the complex radiation pattern of the antenna as a whole,

$$\boldsymbol{I}_n(\theta,\varphi) = \int_{-L_x/2}^{L_x/2}\int_{\psi_1}^{\psi_2} \boldsymbol{J}_n(\boldsymbol{r})\, e^{\ ik(\boldsymbol{r}\times\boldsymbol{e}_r)} \frac{\rho\, d\psi\, dx}{\cos(\psi/2)} \tag{2.18}$$

where $\boldsymbol{J}_n(\boldsymbol{r})$ is the surface density of the current induced on the reflector when exciting the nth waveguide by the wave of unit amplitude,

$$\boldsymbol{e}_r = \boldsymbol{e}_x \sin\theta\cos\varphi + \boldsymbol{e}_y \sin\theta\sin\varphi + \boldsymbol{e}_z \cos\theta$$

is the unit vector directed to the observation point characterized by angles θ and φ measured from the axes z and x, respectively, $\boldsymbol{r} = \boldsymbol{e}_x x + \boldsymbol{e}_y y + \boldsymbol{e}_z z$ is the vector of the integration point on the cylinder, $y = \rho\sin\psi$, $z = \rho\cos\psi$, while ρ is determined by formula (2.12).

According to the physical optics approximation, the current density in (2.18) is determined by formula $\boldsymbol{J}_n = 2[\boldsymbol{n} \quad \boldsymbol{H}_n]$, where

$$\boldsymbol{n}(\boldsymbol{r}) = \quad \boldsymbol{e}_y \sin(\psi/2) + \boldsymbol{e}_z \cos(\psi/2)$$

is the unit vector of the normal to the cylinder surface, and $\boldsymbol{H}_n(\boldsymbol{r})$ is the magnetic field strength from the nth waveguide in the point on the cylinder surface. To calculate this field, we will assume that the waveguide is excited in the H_{10} mode of horizontal polarization yielding the following aperture distribution

$$\begin{aligned} E^i_{x_n} &= H_0\eta_0 \sin\frac{\pi(y_n + b/2)}{b} \\ H^i_{y_n} &= H_0\tilde{\gamma} \sin\frac{\pi(y_n + b/2)}{b} \end{aligned} \tag{2.19}$$

where H_0 is the unit strength of the magnetic field in the aperture center, $\tilde{\gamma} = \sqrt{1 \quad (\lambda/2b)^2}$, while x_n and y_n are the axes of the rectangular Cartesian coordinate system with the origin placed in the center of the waveguide aperture (Figure 2.14). Note, that the maximum admissible period of an array designed for scanning in a small sector may be rather large ($d_m > 1.4\lambda$ for $\theta_m \quad 20°$). As it will be indicated next, the vertical dimension of the waveguide aperture will also be large enough ($b > \lambda$). Calculation of the field radiated from the open end of such a waveguide may be performed by the Huygens-Kirchhoff method with using the undistorted field (2.19) of the incident wave and neglecting the mutual coupling between the

waveguides [48]. As a result, we obtain the following expressions for the current density components on the cylinder:

$$\begin{aligned} J_{nx}(\boldsymbol{r}) &= \tilde{F}_n(u_n,\upsilon_n)[(1 \quad \upsilon_n^2 + \tilde{\gamma}w_n)\cos(\psi_0 \quad \psi/2) + (w_n + \tilde{\gamma})\upsilon_n \sin(\psi_0 \quad \psi/2)] \\ J_{ny}(\boldsymbol{r}) &= \quad \tilde{F}_n(u_n,\upsilon_n)u_n\upsilon_n \cos(\psi/2) \\ J_{nz}(\boldsymbol{r}) &= \quad \tilde{F}_n(u_n,\upsilon_n)u_n\upsilon_n \sin(\psi/2) \end{aligned} \tag{2.20}$$

where

$$\begin{aligned} &\tilde{F}_n(u_n,\upsilon_n) = H_0 \frac{ikabe^{ikr_n}}{4r_n} F_n(u_n,\upsilon_n) \\ &F_n(u,\upsilon) = \frac{\sin(kau/2)}{kau/2} \frac{\cos(kb\upsilon/2)}{(\pi/2)^2 \quad (kb\upsilon/2)^2} \\ &u_n = x_n/r_n,\ \upsilon_n = y_n/r_n,\ w_n = z_n/r_n \\ &r_n = \sqrt{\rho^2 + x_n^{\,2}}, \quad x_n = x \quad x_n \\ &y_n = \quad y\ \cos\psi_0 \quad z\ \sin\psi_0 \\ &z_n = y\ \sin\psi_0 \quad z\ \cos\psi_0 \end{aligned}$$

and x_n is the coordinate of the nth waveguide aperture center.

To calculate the integral (2.18), we represent it in a more convenient form

$$\boldsymbol{I}_n(\theta,\varphi) = \int_{-L_x/2}^{L_x/2} \int_{\psi_1}^{\psi_2} \boldsymbol{j}(\boldsymbol{r}) e^{ik\Phi(\boldsymbol{r},\theta,\varphi)} d\psi dx \tag{2.21}$$

where

$$\boldsymbol{j}(\boldsymbol{r}) = \boldsymbol{J}_n(\boldsymbol{r}) e^{\ ikr_n \rho/\cos(\psi/2)}$$

and

$$\Phi(\boldsymbol{r},\theta,\varphi) = r_n \quad (\boldsymbol{r} \times \hat{\boldsymbol{r}})$$

and then we apply the Ludwig's method [49].

After calculating the radiation pattern (2.17), we calculate the antenna gain

$$G(\theta,\varphi) = \frac{k^2\eta_0}{8\pi P^i} |\boldsymbol{F}(\theta,\varphi)|^2 \tag{2.22}$$

where

$$P^i = \frac{\tilde{\gamma}\eta_0 H_0^2 ab}{4} \sum_{n=1}^{N} |A_n|^2$$

is the total power delivered to the waveguide apertures.

2.4.2 Highest Possible Antenna Gain

It is often useful to compare calculated or measured results obtained when studying of that of another antenna to its highest achievable characteristics. To obtain such characteristics for our parabolic cylindrical antenna, let us consider its model in the form of an infinite linear array of period d illuminating an infinite parabolic cylinder in the horizontal plane. The aperture dimension of the cylinder in the vertical plane is L_y. Since the aperture area allotted to one array cell in such antenna is $L_y d$, the highest achievable array element gain when scanning will be equal to

$$G_{e,m} = \frac{4\pi L_y d}{\lambda^2}\cos\theta \tag{2.23}$$

where angle θ is measured from the normal to the aperture (the z-axis in Figure 2.14). Accounting for the relation between the ideal sector element pattern width $2\theta_m$ with the array period d given earlier in the introduction to the present section, we can rewrite (2.23) as

$$G_{e,m} = \frac{2\pi L_y}{\lambda \sin\theta_m}\cos\theta \tag{2.24}$$

with the ideal element gain being equal to zero at $|\theta| > \theta_m$.

It is of interest to compare the gain (2.24) to the results that can be obtained from consideration of a vertical uniformly excited linear radiator of length L_y. This radiator has an axially symmetrical radiation pattern in the horizontal plane, and its gain is equal to $2L_y/\lambda$ at $L_y >> \lambda$ [45]. If we now distribute the radiated power uniformly over a horizontal sector of width $2\theta_m$, the gain will increase by the factor $2\pi/(2\theta_m)$ to be

$$G_L = \frac{2\pi L_y}{\lambda \theta_m} \tag{2.25}$$

Comparing (2.24) and (2.25), we can conclude that $G_{e,m}$ G_e as θ_m 0, and moreover

$$\frac{1}{\theta_m}\int_0^{\theta_m} G_{e,m}(\theta)\,d\theta = G_L$$

that is, the gain of the ideal element in the infinite parabolic cylindrical hybrid antenna (2.24) averaged over the scan sector equals the axially symmetrical linear antenna gain multiplied by π/θ_m.

The simple relations derived in this section will be used next. They may also be useful when estimating the quality of base station antennas with sector radiation patterns.

2.4.3 Results, Comparison, and Discussion

The algorithm described in Section 2.4.1 has been realized in a FORTRAN code, and the operation of the latter has been tested by calculation of the parabolic cylin-

drical antenna considered in [47]. In particular, the tests have shown that the results obtained using the cells of integration of $\lambda \quad \lambda$ dimensions in Ludwig's method [49] do not differ practically from the results corresponding to the integration cell dimensions $0.5\lambda \quad 0.5\lambda$. After the testing, a numerical study of the antenna under consideration has been performed. The results to be discussed next have been obtained for the antenna with parameters $\psi_1 = 5°$, $\psi_2 = 98°$, and $\psi_0 = 65°$, which are close to the similar antenna parameters in [47]. They also correspond to the recommendations given in [45]. The focal length $f = 27\lambda$ has been chosen to provide the vertical aperture dimension $L_y = 57.9\lambda$ equal to the dimension of the focuser [44]. The vertical dimension of the waveguide aperture chosen to be $b = 1.1\lambda$ provides a –10 dB level of the illumination on the lower and upper edges of the aperture. The choice of the array period d has been based on the analysis of the subarray factor shape [Figure 2.9(a)] for the network shown in Figure 2.15. If it is required to provide a secondary grating lobe level not higher than –15 dB when scanning the main lobe in the specified sector $\theta_m \quad \theta \quad \theta_m$, then d should be taken $\xi \quad 1.4$ times smaller than the maximum admissible period $d_m = 0.5\lambda/\sin\theta_m$. For $\theta_m = 10°$, like in [44], we take $d = 2.056\lambda$ and neglect the waveguide wall thickness (i.e., assume that $a = d/2$).

Let us first consider the influence of the reflector on the radiation pattern of one subarray by specifying $M = 1$ and $N = 6$ in (2.15) and (2.16). The normalized radiation patterns of the antenna with $L_x = 100\lambda$ in the horizontal plane at different horizontal displacement x_f of the subarray from the coordinate system origin are presented in Figure 2.16. The antenna patterns are compared to the subarray pattern in the absence of the cylinder taken in the plane passing over the x-axis, coordinate origin, and normal to the subarray aperture. Comparing the pure subarray pattern (curve 4) to the antenna pattern when the subarray is

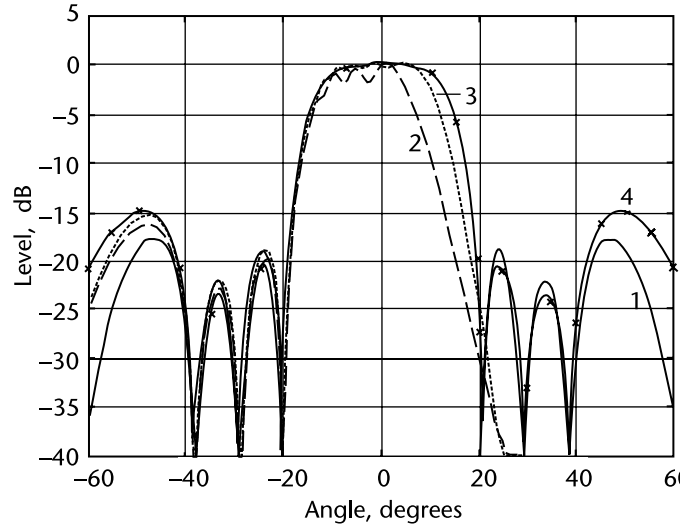

Figure 2.16 Normalized radiation pattern in the scan plane of the reflector illuminated by a subarray with $d = 2.056\lambda$ at different horizontal subarray displacement: (1) $x_f = 0$; (2) $x_f = 43.3\lambda$; (3) $x_f = 39.8\lambda$; and (4) subarray pattern without the reflector.

arranged in the central position $x_f = 0$ (curve 1), we can note that the visible differences take place only in the region of the sidelobes nearest to the side edges of the cylinder observed from the subarray center at the angle 62°. The displacement of the subarray from the center by $x_f = 43.3\lambda$ to the right corresponds to illumination of the right edge at the angle 10° equal to the maximum antenna beam deflection. The illumination level in this case is equal to –1 dB. The subarray pattern (in the presence of the reflector) presented by curve 2 is characterized by significant distortions on the right side and appearance of oscillations on the flat top explained by the edge wave interference. The angle of illumination of the left reflector edge is now greater, and this has led to reduction of the distortions in this region compared to the previous case. At smaller subarray displacement $x_f = 39.8\lambda$ corresponding to the illumination angle 15° of the right edge and the illumination level –5 dB at that edge, the distortions mainly consist in cutting of the right sidelobes (curve 3). Note, that the negative values of θ in Figure 2.16 correspond to the case when $\varphi = 180°$.

The results presented in [50] also show that the displacement of the subarray in the indicated limits does not lead to changing the antenna radiation pattern in the vertical plane.

Calculation of the antenna gain (2.22) in the aperture broadside direction for $x_f = 0$, $x_f = 43.3\lambda$, and $x_f = 39.8\lambda$ yields the values 31.04, 31.88, and 30.92 dB, respectively, while the highest possible element gain (2.23) equals 31.89 dB. When accounting for the loss caused by the illumination nonuniformity in the vertical plane, which we estimate to be 0.35 dB, approximately the same loss for spillover [49, 51], and the anomalous edge effect for the second case, the presented results agree well with the highest element gain (2.23). The remaining minor differences may be attributed to the effect of scattering at the reflector edges that is not taken into account in the present analysis.

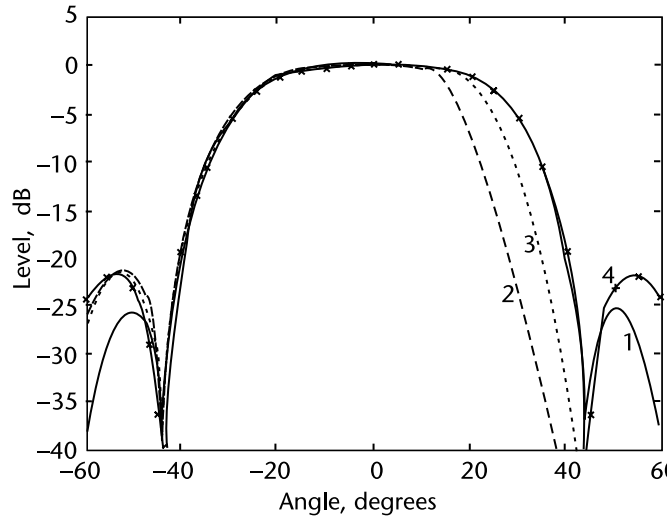

Figure 2.17 Normalized radiation pattern in the scan plane of the reflector illuminated by a subarray with $d = 1.044\lambda$ at different horizontal subarray displacement: (1) $x_f = 0$; (2) $x_f = 36.2\lambda$; (3) $x_f = 28.1\lambda$; and (4) subarray pattern without the reflector.

Figure 2.17 represents the subarray patterns in the plane of scan at $d = 1.044\lambda$ chosen according to the reasoning given earlier for the scan sector $-20° \le \theta \le 20°$. The values of the subarray displacements $x_f = 36.2\lambda$ and $x_f = 28.1\lambda$ correspond to the right-hand reflector edge illumination at the angles $-20°$ and $-30°$, respectively. The levels of the edge illumination are the same as those in the previous case. The results show similar influence of the reflector edges on the element (subarray) pattern, with the exception of the fact that the oscillation level on the flat top in this case is lower. The antenna element gain (2.22) in the broadside for $x_f = 0$, $x_f = 36.2\lambda$, and $x_f = 28.1\lambda$ equals 28.10, 28.05, and 28.09 dB, respectively, with the highest element gain (2.23) being equal to 28.94 dB (i.e., the losses turn out to be similar to those corresponding to the previous case).

Let now the scanning of a beam having a 1° width at the –3-dB level (like in [44]) be required in the sector $-\theta_m \le \theta \le \theta_m$ in the horizontal plane. The dimension of the array with uniform amplitude distribution providing the indicated beam width is 50.76λ. If $\theta_m = 10°$ and $d = 2.056\lambda$, the number of controlled elements (subarrays) will be equal to $M = 25$. Let the outermost subarrays be illuminating the reflector edges at the angle of 15°. Then the reflector length will be $L_x = 70\lambda$. The antenna gain in the direction of phasing calculated according to (2.22) is presented by curve 1 in Figure 2.18.

Similarly to the focuser [44], the antenna gain in the broadside is 45 dB and drops by 0.8 dB at the sector edge, while the gain reduction in [44] is 2 dB. Since the maximum gain of the $70\lambda \times 59.76\lambda$ aperture is equal to 47.21 dB, the reflector aperture efficiency is 60%, versus smaller than 25% in [44], where the transverse focuser dimension is ~200λ and the focal length of the focuser is ~75λ. Note also that the number of controlled elements used in our case is 1.4 times greater than the theoretical minimum, while the element use factor in [44] is 1.7. If we assume that

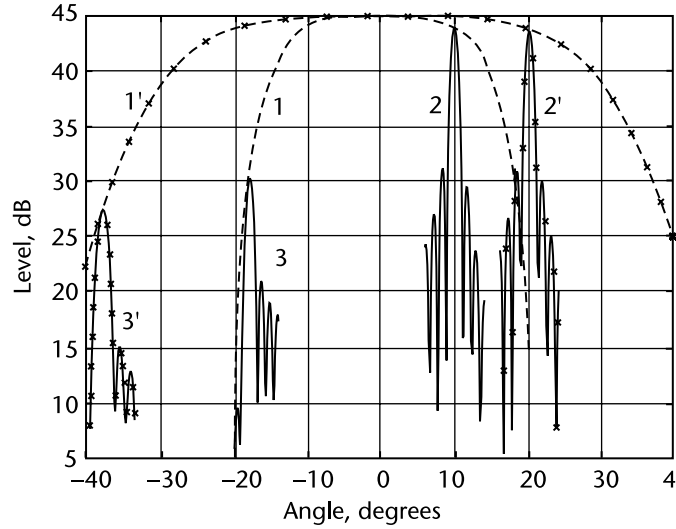

Figure 2.18 Gain of the antenna with $d = 2.056\lambda$, $M = 25$, and $L_x = 70\lambda$: (1) at the peak versus scan angle; (2) in the main lobe region versus observation angle; and (3) in the grating lobe region versus observation angle. Curves 1′, 2′, and 3′ are similar characteristics for antennas with $d = 1.044\lambda$, $M = 49$, and $L_x = 94\lambda$.

the reflector edges are illuminated at the angle of 10°, then $L_x = 63\lambda$. The antenna gain in the broadside in this case decreases by 0.01 to 0.03 dB, while the aperture efficiency increases up to 67%. The gain at the sector edge is 43.95 dB (i.e., by 0.25 dB lower than that for $L_x = 70\lambda$). So, the indicated decrease of the reflector dimension yields insignificant effect. This effect will be even weaker for tapered amplitude distributions applied for reduction of the sidelobe level. Figure 2.18 also contains the antenna radiation pattern in the region of the main lobe arranged at the sector edge, $\theta_0 = 10°$ (curve 2) and in the region of the grating lobe (curve 3).

Similar curves 1 , 2 , and 3 are presented in Figure 2.18 for antenna forming the beam of the same width but with array period $d = 1.044\lambda$ corresponding to scan sector 20° θ 20°. The number of the controlled elements (subarrays) in this case is $M = 49$, while the reflector dimension $L_x = 94\lambda$ has been calculated from the condition of illuminating the reflector edges at the angle of 30°. The gain reduction at the scan sector edge is 1 dB (i.e., just 0.2 dB lower than that for the previous case). However, since the reflector dimension has been increased, the aperture efficiency got lower and became 45%.

So, the comparison with the focuser antenna shows that the parabolic cylindrical antenna provides somewhat better performance in a specified small scan sector. Though the dimension of the array with the sector flat-topped element pattern is larger and the array design is more complex than those of the feed array in the focuser antenna, it utilizes a smaller number of the controlled elements making the greatest contribution to the antenna cost. Moreover, the parabolic cylindrical antenna dimension in the plane of scan turns out to be significantly smaller than that of the focuser antenna (e.g., the cylinder dimension is about one-third of the focuser one for the scan sector of ±10°).

2.5 Quasioptical Analogs of the Chessboard Network

The tracing of targets in some radio systems designed for observation of space objects (see, for instance, [52]) is performed by mechanical turning of the antenna over a wide angular sector combined with electrical beam scanning in a very narrow (less than 1°) sector. The narrow sector flat-topped element patterns in such antennas may be shaped using the network approach described earlier. However, since the element spacing corresponding to very narrow scan sectors can be dozens of wavelengths, the total length of the transmitting lines connecting the array radiators to form the overlapped subarrays will be very long, and this can lead to considerable dissipation losses. In this connection, it is of interest to consider an alternative method based on using quasioptical networks for excitation of the required overlapped subarrays. This method, described first in [19], is based on the fact that semitransparent screens like dielectric plates or wire grids may in some cases be considered quasioptical analogs of directional couplers. This situation is illustrated in Figure 2.19. Using this fact, one can construct many quasioptical networks for forming the overlapped subarrays consisting of large-aperture reflector or lens radiators. One of the examples is a linear array of dual-reflector antenna elements considered in [53].

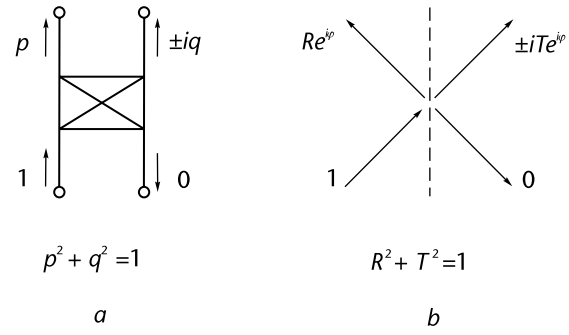

Figure 2.19 Network of a directional coupler (on the left) and its quasioptical analog in the form of a semi-transparent screen.

2.5.1 Features of the Array Geometry

The array cross-section in the plane of scanning is depicted in Figure 2.20. The array whose geometry is assumed to be independent of z is constructed as follows. Each array cell separated from the adjacent cells by vertical semitransparent screens, which we call *primary screens*, contains a main parabolic reflector, an elliptic subreflector, a feed, and a vertical transparent screen called *secondary* and arranged in the plane of the cell symmetry. The feature of this construction is that the main reflector is formed by right and left parabolas with foci situated in the left and right adjacent cells, respectively. The elliptic subreflector, working here as a quasioptical power divider, also consists of two parts. They have one common focus coinciding with the feed phase center. Two other subreflector foci (one of them is situated in point G) coincide with the foci of the right and left parabolas of the right and left adjacent cells, respectively. As the ray tracing in Figure 2.20 shows, the waves radiated by the feed are directed by the subreflector to the external parabolas of the adjacent cells. However, after partial reflection from the primary and secondary semitransparent screens working as quasioptical directional couplers, the waves reach all the parabolas of the three cells. As a result, a three-cell subarray is formed, which can be considered a quasioptical analog of the single-cascaded chessboard network shown in Figure 2.15.

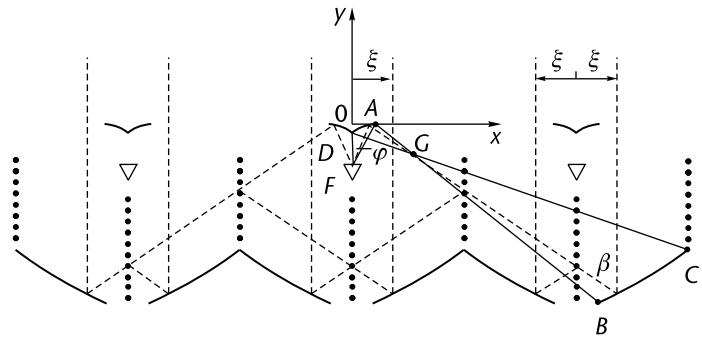

Figure 2.20 Quasioptical network of subarray of dual-reflector antennas.

The array geometric parameters are calculated as follows. Let the subreflector half-width a, cell half-width b, longitudinal dimension h, and x-coordinate x_G of focus G be specified. Then, using the equation

$$\rho = \frac{2f}{1+\cos\beta}$$

written for parabola BC in the polar coordinates with the origin in focus G (Figure 2.20), where f is the focal length of the parabola BC, as well as equation

$$y \quad y_G = \frac{1}{4f}(x \quad x_G)^2 \quad f$$

written for the same parabola in the Cartesian coordinates shown in Figure 2.20, we can obtain the following formulas for the focal length f of the parabola BC and for the y-coordinate of its edge C

$$f = \frac{1}{2}[y_G \quad y_B + \sqrt{(x_B \quad x_G)^2 + (y_G \quad y_B)^2}\,]$$
$$y_C = y_G + \frac{1}{4f}(x_C \quad x_G)^2 \quad f$$

where $x_B = a + 2b$, $y_G = (x_G \quad a)y_B/(2b)$, $y_B = \quad h$, and $x_C = 3b$. The position of the subreflector focus F is determined by the ellipse property, according to which

$$AG + AF = DG + DF \tag{2.26}$$

where

$$AG = \sqrt{(x_G \quad a)^2 + y_G^2}$$
$$AF = \sqrt{a^2 + y_F^2}$$
$$DG = \sqrt{x_G^2 + (y_D \quad y_F)^2}$$
$$DF = y_D \quad y_F$$
$$y_D = y_G + \frac{x_G}{x_C \quad x_G}(y_G \quad y_C)$$

Solving (2.26) with respect to y_F, we obtain

$$y_F = \frac{(y_D \quad AG + DG)^2 \quad a^2}{2(y_D \quad AG + DG)}$$

The relations written earlier for the array geometry allow calculation of the array characteristics, in particular the subarray radiation pattern.

2.5.2 Subarray Pattern

To determine the radiation pattern of the three-cell subarray shown in Figure 2.20, we apply the aperture method (see, for instance, [45]) involving integration of the field distribution over the subarray aperture in the plane $y = 0$. Making appropriate change of the variable for each part of the subarray aperture, we represent the subarray pattern as

$$F(\theta) = \frac{1}{N}\left|\sum_{n=1}^{3}\int_{a}^{b} A_n(\xi)\cos[k(\xi - \xi_n)\sin\theta]d\xi\right| \tag{2.27}$$

where, $A_1(\xi) = R_1(R_2 + T_2)A_0(\xi)$, $A_2(\xi) = T_1R_2A_0(\xi)$ and $A_3(\xi) = T_1T_2A_0(\xi)$ are complex amplitude distributions over the three regions of the aperture; $R_{1,2}(\beta)$ and $T_{1,2}(\beta)$ are reflection and transmission coefficients for a locally plane wave (a beam) impinging the screens at angle β; $A_0(\xi)$ is the amplitude distribution which would take place on the aperture region corresponding to the parabola BC in the absence of the screens; $\xi_1 = 0$, $\xi_2 = 2b$, $\xi_3 = 2b$, $k = 2\pi/\lambda$, θ is the observation angle measured from the y-axis, and

$$N = \sqrt{b\int_{a}^{b}|A_0(\xi)|^2\,d\xi}$$

is the normalizing coefficient involved in (2.27) for taking into account the aperture efficiency reduction caused by nonuniformity of the amplitude distributions over each aperture region, including the blockage of the latter by the subreflector.

The field distribution over the subarray aperture depends on the feed radiation pattern $F_0(\varphi)$. According to the laws of geometric optics applied to the case under consideration

$$A_0(\xi) = \sqrt{\frac{1+\cos\beta}{2f}\frac{d\varphi}{d\beta}}F_0(\varphi) \tag{2.28}$$

where relations between ξ, β, and φ are determined by formulas

$$\beta(\xi) = 2\text{arctg}\frac{2b+\xi - x_G}{2f}$$

$$\varphi(\beta) = \alpha - \arcsin\frac{2e - (1+e^2)\sin(\beta - \alpha)}{1+e^2 - 2e\sin(\beta - \alpha)}$$

where

$$\alpha = \text{arctg}\frac{y_G - y_F}{x_G}$$

and

$$e = \frac{\sqrt{x_G^2 + (y_G \quad y_F)^2}}{AG + AF}$$

is the eccentricity of the elliptic subreflector.

2.5.3 Results of Calculations

The results to be presented next as an example correspond to the following array parameters: $a = 3\lambda$, $b = 25\lambda$, $h = 40\lambda$, and $x_G = 8\lambda$. The feed radiation pattern has been taken in the form

$$F_0(\varphi) = \sin(k \quad \cos\varphi)\cos(ks\sin\varphi)$$

that corresponds to two equiphase filamentary electric currents arranged at height above a conductive screen and spaced $2s$ apart. The screen dimension is assumed to be not larger than $2a$ to avoid additional blockage. The primary and secondary screens are taken in the form of dielectric plates of thickness $t_{1,2}$ and relative permittivity $\varepsilon_{1,2}$. The reflection and transmission coefficients corresponding to the incidence of a plane wave of E-polarization have been calculated by formulas

$$R_j(\beta) = i\frac{(\quad^2_{1,j} - \quad^2_{0,j})\sin \quad_{1,j}}{Q_j}$$

$$T_j(\beta) = \frac{2 \quad_{0,j} \quad_{1,j}}{Q_j}$$

where

$$Q_j = [2 \quad_{0j} \quad_{1j} \cos \quad_{1j} - i(\quad^2_{0j} + \quad^2_{0j})\sin \quad_{1j}]e^{i \quad_{0j}}$$

$$\quad_{0j} = k t_j \sin\beta$$

$$\quad_{1j} = k t_j \sqrt{\quad_j - \cos^2\beta}$$

and $j = 1$ and 2 for the primary and secondary screens, respectively.

The parameters of the screens $t_1 = 0.07\lambda$, $\varepsilon_1 = 14.5$ and $t_2 = 0.13\lambda$, $\varepsilon_2 = 4.2$ have been chosen to provide the transmission coefficients $|T_1|$ and $|T_2|$ at mean angle of illumination of the screens close to the optimum values 0.438 and 0.74 given in Table 2.1. The values for the feed parameters $\quad = 0.48\lambda$ and $s = 0.3\lambda$ provide a minimum sidelobe level.

The amplitude distributions of the field over the subarray aperture are shown in Figure 2.21 by solid curves normalized to the maximum of the amplitude distribution calculated for the case of perfectly conducting screens providing illumination of the parabolas in the central cell only. The indicated distribution corresponding to (2.28) is shown in Figure 2.21 by a curve with small dashes. To compare the

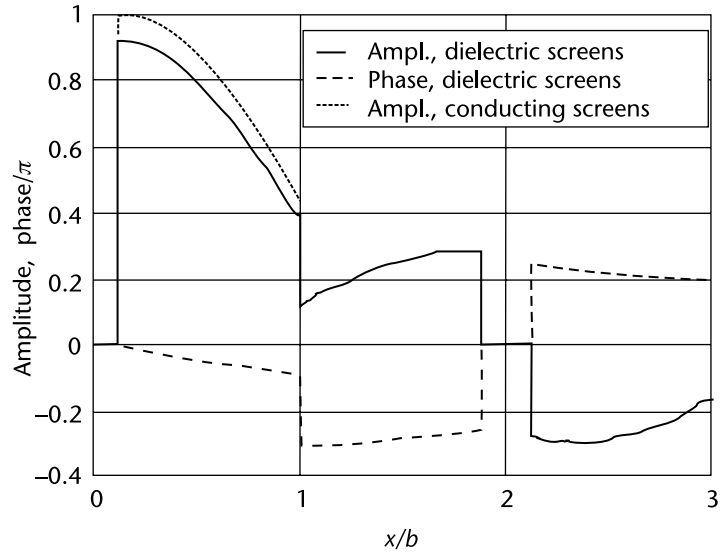

Figure 2.21 Amplitude and phase distributions of the field in the subarray aperture.

amplitude distribution to the curve $\sin x/x$, we have multiplied the magnitude of the distribution over the edge region by –1 and added π to the phase distribution. The phase distributions shown in Figure 2.21 by the curves with larger dashes have been plotted with respect to the phase value at $x = a$ and divided by π.

The subarray pattern (2.27) is shown in Figure 2.22 by a solid line. It is compared to the pattern corresponding to the thin perfectly conducting screens (the line with larger dashes) and to the pattern corresponding to the uniform amplitude distributions over the aperture of each parabola [i.e., similar to that shown in Figure 2.9(b), the curve with smaller dashes].

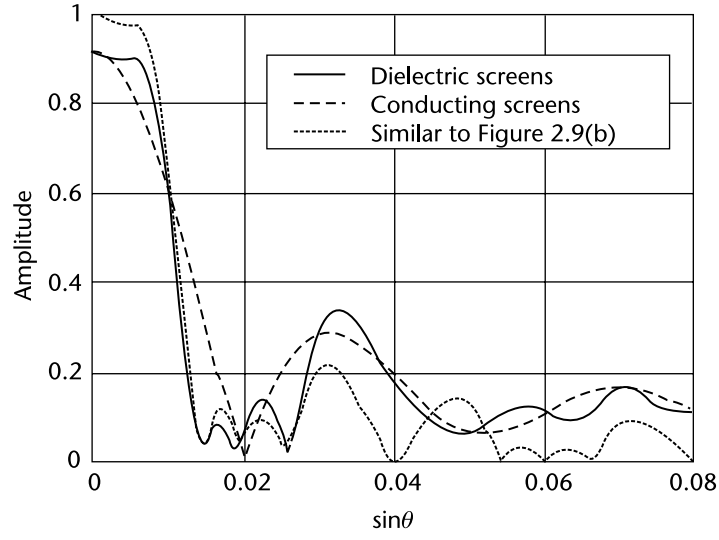

Figure 2.22 Radiation patterns of the subarray of dual-reflector antenna elements.

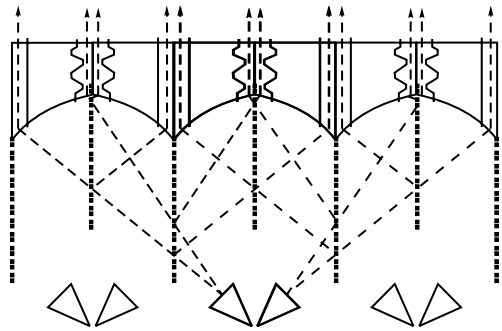

Figure 2.23 Quasioptical network of a subarray with bootlace lens antenna elements.

The results presented in this section show that the quasioptical network provides the sector beam shape similar to that corresponding to the single-cascaded chessboard network with ordinary directional couplers. The slightly increased level of the sidelobe radiation and corresponding reduction of the aperture efficiency are caused here by the subreflector blockage effect. The latter is proportional here to a/b. The blockage effect in dually periodic structures would be proportional to $(a/b)^2$ and therefore significantly weaker. This effect will be absent at all in the quasioptical networks employing lens antenna elements. One such network with bootlace lenses is shown in Figure 2.23; some other networks are described in [19, 54–57].

References

[1] Vendik, O. G., *Antennas with Non-Mechanical Movement of Beam*, Moscow: Sovetskoye Radio, 1965 (in Russian).

[2] Shelton, J. P., "Multiple Feed Systems for Objectives," *IEEE Trans. on Antennas and Propagation*," Vol. AP-13, No. 6, November 1965, pp. 992–994.

[3] Borgiotti, G. V., "An Antenna for Limited Scan in One Plane: Design Criteria and Numerical Simulation," *IEEE Trans. on Antennas and Propagation*, Vol. AP-25, No. 1, 1977, pp. 232–243.

[4] Mailloux, R. J., *Phased Array Antenna Handbook*, Norwood, MA: Artech House, 1994.

[5] Mailloux, R. J., and P. R. Caron, "A Class of Phase Interpolation Circuits for Scanning Phase Arrays," *IEEE Trans. on Antennas and Propagation*, Vol. AP-18, No. 1, 1970, pp. 114–116.

[6] Nemit, J. T., "Network Approach for Reducing the Number of Phase Shifters in a Limited Scan Phase Array," U.S. Patent No. 3803625, Int. Cl. H 01 Q 3/26, 1974.

[7] Seryakov, Y. N., and S. P. Skobelev, "Network Approach to Reducing the Number of Phase Shifters in Linear Phased Array Antennas," *Voprosy Radioelektroniki—Obschetekhnicheskaya Seriya*, No. 1, 1978, pp. 91–99 (in Russian).

[8] Skobelev, S. P., "Network Method of Reducing the Number of Phase Shifters in Phased Array Antennas," *Trudy MFTI—Radiotekhnika i Elektronika*, 1977, pp. 15–20 (in Russian).

[9] Pustovalov, V. I., Y. N. Seryakov, and S. P. Skobelev, "Phased Array Antenna," SU Author's Certificate No. 553891, Int. Cl. H 01 Q 21/00, 1976 (in Russian).

[10] Polukhin, G. A., "Phased Array Antenna," SU Author's Certificate No. 995172, Int. Cl. H 01 Q 21/00, 1983 (in Russian).

[11] Polukhin, G. A., and A. G. Shubov, "Phased Array Antennas with Minimum Number of Modules," *Radiotekhnika*, No. 1, 1982, pp. 31–38 (in Russian).

[12] Mailloux, R. J., and P. R. Franchi, "Phased Array Antenna with Array Elements Coupled to Form a Multiplicity of Overlapped Subarrays," U.S. Patent No. 3938160, Int. Cl. H 01 Q 3/26, 1976.

[13] Mailloux, R. J., "An Overlapped Subarray for Limited Scan Applications," *IEEE Trans. on. Antennas and Propagation*, Vol. AP-22, No. 3, 1974, pp. 487–489.

[14] Skobelev, S. P., "Radiation from an Array of Dual-Mode Waveguides Forming Overlapped Subarrays," *Radiotekhnika*, No. 7, 1987, pp. 62–65 (in Russian).

[15] Mailloux, R. J., et al., "Grating Lobe Control in Limited Scan Arrays," *IEEE Trans. on Antennas and Propagation*, Vol. AP-27, No. 1, 1979, pp. 79–85.

[16] Mailloux, R. J., "Synthesis of Spatial Filters with Chebyshev Characteristics," *IEEE Trans. on Antennas and Propagation*, Vol. AP-24, No. 2, 1976, pp. 174–181.

[17] Franchi, P. R., and R. J. Mailloux, "Theoretical and Experimental Study of Metal Grid Angular Filters for Sidelobe Suppression," *IEEE Trans. on Antennas and Propagation*, Vol. AP-31, No. 3, 1983, pp. 445–450.

[18] Frazita, R. F., A. R. Lopez, and R. J. Giannini, "Limited Scan Antenna System with Sharp Cutoff of Element Pattern," U.S. Patent No. 4041501, Int. Cl. H 01 Q 3/26, 1977.

[19] Skobelev, S. P., "Design Synthesis of Antenna Arrays with Flat-Topped Element Patterns," *Proc. 10th School-Seminar on Wave Diffraction and Propagation*, Moscow, Feb. 7–15, 1993, pp. 369–395.

[20] Wheeler, H. A., "Antenna System Having Modular Coupling Network," U.S. Patent No. 4143379, Int. Cl. H 01 Q 3/26, 1979.

[21] Lopez, A. R., "Array Antenna System," U.S. Patent No. 4321605, Int. Cl. H 01 Q 21/00, 1982.

[22] Wheeler, H. A., "Array Antenna with Limited Scan Sector," SU Author's Certificate No. 1052154, Int. Cl. H 01 Q 3/26, 1983 (in Russian).

[23] Lopez, A. R., "Array Antenna," SU Author's Certificate No. 1077586, Int. Cl. H 01 Q 3/26, 1981 (in Russian).

[24] DuFort, E. C., "Limited Scan Phased Array System," U.S. Patent No. 4228436, Int. Cl. H 01 Q 3/26, 1980.

[25] DuFort, E. C., "Constrained Feeds for Limited Scan Arrays," *IEEE Trans. on Antennas and Propagation*, Vol. AP-26, No. 3, 1978, pp. 407–413.

[26] Kachwalla, Z. A., "Limited-Scan Linear Array Using Overlapping Subarrays," *Journal of Electrical and Electronics Engineering, Australia—IE Aust. and IREE Aust.*, Vol. 3, No. 2, 1983, pp. 126–131.

[27] Herd, J. S., S. M. Duffy, and H. Steyskal, "Design Considerations and Results for an Overlapped Subarray Radar Antenna," *2005 IEEE Aerospace Conf. Dig.*, Big Sky, MT, March 5–12, 2005, pp. 1087–1092.

[28] Duffy, S. M., D. D. Santiago, and J. S. Herd, "Design of Overlapped Subarrays Using an RFIC Beamformer," *2007 IEEE AP-S Int. Symp. Digest*, Aloha, HI, June 9–15, 2007, pp. 1949–1952.

[29] Skobelev, S. P., "Analysis and Synthesis of an Antenna Array with Sectoral Partial Radiation Patterns," *Telecommunications and Radio Engineering*, Vol. 45, No. 11, 1990, pp. 116–119.

[30] Himmelblau, D. M., *Applied Nonlinear Programming*, New York: McGraw-Hill, 1972.

[31] Petrolati, D., et al., "Radiation Pattern Optimization of Skobelev Networks," *Proc. 4th European. Conf. on Antennas and Propagation*, Barcelona, Spain, April 12–16, 2010.

[32] Petrolati, D., et al., "Skobelev Network Optimisation by Sequential Quadratic Programming," *Electronics Letters*, Vol. 46, No. 8, April 15, 2010, pp. 553–554.

[33] Mailloux, R. J., "Antenna Architectures for Large Radar Arrays," *Proc. Millennium Conf. on Antennas and Propagation*, Vol. I, Davos, Switzerland, April 9–14, 2000, p. 174.

[34] Skobelev, S. P., "Phased Array Antenna," SU Author's Certificate No. 1566436, Int. Cl. H 01 Q 21/00, 1990 (in Russian).

[35] Skobelev, S. P., "Analysis, Synthesis, and Results of Measurements for an Array Antenna with Sector Partial Radiation Patterns," *Proc. 26th Scientific Conf. on Antenna Theory and Technology*, Moscow, November 27–29, 1990, Pt. II, pp. 27–28 (in Russian).

[36] Skobelev, S. P., "Arrays of Coupled Rectangular Waveguides with Sector Partial Radiation Patterns in H-Plane," *Radiotekhnika*, No. 7, 1996, pp. 15–17 (in Russian).

[37] Clarricoats, P. J. B., and K. R. Slinn, "Numerical Solution of Waveguide-Discontinuity Problems," *IEE Proc.*, Vol. 114, 1967, pp. 878–886.

[38] Solbach, K., "Below-Resonant-Length Slot Radiators for Traveling-Wave-Array Antennas," *IEEE Antennas and Propagation Magazine*, Vol. 38, No. 1, 1996, pp. 7–14.

[39] Sakakibara, K., et al., "Slotted Waveguide Array Antenna for Automotive Radar Systems," *Proc. Millennium Conf. on Antennas and Propagation*, Vol. I, Davos, Switzerland, April 9–14, 2000, p. 598.

[40] Denisenko, V. V., et al., "Millimeter-Wave Printed Circuit Antenna System for Automotive Applications," *IEEE MTT-S 2001 Intl. Symp. Digest*, Vol. III, Phoenix, AZ, 2001, pp. 2247–2250.

[41] Vilenko, I. L., A. S. Reutov, and A. V. Shishlov, "On Synthesis of Reflector Antennas for Focusing or Scanning in One Plane," *Proc. 28th Moscow Int. Conf. on Antenna Theory and Technology*, Moscow, Russia, September 22–24, 1998, pp. 376–379.

[42] Reutov, A. S., and A. V. Shishlov, "Focuser-Based Hybrid Antennas for One-Dimensional Beam Steering," *Proc. 2000 IEEE Intl. Conf. on Phased Array Systems and Technology*, Dana Point, CA, May 21–25, 2000, pp. 411–414.

[43] Reutov, A. S., and A. V. Shishlov, "Hybrid Focuser-Based Reflector Antennas for Scanning in One Plane," *Proc. LV Scientific Session Devoted to the Day of Radio*, Moscow, Russia, 2000, pp. 72–73 (in Russian).

[44] Reutov, A. S., and A. V. Shishlov, "Hybrid Antennas with Shaped Reflectors for Limited Beam Steering," *Proc. 4th Int. Conf. on Antenna Theory and Techniques*, Vol. 1, Sevastopol, Ukraine, September 9–12, 2003, pp. 264–267.

[45] Markov, G. T., and D. M. Sazonov, *Antennas*, Moscow: Energiya, 1975 (in Russian).

[46] Bakhrakh, L. D., and G. K. Galimov, *Scanning Reflector Antennas*, Moscow: Nauka, 1981 (in Russian).

[47] Kildal, P.-S., "Radiation Characteristics of the EISCAT VHF Parabolic Cylindrical Reflector Antenna," *IEEE Trans. on Antennas and Propagation*, Vol. AP-32, No. 6, 1984, pp. 541–552.

[48] Ajzenberg, G. Z., V. G. Yampol'sky, and O. N. Tereshin, *Antennas of Ultra Short Waves*, Pt. 1, Moscow: Svyaz', 1977 (in Russian).

[49] Ludwig, A. C., "Computation of Radiation Patterns Involving Numerical Double Integration," *IEEE Trans. on Antennas and Propagation*, Vol. 16, No. 6, 1968, pp. 767–769.

[50] Skobelev, S. P., "Parabolic Cylindrical Antenna with a Linear Array Shaping the Sector Partial Radiation Patterns," *Radiotekhnika*, No. 6, 2004, pp. 42–48 (in Russian).

[51] Kildal, P. -S., "Aperture Efficiency and Line Feed Phase Center of Parabolic Cylindrical Reflector Antenna," *IEEE Trans. on Antennas and Propagation*, Vol. AP-32, No. 6, 1984, pp. 553–561.

[52] Tolkachev, A. A., V. V. Denisenko, A. V. Shishlov, and A. G. Shubov, "High Gain Antenna Systems for Millimeter Wave Radars with Combined Electronical and Mechanical Beam Steering," *Proc. 1996 IEEE Intl. Symp. on Phased Array Systems and Technology*, Boston, MA, October 15–18, 1996, pp. 266–271.

[53] Skobelev, S. P., "Shaping of the Sector Partial Radiation Patterns in a Linear Array of Dual-Reflector Antennas," *Technical Physics Letters*, Vol. 22, No. 8, 1996, pp. 37–43 (in Russian).

[54] Skobelev, S. P., "An Optical Network of Shaping Flat-Topped Sector Element Pattern in Arrays of Dual-Reflector Antennas," *Journees Internationales De Nice Sur Les Antennes*, Nice, France, November 12–14, 1996, pp. 462–465.

[55] Skobelev, S. P., "Methods and Results of Design Synthesis of Antenna Arrays with Flat-Topped Sector Partial Patterns," *Proc. IEEE Intl. Symp. on Phased Array Systems and Technology*, Boston, MA, October 15–18, 1996, pp. 438–443.

[56] Skobelev, S. P., et al., "Some Methods and Results in Development of Low-Cost Antenna Array Technology," *Antenn 97—Nordiskt antennsymposium i Goteborg*, Gothenburg, Sweden, May 27–29, 1997, pp. 25–34.

[57] Skobelev, S. P., "Methods of Constructing Optimum Phased-Array Antennas for Limited Field of View," *IEEE Antennas and Propagation Magazine*, Vol. 40, No. 2, 1998, pp. 39–50.

CHAPTER 3

Arrays of Coupled Dual-Mode Waveguides

As shown in the previous chapter, the overlapped amplitude distributions corresponding to shaping sector element patterns can be formed either by using a few (at least two) radiators in each array cell or by excitation of at least two first modes in the aperture of one radiator occupying the whole array cell. The latter case has been realized in [1, 2] as well considered in [3]. The first even and odd modes in the array [1–3] are excited through a beam-forming network consisting of power dividers and directional couplers, as shown in Figure 2.4 of the previous chapter. This technical solution is rather effective for application to the waveguide-horn arrays. However, in the particular cases when the dual-mode waveguide sections have common walls, the array design can be considerably simplified if the excitation of the necessary modes is accomplished through ordinary slots in the common walls instead of the beam-forming network.

Some applications of the slot-coupling elements between transmitting lines in phased arrays for providing wide-angle impedance matching are described in [4, 5]. The slots in the waveguide walls are used also for matching the experimental array shown in Figure 2.12. The capabilities of such an approach for shaping the sector element patterns have first been studied in [6] using rigorous problem formulation for an idealized array geometry in assumption that the waveguide walls are infinitely thin and the single-mode feeding waveguide sections usually used in practice are absent. The improved models, more close to practice, have been considered in [7, 8] for an array of parallel-plate waveguides scanning in the E-plane and in [9] for a similar array scanning in the H-plane.

3.1 A Simplified Model

Consider a two-dimensional problem of H-polarized wave radiation from an infinite array of semi-infinite parallel-plate waveguides of width a with identical slots cut through in the walls. The array geometry in the case of two-slot elements of coupling is shown in Figure 3.1. The waveguide walls are assumed to be infinitely thin and perfectly conducting. Let the waveguides be excited in the TEM modes with magnetic field

$$H_y^i(x,z) = e^{ikz+im} \tag{3.1}$$

for $ma < x < (m + 1)a$, $m = 0, \pm 1\ldots$, satisfying the Floquet condition [10] with parameter (phase increment) (the time dependence is assumed to be taken in the form $e^{i\omega t}$). It is required to determine the field radiated to free space and the field reflected back to the waveguides.

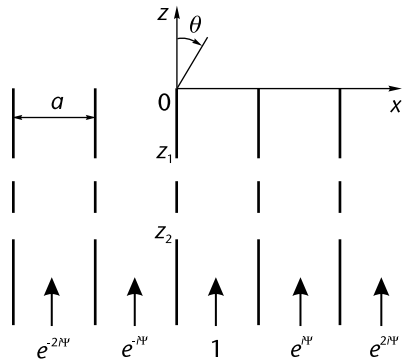

Figure 3.1 Geometry of parallel-plate waveguide array with slot elements of coupling.

To solve the problem, we introduce magnetic currents lying on metallized planar surfaces in the slot region and equivalent to the tangential components of the electric field in the slots. Let $J_y^m(z)$ be magnetic current density in the slot region at $x = +0$. Then, to provide the tangential electric field continuity in the slots, the magnetic current density in the slots at $x =$ 0 must be $J_y^m(z)$. Furthermore, since the total field at excitation (3.1) must satisfy the same Floquet condition, the current density at $x = a$ 0 must be equal to $J_y^m(z)\exp(i$). The magnetic field of such a system of currents in the central waveguide ($0 < x < a$, Figure 3.1) may be determined by formula

$$H_{y1}(x,z) = \int_L f(z') \sum_{n=0} \frac{1 - (-1)^n e^{i\psi}}{(1+\delta_{n0})\gamma_n a} \cos\frac{n\pi x}{a} e^{i\gamma_n|z - z'|} dz' \tag{3.2}$$

where $f(z) = J_y^m(z)/\eta_0$, $\eta_0 = (\mu_0/\varepsilon_0)^{1/2}$ is the wave resistance for free space, L $[z_1,z_2]$ is the slot region,

$$\gamma_n = \sqrt{k^2 - \left(\frac{n\pi}{a} - \psi\right)^2} = i\sqrt{\left(\frac{n\pi}{a} - \psi\right)^2 - k^2} \tag{3.3}$$

are propagation constants of the waveguide modes, and δ_{mn} is the Kronecker symbol. The field corresponding to the magnetic currents in other waveguides will differ from the field (3.2) only by factor $\exp(im$), where m is the waveguide number (index). If the observation point is situated outside the region z_2 z z_1, the expression (3.2) may be rewritten in the form

$$H_{y1}(x,z) = \sum_{n=0} A_n^{\pm} \cos\frac{n\pi x}{a} e^{\pm i\gamma_n z} \tag{3.4}$$

where

$$A_n^{\pm} = \int_L k \frac{1 - (-1)^n e^{i\psi}}{(1+\delta_{n0})\gamma_n a} f(z') e^{\mp i\gamma_n z'} dz' \tag{3.5}$$

The upper and lower signs in (3.4) and (3.5) correspond to $z > z_1$ and $z < z_2$, respectively. As we see, the waveguide waves (3.4) with amplitudes A_n^+ (3.5) come to the waveguide aperture together with the incident TEM waves (3.1). The problem of such an excitation of the thin-walled parallel-plate waveguide array allows us to obtain a rigorous analytical solution. Applying the method of factorization [10, 11] and the principle of superposition, we obtain the following expressions for the scattered (radiated and reflected) field:

$$H_y^s(x,z) = \sum_{q=} B_q e^{i\alpha_q x + i\Gamma_q z}, \quad z > 0 \tag{3.6}$$

$$H_y^s(x,z) = H_{y1}(x,z) + \sum_{n=0} A_n \cos\frac{n\pi x}{a} e^{\ i\gamma_n z}, \quad z < 0 \tag{3.7}$$

where

$$B_q = \frac{\alpha_q G_+(\Gamma_q)}{i(k+\Gamma_q)\Gamma_q a} \sum_{m=0} \frac{(\delta_{m0} + A_m^+)(k+\gamma_m)}{2G_+(\gamma_m)} \frac{1 \quad (\ \ 1)^m e^{\ i}}{\gamma_m \quad \Gamma_q} \tag{3.8}$$

$$\alpha_q = \frac{+2\pi q}{a}$$

$$\Gamma_q = (k^2 - \alpha_q^2)^{1/2} = i(\alpha_q^2 \quad k^2)^{1/2} \tag{3.9}$$

$$A_n = \quad \frac{1 \quad (\ \ 1)^n e^i}{1+\delta_{n0}} \frac{k+\gamma_n}{\gamma_n G_+(\gamma_n)} \tag{3.10}$$

$$\sum_{m=0} \frac{(\delta_{m0} + A_m^+)(k+\gamma_m)}{2G_+(\gamma_m)} \frac{1 \quad (\ \ 1)^m e^{\ i}}{\gamma_m + \gamma_n}$$

$$G_+(\alpha) = \quad \frac{\cos(ka) \quad \cos}{\sin(ka)/(ka)} \div^{1/2} \exp \quad \frac{i\alpha a}{\pi} \ln 2 \div$$

$$(1+\alpha/\Gamma_0) \prod_{p=1} \frac{(1+\alpha/\Gamma_p)(1+\alpha/\Gamma\ _p)}{1+\alpha/\gamma_p}$$

Amplitudes (3.8) of the Floquet modes in the free space and amplitudes $A_n + A_n$ of reflected waveguide modes in the waveguides are determined by still unknown function $f(z)$ proportional to the equivalent magnetic current density in the slots. To find this function, we use the continuity condition for the total magnetic field in the slots. As a result, we obtain the following integral equation:

$$\int_L G(z,z')f(z')dz' = g(z), \quad z \quad L \tag{3.11}$$

where the kernel and right-hand part are determined by formulas

$$G(z,z') = \frac{2k}{a} \sum_{n=0} \frac{1 \quad (\quad 1)^n \cos \quad}{1+\delta_{n0}} \frac{e^{i\gamma_n|z' \quad z|}}{\gamma_n}$$

$$\frac{(k+\gamma_n)e^{\quad i\gamma_n z'}}{\gamma_n G_+(\gamma_n)} \sum_{m=0} \frac{1 \quad (\quad 1)^m \cos \quad}{1+\delta_{m0}} \frac{(k+\gamma_m)e^{\quad i\gamma_m z}}{\gamma_m(\gamma_m+\gamma_n)G_+(\gamma_m)} \tag{3.12}$$

$$g(z) = (1 \quad e^{\quad i \quad}) \; e^{ikz} \quad \frac{2k}{G_+(k)} \sum_{m=0} \frac{1 \quad (\quad 1)^m \cos \quad}{1+\delta_{m0}} \frac{e^{\quad i\gamma_m z}}{\gamma_m G_+(\gamma_m)} \tag{3.13}$$

Function $f(z)$ determined as a result of solving (3.11) by the method of moments is then used for calculation of amplitudes (3.5), (3.8), and (3.10). The accuracy of the calculations has been controlled by means of verifying the power balance relation

$$\sum_n \frac{|A_n + A_n|^2 \gamma_n}{(2 \quad \delta_{n0})k} + \sum_q \frac{|B_q|^2 \Gamma_q}{k} = 1 \tag{3.14}$$

where summation is taken only over propagating waveguide and Floquet modes. The error of fulfillment of (3.14) in all the calculations has not exceeded 0.01%.

As noted earlier (see Chapter 1), the array element pattern is determined by the amplitude of the Floquet mode of zero order (3.8) multiplied by $\cos\theta$ (Figure 3.1). As a result, we obtain the element pattern in the form

$$F(\quad) = \frac{\alpha_0 G_+(\Gamma_0)}{i(k+\Gamma_0)} \sum_{m=0} \frac{(\delta_{m0}+A_m^+)(k+\gamma_m)}{2kaG_+(\gamma_m)} \frac{1 \quad (\quad 1)^m e^{\quad i}}{\gamma_m \quad \Gamma_0} \tag{3.15}$$

where should be replaced by $ka\sin\theta$.

Two examples of the calculated element pattern for array with period $a = 0.8\lambda$ and $a = 1.3\lambda$ are shown in Figures 3.2 and 3.3, respectively. In the first case, there is only one slot in each wall, while the second one corresponds to two slots of identical width . The position of the slots (segment $[z_1, z_2]$) and their width have been selected to provide the slowest decrease of the element pattern level in the sector $\sin\theta \quad 0.7\lambda/2a$ corresponding to the element use factor of about 1.4.

As we see in Figures 3.2 and 3.3, where the array element pattern in the absence of the slots is also presented for comparison, the introduction of the slots allows enhancing the pattern level at the sector edge by about 1 dB. However, the level of the obtained patterns is still considerably lower than the normalized maximum (ideal) level equal to $\sqrt{\cos\theta}$. The reason is insufficiently strong excitation of the array aperture by the odd TM_1 modes because only a portion of their power comes

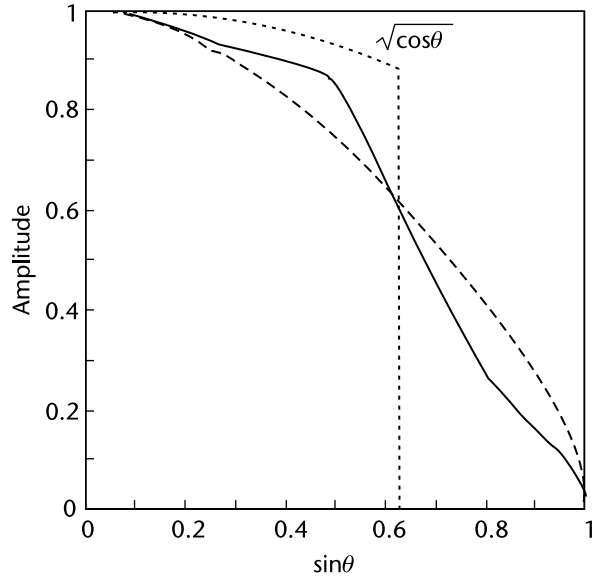

Figure 3.2 Element pattern corresponding to single slots in array with $a = 0.8\lambda$, $z_1 = 0.54\lambda$, $z_2 = 0.96\lambda$, and $= 0.42\lambda$.

to the aperture, while the other portion just goes from the slots down and therefore does not contribute to the radiation. The situation may be improved by means of using single-mode waveguides for exciting the coupled dual-mode sections. The propagating TM_1 modes going down from the slots in this case will come back to the aperture after reflection from the junction of the sections to participate in shaping the element pattern. Such an improved array model is considered next.

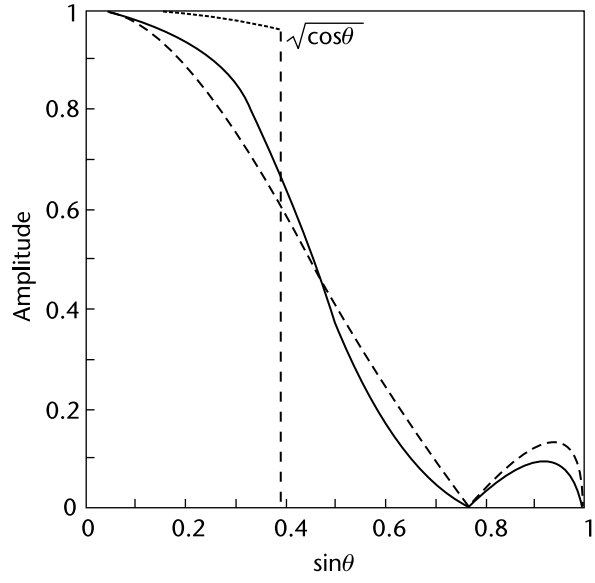

Figure 3.3 Element pattern corresponding to double slots in array with $a = 1.3\lambda$, $z_1 = 0.82\lambda$, $z_2 = 2.3\lambda$, and $= 0.12\lambda$.

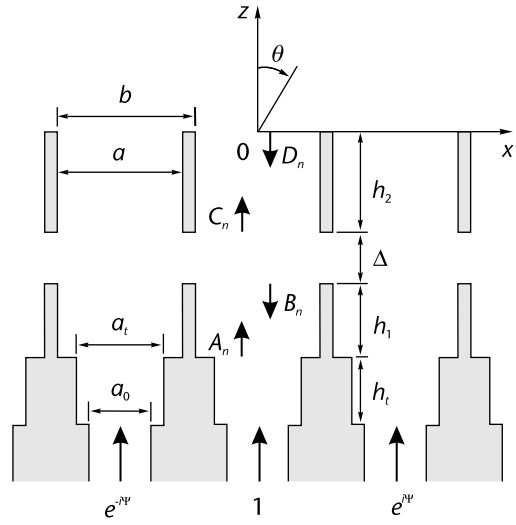

Figure 3.4 Geometry of coupled parallel-plate waveguide array for scanning in E-plane.

3.2 An Improved Model for Scanning in E-Plane

3.2.1 Array Geometry and Excitation

The longitudinal cut of the improved array in the plane of scanning is shown in Figure 3.4. The array is a periodic structure of stepped parallel-plate waveguides. The upper sections have width a and wall thickness b a, where b is the array period (element spacing). These sections are symmetrically attached to lower semi-infinite waveguide sections of width a_0 via intermediate sections of length h_t and width a_t. The upper sections are coupled to each other through the slots of width arranged at distances h_1 from the intermediate sections and h_2 from the aperture.

We assume that the lower sections are excited by TEM waves having unit amplitudes and phases progressing with increment from one waveguide to another. The incident TEM waves are scattered at the step discontinuities with excitation of TM waves with nonzero electric field components E_x and E_z, and magnetic field component H_y so that the array scans its beam in the E-plane.

Further, we will assume that the lower waveguide sections are single-mode, while the upper ones are dual-mode (i.e., $a_0 < \lambda/2$ and $\lambda/2 < a < \lambda$, where λ is the operating wavelength). The array radiation performance depends on the amplitude and phase relations between the dominant TEM mode and TM modes of higher order coming to the aperture. The indicated relations are determined by the geometry of the structure, and the problem therefore is determination of the values for the geometric parameters at which the array gain has minimum decrease when scanning the beam in the sector corresponding to the array period.

3.2.2 Mathematical Model

The most preferable method that can be used for analysis of the array under consideration is the method of generalized scattering matrices [10]. Let S be the scattering matrix of the stepped transition between the lower single-mode section and upper

dual-mode section, $\boldsymbol{R}^{(1)}$ and $\boldsymbol{T}^{(1)}$ be the matrices of the reflection and transmission coefficients, respectively, for the system of slots in the walls of the dual-mode sections, and $\boldsymbol{R}^{(2)}$ and $\boldsymbol{T}^{(2)}$ be similar matrices for the array aperture at excitation of it from the waveguides. We will assume that the matrices $\boldsymbol{R}^{(1)}$, $\boldsymbol{T}^{(1)}$, and $\boldsymbol{R}^{(2)}$ have dimension $N \quad N$, where N is the number of the first modes taken into account in the dual-mode sections, the matrix $\boldsymbol{T}^{(2)}$ has dimension $Q \quad N$, where Q is the number of the Floquet modes taken into account in the field radiated by the array, and the matrix $\boldsymbol{S}$ has dimension $(N + 1) \quad (N + 1)$, with its first $N \quad N$ elements being the coefficients of reflection from the intermediate section (transition) from the side of the dual-mode section. All the elements of the indicated matrices with the exception of those of the matrix $\boldsymbol{S}$ depend on the controlling phase . Using the matrices involved in the consideration, we can write the following system of linear algebraic equations

$$\begin{aligned} A_m \quad & \sum_{n=1}^{N} e_n^{(1)} S_{mn} B_n = S_{m,N+1} \\ & \sum_{n=1}^{N} e_n^{(1)} R_{mn}^{(1)} A_n + B_m \quad \sum_{n=1}^{N} e_n^{(2)} T_{mn}^{(1)} D_n = 0 \\ & \sum_{n=1}^{N} e_n^{(1)} T_{mn}^{(1)} A_n + C_m \quad \sum_{n=1}^{N} e_n^{(2)} R_{mn}^{(1)} D_n = 0 \\ & \sum_{n=1}^{N} e_n^{(2)} R_{mn}^{(2)} C_n + D_m = 0 \end{aligned} \tag{3.16}$$

for the complex amplitudes of the waves going from the transition to the slots (A_n), from the slots to the transition (B_n), from the slots to the aperture (C_n), and from the aperture to the slots (D_n) (Figure 3.4), where $m = 1, 2, \ldots, N$ (unlike the previous section, the numbers of the waveguide modes begin with 1 rather than 0, and that is done for convenience of the subsequent operation), $e_n^{(j)} = \exp(i\gamma_n h_j)$, $j = 1$ or 2, h_1 and h_2 are the lengths of the lower and upper parts of the dual-mode sections (Figure 3.4), and

$$\gamma_n = \sqrt{k^2 \quad \frac{(n \quad 1)\pi}{a}^2} = i\sqrt{\frac{(n \quad 1)\pi}{a}^2 \quad k^2} \tag{3.17}$$

are propagation constants of the waves in the dual-mode section.

The solution of the system (3.16) then allows us to calculate the array reflection coefficient

$$R(\quad) = S_{N+1,N+1} + \sum_{n=1}^{N} e_n^{(1)} S_{N+1,n} B_n(\quad) \tag{3.18}$$

amplitudes of the Floquet modes above the aperture

$$T_q(\quad) = \sum_{n=1}^{N} e_n^{(2)} T_{qn}^{(2)}(\quad) C_n(\quad) \tag{3.19}$$

and array element pattern

$$F(\theta) = \sqrt{\frac{b}{a_0}} \, | \, T_0(kb\sin\theta) \, | \cos\theta \tag{3.20}$$

normalized to the maximum value of the ideal element pattern (1.117). Note, also, that $|F(0)|^2$ corresponds to the coefficient of power transmission to the main lobe.

The simple algorithm presented here allows us to perform calculations of the array characteristics at specified values of its geometrical parameters. The necessary elements of the scattering matrices for the transition section, slots, and array aperture are calculated with using the well-known method of projective mode matching at the junctions of the sections [12, 13]. The technique and some details of the realization of the indicated method for the structure under consideration are described in [14]. An example demonstrating the calculation of the scattering matrix elements for the slots and array aperture is presented in Appendix 3A.

3.2.3 Highest Characteristics at Dual-Mode Excitation

Although the field radiated by the array is formed by an infinite number of the waveguide modes coming to the array aperture, the first two propagating modes TM_1 (which is the TEM mode) and TM_2 reaching the dual-mode waveguide aperture without attenuation give the highest contribution. In this connection, it is of interest to consider an auxiliary problem that determines the amplitude and phase relations with which the indicated two waves must come to the aperture to provide a maximum of the element pattern level for specified observation angle.

So, let the waves TM_1 and TM_2 be coming to the waveguide aperture with real amplitudes C_1 and C_2, as well as with phases $\quad_1$ and $\quad_2$, respectively. The phases are assumed to be measured with respect to the aperture plane, while the amplitudes satisfy the normalization condition on their total power

$$\gamma_1 a C_1^2 + \frac{\gamma_2 a}{2} C_2^2 = 1 \tag{3.21}$$

where the propagation constants $\quad_n$ are determined by formula (3.17).

Let also $F_1(\theta)$ and $F_2(\theta)$ be the element (waveguide) amplitude patterns corresponding to separate excitation of the waveguide in the TM_1 and TM_2 modes of unit power, and let $\quad_1(\theta)$ and $\quad_2(\theta)$ be the appropriate phase patterns. Then the complex pattern of the waveguide at its simultaneous excitation by the two modes may be written in the form

$$F = \alpha C_1 F_1 e^{i(\quad_1 + \quad_1)} + \beta C_2 F_2 e^{i(\quad_2 + \quad_2)}$$

where $\alpha = (\gamma_1 a)^{1/2}$ and $\beta = (\gamma_2 a/2)^{1/2}$. Accounting for this expression, we may write the waveguide power pattern as

$$P = FF = (\alpha C_1 F_1)^2 + (\beta C_2 F_2)^2 + 2\alpha\beta C_1 F_1 C_2 F_2 \cos(+) \tag{3.22}$$

with = $_2$ $_1$ and = $_2$ $_1$.

It is clear that the maximum of function (3.22) will be achieved first of all when the complex patterns are added in-phase; that is, at

$$= + 2\pi n, \quad n = 0, \pm 1, \ldots \tag{3.23}$$

To optimize the amplitude relations, let us express C_1 via C_2 from (3.21), substitute the resulting expression in (3.22), and equate $\partial P/\partial C_2$ to zero. Then, taking (3.23) into account, we obtain the equation

$$F_2 \quad \frac{\beta C_2 F_1}{\sqrt{1 \quad \beta^2 C_2^2}} = 0$$

from which

$$C_2 = \frac{F_2}{\beta\sqrt{F_1^2 + F_2^2}} \tag{3.24}$$

Using (3.24) together with (3.21), we find

$$C_1 = \frac{F_1}{\alpha\sqrt{F_1^2 + F_2^2}} \tag{3.25}$$

Using the last two expressions, we can determine the optimum ratio of the amplitudes C_1 and C_2

$$\frac{C_2(\theta)}{C_1(\theta)} = \sqrt{\frac{2\gamma_1}{\gamma_2}}\frac{F_2(\theta)}{F_1(\theta)} \tag{3.26}$$

providing maximum of the waveguide power pattern (3.22) at the dual-mode excitation equal to $F_1^2 + F_2^2$.

Thus, the array gain in a specified direction at dual-mode excitation of the waveguides achieves its maximum level when the complex waveguide patterns corresponding to each mode add in phase and the amplitudes of the dual-mode excitation obey the relation (3.26).

To illustrate the highest achievable radiation pattern of the dual-mode waveguide, let us assume that the waveguide wall thickness is equal to zero (i.e., $a = b$. The problem of excitation of such an array has a rigorous analytical solution obtained by the method of factorization [10] and presented in the previous section. Using (3.15) and accounting for the numbering of the waveguide modes taken in this section, we may obtain the following expressions for the waveguide amplitude patterns corresponding to each type of excitation

$$F_1(\theta) = \frac{2\gamma_1 \cos\theta}{\gamma_1 + \Gamma_0} \sqrt{\frac{\gamma_1 + \gamma_2}{\gamma_1 \quad \gamma_2}}$$

$$\sqrt{\frac{\Gamma_0 - \gamma_2}{\Gamma_0 + \gamma_2}} \tag{3.27}$$

$$\frac{1}{2} \frac{\Gamma_0 + \Gamma_{\ 1}}{\Gamma_0 + \gamma_2} \sqrt{\frac{\gamma_2 \quad \Gamma_{\ 1}}{\gamma_2 + \Gamma_{\ 1}} \quad 1 + \frac{2b}{\lambda} \sin\theta \div}$$

$$F_2(\theta) = \frac{2k\sqrt{\gamma_1 \gamma_2}\, \sin\theta \cos\theta}{(\gamma_1 + \Gamma_0)(\gamma_2 + \Gamma_0)} \sqrt{\frac{\gamma_1 + \gamma_2}{\gamma_1 \quad \gamma_2}}$$

$$1 \tag{3.28}$$

$$\frac{1}{2} \frac{\Gamma_0 + \Gamma_{\ 1}}{\gamma_2 + \Gamma_{\ 1}} \sqrt{3 \quad \frac{2b}{\lambda} \sin\theta}$$

where $\Gamma_0 = k\cos\theta$ and $\Gamma_{-1} = [k^2 \quad (k\sin\theta - 2\pi/b)^2]^{1/2}$ are propagation constants of the Floquet modes (3.9) of zero and minus first orders, respectively. The upper lines in the figure brackets in (3.27) and (3.28) should be used at $0 \quad \sin\theta \quad \lambda/b \quad 1$, while the lower ones are valid at $\lambda/b \quad 1 \quad \sin\theta \quad 1$. The patterns (3.27) and (3.28) as well as the limiting pattern $\sqrt{F_1^2 + F_2^2}$ corresponding to the optimum dual-mode excitation of the waveguides in array with $a = b = 0.8\lambda$ are shown in Figure 3.5. The limiting pattern is compared to the ideal normalized element pattern $\sqrt{\cos\theta}$, as well as to the single-mode waveguide amplitude pattern $2\cos\theta/(1 + \cos\theta)$, which is easy to obtain from (3.27) at the condition that $a = b < \lambda/2$ when γ_2 is imaginary.

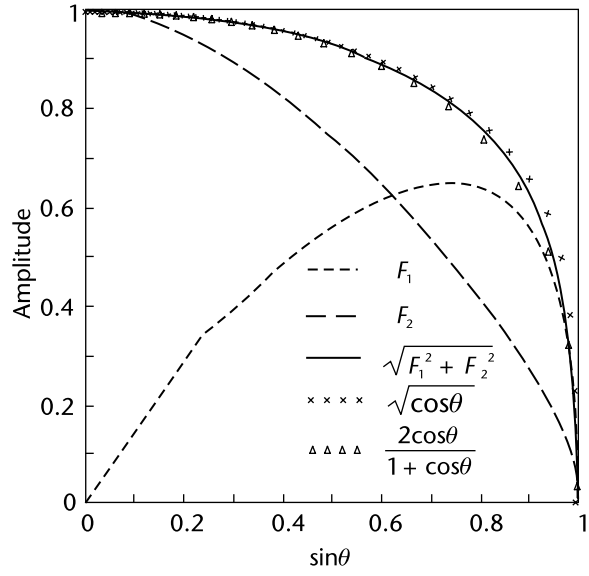

Figure 3.5 Radiation patterns of dual-mode waveguide in the E-plane of array with $a = b = 0.8\lambda$.

The comparison shows that the pattern at the optimum dual-mode excitation is only slightly lower than the ideal element pattern for large angles of observation because of the increase of the reflection from the aperture, and it practically coincides with the single-mode waveguide pattern. The latter feature means that the gain of the array of optimally excited dual-mode waveguides when scanning is practically the same as that of the array using a doubled number of single-mode phased waveguides occupying the same aperture.

3.2.4 Optimization of the Structure

Optimization of the array geometry is carried out as follows. First, for specified element spacing b, wall thickness $b \quad a$ of the dual-mode sections, and width a_0 of the input single-mode waveguides, we carry out numerical experimentation to determine the width a_t and length h_t of the transition section providing the best match between the single-mode and dual-mode sections for the dominant TM_1 (TEM) mode at a specified frequency. Then, we specify the observation angle value θ (the recommended value resulting from the practical calculations is $\theta \quad \arcsin[\lambda/(4b)]$) as well as the slot width and determine the distance h_1 from the transition to the slots providing the necessary value for $|C_2/C_1|$ calculated in advance according to (3.26). If the necessary value for the indicated ratio is not possible to obtain for the specified , we specify another value for this parameter and repeat the procedure. The amplitudes D_n of the waves reflected from the aperture are excluded from consideration at this stage of the optimization process, and therefore we solve only $3N$ equations of the system (3.16) with $3N$ unknowns. After determining the distance h_1 and width , we determine the distance h_2 from the slots to the aperture providing maximum of the element pattern (3.20) in the specified direction. This corresponds to satisfaction of the phase relation (3.23). This stage requires solution of all the $4N$ equations of the system (3.16) with all the $4N$ unknowns.

Note that it is possible to obtain a few different values for each of the parameters h_t, h_1, and h_2 in the optimization process that satisfy the conditions indicated earlier. In this case, it is preferable to select the smallest of them because such a choice provides weaker dependence of the array characteristics on frequency.

3.2.5 Numerical Results

The technique developed for analysis and optimization of the array of coupled dual-mode waveguides scanning in E-plane has been realized in a package of codes including subroutines calculating the scattering matrices of the stepped transition, system of slots in the waveguide walls, and array aperture. The texts of the codes are available in [14]. The elements of the generalized matrices of scattering are calculated by accounting for 20 to 40 waves in each waveguide section and 200 to 300 Floquet modes in the slot region and free space above the aperture. Calculations of the array characteristics as a whole have been performed by accounting for two propagating modes TM_1 and TM_2 as well as two evanescent modes TM_3 and TM_4. The order of the system (3.16) therefore has been equal to 16. The results obtained for the array with element spacings $b = 0.8\lambda$, $b = 0.9\lambda$, and $b = \lambda$ are presented in Figures 3.6, 3.7, and 3.8, respectively. The wall thickness in the dual-mode sections

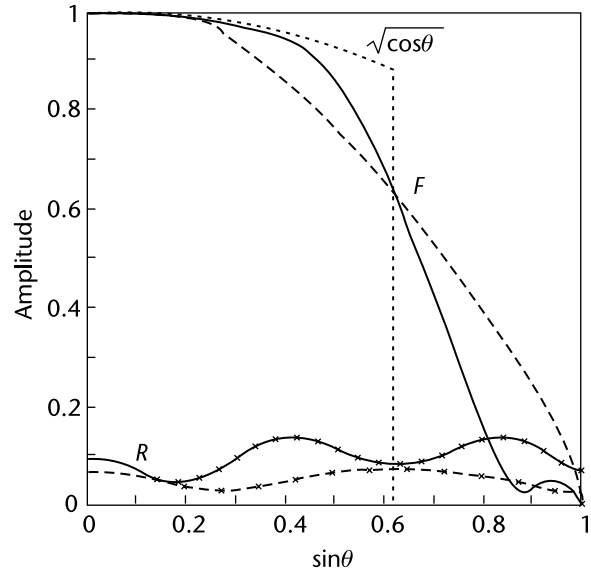

Figure 3.6 Element pattern (F) and reflection coefficient (R) of array with slots for $b = 0.8\lambda$, $a = 0.75\lambda$, $a_0 = 0.4\lambda$, $a_t = 0.565\lambda$, $h_t = 0.207\lambda$, $h_1 = 0.527\lambda$, $h_2 = 0.6\lambda$, and $= 0.3\lambda$; (– – –) is the same array without slots at $h_1 + h_2 = 0.5\lambda$.

and the width of the input single-mode waveguides are $b \quad a = 0.05\lambda$ and $a_0 = 0.4\lambda$, respectively, for all the three cases. The values for the other array parameters determined as a result of optimization are indicated in the figure captions. The presented characteristics are compared to the characteristics corresponding to the absence of the slots in the dual-mode sections of specially determined optimum length. Note that the optimization in the absence of the slots is also of importance,

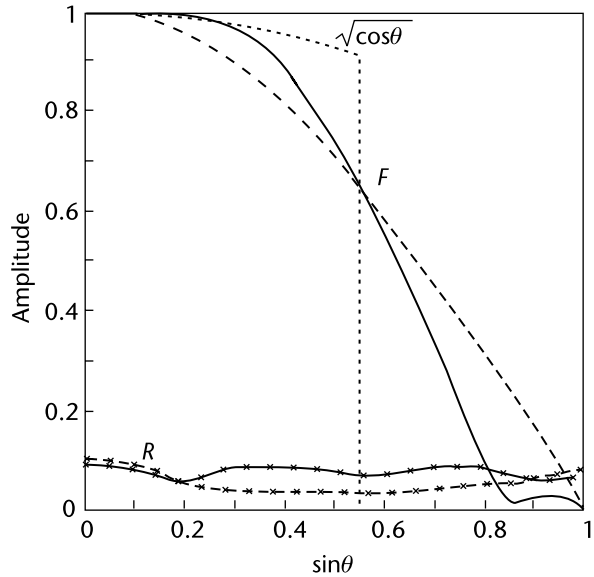

Figure 3.7 Element pattern (F) and reflection coefficient (R) of array with slots for $b = 0.9\lambda$, $a = 0.85\lambda$, $a_0 = 0.4\lambda$, $a_t = 0.616\lambda$, $h_t = 0.191\lambda$, $h_1 = 0.423\lambda$, $h_2 = 0.654\lambda$, and $= 0.3\lambda$; (– – –) is the same array without slots at $h_1 + h_2 = 0.5\lambda$.

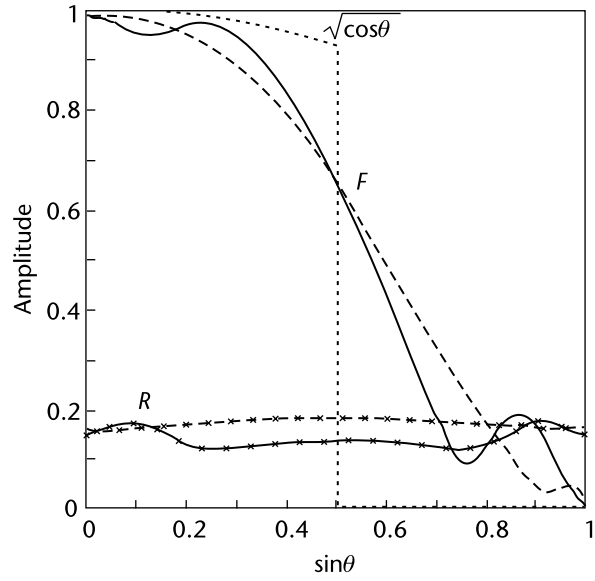

Figure 3.8 Element pattern (F) and reflection coefficient (R) of array with slots for $b = \lambda$, $a = 0.95\lambda$, $a_0 = 0.4\lambda$, $a_t = 0.673\lambda$, $h_t = 0.173\lambda$, $h_1 = 0.4\lambda$, $h_2 = 1.298\lambda$, and $= 0.3\lambda$; (– – –) is the same array without slots at $h_1 + h_2 = 0.5\lambda$.

because the element pattern at some values of the dual-mode section length may even have resonant dips discussed in [15, 16].

Analysis of the results presented in Figures 3.6, 3.7, and 3.8 shows that the element pattern half-width at levels 0.89 (–1 dB) and 0.32 (–10 dB) is approximately equal to 0.69 to 0.74 of w and 1.17 to 1.26 of w, respectively, where $w = \lambda/(2b)$ is the half-width of the ideal sector element pattern also shown in the indicated figures. For comparison, the appropriate half-width values of the theoretical element patterns provided by the dual-mode horns excited through the directional couplers [2] are $0.65w$ and $1.16w$. The behavior of the array characteristics for $b = 0.8\lambda$ and

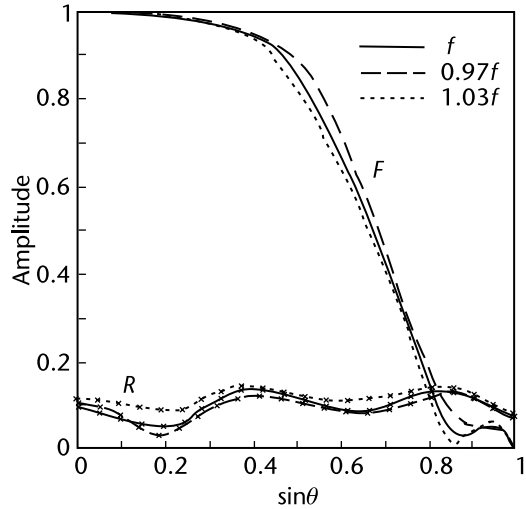

Figure 3.9 Element pattern (F) and reflection coefficient (R) of array with parameters indicated in the caption for Figure 3.6 at frequencies f, $0.97f$, and $1.03f$.

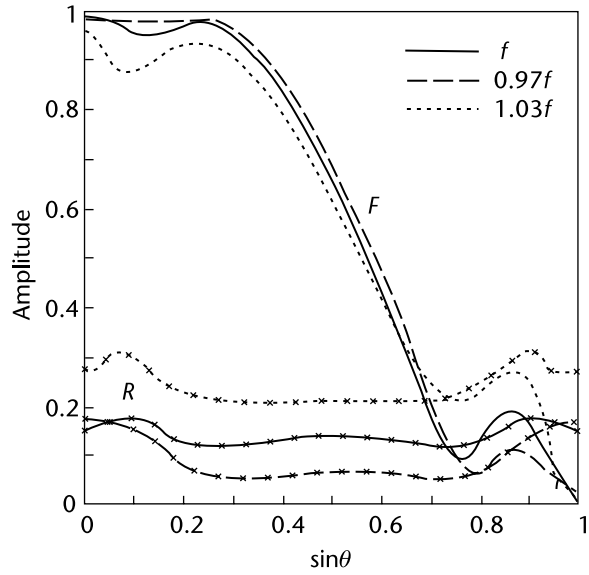

Figure 3.10 Element pattern (*F*) and reflection coefficient (*R*) of array with parameters indicated in the caption for Figure 3.8 at frequencies *f*, 0.97*f*, and 1.03*f*.

$b = \lambda$ in a frequency band from $0.97f$ to $1.03f$, where frequency f corresponds to the wavelength λ, is shown in Figures 3.9 and 3.10, respectively. We can also note that when the element spacing increases to one wavelength, the obtained array match and sector element pattern quality worsens. However the improved model allows us to obtain considerably better results than those presented in Figures 3.2 and 3.3 for the simplified model.

3.3 Array Structure for Scanning in H-Plane

3.3.1 Features of Geometry and Optimum Excitation

The geometry of a parallel-plate waveguide array designed for scanning in H-plane is shown in Figure 3.11. The array is assumed to be excited by the dominant TE_1 modes in semi-infinite single mode waveguides of width $\lambda/2 < a_0 < \lambda$, attached to dual-mode waveguide sections of width $\lambda < a < 1.5\lambda$ via stepped transitions of length h_t and width a_t. Each wall of the dual-mode section has two slots of width each, arranged at distance h from each other. The upper parts of the dual-mode sections contain longitudinal baffles forming symmetrical branchings with single-mode sections of width c and length h_b. The distances from the lower slot to the transition and from the upper one to the branching are equal to h_1 and h_2, respectively.

As we see, this structure somewhat differs from the structure designed for scanning in E-plane (Figure 3.4). The latter uses single slots in the dual-mode section walls. At (or close to) the in-phase excitation of the array with thin walls by the TEM modes, the row of slots is a weak discontinuity. Hence there is no great necessity to apply additional means for matching it. Unlike that, reflection of the TE_1 modes from a row of slots when scanning in the H-plane in a general case may be

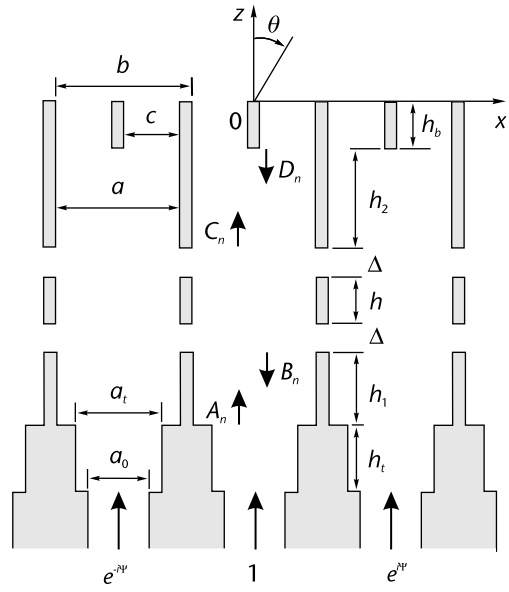

Figure 3.11 Geometry of array of coupled parallel-plate waveguide for scanning in H-plane.

considerable. The improvement of the match in this case is performed using two rows of identical slots arranged at appropriate distance.

The second difference is the presence of branchings at the aperture of the H-plane array. At the in-phase excitation of the E-plane array, the dominant TEM modes come to aperture. They have uniform field distribution across the waveguide, and this fact provides the aperture efficiency close to 100%. The dominant modes in the H-plane array are TE_1 modes with cosine field distribution. Such a distribution over an aperture exceeding the operating wavelength yields an aperture efficiency of about 81% or array gain reduction by 0.91 dB. The baffles introduced at the dual-mode waveguide apertures allow us to avoid the indicated reduction. An alternative modification could be dielectric plates of thickness $0.25\lambda/\sqrt{\varepsilon\ \ 1}$ and relative permittivity ε arranged on the waveguide walls, allowing us to obtain the uniform field distribution over the empty part of the waveguide cross-section [17, 18]. The high efficiency of such an aperture is possible at only small plate thickness and appropriately large plate permittivity; however, increasing the permittivity results in decreasing the operating frequency bandwidth.

Similarly to the case of the E-plane considered in the previous section, the analysis of the H-plane array is carried out using the method of generalized scattering matrices. The system of equations (3.16) for the amplitudes A_n, B_n, C_n, and D_n indicated in Figure 3.11 remains valid. However, the propagation constants (3.17) should be replaced by the propagation constants

$$\gamma_n = \sqrt{k^2 \quad \frac{n\pi}{a} \div^2} = i\sqrt{\frac{n\pi}{a} \div^2 \quad k^2} \tag{3.29}$$

Furthermore, the matrices $\boldsymbol{R}^{(1)}$ and $\boldsymbol{T}^{(1)}$ now correspond to two rows of slots, and the matrices $\boldsymbol{R}^{(2)}$ and $\boldsymbol{T}^{(2)}$ take into account the presence of the baffles in the

dual-mode sections. The details of calculation of the scattering matrix elements for the transition, system of slots, and modified aperture can be found in [14]. The technique developed for calculation of the modified aperture characteristics is presented in Appendix 3B as an example.

Solution of the system (3.16) allows the calculation of the array characteristics. The reflection coefficient is determined by (3.18), while the expression (3.20) for the normalized element pattern should be replaced now by

$$F(\theta) = \sqrt{\frac{2kb}{\gamma_1^{(0)} a_0}} \, | \, T_0(kb \sin\theta) \, | \cos\theta \tag{3.30}$$

where $\gamma_1^{(0)} = \sqrt{k^2 \quad (\pi / a_0)^2}$ is the propagation constant of the dominant TE_1 mode in the input single-mode waveguide sections.

The optimum ratio for amplitudes C_2 and C_1 of the TE_2 and TE_1 modes in the dual-mode sections providing maximization of the array gain at the dual-mode excitation is determined in [9] in a similar way as is done in Section 3.2.3 for the E-plane array case. As a result, if the total power carried by the indicated modes is equal to unity; that is,

$$(\gamma_1 C_1^2 + \gamma_2 C_2^2) a / 2 = 1 \tag{3.31}$$

the optimum amplitude ratio is determined by formula

$$\frac{C_2(\theta)}{C_1(\theta)} = \sqrt{\frac{\gamma_1}{\gamma_2}} \frac{F_2(\theta)}{F_1(\theta)} \tag{3.32}$$

where $F_1(\theta)$ and $F_2(\theta)$ are values of the amplitude array element patterns (for a dual-mode waveguide with baffles) corresponding to excitation of the waveguide in the TE_1 and TE_2 modes of unit power, respectively. As with the E-plane case, the maximum level of the power element pattern equals $F_1^2 + F_2^2$ and only slightly differs from the ideal normalized power pattern $\cos\theta$ for $\theta \quad 2\lambda/b \quad 1$ (i.e., in the region of single-beam scanning in the waveguide array with spacing equal to $b/2$).

3.3.2 Computed Array Characteristics

The technique of H-plane array geometry optimization as a whole is similar to that described in Section 3.2.3 for the E-plane case. Appropriate selection of the transition length h_t and width a_t provides perfect match between the single-mode and dual-mode waveguide sections at a specified frequency. The length of the baffles in the dual-mode sections at the aperture is selected to provide the best array match to free space at the array excitation in the dominant TE_1 modes when the controlling phase value is zero or close to zero. Further, we specify the slot width and select the distance between the slots h providing their perfect match at in-phase excitation of the dual-mode sections in the TE_1 modes. Then, at specified value of $\sin\theta$ close to $\lambda/(4b)$, we select the distance between the transition and slots h_1 providing the optimum ratio for amplitudes of the second and first modes (3.32). If the required value

fails to be achieved at the specified slot width, we specify a new value the latter and repeat the procedure. After selecting the slot width, the optimization of the array geometry is completed by selection of the distance between the slots and baffles h_2 providing maximum of the element pattern (3.30) in the specified direction.

The source FORTRAN code realized according to the technique described earlier is presented in [14]. The code uses subroutines developed on the basis of the mode-matching method for calculation of the generalized scattering matrices of the transition, doubled slots, and array aperture taking the baffles into account. The calculations have been performed taking into account 20 to 40 waveguide modes in each section and 200 to 300 Floquet modes in the slot region and free space above the aperture. The system (3.16) is solved by accounting for the first four waveguide modes of the dual-mode sections. Since the optimization process consists of a succession of simple operations, it is easily performed in an interactive mode.

The results presented next as an example have been obtained for the array with specified element spacing $b = 1.295\lambda$, dual-mode section width $a = 1.25\lambda$, and input single-mode waveguide width $a_0 = 0.795\lambda$. The values for the other array parameters found as a result of the optimization process are indicated in the caption for Figure 3.12, where the calculated magnitude of the array reflection coefficient (3.18) and element pattern (3.30) are shown together with the normalized ideal element pattern $\sqrt{\cos\theta}$ of width corresponding to the indicated element spacing.

The behavior of the array characteristics in the center and at the edges of a 3% frequency band is demonstrated in Figure 3.13. The sector shape of the element pattern is kept sufficiently well, and the array match remains satisfactory. The bandwidth in the case under consideration is somewhat narrower than that for the E-plane array because of greater element spacing in the H-plane array.

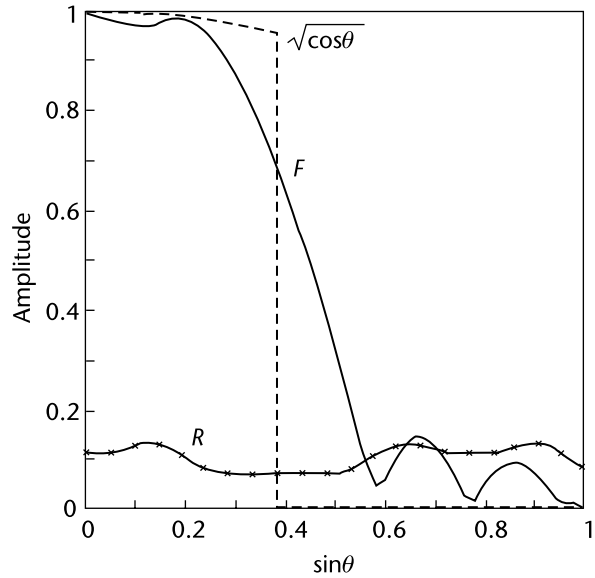

Figure 3.12 Element pattern (F) and magnitude of reflection coefficient (R) of H-plane array with parameters $b = 1.295\lambda$, $a = 1.25\lambda$, $a_0 = 0.795\lambda$, $a_t = 0.929\lambda$, $h_t = 0.232\lambda$, $h_1 = 0.689\lambda$, $h_2 = 0.27\lambda$, $= 0.425\lambda$, $h = 0.313\lambda$, and $h_b = 0.643\lambda$.

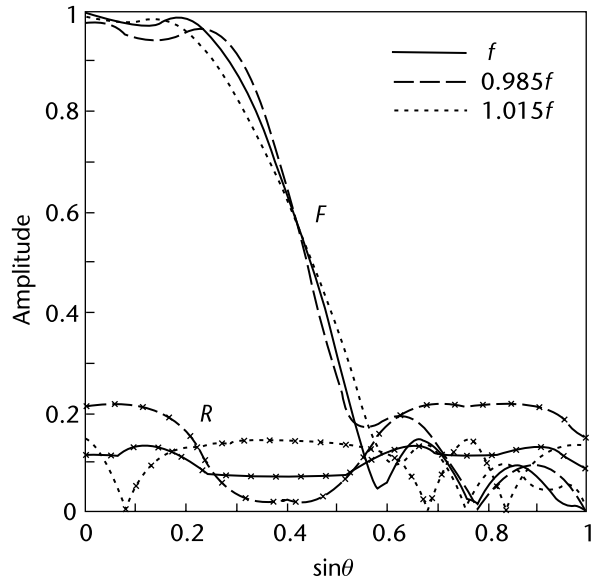

Figure 3.13 Reflection coefficient (R) and element pattern (F) of the H-plane array with parameters indicated in caption to Figure 3.12 at frequencies f, $0.985f$, and $1.015f$.

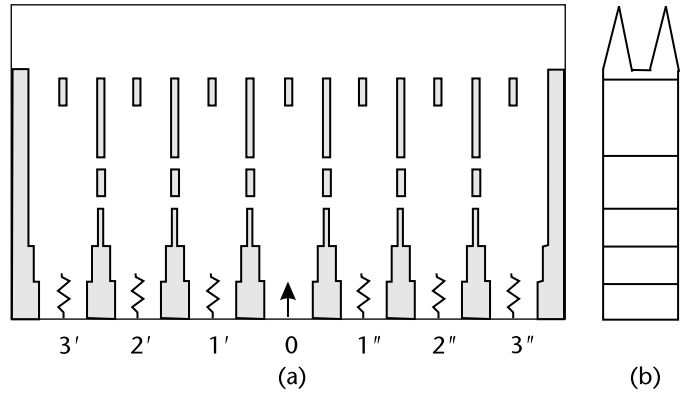

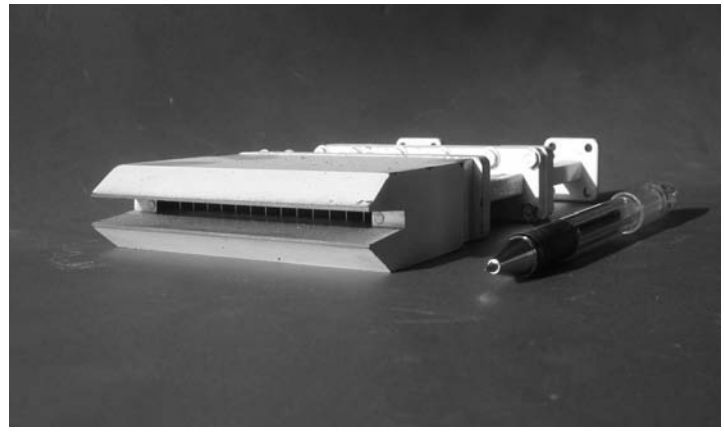

(c)

Figure 3.14 Experimental linear array breadboard of coupled dual-mode rectangular waveguides: (a) cut in the H-plane, (b) side view, and (c) general view.

3.4 Experimental Study of the H-Plane Array

Verification of the numerical results presented earlier and possibilities of practical realization of the proposed structures for operation in the K_a frequency band have been carried out with using an experimental linear array of rectangular waveguides coupled through the slots in common narrow walls [19–22]. The cut of this array in the H-plane, its side view, and its general view are shown in Figure 3.14. Unlike the theoretical model in the form of an infinite periodic structure of parallel-plate waveguides, the experimental array breadboard consists of seven elements the apertures of which radiate in a common horn section. As shown in Figure 3.14(b), the array is built of six blocks: single-mode waveguides, transition sections, dual-mode sections without slots, dual-mode sections with slots, dual-mode sections with baffles, and a horn section. The waveguide channels in each block have been performed using the electro-erosion method. The accuracy of block attachment is provided by using

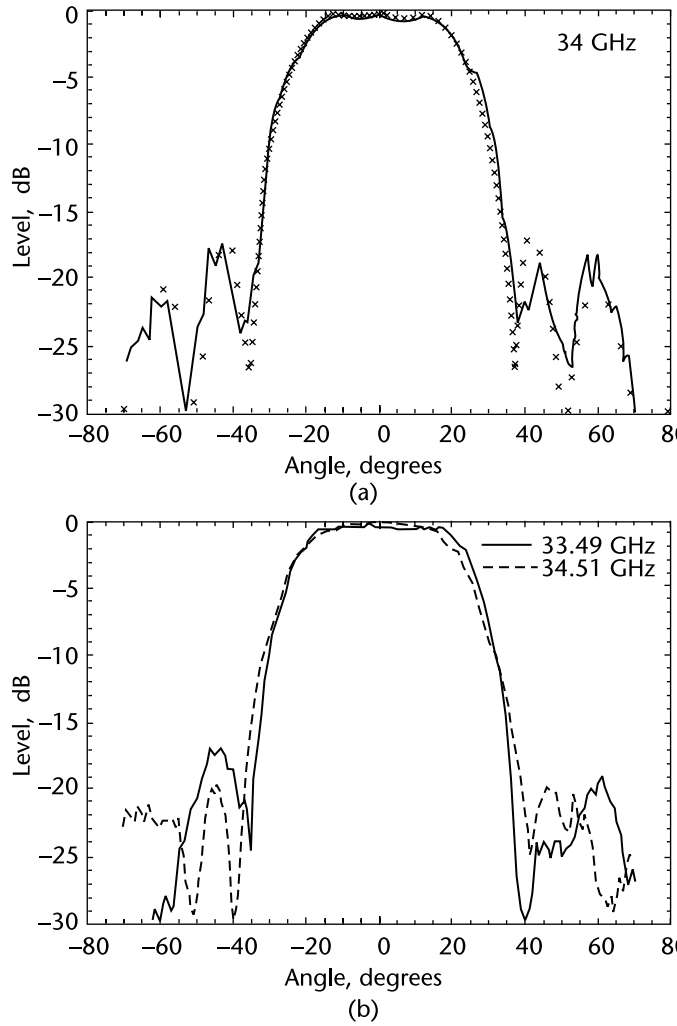

Figure 3.15 Measured radiation patterns of the central array element at frequencies (a) 34 GHz as well as (b) 33.49 and 34.51 GHz; ( ) is calculated element pattern at 34 GHz.

appropriate guide pins, while the blocks are tightened together by four longitudinal screws. The values of the geometric parameters in the H-plane in millimeters correspond to the values in wavelength indicated in the caption for Figure 3.12. The waveguide width in the E-plane equals the standard value 3.4 mm, while the length of the horn section and its aperture width equal 25 and 7 mm, respectively.

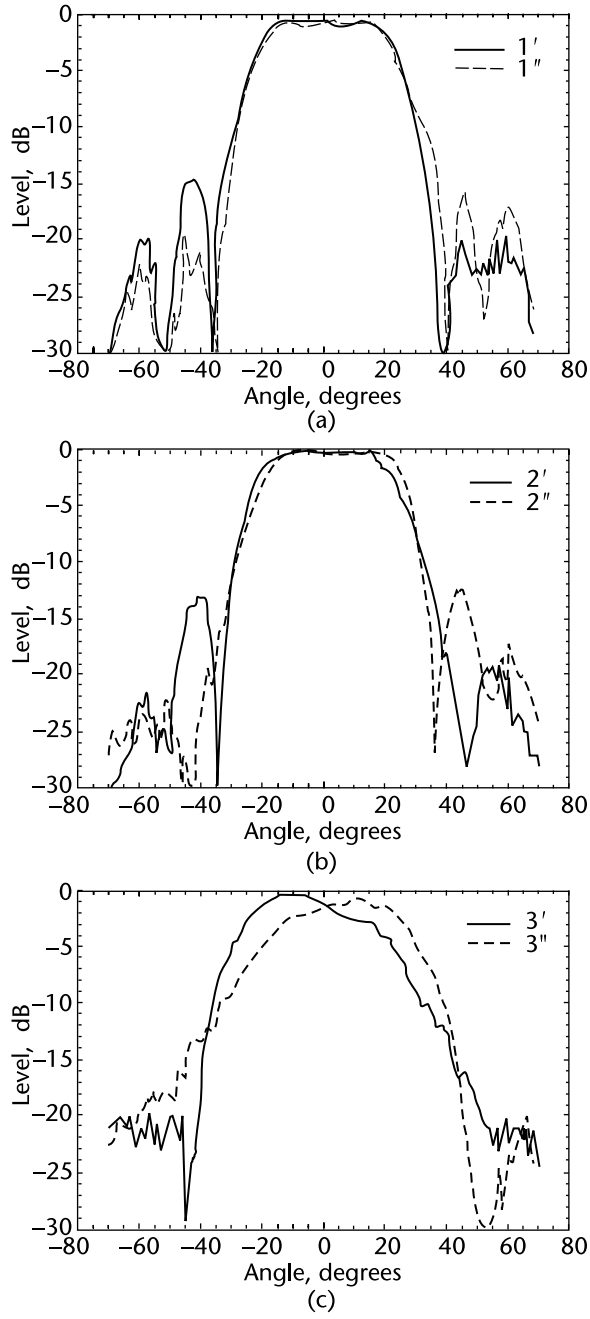

Figure 3.16 Measured array radiation patterns at excitation of its (a) first (1′ and 1″), (b) second (2′ and 2″), and (c) third (3′ and 3″) lateral inputs at frequency 34 GHz.

The measurements of the array characteristics have been performed in the frequency band (34±1) GHz. The VSWR of the central element in the indicated band varies from 1.09 to 1.27 [19]. The results of the array radiation pattern measurement corresponding to excitation of the central element at frequencies 34, 33.49, and 34.51 GHz and providing the other array inputs with matching loads are presented in Figure 3.15. Comparison of the measured element pattern with theoretical element pattern recalculated from Figure 3.12 to decibels presented in Figure 3.15(a) shows good agreement between the theory and experiment.

The measured radiation patterns of the central array element at frequencies 33.49 and 34.51 GHz shown in Figure 3.15(b) confirm the theoretical conclusion that shape of the sector beam in the 3% frequency band remains practically changeless.

The study of the array edge effect on the array element pattern shape has been carried out by means of the array pattern measurement at excitation of the array lateral inputs. The patterns measured at frequency 34 GHz are presented in Figure 3.16. The results show that the pattern shape in the sector beam region at excitation of each lateral input except for the edge one is practically identical. The overall change of the pattern shape consists of only a slight increase of the sidelobe level at the side of the nearest edge. The array pattern shape corresponding to excitation of the edge inputs [3' and 3", Figure 3.14(a)] already considerably differs from the sector one. The results obtained in this study allow us to draw a conclusion that the excitation of one array input results in efficient excitation of only three array cells just as it takes place in the array with power dividers and directional couplers shown in Figure 2.12.

Comparison of the calculated and measured results presented here both for the E-plane array and for the H-plane array with the data available in [2] shows that shaping of the sector element patterns in the arrays of dual-mode waveguides with simple slot elements of coupling is possible with quality corresponding to that achieved in more complex arrays based on using power dividers and directional couplers.

References

[1] Mailloux, R. J., and P. R. Franchi, "Phased Array Antenna with Array Elements Coupled to Form a Multiplicity of Overlapped Subarrays," U.S. Patent No. 3938160, Int. Cl. H 01 Q 3/26, 1976.

[2] Mailloux, R. J., "An Overlapped Subarray for Limited Scan Application," *IEEE Trans. on Antennas and Propagation*, Vol. AP-22, No. 3, March 1974, pp. 487–489.

[3] Skobelev, S. P., "Radiation from an Array of Dual-Mode Waveguides Forming Overlapped Subarrays," *Radiotekhnika*, No. 7, 1987, pp. 62–65 (in Russian).

[4] Hannan, P. W., D. S. Lerner, and G. H. Knittel, "Impedance Matching a Phased-Array Antenna over Wide Scan Angles by Connecting Circuits," *IEEE Trans. on Antennas and Propagation*, Vol. AP-13, No. 1, 1965, pp. 28–34.

[5] Vendik, O. G., and L. V. Ryzhkova, "Synthesis of a Circuit for Compensation of Mutual Coupling Between Radiators in a Phased Antenna Array," *Antenny*, No. 4, 1968, pp. 42–50 (in Russian).

[6] Skobelev, S. P., "Radiation from Array of Planar Waveguides with Slotted Coupling Elements," *Sov. J. Communication Technology & Electronics*, Vol. 32, No. 7, 1987, pp. 170–172.

[7] Skobelev, S. P., and A. S. Vyazigin, "Forming Flat-Topped Element Patterns in Antenna Arrays of Two-Mode Waveguides," *Electronics Letters*, Vol. 29, No. 15, July 22, 1993, pp. 1326–1327.

[8] Vyazigin, A. S., and S. P. Skobelev, "Analysis and Optimization of an Array of Dual-Mode Waveguides with Slotted Elements of Coupling," *Radiotekhnika*, No. 1, 1996, pp. 30–32 (in Russian).

[9] Vyazigin, A. S., and S. P. Skobelev, "Shaping Sector Partial Patterns in an Antenna Array of Coupled Dual-Mode Waveguides," *Radiotekhnika i Electronika*, Vol. 38, No. 9, 1993, pp. 1554–1559 (in Russian).

[10] Mittra, R., and S. W. Lee, *Analytical Techniques in the Theory of Guided Waves*, New York: Macmillian Company, 1971.

[11] Weinshtein, L. A., *The Theory of Diffraction and the Factorization Method*, Boulder, CO: Golem, 1969.

[12] Clarricoats, P. J. B., and K. R. Slinn, "Numerical Solution of Waveguide-Discontinuity Problems," *IEE Proc.*, Vol. 114, No. 7, 1967, pp. 878–886.

[13] Diamond, B. L., "A Generalized Approach to the Analysis of Infinite Planar Array Antennas," *IEEE Proc.*, Vol. 56, No. 11, 1968, pp. 1837–1851.

[14] Vyazigin, A. S., "Shaping of Sector Partial Radiation Patterns in Antenna Arrays of Dual-Mode Waveguides," Master's Thesis, Moscow Institute of Physics and Technology, 1993 (in Russian).

[15] Mailloux, R. J., "Surface Waves and Anomalous Wave Radiation Nulls in Phased Arrays of TEM Waveguides with Fences," *IEEE Trans. on Antennas and Propagation,* Vol. 20, No. 2, March 1972, pp. 160–166.

[16] Mailloux, R. J., *Phased Array Antenna Handbook,* Norwood, MA: Artech House, 1994.

[17] Yegorov, Y. V., *Partially Filled Rectangular Waveguides*, Moscow: Sovetskoye Radio, 1967 (in Russian).

[18] Tsandoulas, G. N., and W. D. Fitzgerald, "Aperture Efficiency Enhancement in Dielectrically Loaded Horns," *IEEE Trans. on Antennas and Propagation,* Vol. 20, No. 1, January 1972, pp. 69–74.

[19] Skobelev, S. P., and A. S. Vyazigin, "Results of Development and Experimental Study of a Linear Antenna Array of Coupled Rectangular Waveguides," *Technical Physics Letters*, Vol. 19, No. 15, 12 August 1993, pp. 72–77 (in Russian).

[20] Skobelev, S. P., and A. S. Vyazigin, "A Linear Antenna Array of Two-Mode Slot-Coupled Waveguides with Flat-Topped Element Patterns," *1994 IEEE AP-S Intl. Symp. Digest*, Vol. 2, University of Washington, Seattle, WA, June 19–24, 1994, pp. 1268–1271.

[21] Skobelev, S. P., and A. S. Vyazigin, "Shaping Flat-Topped Element Patterns in a Linear Antenna Array of Dual-Mode Slot-Coupled Waveguides," *Proc. 27th Scientific Conf. on Antenna Theory and Technology*, Moscow, Russia, August 23–25, 1994, pp. 103–105 (in Russian).

[22] Skobelev, S. P., and A. S. Vyazigin, "Shaping Flat-Topped Element Patterns in a Linear Antenna Array of Dual-Mode Slot-Coupled Waveguides," *Journees Internationales De Nice Sur Les Antennes (JINA)*, Nice, France, November 8–10, 1994, pp. 674–677.

[23] Mittra, R., (ed.), *Computer Techniques for Electromagnetics*, New York: Pergamon Press, 1973.

Appendix 3A Calculation of the Scattering Matrix Elements for the Slots in the Waveguide Walls

Consider the slot region in the E-plane array of dual-mode waveguides shown in Figure 3.4. The geometry of this region is separately depicted in Figure 3A.1. The waveguide width, element spacing, and slot width are the same as those in Figure 3.4.

Let the lower waveguide sections be excited in the TM_m modes of unit amplitude and phase increment between adjacent waveguides. The magnetic fields in the lower and upper sections of the central waveguide are represented by superpositions of TM modes

$$H_{y0}(x,z) = \sum_{n=1} (\delta_{mn} e^{i\gamma_n z} + R_n e^{\ i\gamma_n z}) \cos\frac{(n\quad 1)\pi(x+a/2)}{a} \tag{3A.1}$$

$$H_{y1}(x,z) = \sum_{n=1} T_n e^{i\gamma_n (z\quad)} \cos\frac{(n\quad 1)\pi(x+a/2)}{a} \tag{3A.2}$$

with unknown amplitudes R_n and T_n.

The magnetic field in the slot region is represented by a superposition of Floquet modes

$$H_{y2}(x,z) = \sum_{q=} (A_q e^{i\Gamma_q z} + B_q e^{\ i\Gamma_q (z\quad)})\, e^{i\alpha_q x} \tag{3A.3}$$

where A_q and B_q are unknown amplitudes of the modes propagating or evanescent in the positive and negative directions, respectively. The propagation constants of the waveguide modes (3A.1) and (3A.2) as well as Floquet modes (3A.3) are determined by formulas (3.17) and (3.9).

Matching the fields (3A.1) and (3A.3) in the aperture of the lower section and projecting the functional equation on the waveguide mode transverse functions, we obtain algebraic equations

$$R_n = \quad \delta_{mn} + (2 \quad \delta_{1n}) \sum_{q=} (A_q + B_q e_q) Q_{nq} \tag{3A.4}$$

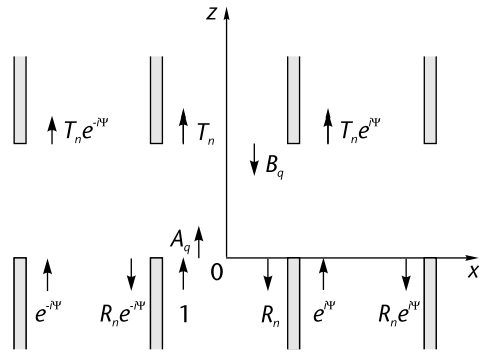

Figure 3A.1 Geometry of the slot region in the waveguide array of Figure 3.4.

where $n = 1, 2, \ldots$; $e_q = \exp(i\Gamma_q \quad)$, and

$$Q_{nq} = \frac{1}{a}\int_{a/2}^{a/2} \cos\frac{(n \quad 1)\pi(x+a/2)}{a} e^{i\alpha_q x}\, dx$$

$$= i\alpha_q a \frac{e^{\ i\alpha_q a/2} \quad (\ 1)^{n\ 1} e^{i\alpha_q a/2}}{(\alpha_q a)^2 \quad (n \quad 1)^2\pi^2} \tag{3A.5}$$

Similar projective matching of the fields (3A.2) and (3A.3) in the input aperture of the upper section of the central waveguide at $z =$ yields

$$T_n = (2 \quad \delta_{1n}) \sum_{q=} (A_q e_q + B_q) Q_{nq} \tag{3A.6}$$

The transverse electric field strength component E_x in the waveguide sections and slot region is determined by formula (1.104) applied to expressions (3A.1), (3A.2), and (3A.3). This component must be continuous in the apertures of the lower and upper waveguide sections and zero on the flanges. These conditions result in two functional equations. Projecting them on the Floquet mode transverse functions $\exp(\ i\alpha_p x)$, where $p = 0, \pm1, \pm2, \ldots$ we obtain two more subsystems of algebraic equations

$$(A_p \quad B_p e_p)\Gamma_p b/a = \sum_{n=1} \gamma_n(\delta_{mn} \quad R_n) Q_{np} \tag{3A.7}$$

$$(A_p e_p \quad B_p)\Gamma_p b/a = \sum_{n=1} \gamma_n T_n Q_{np} \tag{3A.8}$$

where the asterisk means complex conjugation.

Substituting (3A.4) and (3A.6) in (3A.7) and (3A.8), we reduce the latter two to the system

$$\sum_{q=} [(\sigma_{pq} + \delta_{pq}\Gamma_q b/a)A_q + (\sigma_{pq} \quad \delta_{pq}\Gamma_q b/a)e_q B_q] = 2\gamma_m Q_{mp} \tag{3A.9}$$

$$\sum_{q=} [(\sigma_{pq} \quad \delta_{pq}\Gamma_q b/a)e_q A_q + (\sigma_{pq} + \delta_{pq}\Gamma_q b/a)B_q] = 0 \tag{3A.10}$$

where

$$\sigma_{pq} = \sum_{n=1} (2 \quad \delta_{1n})\gamma_n Q_{np} Q_{nq} \tag{3A.11}$$

The infinite algebraic systems (3A.9) and (3A.10) are solved by the method of truncation with subsequent application of the Gauss elimination method. The truncation should be performed by taking into account the problem of relative convergence (see, for instance, the appendix to Chapter 5 in [23]). According to that, the finite number of the Floquet modes in (3A.3) should be no less than the number of the waveguide modes in (3A.1), (3A.2), or (3A.11) multiplied by b/a.

The amplitudes A_q and B_q determined as a result of the solution of the system (3A.9) and (3A.10) are used for calculating the amplitudes of the reflected and transmitted waveguide modes by formulas (3A.4) and (3A.6), respectively. These amplitudes form the mth columns in matrices $\boldsymbol{R}^{(1)}$ and $\boldsymbol{T}^{(1)}$, respectively, used in system (3.16).

Note also that if we exclude the amplitudes B_q from expression (3A.4) and equations (3A.9), the indicated expressions will correspond to the waveguide array aperture faced to free space. The amplitudes A_q found as a result of the solution in this case form the columns of the matrix of transmission coefficients $\boldsymbol{T}^{(2)}$ for the array aperture.

Appendix 3B Analysis of the Modified H-Plane Array Aperture

A fragment of the geometry containing the modified aperture of the array shown in Figure 3.11 is presented separately in Figure 3B.1. The dual-mode waveguide sections are assumed to be excited in TE_p modes of unit amplitude coming to the baffles. The incident modes have progressive phases with increment between adjacent waveguides.

The total electric field in the dual-mode section of the central waveguide is described by a sum of the TE modes

$$E_{y0}(x,z) = \sum_{q=1} (\delta_{pq} e^{i\gamma_q(z+h_b)} + R_q e^{\ i\gamma_q(z+h_b)}) \sin\frac{q\pi(x+a/2)}{a} \tag{3B.1}$$

with unknown amplitudes R_q of the reflected modes and propagation constants (3.29). The electric field in the left-hand section of the branching is represented in the form

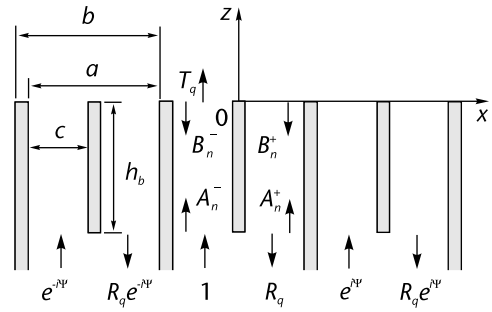

Figure 3B.1 Geometry of the modified waveguide array aperture in the H-plane.

$$E_{y1}(x,z) = \sum_{n=1} (A_n e^{i\gamma_{cn}(z+h_b)} + B_n e^{-i\gamma_{cn}z}) \sin\frac{n\pi(x+a/2)}{c} \tag{3B.2}$$

where A_n and B_n are unknown amplitudes of the forward and backward modes and

$$\gamma_{cn} = \sqrt{k^2 - (n\pi/c)^2} = i\sqrt{(n\pi/c)^2 - k^2} \tag{3B.3}$$

are propagation constants. The electric field in the right-hand section of the branching is written in a similar form

$$E^+_{y1}(x,z) = \sum_{n=1} (A^+_n e^{i\gamma_{cn}(z+h_b)} + B^+_n e^{-i\gamma_{cn}z}) \sin\frac{n\pi(a/2 - x)}{c} \tag{3B.4}$$

with unknown amplitudes A^+_n and B^+_n, while the electric field above the array aperture is a superposition of the Floquet modes

$$E_{y2}(x,z) = \sum_{q=} T_q e^{i\alpha_q x + i\Gamma_q z} \tag{3B.5}$$

with unknown amplitudes T_q.

The electric field (3B.1) must be equal to the fields (3B.2) and (3B.4) in the input apertures of the waveguide branching at $z = -h_b$ and zero on the baffle face. Projecting of this boundary condition on the transverse functions of the dual-mode section results in expression of the reflected mode amplitude via the amplitudes of the modes in the branching sections

$$R_q = -\delta_{pq} + \frac{c}{a} \sum_{n=1} [A_n + B_n e_n + (-1)^{q-1}(A^+_n + B^+_n e_n)] P_{nq} \tag{3B.6}$$

where $e_n = \exp(i\gamma_{cn}h_b)$ and

$$P_{nq} = \frac{2}{c} \int_{a/2}^{a/2+c} \sin\frac{n\pi(x+a/2)}{c} \sin\frac{q\pi(x+a/2)}{a} dx$$

$$= \frac{2}{(-1)^{q-1}c} \int_{a/2-c}^{a/2} \sin\frac{n\pi(a/2 - x)}{c} \sin\frac{q\pi(x+a/2)}{a} dx \tag{3B.7}$$

$$= \frac{\sin[\pi(n - qc/a)]}{\pi(n - qc/a)} - \frac{\sin[\pi(n + qc/a)]}{\pi(n + qc/a)}$$

In turn, the electric field above the aperture (3B.5) must be equal to the fields (3B.2) and (3B.4) in the output apertures of the branching sections and zero on the upper baffle face and waveguide flanges. Projecting this equality on the complex-conjugated transverse functions of the Floquet modes, we obtain

$$T_q = \frac{c}{b} \sum_{n=1} [(A_n e_n + B_n) Q_{nq} + (A_n^+ + B_n^+ e_n) Q_{nq}] \tag{3B.8}$$

where

$$Q_{nq} = \frac{1}{c} \int_{a/2}^{a/2+c} \sin \frac{n\pi(x+a/2)}{c} e^{\ i\alpha_q x} dx \tag{3B.9}$$

$$= n\pi \frac{(\ 1)^n e^{\ i\alpha_q c}}{(\alpha_q c)^2} \frac{1}{(n\pi)^2} e^{i\alpha_q a/2}$$

Additional relations between the unknown amplitudes of the fields in the regions of the structure necessary for solution of the problem are obtained by matching the magnetic field strength transverse component H_x determined by formula (1.101) applied to expressions (3B.1), (3B.2), (3B.4), and (3B.5). The projective matching of the transverse magnetic fields in the input (at $z = \ h_b$) and output (at $z = 0$) apertures of the left-hand and right-hand branching sections by using the orthogonality property of the transverse wave functions for the indicated sections results in the algebraic equations

$$(A_m \quad B_m e_m)\gamma_{cm} = \sum_{q=1} (\delta_{pq} \quad R_q)\gamma_q P_{mq} \tag{3B.10}$$

$$(A_m^+ \quad B_m^+ e_m)\gamma_{cm} = \sum_{q=1} (\delta_{pq} \quad R_q)\gamma_q (\ 1)^{q\ 1} P_{mq} \tag{3B.11}$$

$$(A_m e_m \quad B_m)\gamma_{cm}/2 = \sum_{q=} T_q \Gamma_q Q_{mq} \tag{3B.12}$$

$$(A_m^+ e_m \quad B_m^+)\gamma_{cm}/2 = \sum_{q=} T_q \Gamma_q Q_{mq} \tag{3B.13}$$

Substituting (3B.6) and (3B.8) in (3B.10) through (3B.13), we reduce the latter to the algebraic system for unknown amplitudes A_n, B_n, A_n^+, and B_n^+

$$\sum_{n=1} [(\sigma_{1mn} + \delta_{mn}\gamma_{cn})A_n + \sigma_{2mn} A_n^+ \tag{3B.14}$$

$$+(\sigma_{1mn} \quad \delta_{mn}\gamma_{cn}) e_n B_n + \sigma_{2mn} e_n B_n^+] = 2\gamma_p P_{mp}$$

$$\sum_{n=1}[\sigma_{2mn}A_n+(\sigma_{1mn}+\delta_{mn}\gamma_{cn})A_n^+ +\sigma_{2mn}e_nB_n+(\sigma_{1mn}\quad\delta_{mn}\gamma_{cn})e_nB_n^+]=2(\quad 1)^{p\quad 1}\gamma_pP_{mp} \tag{3B.15}$$

$$\sum_{n=1}[(\bar{\sigma}_{1mn}\quad\delta_{mn}\gamma_{cn})e_nA_n+\bar{\sigma}_{2mn}e_nA_n^+ +(\bar{\sigma}_{1mn}+\delta_{mn}\gamma_{cn})B_n+\bar{\sigma}_{2mn}B_n^+]=0 \tag{3B.16}$$

$$\sum_{n=1}[\bar{\sigma}_{3mn}e_nA_n+(\bar{\sigma}_{4mn}\quad\delta_{mn}\gamma_{cn})e_nA_n^+ +\bar{\sigma}_{3mn}B_n+(\bar{\sigma}_{4mn}+\delta_{mn}\gamma_{cn})B_n^+]=0 \tag{3B.17}$$

where $m = 1, 2, \ldots$; and

$$\sigma_{1mn}=\frac{c}{a}\sum_{q=1}\gamma_qP_{mq}P_{nq} \tag{3B.18}$$

$$\sigma_{2mn}=\frac{c}{a}\sum_{q=1}(\quad 1)^{q\quad 1}\gamma_qP_{mq}P_{nq} \tag{3B.19}$$

$$\bar{\sigma}_{1mn}=\frac{2c}{b}\sum_{q=}\Gamma_qQ_{mq}Q_{nq} \tag{3B.20}$$

$$\bar{\sigma}_{2mn}=\frac{2c}{b}\sum_{q=}\Gamma_qQ_{mq}Q_{nq} \tag{3B.21}$$

$$\bar{\sigma}_{3mn}=\frac{2c}{b}\sum_{q=}\Gamma_qQ_{mq}Q_{nq} \tag{3B.22}$$

$$\bar{\sigma}_{4mn}=\frac{2c}{b}\sum_{q=}\Gamma_qQ_{mq}Q_{nq} \tag{3B.23}$$

The system of (3B.14) through (3B.17) is solved by the method of truncation with subsequent application of the Gauss elimination method. If, when truncating,

N first waveguide modes of each direction are taken into account in each section of the branching resulting in the system order $4N$, one should account for no less than Na/c modes in the dual-mode section and no less than Nb/c Floquet modes in free space. The amplitudes A_n, B_n, A_n^+, and B_n^+ found as a result of solution of the system are then used for calculation of the reflected waveguide mode amplitudes (3B.6) and radiated Floquet mode amplitudes (3B.8). The indicated amplitudes are elements of the generalized matrices of reflection coefficients $\boldsymbol{R}^{(2)}$ and transmission coefficients $\boldsymbol{T}^{(2)}$.

CHAPTER 4

Arrays with Reactively Loaded Radiators

4.1 On Application of Reactive Loads in Array Antennas

The overlapped subarrays with sector radiation patterns in the arrays considered in the previous two chapters are formed by using coupling elements specially introduced between constrained transmitting lines over which the microwave power comes to array radiators. Meanwhile, it is well known that natural mutual coupling over free space always exists between the radiators. In some cases, such interaction between the radiators can cause the undesirable blindness effects [1]. However, there are the cases when the mutual coupling over free space can be used effectively. This was done in [2, 3] for synchronization and phasing of self-excited oscillators in active transmitting phased array antennas. The authors of [4] proposed to arrange rows of passive reactively loaded waveguides between driven waveguides for elimination of the blindness effects. The paper [5] described application of reactively loaded elements in adaptive phased arrays for communications systems, while [6] demonstrates control of the scattering properties of radar targets by means of reactive loads. A general approach to the design synthesis of the array antennas with reactive loads has been formulated in [7]. Some examples concerning a solution of the synthesis problem formulated for nonscanning arrays with sector, cosecant, and directive beams can be found in [8] (an array of impedance filaments), [9, 10] (waveguide arrays), and [11–13] (dipole arrays).

Application of the passive reactively loaded radiated in phased arrays designed for shaping sector partial radiation patterns is illustrated by the networks shown in Figure 4.1. Only small portion of the radiators here is excited by the signals coming directly from the phase shifters. All the other radiators are passive. Their excitation is provided due to their coupling with the driven radiators and between themselves over free space, while the array characteristics are determined by the reactive load values. The reactive loads in such an approach play the role of a beam-forming network (like those considered in Chapter 2), although the network itself is either absent completely [Figure 4.1(a)] or has the simplest configuration [Figure 4.1(b)]. Effective shaping of the sector partial patterns in such arrays is possible only at sufficiently strong interaction between the driven and passive radiators. Such an interaction can be provided between parallel nonstaggered dipoles in the H-plane [11–13] or between rectangular waveguides in the E-plane [9, 10]. The possibility of the grating lobe suppression by using passive radiators has been considered in [14, 15]. These works analyze linear arrays of controlled dipoles where only one passive dipole is arranged between two adjacent driven dipoles. Because of insufficiently strong coupling, the effectiveness of the grating lobe suppression there is

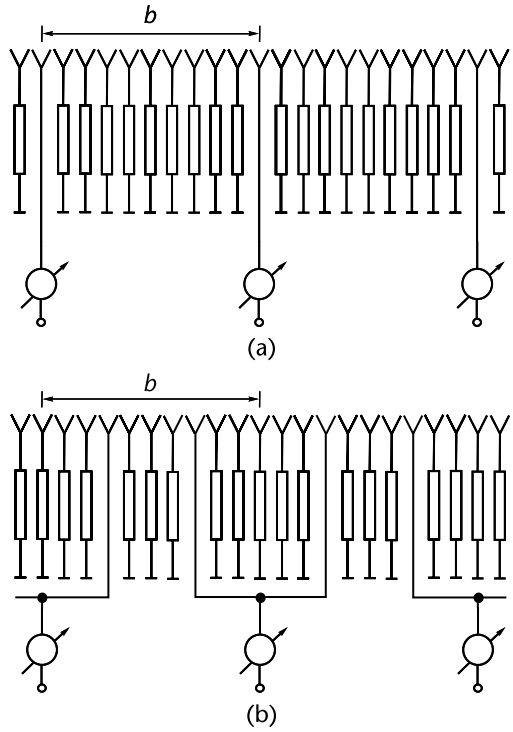

Figure 4.1 Networks of phased array antennas with reactively loaded radiators excited over free space from (a) one and (b) two controlled radiators in a cell.

lower than in the arrays using beam-forming networks. Therefore, the radiators in the networks shown in Figure 4.1 must be arranged sufficiently close to each other; hence, the number of the passive radiators must be sufficiently large.

If one controlled radiator in the array cell [Figure 4.1(a)] is insufficient for excitation of the subarray including radiators of no less than three cells, then two controlled radiators can be used and arranged near the cell edges as shown in Figure 4.1(b). Other approaches to forming subarrays of necessary extent are the arrangement of either the driven radiator above the cell aperture or passive scatterers in front of the driven radiator. The latter approach has been implemented in a C-band waveguide array [16] whose module is shown in Figure 4.2. The module consists of linear arrays of rectangular waveguides excited by H-plane horns having dielectric plates on the walls for providing a uniform amplitude distribution in the horn aperture [17, 18]. The waveguides contain feedthrough phase shifters for providing wide-angle beam scanning in a ±40° sector in the H-plane (horizontal plane in Figure 4.2). The space between the controlled linear arrays arranged with spacing 3.42λ is filled in with corrugated structures formed by short-circuited parallel-plate waveguides. The latter are effectively excited due to the scatterers installed in front of the linear arrays as well as in front of some passive parallel-plate waveguides. The positions of the short circuits determining the reactive load values as well as the positions of the scatterers have been selected so that each linear array forms a sector radiation pattern providing high gain in the sector of ±6.5° in E-plane.

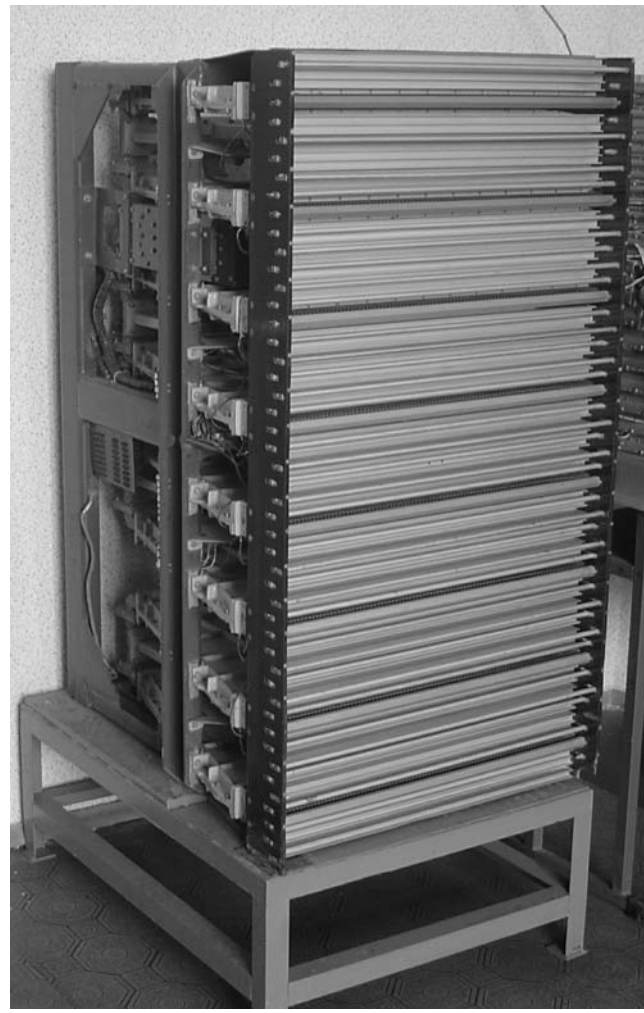

Figure 4.2 Phased array antenna module of C-band for wide-angle scanning in horizontal (H) plane and in sector of ±6.5° in vertical (E) plane.

The possibility of shaping the sector partial patterns (or controlled element patterns) in arrays employing reactively loaded radiators is studied in this chapter by using two models. The first model is a modulated corrugated structure excited by specified electric and magnetic currents arranged above the structure [19]. In the second model, a small portion of the parallel-plate waveguides are excited by TEM waves of specified amplitudes, while all the other wavegudes contain short circuits [20, 21] whose positions determine the values of the reactive loads.

4.2 Modulated Corrugated Structure Excited by Electric and Magnetic Currents

The infinite corrugated structure with modulation period b arranged in rectangular Cartesian coordinate system $0xyz$ is shown in Figure 4.3. The structure is

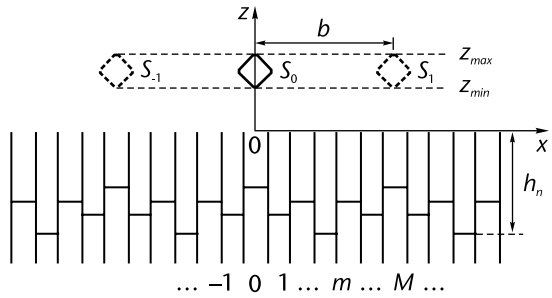

Figure 4.3 Modulated corrugated structure excited by electric and magnetic currents.

assumed to be perfectly conducting, uniform along the *y*-axis, and consisting of sort-circuited parallel-plate waveguides of identical width with infinitely thin walls. Let M be a specified number of waveguides per period, $a = b/M$ be the waveguide width, and h_m be distance from the aperture to the short circuit in the mth waveguide satisfying the condition of periodicity

$$h_{m+Mq} = h_m, \quad q = 0, \pm 1, \pm 2, \ldots \tag{4.1}$$

Of primary interest is the radiation pattern corresponding to excitation of the structure by local sources arranged, for instance, in region S_0 above the waveguide apertures. To solve the problem of such a local excitation, we will use a known approach that first solves a problem of quasi-periodic excitation and then uses a relation between the fields corresponding to both types of excitation (see Chapter 1 or [22, 23]).

4.2.1 Quasi-Periodic Excitation

Let the structure be excited by electric and magnetic currents located in a periodic system of regions S_q, where $q = 0, \pm 1, \pm 2, \ldots$, formed by parallel transfer of the region S_0 along the x-axis with period b in a strip $0 < z_{\min} \quad z \quad z_{\max}$ (Figure 4.3). We will assume that the current distribution is independent of y and that the currents of adjacent regions differ only by the factor $\exp(iU)$, where U is the phase difference determining the main lobe direction. So, we write the current distribution as

$$\boldsymbol{j}_p^{e,m}(U,x,z) = \sum_{q=} {}_q(x,z)\boldsymbol{j}^{e,m}(x \quad qb,z)e^{iqU} \tag{4.2}$$

where $\boldsymbol{j}^{e,m}(x,z)$ are vectors of the electric and magnetic current density in S_0 with nonzero components $j_x^e(x,z)$, $j_z^e(x,z)$, and $j_y^m(x,z)$, and

$${}_q(x,z) = \begin{cases} 1, (x,z) \quad S_q, \\ 0, (x,z) \quad S_q \end{cases}$$

is the characteristic function. The indicated current distribution corresponds to the case of H polarization defined in Chapter 1.

The total electromagnetic field to be determined may be expressed via the transverse component of the magnetic field H_y, which we represent in the form

$$H_y(U,x,z) = \psi(U,x,z) = \psi_0(U,x,z) + \psi^s(U,x,z) \tag{4.3}$$

where ψ_0 is the field created by currents (4.2) in the absence of the structure, and ψ^s is the field scattered by the structure.

The field ψ_0 being of interest for further operations in the regions $z < z_{\min}$ and $z > z_{\max}$ can be found via vector potentials determined by currents (4.2) as

$$A^{e,m}(U,x,z) = \frac{i}{4} \int_{S_0} [j^{e,m}(x\ ,z\ ) \quad \sum_{q=} e^{iqU} H_0^{(1)}(k\rho_q)]dS \tag{4.4}$$

where

$$\rho_q = \sqrt{(x \quad x \quad qb)^2 + (z \quad z\ )^2}$$

and $H_0^{(1)}(\ldots)$ is the Hankel function of first kind and zero order (the time dependence is assumed to be taken in the form $e^{\ i\omega t}$). Applying the Poisson's summation formula [24] to (4.4) as well as formulas (1.22) we obtain the following superposition of the Floquet modes

$$\psi_0(U,x,z) = \sum_{q=} B_q^{\pm}(U) e^{i\alpha_q x \pm i\Gamma_q z} \tag{4.5}$$

with amplitudes

$$B_q^{\pm}(U) = \frac{1}{2\Gamma_q b} \int_{S_0} (\alpha_q j_z^e \mp \Gamma_q j_x^e \quad k j_y^m / \eta_0) e^{\ i\alpha_q x\ \mp i\Gamma_q z}\ dS \tag{4.6}$$

and propagation constants

$$\begin{aligned} \alpha_q &= \frac{U + 2\pi q}{b} \\ \Gamma_q &= \sqrt{k^2 \quad \alpha_q^2} = i\sqrt{\alpha_q^2 \quad k^2} \end{aligned} \tag{4.7}$$

The upper and lower signs in (4.5) and (4.6) should be taken at $z > z_{\max}$ and $z < z_{\min}$, respectively.

When determining the scattered field ψ^s, we will suggest that only the dominant TEM modes are propagating in the waveguides (i.e., $a < \lambda/2$), while the short circuits are arranged sufficiently far from the apertures so that their interaction with the apertures over higher order modes arising at the apertures as a result of scattering is negligible.

When the structure is illuminated by field (4.5), the TEM-modes propagating in both directions are formed between the waveguide apertures and short circuits. Let us continuously extend the field of those modes in each waveguide down to , and

take into account the presence of the short circuits as follows. Let $A_m(U)$ be the amplitude of the TEM mode coming to the *mth* waveguide aperture. Then the amplitude of the mode going down from the aperture will be equal to $A_m(U)\exp(\ i2kh_m)$, so that the total transverse electric field vanishes on the short circuit. As a result, we reduce the initial problem of determining the scattered field ψ^s to two classical problems. The first corresponds to excitation of the structure without the short circuits by the Floquet mode field (4.5). The second corresponds to excitation of the same structure by the waveguide TEM modes coming to the apertures.

The first problem is solved similarly to the problem of a plane wave scattering considered, for example, in [25]. Applying the method of factorization [25] to our problem and using the principle of superposition, we obtain the field reflected from the waveguide apertures back to the free space region $z > 0$

$$\psi_1^s(U,x,z) = \sum_{q=} \frac{B_q(U)\alpha_q G_{q+}(\Gamma_q)}{(k+\Gamma_q)a} \sum_{n=} (\ 1)^n \frac{\alpha_{q+Mn} G_{q+}(\Gamma_{q+Mn}) e^{i\alpha_{q+Mn}x + i\Gamma_{q+Mn}z}}{(k+\Gamma_{q+Mn})(\Gamma_q+\Gamma_{q+Mn})\Gamma_{q+Mn}} \tag{4.8}$$

and the amplitudes of the TEM modes going from waveguide apertures in the region $z < 0$

$$T_m(U) = \sum_{q=} B_q(U) \frac{G_{q+}(\Gamma_q)}{G_{q+}(k)} \frac{\sin(\alpha_q a/2)}{\alpha_q a/2} e^{im\alpha_q a} \tag{4.9}$$

where

$$G_{q+}(\alpha) = k \frac{\cos(ka)\ \ \cos(\alpha_q a)}{\sin(ka)} \div^{1/2} \exp\ \frac{i\alpha a}{\pi} \ln 2 \div (1+\alpha/\Gamma_0) \prod_{p=1} \frac{(1+\alpha/\Gamma_{q+Mp})(1+\alpha/\Gamma_{q\ \ Mp})}{1+\alpha/\gamma_p} \tag{4.10}$$

is a function analytical and nonzero everywhere in the upper half-plane of complex variable α, and

$$\gamma_p = \sqrt{k^2\ \ (p\pi/a)^2} = i\sqrt{(p\pi/a)^2\ \ k^2}$$

are propagation constants of the waveguide modes. Changing the order and summation indices in (4.8), we rewrite the latter in a form more convenient for the further calculations:

$$\psi_1^s(U,x,z) = \sum_{q=} D_q(U) e^{i\alpha_q x + i\Gamma_q z} \tag{4.11}$$

where

$$D_q(U) = \frac{\alpha_q G_{q+}(\Gamma_q)}{(k+\Gamma_q)\Gamma_q a} \quad (-1)^n \frac{B_{q+Mn}(U)\alpha_{q+Mn}G_{q+}(\Gamma_{q+Mn})}{(k+\Gamma_{q+Mn})(\Gamma_q+\Gamma_{q+Mn})} \tag{4.12}$$

Consider now the second problem. Let the structure without the short circuits be excited by the TEM modes coming to the apertures with amplitudes $A_m(U)$ satisfying the condition

$$A_{m+Mq}(U) = A_m(U)e^{iqU} \tag{4.13}$$

resulting from (4.1) and (4.2). Taking into account (4.13), we represent the field exciting the structure in the form

$$\psi_2^i(U,x,z) = \sum_{m=0}^{M-1} A_m(U)e^{imu} \sum_{q=} \Psi_{m+Mq}(x,z)e^{i(m+Mq)u} \tag{4.14}$$

where $u = U/M$ and

$$\Psi_m(x,z) = \begin{cases} e^{ikz}, & |x - ma| < a/2 \\ 0, & |x - ma| > a/2 \end{cases} \tag{4.15}$$

Since

$$\sum_{p=0}^{M-1} e^{i2\pi p(n-m)/M} = \begin{cases} M, & n = m + Mq \\ 0, & n \neq m + Mq, \ q = 0, \pm 1, \ldots \end{cases}$$

then

$$\sum_{q=} \Psi_{m+Mq}(x,z)e^{i(m+Mq)u} = \frac{1}{M}\sum_{m=0}^{M-1} e^{-i2\pi pm/M} \sum_{q=} \Psi_q(x,z)e^{iq(u+2\pi p/M)}$$

and therefore

$$\psi_2^i(U,x,z) = \sum_{m=0}^{M-1} A_m(U)e^{imu} \sum_{p=0}^{M-1} \psi_0^i(u+2\pi p/M,x,z)e^{-i2\pi p/M} \tag{4.16}$$

where

$$\psi_0^i(u,x,z) = \sum_{q=} \Psi_q(x,z)e^{iqu} \tag{4.17}$$

The expression (4.16) relates the excitation fields (4.14) and (4.17). According to the principle of superposition, the same relation will take place for the scattered fields corresponding to the excitation fields. The solution of the problem corresponding to excitation of the parallel-plate waveguide array by field (4.17) is

known (see, for example, [22, 25]). Accounting for the notations used in (4.7), we write that solution as

$$\psi_0^s(u,x,z) = \sum_{q=} B_q(u) e^{i\alpha_{Mq}x + i\Gamma_{Mq}z} \tag{4.18}$$

where

$$B_q(u) = \frac{(-1)^q \alpha_{Mq}}{\Gamma_{Mq} a} \frac{2\sin(u/2)}{k - \Gamma_{Mq}} \exp\left\{ i \frac{(\Gamma_{Mq} - k)a}{\pi} \ln 2 \right\} \frac{k}{k + \Gamma_{Mq}} \frac{\Gamma_0 + \Gamma_{Mq}}{\Gamma_0 + k} \prod_{p=1} \frac{1 + k/\gamma_p}{1 + \Gamma_{Mq}/\gamma_p} \prod_{p=1} \frac{(1 + \Gamma_{Mq}/\Gamma_{Mp})(1 + \Gamma_{Mq}/\Gamma_{-Mp})}{(1 + k/\Gamma_{Mp})(1 + k/\Gamma_{-Mp})} \tag{4.19}$$

Using (4.16) and (4.18), we obtain the following expression for the field scattered by the array in the region $z > 0$

$$\psi_2^s(U,x,z) = \frac{1}{M} \sum_{m=0}^{M-1} A_m(U) e^{-imu} \sum_{p=0}^{M-1} e^{-i2\pi pm/M} \sum_{q=} B_q(u + 2\pi p/M) e^{i\alpha_{p+Mq}x + i\Gamma_{p+Mq}z} \tag{4.20}$$

where we have accounted for $\alpha_{Mq}(U + 2\pi p) = \alpha_{p+Mq}(U)$.

The amplitudes $A_m(U)$ in formula (4.20) are still unknown. To determine them, we will use a technique similar to that described in [1]. The TEM modes going down from the apertures are created not only by interaction between the waveguides as takes place in [1], but also due to the field (4.5) exciting the waves with amplitudes (4.9). Accounting for (4.13), we may express that fact for waveguide with number 0 in the following form

$$A_0 e^{-i2kh_0} = T_0 + \sum_{m=0}^{M-1} A_m \sum_{q=} C_{m+Mq} e^{iqU} \tag{4.21}$$

where C_m is the coefficient of coupling between two waveguides with the difference of their numbers equal to m. Carrying out some elementary transformation in (4.21), we may rewrite it as an algebraic equation:

$$A_0(U)[R_0(U/M) - e^{-i2kh_0}] + \sum_{m=1}^{M-1} A_m(U) R_m(U/M) = -T_0(U) \tag{4.22}$$

where

$$A_m(U) = A_m(U)e^{\ imU/M}$$
$$T_m(U) = T_m(U)e^{\ imU/M} \tag{4.23}$$
$$R_m(u) = \sum_{q=} C_{m+Mq}e^{i(m+Mq)u}$$

Considering similarly the waveguides with numbers 1, 2, . . . , M 1, we obtain M 1 more algebraic equations for $A_m(U)$

$$\sum_{m=0}^{n\ 1} A_m(U)R_{M+m\ n}(U/M) + A_n(U)[R_0(U/M) \quad e^{\ i2kh_n}] + \sum_{m=n+1}^{M\ 1} A_m(U)R_{m\ n}(U/M) = \quad T_n(U), \quad n = 1, 2, \ldots, M \quad 2 \tag{4.24}$$

$$\sum_{m=0}^{M\ 2} A_m(U)R_{m+1}(U/M) + A_{M\ 1}(U)[R_0(U/M) \quad e^{\ i2kh_{M\ 1}}] = \quad T_{M\ 1}(U) \tag{4.25}$$

To calculate functions (4.23) determining the matrix elements of (4.22), (4.24), and (4.25), we take advantage of the properties of the function

$$R(u) = \sum_{n=} C_n e^{inu} \tag{4.26}$$

which is the reflection coefficient of the parallel-plate waveguide array excited by field (4.17). Rewriting (4.26) in the form

$$R(u) = \sum_{m=0}^{M\ 1} \sum_{q=} C_{m+Mq}e^{i(m+Mq)u}$$

and replacing u by $u + 2\pi p/M$, $p = 0,1,2, \ldots, M$ 1, we obtain the following algebraic system

$$\sum_{m=0}^{M\ 1} R_m(u)e^{i2\pi pm/M} = R(u + 2\pi p/M) \tag{4.27}$$

Solving (4.27), we determine $R_m(u)$. To calculate function (4.26) itself, we may take advantage of the exact formula [22]

$$R(u) = e^{i2S(k)} \begin{cases} (k \quad \Gamma_0)/(k + \Gamma_0), & |u| \quad ka \\ \exp(\ 2i\,\mathrm{arctg}\,|\Gamma_0/k|), & |u| > ka \end{cases} \tag{4.28}$$

where

$$S(x) = \frac{ax}{\pi}\ln 2 + \sum_{n=1} \operatorname{arctg}\frac{x}{|\Gamma_{Mn}|} + \operatorname{arctg}\frac{x}{|\Gamma_{Mn}|} \quad \operatorname{arctg}\frac{x}{|\gamma_n|} \div \tag{4.29}$$

Formula (4.28) is convenient for performing calculations at $|u| \quad \pi$. If $|u| > \pi$, one may use its property of periodicity $R(u + 2\pi q) = R(u)$, $q = 0, \pm 1, \ldots$

Thus, the expression (4.20) and the subsequent algorithm yield the solution of the second problem. The total field scattered by the structure in the region $z > 0$ is determined by summation of the fields (4.11) and (4.20).

4.2.2 Radiation Pattern at Local Excitation

Let now the structure be excited by the current distribution $\boldsymbol{j}^{e,m}(x,z)$, localized only in the region S_0 (Figure 4.3). This distribution relates to the quasi-periodic distribution (4.2) by means of a linear operator of integration over phase U

$$\boldsymbol{j}^{e,m}(x,z) = \frac{1}{2\pi}\int_{\pi}^{\pi} \boldsymbol{j}_p^{e,m}(U,x,z)\,dU \tag{4.30}$$

According to the principle of superposition, the same relation will be valid for the fields corresponding to the current distributions (4.30) and (4.2). Therefore, the radiation pattern of the structure excited by the currents (4.30) may be expressed as follows:

$$F(\theta) = \frac{1}{2\pi}\int_{\pi}^{\pi} F_p(U,\theta)\,dU \tag{4.31}$$

where θ is the angle measured from the z-axis and $F_p(U,\theta)$ is the radiation pattern of the structure at excitation of it by currents (4.2). This pattern is determined by the field distribution at height $h > z_{\max}$ as follows

$$F_p(U,\theta) = \frac{e^{\ ikh\cos\theta}\cos\theta}{b} \quad \psi(U,x,h)e^{\ ikx\sin\theta}dx \tag{4.32}$$

Substituting ψ in (4.32) by the sum of fields (4.5), (4.11), and (4.19), we obtain

$$\begin{aligned} F_p(U,\theta) = {} & 2\pi e^{\ ikh\cos\theta}\cos\theta \\ & [B_q^+(U) + D_q(U)]e^{i\Gamma_q h}\delta(U \quad kb\sin\theta + 2\pi q) \\ & q= \\ & + \frac{1}{M}\sum_{m=0}^{M\ 1} A_m(U)\sum_{p=0}^{M\ 1} e^{\ i2\pi pm/M} \qquad B_q[(U+2\pi p)/M] \\ & q= \\ & e^{i\Gamma_{p+Mq}h}\delta[U \quad kb\sin\theta + 2\pi(p+Mq)] \end{aligned} \tag{4.33}$$

where $\delta(\ldots)$ is the delta function. Substitution of (4.33) in (4.31) yields final expression for the radiation pattern of the structure at local excitation of it

$$F(\theta) = B_0^+(kb\sin\theta) + D_0(kb\sin\theta) + \frac{1}{M}B_0(ka\sin\theta)\sum_{m=0}^{M\ 1} A_m(kb\sin\theta)\ \cos\theta \tag{4.34}$$

in which B_0^+ and D_0 are determined from (4.6) and (4.12), respectively, $A_m(U)$ are calculated as a result of solution of equations (4.22), (4.24), and (4.25), and B_0 is determined by formula

$$B_0(u) = \frac{2k}{k+\Gamma_0}e^{i[S(k)\ \ S(\Gamma_0)]}$$

resulted from (4.20) and (4.29). Note that the infinite series (4.12) converges so fast that accounting for only the zero order term is sufficient for calculation of D_0 at $z_{min} > a$.

4.2.3 Shaping of Sector Radiation Pattern

The expression (4.34) for the radiation pattern of the structure excited by localized sources as well as the algorithm developed earlier for calculating the coefficients used in (4.34) allow us to consider the problem of shaping the sector radiation pattern. Let the structure be excited by two filamentary Huygens elements arranged at height z_0 above the waveguide apertures and spaced at distance $2x_0$ from each other. Such a choice is made because the Huygens element is a simple and sufficiently good model of an aperture feed, and selection of the distance between the filaments allows us to control the field of illumination. The components of the feed current density are specified in the form

$$\begin{aligned} j_x^e(x,z) &= j_y^m(x,z)/\eta_0 \\ &= \frac{1}{2}b[\delta(x+x_0)+\delta(x\quad x_0)]\delta(z\quad z_0) \end{aligned} \tag{4.35}$$

$$j_z^e(x,z) = 0, \quad (\pm x_0, z_0)\quad S_0$$

where the relation between the amplitudes of the electric and magnetic currents has been chosen to steer the feed radiation pattern toward the structure. We will also assume that the structure is symmetric with respect to the coordinate system origin; that is,

$$h_{\ m} = h_m, \quad m = 0,1,2,\ldots \tag{4.36}$$

and therefore the radiation pattern of the structure will be an even function of the observation angle θ. This condition allows restricting the consideration of the pattern only by $\theta\quad 0$.

The problem of synthesis of the sector radiation pattern at the conditions indicated previously may be stated as follows: it is required to find such positions of the short circuits h_m, which provide minimum of the maximum pattern level in the region of the grating lobe movement τ_1 with respect to the minimum pattern level in the region of the main lobe scanning τ_0; that is, to find minimum of the following function of many variables

$$g(\boldsymbol{h}) = \max_{\theta \in \tau_1} |F(\theta)| / \min_{\theta \in \tau_0} |F(\theta)| \tag{4.37}$$

where $\boldsymbol{h}$ is the vector of the short-circuit positions that contains $1 + M/2$ components for even M or $(1 + M)/2$ components for odd M with accounting for the geometry of the structure (Figure 4.3) and symmetry relation (4.36). The half-width of the scan sector τ_0 is specified in the form

$$\theta_{\max} = \arcsin \frac{\lambda}{2\zeta b} \tag{4.38}$$

where $\zeta \quad 1$ is the element use factor (see Chapter 1 or [26]), which is also assumed to be specified.

The solution of the synthesis problem stated earlier has been obtained using a developed FORTRAN code including subroutines calculating the pattern (4.34) and the objective function (4.37), as well as a subroutine performing a search for a minimum of (4.37) on the basis of the method of deformable polyhedron described in [27]. Some results of the sector pattern synthesis are presented in Figure 4.4. The geometric parameters corresponding to the patterns are given in Table 4.1.

Note that as it follows from the system of equations (4.22), (4.24), and (4.25), as well as from expression (4.34), the pattern will not be changed if we add an entire number of half-wavelengths to the found positions of the short circuits. The nonshaded regions in Figure 4.4 correspond to the scan sector of the main lobe $(0 \quad \sin\theta \quad \sin\theta_{\max})$ as well as the regions of the grating lobe movement. The shaded regions were excluded from the consideration in the process of calculation of the objective function (4.37).

The presented examples show that the radiation pattern level in the grating lobe regions does not exceed –13 dB, which may be acceptable for some applications.

The results have shown that two spaced current filaments are preferable than one filament for the sector pattern synthesis at $z_0 > \lambda/2$. This feature can be explained as follows. The radiation pattern of the structure without the short circuits is determined by the first two terms in square brackets of (4.34). This pattern corresponding to one current filament exciting the structure is shown by the dashed curve 1 in Figure 4.4(c). As we see, this pattern normalized to the filament pattern maximum has rather high sidelobes. The use of two filaments arranged at an appropriate distance from each other allows significant reduction of the sidelobe level, as demonstrated by the dashed curve 2 in Figure 4.4(c). This, in turn, creates favorable conditions for shaping the sector flat-topped pattern corresponding to the third term in (4.34) depending on the short-circuit positions. The selection of filament spacing is performed as follows. The analysis of the first and second terms in (4.34) shows that they have a common factor $\cos(kx_0 \sin\theta)$. Therefore, if we choose

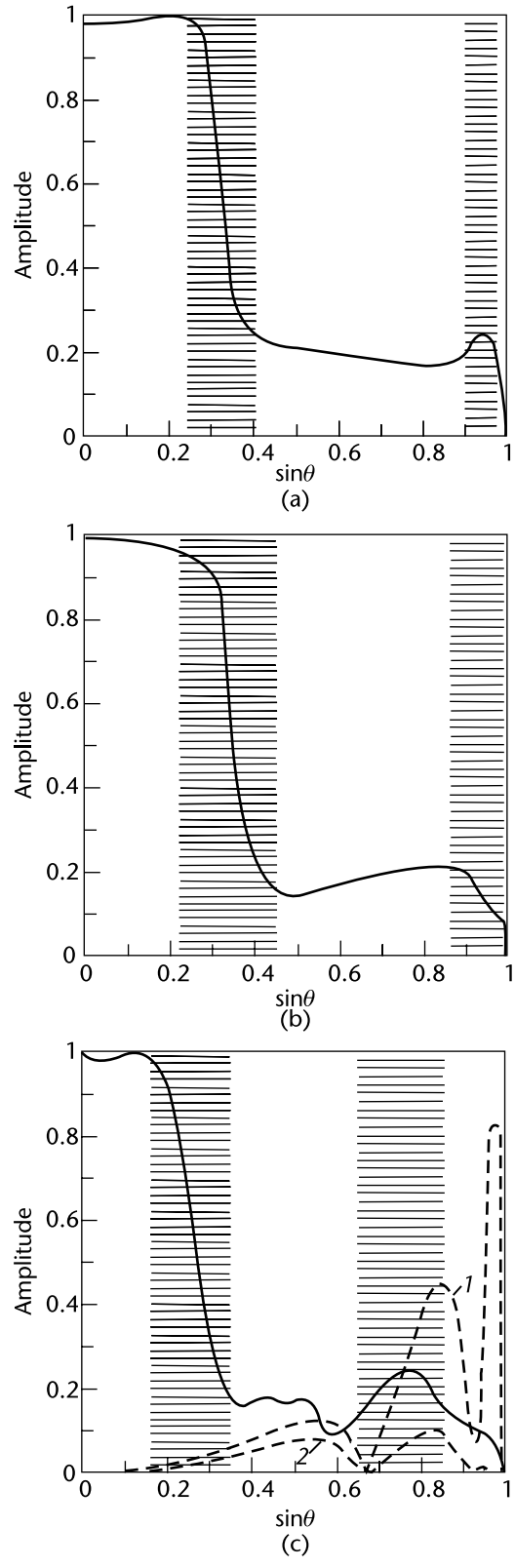

Figure 4.4 (a–c) Radiation patterns of the structure with parameters indicated in Table 4.1 at local excitation by currents (4.34).

Table 4.1 Geometrical Parameters Corresponding to the Radiation Patterns Shown in Figure 4.4

Figures	x_0/λ	z_0/λ	b/λ	M	ζ	h_m/λ	$m = 0, 1, \ldots, M/2$				
4.4(a)	0.000	0.20	1.5	10	1.4	0.474	0.585	0.620	0.531	0.832	0.580
4.4(b)	0.258	1.00	1.5	10	1.5	0.525	0.537	0.599	0.734	0.576	0.562
4.4(c)	0.255	1.33	2.0	10	1.6	0.691	0.578	0.587	0.700	0.621	0.629

$x_0 = \pi/(2k \sin\theta)$, where θ is the angle corresponding to the highest sidelobe position, the indicated factor vanishes in the direction of θ and the level of the other sidelobes gets low.

4.3 Modulated Corrugated Structure with Active Waveguides

The second model to be considered corresponds to the arrays with reactively loaded radiators schematically shown in Figure 4.1. The model is an infinite periodic structure of parallel-plate waveguides presented in Figure 4.5, where $b = (a + t)M$ is the period, a is the waveguide width, t is the waveguide wall thickness, $M = M + M$ is the total number of the waveguides on the period with M being the number of the active waveguides excited in the TEM modes of specified amplitude, and M is the number of the passive waveguides excited due to interaction with the active guides and between themselves over free space. The passive guides are provided with short circuits, the positions of which determine the values of the reactive loads. The short-circuit positions form a periodic function of the waveguide number; that is,

$$h_{m+Mq} = h_m, \quad m \quad M \ , \quad q = 0, \pm 1, \pm 2, \ldots \tag{4.39}$$

The waveguide walls and short circuits are assumed to be perfectly conducting.

The array element pattern here is the array pattern corresponding to excitation of the active waveguides located on only one period (in one array cell). The active guides of all the other cells are assumed to be loaded with matching resistances, as shown in Figure 4.5. Let the active waveguides of the central cell be excited by the TEM mode field that we write in the form

$$H_y^i(x,z) = \psi^i(x,z) = \sum_{m \ M} A_m \ _m(x,z) \tag{4.40}$$

where A_m is a specified amplitude and $_m(x,z)$ is the function defined by formula (4.15). Further, we will suppose that the waveguides are single-mode ones, and the

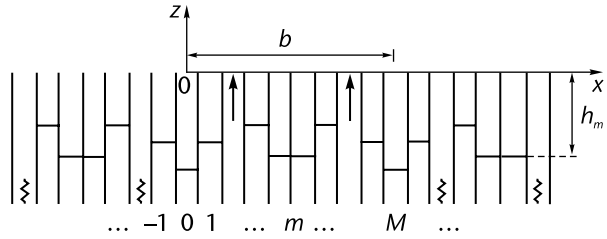

Figure 4.5 Modulated corrugated structure excited from active waveguides.

short circuits are arranged sufficiently far from the apertures so that their interaction with the apertures over evanescent higher order modes is negligible. At the indicated conditions, it is required to determine the array element pattern at excitation (4.40).

4.3.1 Analysis and Synthesis

We determine the array element pattern via the array pattern corresponding to excitation of all the active waveguides by the specified field

$$\psi_p^i(U,x,z) = \sum_{m\ M} A_m \sum_{q=} \psi_{m+Mq}(x,z)e^{iqU} \tag{4.41}$$

satisfying the condition of quasi-periodicity

$$\psi_p^i(U,x+b,z) = \psi_p^i(U,x,z)e^{iU} \tag{4.42}$$

and related with the field (4.40) by means of the transformation

$$\psi^i(x,z) = \frac{1}{2\pi}\int_{\pi}^{\pi} \psi_p^i(U,x,z)dU \tag{4.43}$$

Since the structure under consideration is periodic, the total field corresponding to excitation (4.41) will also satisfy the condition (4.42). In particular, formula (4.13) will be valid for the amplitudes of the TEM modes coming to the apertures of all the waveguides. With accounting for (4.13), the array pattern corresponding to quasi-periodic excitation (4.41) is determined by formula

$$F_p(U,\theta) = 2\pi f(\theta)\sum_{m=0}^{M\ 1} A_m(U)e^{\ imka\ \sin\theta} \sum_{q=} \delta(U \quad kb\sin\theta \quad 2\pi q) \tag{4.44}$$

where $a = b/M$, θ is the observation angle measured from the z-axis, $f(\theta)$ is the pattern of a waveguide embedded in the array without short circuits, and $\delta(\ldots)$ is the delta function. Applying the operation (4.43) to the pattern (4.44), we obtain the array element pattern corresponding to excitation (4.40)

$$F(\theta) = f(\theta)\sum_{m=0}^{M\ 1} A_m(kb\sin\theta) \tag{4.45}$$

where $A_m(U) = A_m(U)\exp(\ imu)$ and $u = U/M$.

The amplitudes of the backward waves going from the passive waveguide apertures to the short circuits are related to the forward wave amplitudes $A_n(U)$ as $A_n(U)\exp(-i2kh_n)$, where $n \quad M$, and determined via the coupling coefficients by formula

$$A_n(U)\exp(\ i2kh_n) = \sum_{m=0}^{M\ 1} A_m(U) \sum_{q=} C_{m\ n+Mq}e^{iMqu} \tag{4.46}$$

where C_n is the coupling coefficient corresponding to a pair of waveguides, the difference of numbers of which is equal to n. Multiplying (4.46) by $\exp(\ imu)$ and carrying out simple operations, we obtain the following system of linear algebraic equations for $A_m(U)$:

$$\sum_{m\ M} A_m(U)[R_{m\ n}(u) \quad \delta_{mn}\exp(\ i2kh_m)] = \sum_{m\ M} A_m(U)R_{m\ n}(u) \tag{4.47}$$

where $n \quad M$ and δ_{mn} is the Kronecker symbol. The functions $R_n(U)$ are determined by (4.23) and calculated by means of solution of the linear algebraic system (4.27). The values of the reflection coefficient $R(U)$ standing in the right-hand side of (4.47) and corresponding to the array without the short circuits are calculated either by using rigorous formula (4.28) valid for the walls of zero thickness or by using the mode-matching method [28, 29] or the integral equation method [1] in the general case. Note that the system (4.47) differs from the system of equations (4.22), (4.24), and (4.25) mainly by the right-hand side, determined by amplitudes of the waves excited from specified sources. In the case in question, the indicated amplitudes are specified in (4.40), while those considered in Section 4.2 are determined by electric and magnetic currents arranged above the structure.

Thus, the calculation of the array element pattern (partial array pattern) at specified positions of short circuits is reduced to successive solution of two linear algebraic systems (4.27) and (4.47). The dimension of the former equals the total number M of the waveguides in the cell, while that of the latter equals the number M of the passive waveguides in the cell.

The technique described here is a part of the procedure designed for solving the problem of synthesis of the array with the sector element pattern. We state the synthesis problem as follows. Provided that the array period b, positions and number

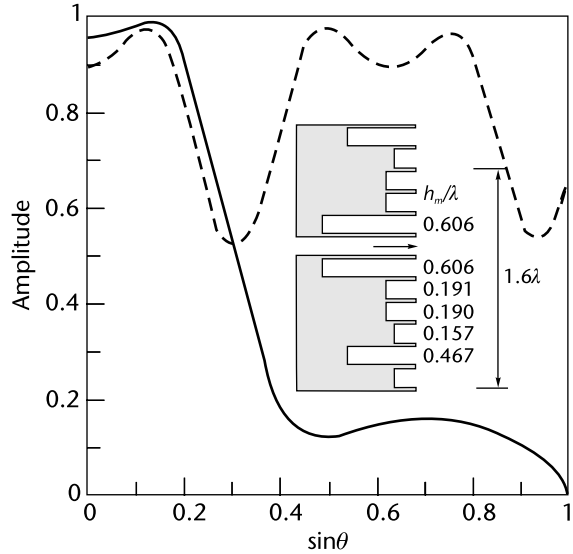

Figure 4.6 Element pattern (——), radiation efficiency (– – –), and geometry of array with $b = 1.6\lambda$, $M = 10$, $M = 1$, and $t = 0$.

of active and passive waveguides on the period, amplitudes of incident waves in the active waveguides, and scan sector τ_0 width $\theta \quad \theta_{\max} < \arcsin[\lambda/(2b)]$ are specified, it is required to find the short-circuit positions in the passive waveguides, at which the objective function

$$g(\boldsymbol{h}) = \min_{\theta \ \tau_0} |F(\theta)| \tag{4.48}$$

achieves its maximum value. We will also suppose that, together with the condition of periodicity (4.39), the structure is mirror-symmetric with respect to the middle of the array cell.

4.3.2 Calculated and Measured Results

Some results of the synthesis of the waveguide arrays with corrugated structures [21, 30–32] are presented in Figures 4.6 through 4.9. Numerical experiments have shown that the sector element patterns of relatively good quality in arrays with period from one to two wavelengths may be obtained using only one active waveguide per period. Two active guides in each cell should be used for array periods from two to four wavelengths. The total number of the waveguides in each cell should be chosen so that the waveguide width is of the order of 0.1λ to 0.2λ.

To characterize the array match to free space when scanning, we use the array radiation efficiency determined by formula [21]

$$\eta(U) = 1 \quad \frac{\sum_{n \ M} |R_{0n}(U)|^2}{\sum_{n \ M} |A_n|^2} \tag{4.49}$$

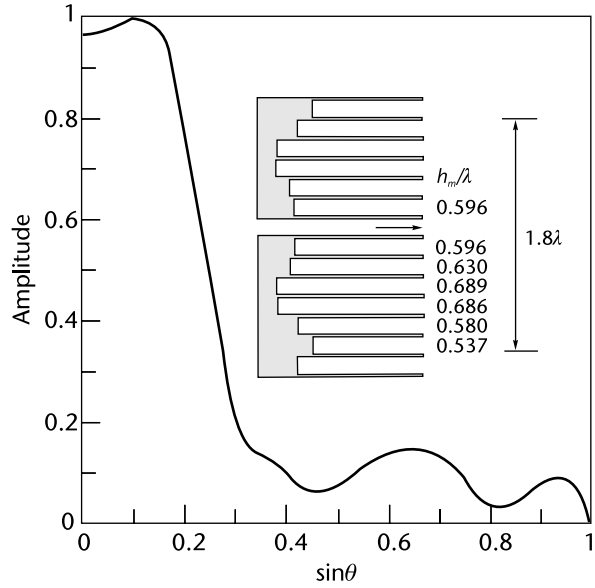

Figure 4.7 Element pattern and geometry of array with $b = 1.8\lambda$, $M = 12$, $M = 1$, and $t = 0$.

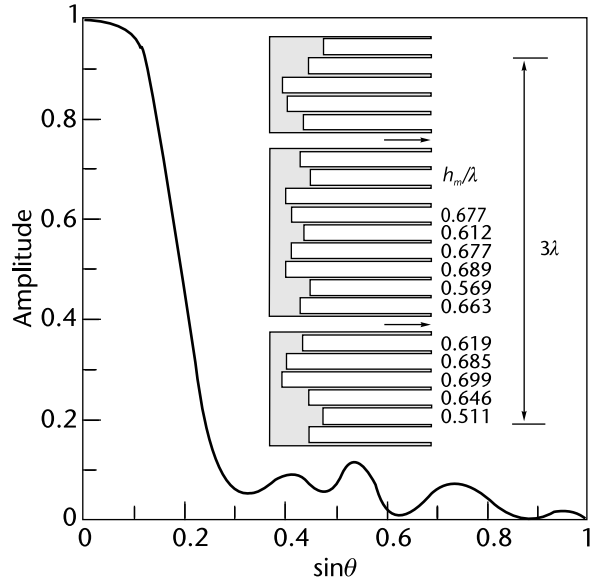

Figure 4.8 Element pattern and geometry of array with $b = 3\lambda$, $M = 20$, $M = 2$, and $t = 0$.

where

$$R_{0n}(U) = e^{imu} \sum_{m=0}^{M\ 1} A_m(U) R_{m\ n}(u) \tag{4.50}$$

are complex amplitudes of the TEM waves reflected back from the apertures of the active waveguides. The calculated radiation efficiencies (4.49) are shown in Figures 4.6 and 4.9 by dashed lines. These results show that the sector element patterns can be realized at relatively good match of the array to free space.

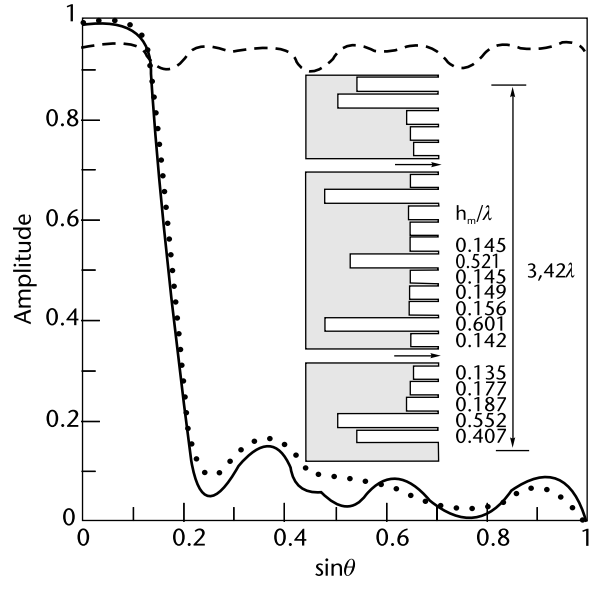

Figure 4.9 Calculated (——) and measured (· · · ·) element patterns, radiation efficiency (– – –), and geometry of array with $b = 3.42\lambda$, $M = 22$, $M = 2$, and $t = 0.035\lambda$.

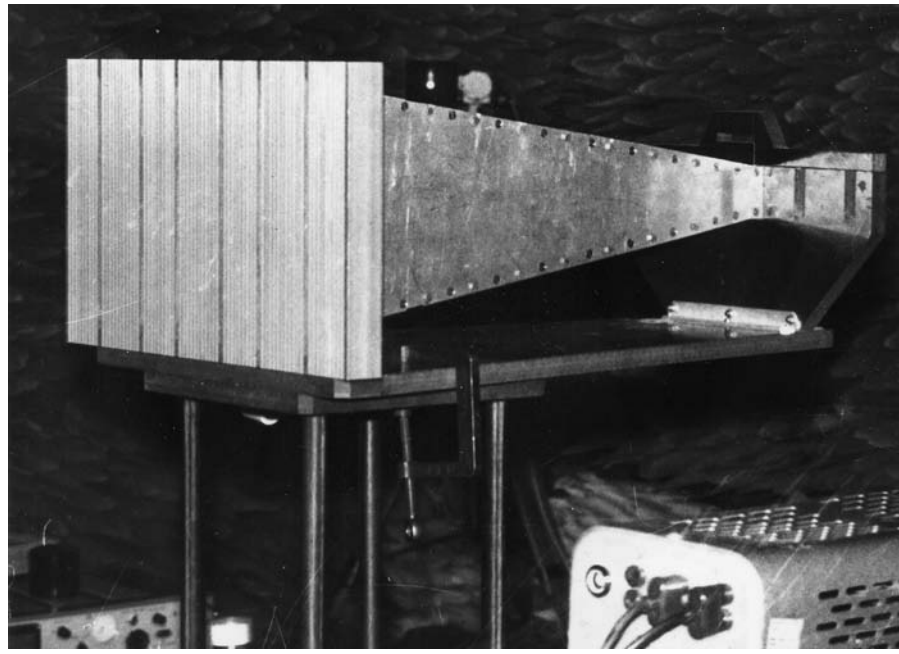

Figure 4.10 Breadboard of a C-band array with modulated corrugated structure.

The theoretical results obtained for the array with period $b = 3.42\lambda$ have been used for the development of an experimental breadboard for a C-band array shown in Figure 4.10. The corrugated structure comprises three array cells in the E-plane. It is excited through a two-channel power divider and two H-plane horns. The lateral slots corresponding to active waveguides of the structure are provided with matching loads. The measured radiation pattern of the central array element is shown in Figure 4.9 by a dotted line. We can see good agreement between the calculated and measured results in the region of the sector beam and only small difference between the results in the sidelobe radiation region. These results characterize good agreement between the theoretical model and real design.

References

[1] Amitay, N., V. Galindo, and C. P. Wu, *Theory and Analysis of Phased Array Antennas*, New York: Wiley-Interscience, 1972.

[2] Seryakov, Y. N., "Active Transmitting Array Using Mutual Coupling of Radiators for Sinchronization and Phasing of Self-Excited Oscillators," *Proc. of the Moscow Aviation Institute*, D. I. Voskresensky, (ed.), No. 203, 1970 (in Russian).

[3] Cullen, A. L., "Phase-Interpolation Locking: New Technique for Beam-Steered Active Antennas," *Electronics Letters*, Vol. 10, No. 6, 1974, pp. 81–82.

[4] Hessel, A., and G. H. Knittel, "A Loaded Ground Plane for the Elimination of Blindness in a Phased-Array Antenna," *1969 IEEE Group on Antennas and Propagation Intl. Symp. Digest*, Vol. 7, 1969, pp. 163–169.

[5] Sibille, A., "Reactively Loaded Adaptive Circular Arrays for Wireless Communications," *1998 IEEE Intl. Antennas Propagat. Symp. Dig.*, Vol. 36, June 1998, pp. 2232–2235.

[6] Harrington, R. F., and J. R. Mautz, "Control of Radar Scattering by Reactive Loading," *IEEE Trans. on Antennas and Propagation*, Vol. 20, No. 4, July 1972, pp. 446–454.

[7] Chaplin, A. F., *Analysis and Synthesis of Antenna Arrays*, Lvov, Ukraine: Vishcha Shkola, 1987 (in Russian).

[8] Chaplin, A. F., and V. F. Makkaveyeva, "Synthesis of an Array of Impedance Filaments," *Izvestiya Vuzov—Radiofizika*, Vol. 20, No. 2, 1977, pp. 274–279 (in Russian).

[9] Luzwick, J., and R. F. Harrington, "A Reactively Loaded Aperture Antenna Array," *IEEE Trans. on Antennas and Propagation*, Vol. 26, No. 4, July 1978, pp. 543–547.

[10] Arndt, F., et al., "Generalized Moment Method Analysis of Planar Reactively Loaded Rectangular Waveguide Arrays," *IEEE Trans. on Antennas and Propagation*, Vol. 37, No. 3, March 1989, pp. 329–338.

[11] Seth, D. P. S., and Y. L. Chow, "On Linear Parasitic Array of Dipoles with Reactive Loading," *IEEE Trans. on Antennas and Propagation*, Vol. 21, No. 3, May 1973, pp. 286–292.

[12] Harrington, R. F., "Reactively Controlled Directive Arrays," *IEEE Trans. on Antennas and Propagation,* Vol. 26, No. 3, May 1978, pp. 390–395.

[13] Kondratiev, A. S., "An Elementwise Synthesis Method for Reactively Loaded Antenna Arrays," *Proc. Millennium Conference on Antennas and Propagation*, Vol. I, Davos, Switzerland, April 9–14, 2000, p. 194.

[14] Chen, C. C., and Y. P. Liu, "Suppression of Grating Lobes by Parasitic Array Elements," *1975 IEEE AP-S Int. Symp. Digest*, Vol. 13, June 1975, pp. 185–188.

[15] Naymushin, M. P., B. S. Sobolev, and A. A. Avksentiyev, "Application of Passive Elements in Antenna Arrays," *Antennas and Microwave Blocks of Radiotechnical Devices*, Sverdlovsk, Russia: Ural Polytechnic Institute Press, 1976, pp. 42–47 (in Russian).

[16] Dubrov, Y. B., V. D. Korotkov, and S. P. Skobelev, "Antenna Array for Scanning in a Limited Sector," SU Author's Certificate No. 1541692, Int. Cl. H 01 Q 21/00, 1989.

[17] Yegorov, Y. V., *Partially Filled Rectangular Waveguides*, Moscow: Sovetskoye Radio, 1967 (in Russian).

[18] Tsandoulas, G. N., and W. D. Fitzgerald, "Aperture Efficiency Enhancement in Dielectrically Loaded Horns," *IEEE Trans. on Antennas and Propagation,* Vol. 20, No. 1, January 1972, pp. 69–74.

[19] Skobelev, S. P., "Analysis and Synthesis of a Modulated Corrugated Structure Excited by Electric and Magnetic Currents," *Izvestiya Vuzov—Radiofizika*, Vol. 27, No. 12, 1984, pp. 1557–1566 (in Russian).

[20] Korotkov, V. D., and S. P. Skobelev, "Radiators with Overlapped Apertures for Scanning Antennas," *Proc. All-Union Symp. on Wave Diffraction and Propagation*, Vol. 2, Tbilisi, Georgia, 1985, p. 295 (in Russian).

[21] Korotkov, V. D., and S. P. Skobelev, "Formation of Sector-Shaped Element Directivity Patterns in Antenna Arrays with Ribbed Structures," *Journal of Communications Technology and Electronics*, Vol. 39, No. 9, 1994, pp. 108–113.

[22] Mittra, R., and S. W. Lee, *Analytical Techniques in the Theory of Guided Waves*, New York: Macmillian Company, 1971.

[23] Ilyinsky, A. S., and A. G. Sveshnikov, "Numerical Methods in the Problems of Diffraction on Nonuniform Periodic Structures," *Collective Volume of Scientific-Methodical Papers on Applied Electrodynamics*, No. 1, 1977, pp. 51–93 (in Russian).

[24] Korn, G. A., and T. M. Korn, *Mathematical Handbook*, 2nd ed., New York: McGraw-Hill, 1968.

[25] Weinshtein, L. A., *The Theory of Diffraction and the Factorization Method*, Boulder, CO: Golem, 1969.

[26] Patton, W., "Limited Scan Arrays," in *Phased Array Antennas: Proc. 1970 Phased Array Symp.*, A. A. Oliner and G. A. Knittel, (eds.), Dedham, MA, 1972, pp. 254–270.

[27] Himmelblau, D. M., *Applied Nonlinear Programming*, New York: McGraw-Hill, 1972.

[28] Clarricoats, P. J. B., and K. R. Slinn, "Numerical Solution of Waveguide-Discontinuity Problems," *IEE Proc.*, Vol. 114, No. 7, 1967, pp. 878–886.

[29] Diamond, B. L., "A Generalized Approach to the Analysis of Infinite Planar Array Antennas," *IEEE Proc.*, Vol. 56, No. 11, 1968, pp. 1837–1851.

[30] Korotkov, V. D., S. P. Skobelev, and Y. B. Dubrov, "A Linear Antenna Array for Scanning in a Limited Sector," SU Author's Certificate No. 1337957, Int. Cl. H 01 Q 21/00, 1987 (in Russian).

[31] Korotkov, V. D., S. P. Skobelev, and Y. B. Dubrov, "A Linear Antenna Array for Scanning in a Limited Sector," SU Author's Certificate No. 1337956, Int. Cl. H 01 Q 21/00, 1987 (in Russian).

[32] Korotkov, V. D., S. P. Skobelev, and Y. B. Dubrov, "A Linear Antenna Array for Scanning in a Limited Sector," SU Author's Certificate No. 1337955, Int. Cl. H 01 Q 21/00, 1987 (in Russian).

CHAPTER 5

Waveguide Arrays with Protruding Dielectric Elements

As shown in Chapter 4, the natural mutual coupling between array radiators over free space can be effectively used for the formation of overlapped subarrays with sector radiation patterns. The feeding system of the subarrays with reactively loaded radiators in this case is significantly simplified in comparison with the feeding systems based on the multiport beam-forming circuits considered in Chapter 2. However, sector patterns of high quality can be formed only at sufficiently strong interelement interaction. Realization of such interaction between linear dipoles or open-ended waveguides considered in Chapter 4 requires the use of large number of the indicated radiators densely arranged in each array cell. There exists another class of radiators between which strong interaction can be realized. This class includes radiators of longitudinal type, in particular, dielectric rods. Such radiators, being sections of open transmitting lines, can support traveling waves, which provide the required interaction. Since the interaction occurs with wave traveling along the radiator, the coupling is mainly transferred in the direction of the wave movement. Therefore, unlike the arrays of open-ended waveguides or dipoles, the interaction between inputs of dielectric rods is considerably weaker, and that is their positive feature. Another positive feature is the possibility of using only one longitudinal element in the array cell with transverse dimensions up to one wavelength and a half, and this may be simpler than a few reactively loaded waveguides or dipoles in each cell. Moreover, the design of such a radiating structure may be very simple because a dielectric radiator is just an extension of waveguide filling protruding beyond the aperture.

5.1 Waveguide-Dielectric Arrays and Structures

Array antennas with dielectric radiators have been known since 1950s. A laboratory breadboard of a scanning array consisting of four hollow dielectric bars with waveguide excitation designed in 1955 is described in [1]. Paper [2] of 1963 (see also [3]) presents results of a study demonstrating shaping a flat-topped pattern of ±32° width corresponding to excitation of the central element in a linear five-element array of polystyrene rods of 6λ length arranged with 0.75λ element spacing, where λ is the operating wavelength. Application of dielectric protrusions for improvement of waveguide array match with free space is studied in [4] of 1967. A nine-element linear array of ceramic rods operating in the X-band is described in [5]. Reference [6] describes shaping of a sector element pattern in an infinite array of dielectric plates arranged on a screen and excited by specified currents. There has

been demonstrated a sector pattern of ±30° width shaped at plate height of 3.4λ and element spacing of λ, as well as a sector pattern of ±21° width shaped at plate height of 6.8λ and element spacing of 1.35λ. The mechanism of shaping flat-topped partial patterns in arrays of dielectric-rod elements is discussed in [7, 8], using an approximate approach to calculation of the dielectric structure eigenmodes and without accounting for real conditions of the rod excitation. Survey [9] contains cases of applications of dielectric rod radiators in a number of X-band mobile radar arrays for shaping flat-topped element patterns. In particular, an element pattern of ±42° width is formed in the principal planes of one of the hexagonal radar array with element spacing of 0.755λ.

One of the relatively recent developments in the area in question is a K_a-band array [10] consisting of large-aperture phased transmit/receive modules of reflective type [11]. One such module is shown in Figure 5.1(a). The module has transverse dimension of about 70λ and comprises about 3,600 waveguide-rod radiators arranged in a hexagonal lattice with element spacing of 1.1λ. The indicated spacing has been dictated by transverse dimensions of ferrite phase shifters [12] used in the array. The radiating structure of the module was designed experimentally [13] using a small breadboard shown in Figure 5.1(b). The diameter of the circular waveguide and, respectively, a protruding dielectric rod having cylindrical-conical shape was selected to provide the best match of the array to free space, while the protrusion length was determined to form a flat-topped element pattern suppressing the array factor grating lobes appearing in the visible space when scanning the main beam. As a result, there was obtained a flat-topped element pattern of width ±25° in the principal array planes. The module [11] has become a base for development of a self-dependent radar [14], where the initial module feed has been replaced by a monopulse one. Another recent example demonstrating application of the dielectric rods is an active phased array antenna designed for a stratospheric communication system considered in [15].

Another type of dielectric radiator for arrays of the K_a and higher frequency bands where the rod radiator dimensions are small has been proposed in [13, 16]. This radiator is an integrated element of a perforated dielectric plate 2 shown in Figure 5.2(a, b), which is arranged on a metallic plate 1 having waveguide channels. The lower face of the dielectric plate has protrusions 3 shown in Figure 5.2(a), where the plate 2 is depicted in its elevated position. The indicated protrusions enter the waveguide channels in plate 3 and serve as matching elements between the waveguides and dielectric radiators. The holes in the plate forming the dielectric radiators are performed in such a way that their axes are placed between the axes of the waveguide channels. The upper face of the dielectric plate has dimples arranged just on the waveguide axes serving for matching the plate to free space. The element patterns of the array with a polyethylene plate corresponding to excitation of the central waveguide in the TE_{11} mode of circular polarization measured in the horizontal and vertical planes are shown in Figure 5.2(c). These patterns are close to the patterns of the corresponding dielectric rod array element available in [14].

Note that the holes in the plate may be nonreach-through ones [13, 16]. The function of the dielectric radiators in this case is combined with the function of a dielectric radome. One of the modifications of such a structure in the form of the rectangular bars supporting a dielectric layer has been analyzed in [17].

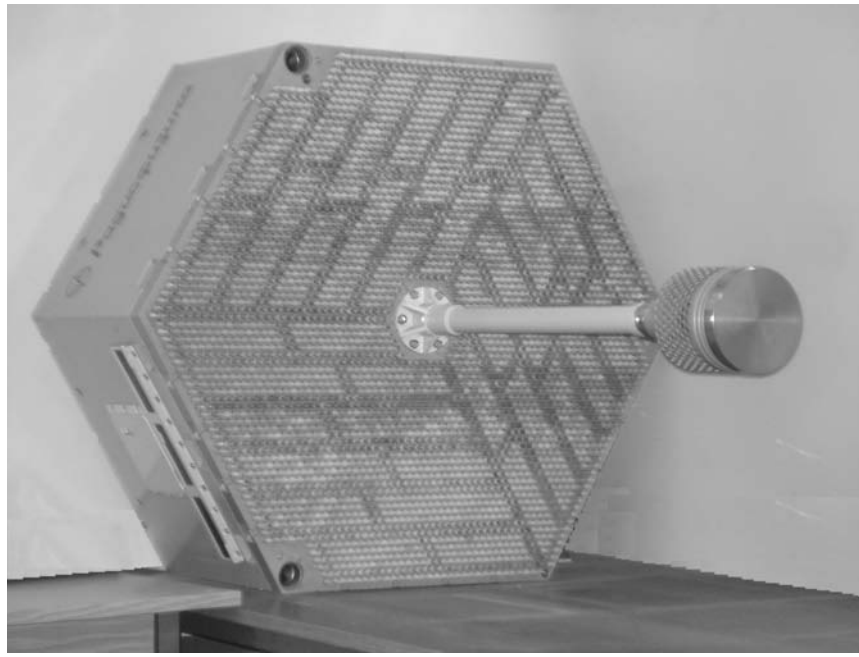

(a)

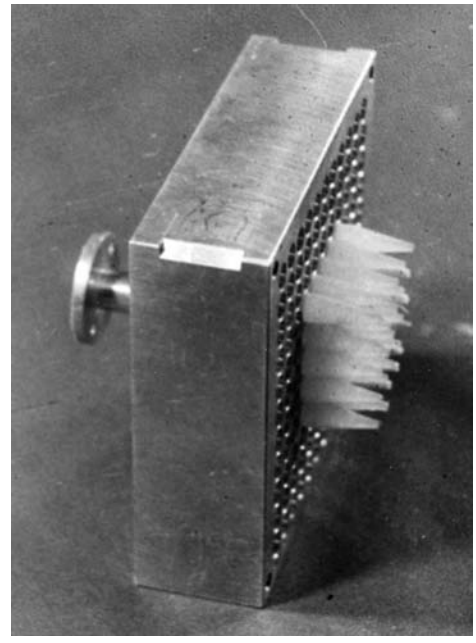

(b)

Figure 5.1 (a) Module of K_a-band waveguide-rod array of reflective type [10], and (b) a breadboard used for optimization of the radiating structure.

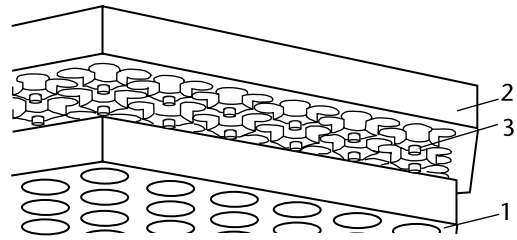

(a)

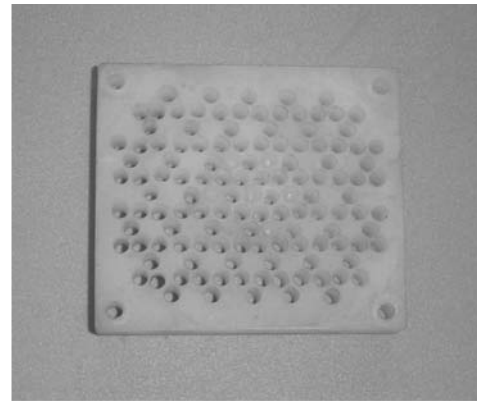

(b)

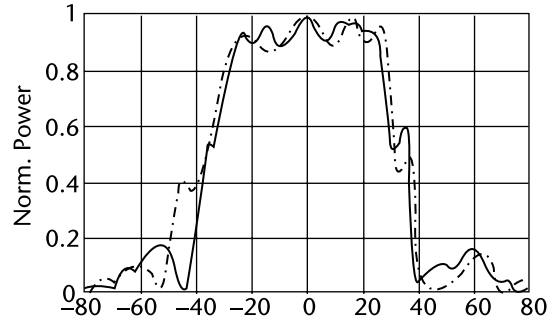

(c)

Figure 5.2 (a) Sketch of circular waveguide array with dielectric structure, (b) photograph of polyethylene structure, and (c) measured central element power pattern in horizontal (——) and vertical (– • – • –) planes.

5.2 Overview of the Methods and Results

The attractiveness of using dielectric elements protruding from waveguides as phased array radiators initiated and stimulated development of the methods for analysis of the arrays with such elements in rigorous statement of the problem over a few latest decades. The literature describes a few methods that can be applied to solution of the problem.

5.2.1 Mode-Matching Method

If the protruding dielectric elements are longitudinally uniform, the problem may be solved by the method of projective matching of the fields on the boundaries of the adjacent regions, for which it is necessary to know their eigenmodes and propagation constants. The eigenmodes of rectangular and circular waveguides, as well as the vector Floquet modes for representation of fields near periodic structures, are well known (see Chapter 1 or, for instance, [18]). The eigenmode parameters for periodic dielectric structures are determined by numerical methods. Determination of the propagation constants with high accuracy in two-dimensional problems for arrays of dielectric plates considered in [19, 20] from relatively simple dispersion equations can be done without great difficulties. In three-dimensional cases, the problem becomes significantly more difficult. The problem for periodic structures of dielectric cylinders may be reduced to determination of eigenvalues and eigenvectors for matrices of high order. Such matrices have been obtained using the Galerkin method in [21] on the basis of the Maxwell operator and in [22] on the basis of transverse magnetic field strength components. Some algorithms of the mode-matching method for arrays of circular waveguides with protruding cylindrical rods are described in [23, 24]. The numerical results presented in [18, 20, 23, 25] are obtained for arrays with relatively small element spacing from 0.5λ to 0.68λ. The studies mainly concerned the array matching to free space by means of selecting the protruding element parameters, as well elimination of the blindness effects. The problem of shaping of the flat-topped element patterns has not been considered.

If the protruding array elements are not longitudinally uniform (an example is conical rods), such arrays may be analyzed using the step-wise approximation of the elements with subsequent application of the mode-matching method, as it has been proposed in [24], where the reflection coefficient for an array of circular waveguides with two-step protruding cylindrical elements has been calculated as an example. A similar approach has been described in [25].

5.2.2 Incomplete Galerkin Method

This method allows reduction of the problem to systems of ordinary differential equations for coefficients of expansion of the fields in the cross-section of a dielectric structure. An algorithm developed on its basis is described in [26, 27], though it does not present any numerical results for arrays of protruding rods. A modification of the algorithm for the case of uniform cylindrical rods is presented in [28, 29], where the problem is again reduced to determination of the propagation constants for the waves in the dielectric structure. The results obtained in [28] relate to the same arrays as those considered in [23]. The array element pattern shape in [28, 29] has not been studied. The algorithm mentioned earlier has been applied in [30] to waveguide arrays with conical rods. The calculated results for the matching performance have been presented for a hexagonal array with element spacing of 0.64λ. The length and relative permittivity of the conical rods protruding from the waveguides are about 0.5λ and 2.3, respectively. The diameter of the waveguides is 0.46λ.

An algorithm based on the cross-section method that is similar to the incomplete Galerkin method has been developed in [31] for analysis of parallel-plate waveguide arrays with dielectric inserts and protrusions of arbitrary shape. The presented results concern improvement of the array match by means of selecting the dielectric plate parameters arranged on the waveguide flanges. One example of shaping a quasi-sector element pattern is also given; however, the pattern width is almost twice as narrow as the width of the ideal sector element pattern corresponding to the specified array period.

5.2.3 Projective Resonator Method

The projective resonator method has been applied in [32] for solution of a three-dimensional problem for an array of waveguides with protrusions of arbitrary shape. The electric field in a volumetric periodic cell containing the protrusion is represented by an expansion over the eigenmodes of a rectangular resonator with upper perfect magnetic wall, while the magnetic field is expanded over the eigenmodes of a rectangular resonator with upper perfect electric wall. The eigenmodes also satisfy the Floquet boundary conditions on the sidewalls of the resonator. The indicated expansions are substituted in the Maxwell equations written for the cell in question, and the resulting expressions are projected on the same basis functions. The process of projection accounts for conditions of matching the fields in the resonator to the waveguide modes in the waveguide aperture and to the Floquet modes in free space. As a result, the problem is reduced to a system of linear algebraic equations for unknown coefficients of expansion. Reference [32] contains all the necessary relations; however, no numerical results have been presented.

5.2.4 Method of Surface Integral Equations and Method of Auxiliary Sources

No publications where the former method is applied to the analysis of waveguide array with protruding dielectric elements themselves are known by the author. However, the method of surface integral equations has been applied to analysis of similar structures comprising dielectric-resonator elements as described in [33, 34] and in the papers referenced there. This method involves all the components of the corresponding tensor Green's functions containing singularities, and that feature makes the algorithm of calculation rather cumbersome.

A simpler alternative excluding the Green's function singularities and requiring no integration is the method of auxiliary sources. Reviews of the problems solved using that method and its modifications can be found in [35–37]. The first application of the method to the problems associated with array antennas seems to be described in [38] considering an array of parallel-plate waveguides with an array of obstacles arranged in front of the waveguide apertures. Further modifications of the method have been developed in [35, 39, 40], where first solutions have been obtained to the two-dimensional problems for parallel-plate waveguide arrays with protruding dielectric elements of arbitrary shape with smooth boundary. The influence of the protrusion shape on the array performance, along with shaping of a sec-

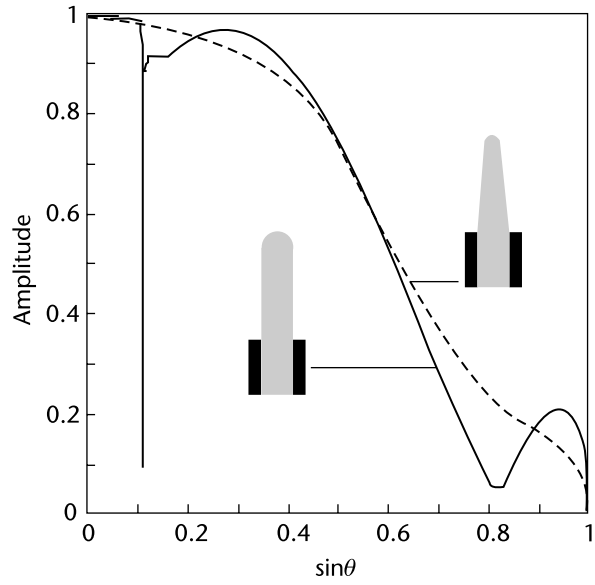

Figure 5.3 Element patterns for array [35] with element spacing 0.9λ, protrusion relative permittivity 2, height 1.4λ, width at the base 0.6λ, radius of smoothing at the top 0.3λ, and 0.15λ.

tor element pattern, has been demonstrated, as shown in Figure 5.3 as an example. A generalization of the method for a three-dimensional case of a circular waveguide array with axially symmetric rods of smooth shape is described in [41] using ring electric and magnetic currents as auxiliary sources.

5.2.5 Method of Integral Equations for Polarization Currents

Besides the integral equations for equivalent surface electric and magnetic currents mentioned earlier, the problem may also be formulated in the form of integral equations for polarization currents in protruding dielectric elements combined with projective matching of the fields in the waveguide apertures. The first algorithms on this basis for solution of two-dimensional problems have been developed in [42, 43]. Then, such an approach has been further developed in [44, 45] for the case of E-polarization and in [46] for the case of H-polarization. Geometry of the structure considered in [44–46] is shown in Figure 5.4(a). Simplification of the algorithms for calculation has been achieved there by means of involving eigenfunctions of appropriate rectangular resonators.

The papers [42–46] (see also Chapter 8 in [47]) contain results of shaping sector element patterns by means of selection of the protrusion parameters. One of the examples corresponding to the case of H-polarization is given in Figure 5.4(b). In addition, [45] demonstrates the influence of dissipation loss in the protrusions on the blindness effects that may take place in such arrays. No algorithms based on the method of volume integral equations have been developed for the three-dimensional case of the waveguide-rod arrays. However, a relational problem of plane electromagnetic wave scattering by absorbing periodic structures with pyramidal elements has been considered and solved in [48].

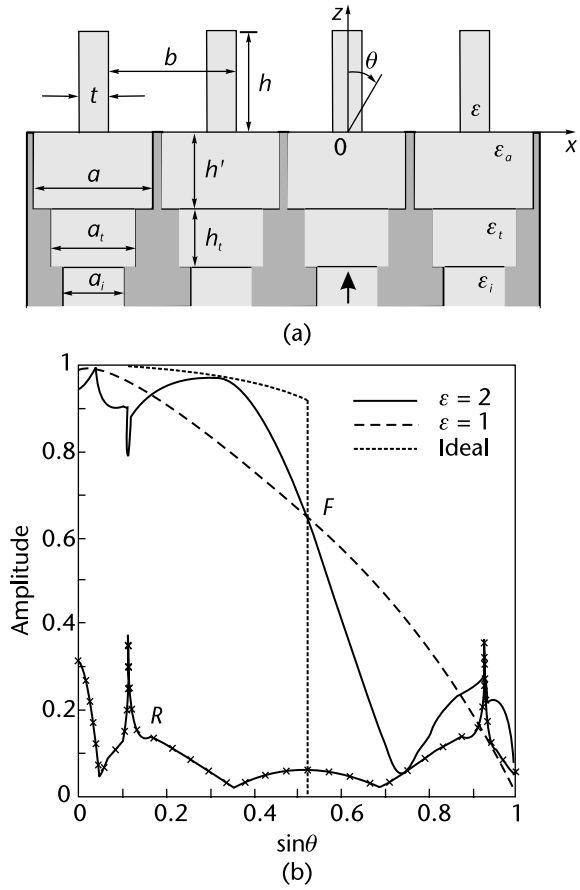

Figure 5.4 (a) Geometry and (b) characteristics of array with $a_i = 0.4\lambda$, $a_t = 0.45\lambda$, $h_t = 0.25\lambda$, $\varepsilon_i = \varepsilon_t = 1$, $a = 0.57\lambda$, $h = 0.3\lambda$, $b = 0.96\lambda$, $\varepsilon_a = \varepsilon = 2$, $t = 0.5\lambda$, and $h = 1.2\lambda$, obtained by the method of integral equations for polarization currents at excitation of waveguides in TEM modes.

5.2.6 Finite Element Method and Commercial Codes

The finite element method comprising a few hybrid modifications (see, for instance, [49]) is one the most powerful means for electromagnetic simulation. Its application to analysis of waveguide-rod arrays may be found in [50], where an array of rectangular waveguides filled with dielectric protruding above the apertures is modeled. The solution obtained first for the corresponding infinite periodic structure is used then for analysis of a finite array, which was earlier studied experimentally in [20]. A similar infinite array with an integrated one-layer radome has been considered in [17] by applying the hybrid finite element method. The finite element method, in which the domain of determining the solution is restricted by an ideally absorbing layer, has been implemented in the well-known commercial codes HFSS and Microwave Studio. Note that the analysis of the array with bars of rectangular cross-section protruding at $\lambda/2$ carried out in [50] involves an algebraic system with 7,105 unknown coefficients. The rods that allow shaping of a sector element pattern are usually several times longer. Therefore, application of the finite element method to the analysis of arrays with long dielectric elements would require significantly greater computer resources.

5.3 Hybrid Projective Method in Two-Dimensional Problems (E-Polarization)

The review presented earlier shows that the existing methods that may be applied to the analysis of the waveguide-dielectric arrays have definite restrictions. The results obtained for the arrays in question do not cover some important cases, either. In particular, there are no results in the literature for long-sharpened protruding elements that are necessary both for shaping the sector element patterns of high quality and for providing good match of the array to free space. So, further studies in this area remain of interest both from the viewpoint of the methodology and from the viewpoint of investigating the properties of such arrays themselves.

In [51], there has been proposed a hybrid projective method applied to analysis and optimization of one-dimensionally periodic arrays of stepped parallel-plate waveguides (or stepped horns) filled completely with dielectric protruding above the apertures. The method of [51] is similar to the incomplete Galerkin method [27], reducing the problem to systems of ordinary differential equations. However, unlike [27], the mentioned systems are solved by the one-dimensional finite element method, as done in [52] in an analysis of periodic purely dielectric structures. As shown in [51], the best array performances are achieved when the protrusion width is considerably smaller than the waveguide width. This circumstance imposes restriction on the value of the dielectric material filling the waveguide. The use of dense dielectric does not allow the provision of good array match that is especially necessary for the case of H-polarization. In this case, one is forced to use a dielectric of smaller permittivity for filling the waveguide and denser dielectric for the protruding element that is not the best solution from the view of the mechanical design. More promising is an array structure considered in [53–55], where the dielectric elements, emerging from the feeding waveguides and protruding to free space, only partially fill in the stepped waveguides, as described later.

5.3.1 Array Geometry and Excitation

The general geometry of the array to be considered in this section and detailed geometry of its waveguide-dielectric element in the plane $0xz$ of a rectangular Cartesian coordinate system $0xyz$ are shown in Figure 5.5(a, b), respectively. The array is a periodic structure of period b formed by input parallel-plate waveguides of width a_w feeding the stepped horns. The width and height of the lower horn section are a_0 and h_0, while the same parameters of the upper (radiating) section are a and h_1, respectively. The widths of the dielectric plate at the base and top of the lower section are t_{00} and t_{01}, and those at the base and aperture of the upper section are t_{10} and t_{11}. The protrusion of height h has width t_0 at its base and width t_1 at the top. The input waveguides are completely filled with dielectric of relative permittivity ε_w, while the relative permittivity of the plates in the lower and upper horn sections as well as that protruding to free space are ε_t, ε_a, and ε, respectively. The surfaces of the input waveguides and stepped horns are assumed to be perfectly conducting. Selecting the indicated array parameters, we may obtain various array configurations, including those that have already been considered in the literature and may be used for validation of the algorithm developed later.

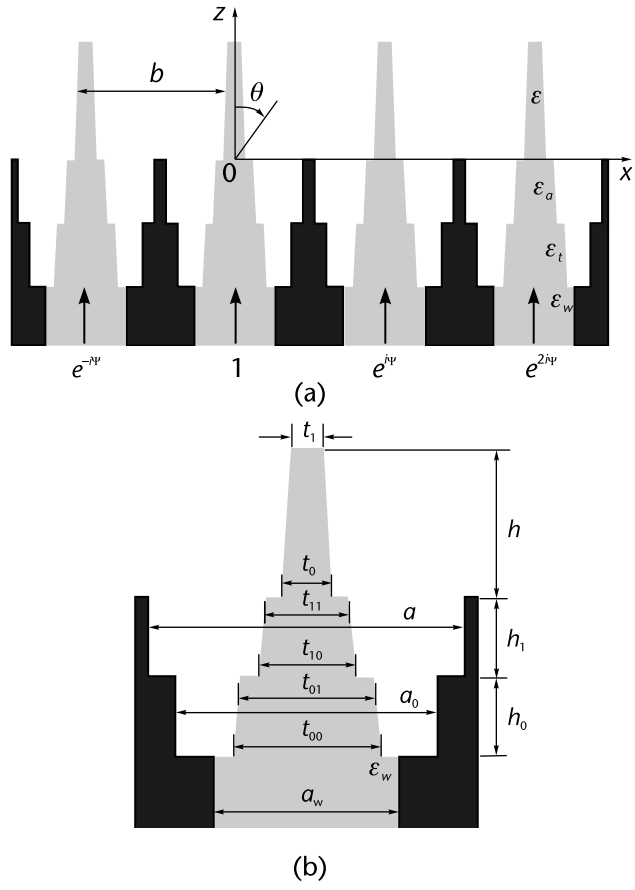

Figure 5.5 (a) General array geometry and (b) detailed geometry of waveguide-dielectric element.

The input waveguides are assumed to be excited in their dominant modes TE_{10} of unit amplitude and with phase increment $= kb \sin\theta$ between adjacent waveguides. The problem then is the determination of the scattered field and, in particular, the calculation of the array reflection coefficient and element pattern, which are of primary interest in practice.

5.3.2 Representation of the Fields

The excitation of the input waveguides in the TE modes corresponds to the case of E-polarization when only the electromagnetic field components E_y, H_x, and H_z are not equal to zero identically. Assuming that the harmonic time dependence is chosen in the form $e^{i\omega t}$, we may write the total electric field in the central input waveguide as a superposition of the incident and reflected TE modes

$$E_y(x,z \quad z\ ) = \sum_{n=1} (\delta_{n1} e^{i\gamma_{wn}(z\ \ z\ )} + R_n e^{\ i\gamma_{wn}(z\ \ z\ )}) \sin\frac{n\pi(x + a_w/2)}{a_w} \tag{5.1}$$

where $z = (h_0 + h_1)$, $\gamma_{wn} = [k^2\varepsilon_w - (n\pi/a_w)^2]^{1/2}$ are propagation constants, δ_{1n} is the Kronecker symbol, and R_n are amplitudes of the reflected modes to be determined.

The radiated electric field above the protrusions is a superposition of Floquet modes

$$E_y(x, z \quad h) = \sum_{q=}^{+} T_q e^{i\alpha_q x + i\Gamma_q(z \quad h)} \tag{5.2}$$

with propagation constants (1.99) and unknown amplitudes T_q.

The electric fields in the lower and upper horn sections as well as in the free space region containing the protrusions are represented as expansions over complete systems of transverse functions in the indicated regions

$$E_y(x, z \quad z \quad z) = \sum_{q=1} \bar{E}_q(z) \sin\frac{q\pi(x + a_0/2)}{a_0} \tag{5.3}$$

$$E_y(x, z \quad z \quad 0) = \sum_{n=1} \tilde{E}_n(z) \sin\frac{n\pi(x + a/2)}{a} \tag{5.4}$$

$$E_y(x, 0 \quad z \quad h) = \sum_{q=}^{+} E_q(z) e^{i\alpha_q x} \tag{5.5}$$

with unknown coefficients depending on the longitudinal coordinate z, and $z = h_1$.

5.3.3 Projective Matching of the Fields on the Boundaries

The electric field (5.3) must vanish on the flange of the input waveguide and be equal to field (5.1) in the input waveguide aperture at $z = z$. Projecting this equality on the transverse functions used in expansion (5.3), we obtain the following algebraic subsystem

$$\frac{a_w}{a_0} \sum_{n=1} R_n Q_{np}^{(0)} \quad \bar{E}_p(z) = \frac{a_w}{a_0} Q_{1p}^{(0)}, \quad p = 1, 2, \ldots, \tag{5.6}$$

with coefficients

$$\begin{aligned} Q_{np}^{(0)} &= \frac{2}{a_w} \int_{a_w/2}^{a_w/2} \sin\frac{n\pi(x + a_w/2)}{a_w} \sin\frac{p\pi(x + a_0/2)}{a_0} dx \\ &= \cos\frac{\pi(n \quad p)}{2} \frac{\sin\frac{\pi}{2}(n \quad p\frac{a_w}{a_0}\div)}{\frac{\pi}{2}(n \quad p\frac{a_w}{a_0}\div)} \quad (\ 1)^q \frac{\sin\frac{\pi}{2}(n + p\frac{a_w}{a_0}\div)}{\frac{\pi}{2}(n + p\frac{a_w}{a_0}\div)} \end{aligned} \tag{5.7}$$

The transverse magnetic field component H_x in the input waveguide aperture at $z = z$ must be equal to the field component $H_x(x, z\ )$ in the lower horn section. The indicated components are proportional to $\partial E_y/\partial z$, where E_y is determined by (5.1) and (5.3). Projecting the equality of the indicated magnetic fields on the transverse functions of the input waveguide, we obtain one more algebraic subsystem

$$i\gamma_{wm}R_m + \sum_{q=1} \bar{E}_q(z\ )Q^{(0)}_{mq} = i\gamma_{wm}\delta_{m1} \tag{5.8}$$

where $m = 1, 2, \ldots,$, and the prime at the unknown coefficient denotes the derivative over the argument.

The similar projective matching of the transverse electric and magnetic field components at $z = z\ = \ h_1$ and $z = 0$ gives the following relations

$$\frac{a_0}{a}\sum_{q=1} \bar{E}_q(z\ )Q^{(1)}_{qm} \quad \tilde{E}_m(z\ ) = 0, \quad m = 1, 2, \ldots, \tag{5.9}$$

$$\bar{E}_p(z\ ) = \sum_{n=1} \tilde{E}_n(z\ )Q^{(1)}_{pn}, \quad p = 1, 2, \ldots, \tag{5.10}$$

$$\frac{a}{b}\sum_{n=1} \tilde{E}_n(0)Q_{np} \quad E_p(0) = 0, \quad p = 0, \pm 1, \ \ldots, \pm \tag{5.11}$$

$$\tilde{E}_m(0) = 2\sum_{q=} E_q(0)Q^{*}_{mq}, \quad m = 1, 2, \ldots, \tag{5.12}$$

where coefficients $Q^{(1)}_{qm}$ are determined by formula (5.7) where n, p, a_w, and a_0 should be replaced by q, m, a_0, and a, respectively, while coefficients Q_{np} are determined by formula

$$\begin{aligned} Q_{np} &= \frac{1}{a}\int_{a/2}^{a/2} \sin\frac{n\pi(x + a/2)}{a} e^{\ i\alpha_p x}dx \\ &= n\pi\frac{e^{i\alpha_p a/2} \quad (\ 1)^n e^{\ i\alpha_p a/2}}{(n\pi)^2 \quad (\alpha_p a)^2} \end{aligned} \tag{5.13}$$

and the asterisk at this coefficient in (5.12) means complex conjugation.

Finally, since fields (5.2) and (5.5) are expanded over the same transverse functions, matching of the transverse electric and magnetic components at $z = h$ gives two more relations

$$E_q(h) = T_q \tag{5.14}$$

$$E_q(h) = i\Gamma_q T_q \tag{5.15}$$

which will be used later in the process of obtaining final system of algebraic equations.

5.3.4 Application of the Finite Element Method

The electric field (5.3) in the lower horn section at $z \quad z \quad z$ must satisfy the Helmholtz equation

$$\frac{^2E_y}{x^2} + \frac{^2E_y}{z^2} + k^2\tilde{\varepsilon}(x,z)E_y = 0 \tag{5.16}$$

where $\tilde{\varepsilon}(x,z) = \varepsilon_t$ in the dielectric and $\tilde{\varepsilon}(x, z) = 1$ in the gaps. Substituting (5.3) in (5.16) and projecting (5.16) on a pth transverse function of the section in question multiplied by $2/a_0$, we obtain a system of ordinary differential equations similar to those derived in [27, 56]

$$\frac{d^2\overline{E}_p(z)}{dz^2} + \overline{\gamma}_p^2\overline{E}_p(z) + k^2 \sum_{q=1} \overline{W}_{pq}\overline{E}_q(z) = 0 \tag{5.17}$$

where $\overline{\gamma}_p = [k^2 \quad (p\pi/a_0)^2]^{1/2}$, $p = 1, 2, \ldots, \quad ,$

$$\begin{aligned}\overline{W}_{pq}(z) &= \frac{2(\varepsilon_t \quad 1)}{a_0} \int_{t/2}^{t/2} \sin\frac{q\pi(x+a_0/2)}{a_0}\sin\frac{p\pi(x+a_0/2)}{a_0}dx \\ &= \frac{2(\varepsilon_t \quad 1)}{a_0}\cos\frac{\pi(p \quad q)}{2} \quad \frac{\sin\dfrac{\pi t(p \quad q)}{2a_0}}{\dfrac{\pi(p \quad q)}{a_0}} \quad (\ 1)^q \frac{\sin\dfrac{\pi t(p+q)}{2a_0}}{\dfrac{\pi(p+q)}{a_0}}\end{aligned} \tag{5.18}$$

and $t(z) = t_{00} \quad (t_{00} \quad t_{01})(z \quad z \ )/h_0$ is the width of the dielectric part in the section [Figure 5.5(b)].

Further, unlike [27, 56], we will solve system (5.17) applying the one-dimensional finite element method [49, 52]. Using the piecewise-linear approximation of the unknown functions $\overline{E}_q(z)$ in (5.3), we represent them as

$$\overline{E}_q(z) = \sum_{s=1}^{\bar{N}} \overline{E}_{sq} f_s(z) \tag{5.19}$$

where $\overline{E}_{sq}$ are unknown constant coefficients, $\bar{N}$ is the number of nodes including the edge points at $z = z \quad$ and $z = z \ = \ h_1$, as well as

$$f_s(z) = \frac{1}{} \begin{array}{l} z \quad z_{s\ 1}, \quad z_{s\ 1} \quad z \quad z_s, \quad s > 1 \\ z_{s+1} \quad z, \quad z_s \quad z \quad z_{s+1}, \quad s < \bar{N} \\ 0, \quad z < z_{s\ 1}, \ z > z_{s+1} \end{array} \tag{5.20}$$

are *triangular* functions with node coordinates $z_s = z \ + (s \quad 1)$ and spacing between the nodes $\quad = h_0/(\bar{N} \quad 1)$. Substituting (5.19) in (5.17), multiplying (5.17) by $f_s(z)$, and integrating the obtained expression over z from $z \quad$ to z , we reduce differential equations (5.17) to algebraic equations

$$\bar{E}_p(z\ )\delta_{s\ 1}+\sum_{s=1}^{\bar{N}}\sum_{q=1}\left[\frac{\bar{\gamma}_q^2}{k}\bar{I}_{s\ s}^{(0)}\quad k\bar{I}_{s\ s}^{(1)}\div\delta_{pq}+k\bar{J}_{s\ s}^{pq}\right]\bar{E}_{sq}$$

$$+\delta_{s\ \bar{N}}\sum_{n=1}\tilde{E}_n(z\ )Q_{pn}^{(1)}=0 \tag{5.21}$$

where $s\ =1,2,\ldots,\bar{N}$; $p=1,2,\ldots,\quad$;

$$\bar{I}_{s\ s}^{(0)}=k\int_z^z f_s\,f_s\,dz \tag{5.22}$$

$$\bar{I}_{s\ s}^{(1)}=\frac{1}{k}\int_z^z f_s\,f_s\,dz \tag{5.23}$$

$$\bar{J}_{s\ s}^{pq}=k\int_z^z f_s\,\bar{W}_{pq}f_s dz \tag{5.24}$$

The first and last terms in (5.21) are formed as a result of integration of the first term in (5.17) by parts. Furthermore, the final form of the last term in (5.21) has been obtained with account for (5.10). The nonzero values of integrals are calculated using explicit expressions given in Appendix 5A. Note also that the expressions for (5.24) have been obtained using the piecewise-linear approximation of functions (5.18) in the form

$$\bar{W}_{pq}(z)=\bar{W}_{pq}^{s}f_s(z)+\bar{W}_{pq}^{s+1}f_{s+1}(z)$$

for $z_s\quad z\quad z_{s+1}$ where $\bar{W}_{pq}^{s}=\bar{W}_{pq}(z_s)$.

The electric field (5.4) in the upper horn section is considered similarly. The unknown variable coefficients in (5.4) are represented in the form of a superposition of $\tilde{N}$ triangular functions; that is,

$$\tilde{E}_n(z)=\sum_{s=1}^{\tilde{N}}\tilde{E}_{sn}f_s(z) \tag{5.25}$$

with unknown constant coefficients $\tilde{E}_{sn}$. The nodes of triangular functions are located in points $z_s=z\ +(s\quad 1)\quad$, where $\quad=h_1/(\tilde{N}\quad 1)$. Application of the finite element method, as described earlier, results in a linear algebraic subsystem

$$\tilde{E}_m(z\ )\delta_{s\ 1}+\sum_{s=1}^{\tilde{N}}\sum_{n=1}\left[\frac{\tilde{\gamma}_n^2}{k}\tilde{I}_{s\ s}^{(0)}\quad k\tilde{I}_{s\ s}^{(1)}\div\delta_{mn}+k\tilde{J}_{s\ s}^{mn}\right]\tilde{E}_{sn}$$

$$+2\delta_{s\ \tilde{N}}\sum_{q=}E_q(0)Q_{mq}=0 \tag{5.26}$$

where $s = 1, 2, ..., \tilde{N}$; $m = 1, 2, ...,$; $\tilde{\gamma}_n = [k^2 \quad (n\pi/a)^2]^{1/2}$. The coefficients $\tilde{I}^{(0)}_{s\,s}$, $\tilde{I}^{(1)}_{s\,s}$, and $\tilde{J}^{mn}_{s\,s}$ are determined by formulas (5.22) through (5.24), where the integration limits should be replaced by z and 0. Function $\overline{W}_{pq}$ in (5.24) should be replaced by function $\widetilde{W}_{mn}$ determined by formula (5.18), where p, q, a_0, and ε_t should be replaced by m, n, a, and ε_a, respectively, and the dielectric insertion width should be determined as $t(z) = t_{10} \quad (t_{10} \quad t_{11})(z \quad z\,)/h_1$. The last term in (5.26) has been obtained with account for (5.12).

The electric field (5.5) in the free space regions containing the protruding elements at $0 \quad z \quad h$ must satisfy the Helmholtz equation (5.16). Substitution of (5.5) in (5.16) and projection of (5.16) on $\exp(\ i\alpha_p x)/b$ give a system of ordinary differential equations of the following form

$$\frac{d^2E_p}{dz^2} + \ {}^2_p E_p + k^2 \sum_{q=} W_{pq}E_q = 0 \tag{5.27}$$

where $p = 0, \pm 1, ..., \pm$,

$$W_{pq}(z) = \frac{(\varepsilon \quad 1)}{b}\int_{t/2}^{t/2} e^{i(\alpha_q \quad \alpha_p)x}dx = (\varepsilon \quad 1)\frac{\sin[\pi(q \quad p)t/b]}{\pi(q \quad p)} \tag{5.28}$$

and $t = t(z) = t_0 \quad (t_0 \quad t_1)z/h$ is the protrusion width.

Applying the finite element method to solving (5.27), as has been done earlier for the fields in the stepped horn sections, we obtain algebraic equations

$$E_p(0)\delta_{s\,1} + \sum_{s=1}^{N}\sum_{q=} A^{s\,s}_{pq}E_{sq} + i\Gamma_p E_{Np}\delta_{s\,N} = 0 \tag{5.29}$$

where $s = 1, 2, ..., N$; $p = 0, \pm 1, ..., \pm$; E_{sq} are unknown values of the variable coefficients in expansion (5.5) in N points with coordinates $z_s = (s \quad 1)$, $= h/(N \quad 1)$, $E_{Np} = E_p(h)$, and

$$A^{s\,s}_{pq} = \ \Gamma^2_p \int_0^h f_s\,f_s dz \quad \int_0^h f_s\,f_s dz \ \ \delta_{pq} + k^2 \int_0^h f_s\,W_{pq}f_s dz \tag{5.30}$$

are matrix elements, in which the integrals are calculated similarly to that described earlier for the horn sections. The first and third terms in (5.29) are formed as a result of integrating expression d^2E_p/dz^2 in (5.27) by parts and accounting for expression (5.15).

5.3.5 Algebraic System and Array Characteristics

The subsystems (5.8), (5.6), (5.21), (5.9), (5.26), (5.11), and (5.29) in the indicated order constitute a complete system of linear algebraic equations for unknown coefficients R_m, $\overline{E}_q(z\ )$, $\overline{E}_{sq}$, $\tilde{E}_m(z\ )$, $\tilde{E}_{sn}$, $E_q(0)$, and E_{sq}. Note that $\overline{E}_p(z\ )$ in (5.6), $\overline{E}_q(z\ )$ and $\tilde{E}_m(z\ )$ in (5.9), as well as $\tilde{E}_n(0)$ and $E_p(0)$ in (5.11) are equal to $\overline{E}_{1p}$, $\overline{E}_{\tilde{N}q}$, $\tilde{E}_{1m}$, $\tilde{E}_{\tilde{N}m}$, and E_{1p}, respectively. We solve this infinite system by the method of truncation

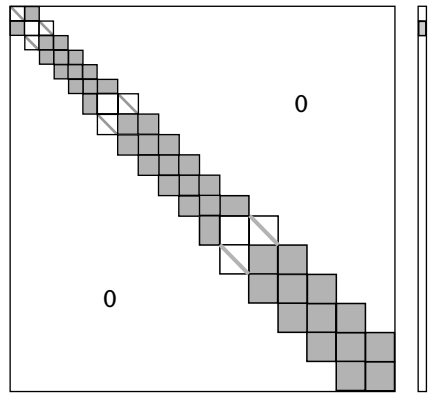

Figure 5.6 Structure of the linear algebraic system.

with account for M_w first waveguide modes in (5.1), $\overline{M}$ transverse functions for the lower horn section in (5.3), $\tilde{M}$ transverse functions for the upper horn section in (5.4), as well as M first transverse functions for the region containing the protrusions in (5.5) and for free space above the protrusions in (5.2). So, the order of the truncated system for the unknowns listed earlier is equal to $M_w + (\overline{N}+1)\overline{M} + (\tilde{N}+1)\tilde{M} + (N+1)M$. Since the products of the s th and sth triangular functions are equal to zero for $|s \quad s| > 1$, the matrix of the system has a block-banded structure shown in Figure 5.6, where the blocks containing nonzero elements are shown in gray and the blocks with a diagonal lines contain nonzero elements arranged only on its diagonals.

After obtaining the numerical solution of the truncated algebraic system, we have the reflected mode amplitudes, including the array reflection coefficient R_1, as well as the radiated Floquet mode amplitudes $T_q = E_{Nq}$. They are used for verification of the power balance relation [39]

$$\underset{n}{\frac{\mathrm{Re}\{\gamma_{wn}\}}{\gamma_{w1}} |R_n|^2} + \underset{q}{\frac{2b}{\gamma_{w1}a_w} |T_q|^2 \,\mathrm{Re}\{\Gamma_q\}} = 1 \tag{5.31}$$

and for calculation of the array element pattern

$$F(\theta) = \sqrt{\frac{2kb}{\gamma_{w1}a_w}} |T_0(kb\sin\theta)| \cos\theta \tag{5.32}$$

normalized so that $F^2(0)$ equals the coefficient of power transmission in the main array beam.

5.3.6 Realization, Validation, and Numerical Results

The algorithm described earlier has been realized in a FORTRAN code. The system of algebraic equations is solved using the Gauss' elimination method with selection of a leading element in a column. The block-banded structure of the matrix has also been taken into account. Due to that, the computation time has been shortened a few times compared to the case when the zero blocks are not excluded in the processing.

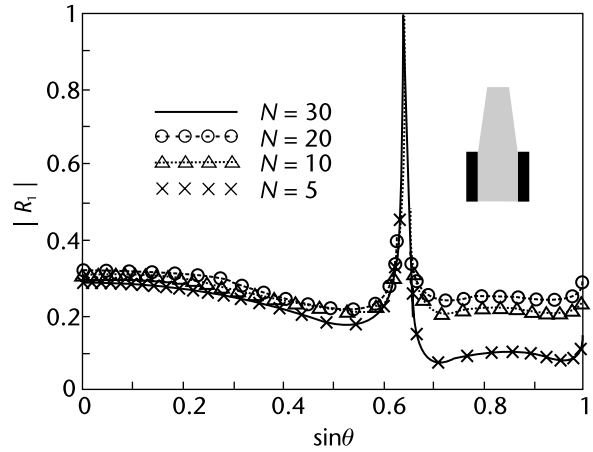

Figure 5.7 Reflection coefficient of array with $b = 0.6\lambda$, $a_w = a_0 = a = t_{00} = t_{01} = t_{10} = t_{11} = t_0 = 0.4\lambda$, $t_1 = 0.2\lambda$, $h_0 = h_1 = 0.1\lambda$, $h = 0.6\lambda$, and $\varepsilon_w = \varepsilon_t = \varepsilon_a = \varepsilon = 2$, excited in TE_{10} mode, calculated at $N = 5$ (×××), 10 ( ), 20 (○○○), 30 (——), and constant $\bar{N}$, $N = 5$, $M_w = \bar{M} = M = 20$, $M = 31$.

Validation of the code operation has been verified by a few ways described in [18]. The tests involved the power balance relation (5.31), convergence of the results with increasing the number of triangular functions in the finite element method and the number of the coefficients taken into account in expansions of the fields over transverse functions, as well as comparison of the results obtained by the method in question with the data obtained by other methods and available in the literature for some special cases that can be modeled making appropriate selection of the parameters for the structure shown in Figure 5.5.

One of the examples characterizing convergence of the array reflection coefficient with increasing the number of nodes N for the free space region containing the protruding elements is shown in Figure 5.7. The array parameters are indicated in the figure caption. The results have been obtained at the number of Floquet mode transverse functions $M = 31$, which is deliberately large enough for the indicated element spacing. The number of the waveguide modes $M_w = 20$ has been chosen here and later so that $M_w \quad Ma_w/b$. The solid curve corresponds to $N = 30$. We see that the other curves obtained at smaller values of N quickly approach the solid curve as N increases. The test for convergence of the results on M has shown that the results at $M = 11$ and $M_w = 7$ already practically coincide with those corresponding to $M = 31$ and $M_w = 20$, and, for this reason, the corresponding plots are not presented here. Other results on study of the convergence may be found in [51, 57]. Some recommendations on choosing the number of the nodes in the one-dimensional finite element method are given in [52]. Note that the greater the angle between the side surfaces and the z-axis is and the greater the dielectric element permittivity is, the smaller the node spacing should be for providing high accuracy of calculations at the piecewise linear approximation chosen for functions (5.18) and those ones similar to them.

A few examples on comparing the results obtained using the algorithm described earlier to the results available in the literature for some simpler cases of the array geometry are given in [57]. Here, in Figure 5.8, we present the results of shaping the sector element pattern for the structure shown in Figure 5.4(a). This structure

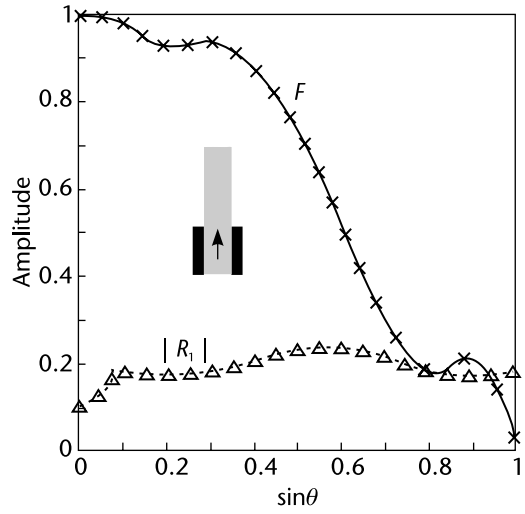

Figure 5.8 Reflection coefficient and element pattern of array with $b = 0.91\lambda$, $a_w = a_0 = a = t_{00} = t_{01} = t_{10} = t_{11} = 0.57\lambda$, $t_0 = t_1 = 0.5\lambda$, $h_0 = h_1 = 0.1\lambda$, $h = 1.4\lambda$, and $\varepsilon_w = \varepsilon_t = \varepsilon_a = \varepsilon = 2$, excited in TE_{10} mode, calculated at $M_w = \bar{M} = M = 14$, $M = 21$, $\bar{N}$, $N = 5$, and $N = 41$; (,) – present method, (—, - - -) – method of [45].

excited in the TE_{10} modes was first studied in [45] by the method of integral equations for polarization current in the protrusion. As the comparison shows, the hybrid projective method gives practically the same results. Note also that the power balance relation (5.31) in all calculations is satisfied with accuracy of at least six decimal digits. So, all the tests have shown good capabilities of the proposed algorithm for numerical study of the two-dimensional models for waveguide-dielectric arrays. Some results of such a study are presented later.

The purpose of the study has been to reveal the array capabilities of shaping the sector element patterns. The numerical experiments have shown that the best results, as a rule, are achieved at the maximum possible width of the upper horn section at a specified element spacing and when the section supports two propagating modes. The use of sharpened dielectric elements provides their good match to free space since the modes in the dielectric structure smoothly change for ordinary Floquet modes in free space above the protrusions. The selection of the element length and its width at the base is initially made in the absence of the stepped transitions (i.e., at $a_w = a_0 = a$) as well as at total filling of the waveguide sections with dielectric. At specified permittivity and some large length of the dielectric protrusions, the protrusion width at the base is selected to minimize the reflection coefficient of the dominant mode. Then the protrusion length is selected to provide the sector shape of the element pattern. The next operation is the selection of the lower horn section parameters a_0 and h_0 to match the input section to the upper section at their specified widths. The purpose of the final operation is the selection of the upper section height h_1, allowing either avoidance or minimization of the undesirable resonance effects.

The results of the application of the technique described earlier to optimization of the array excited in the TE_{10} modes are shown in Figures 5.9 through 5.11. The permittivity of dielectric material used in all the sections of the array with element spacing $b = 0.8\lambda$ (Figure 5.9), $b = 0.91\lambda$ (Figure 5.10), and $b = 1.1\lambda$ (Figure 5.11) is

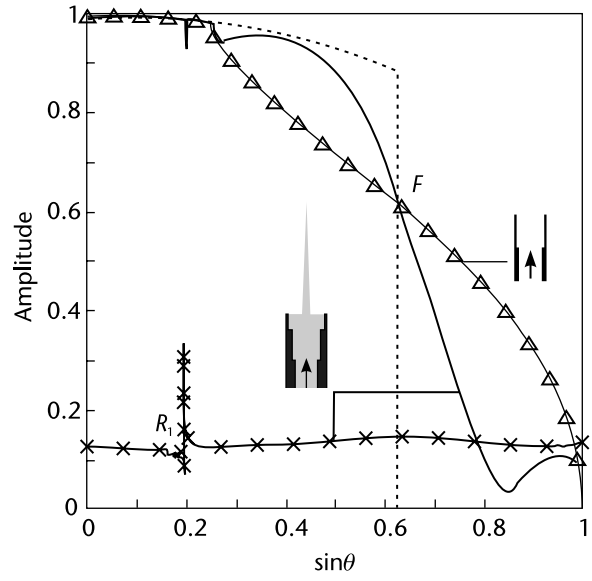

Figure 5.9 Reflection coefficient ( ) and element pattern (——) of array with $b = 0.8\lambda$, $a_w = 0.55\lambda$, $a_0 = t_{00} = t_{01} = 0.629\lambda$, $h_0 = 0.5\lambda$, $a = t_{10} = t_{11} = 0.78\lambda$, $h_1 = 0.22\lambda$, $t_0 = 0.16\lambda$, $t_1 = 0$, $h = 2.1\lambda$, and $\varepsilon_w = \varepsilon_t = \varepsilon_a = \varepsilon = 2.56$, excited in TE_{10} modes, calculated at $M_w = 12$, $\bar{M} = 14$, $M = 16$, $M = 19$, $\bar{N} = 21$, $N = 11$, and $N = 49$; (- - - -) is the ideal element pattern and (———) is the element pattern of array without dielectric at $a_w = a_0 = 0.618\lambda$, and $h_1 = 0.914\lambda$.

equal to 2.56, 2, and 1.5, respectively. All the other array parameters are indicated in the figure captions. The obtained element patterns are compared to the normalized ideal sector element patterns (see Chapter 1) equal to $\sqrt{\cos\theta}$ for $0 \quad \sin\theta < \lambda/(2b)$, $\sqrt{0.5\cos\theta}$ for $\sin\theta = \lambda/(2b)$, and 0 for $\lambda/(2b) < \sin\theta \quad 1$. The comparison is also made

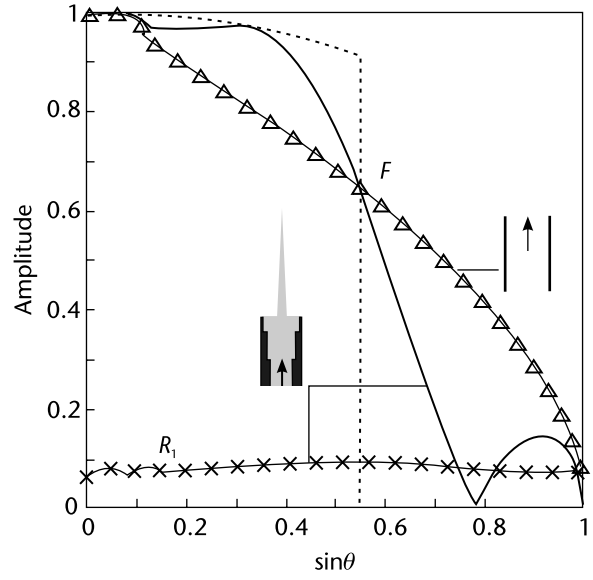

Figure 5.10 The same as in Figure 5.9 at $b = 0.91\lambda$, $a_w = 0.6\lambda$, $a_0 = t_{00} = t_{01} = 0.694\lambda$, $h_0 = 0.59\lambda$, $a = t_{10} = t_{11} = 0.89\lambda$, $h_1 = 0.215\lambda$, $t_0 = 0.21\lambda$, $t_1 = 0$, $h = 2.2\lambda$, $\varepsilon_w = \varepsilon_t = \varepsilon_a = \varepsilon = 2$, $M_w = 14$, $\bar{M} = 16$, $M = 18$, $M = 19$, $\bar{N} = 23$, $N = 11$, and $N = 49$; (———) is the element pattern of array without dielectric at $a_w = a_0 = a$.

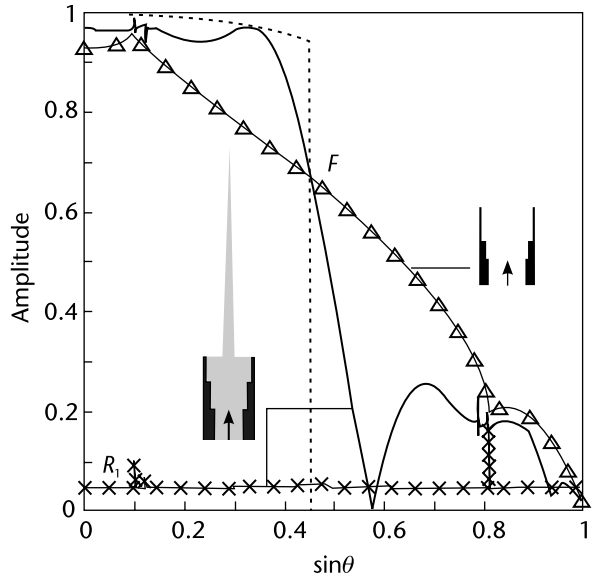

Figure 5.11 The same as in Figure 5.9 at $b = 1.1\lambda$, $a_w = 0.6\lambda$, $a_0 = t_{00} = t_{01} = 0.71\lambda$, $h_0 = 0.67\lambda$, $a = t_{10} = t_{11} = 1.05\lambda$, $h_1 = 0.6\lambda$, $t_0 = 0.3\lambda$, $t_1 = 0$, $h = 4.9\lambda$, and $\varepsilon_w = \varepsilon_t = \varepsilon_a = \varepsilon = 1.5$, $M_w = 14$, $\bar{M} = 16$, $M = 20$, $M = 21$, $\bar{N} = 25$, $N = 23$ and $N = 71$; (——) is the element pattern of array without dielectric at $a_w = 0.75\lambda$, $a_0 = 0.85\lambda$, $h_0 = 0.28\lambda$, and $h_1 = 0.6\lambda$.

with waveguide arrays without dielectric. The results shown in Figure 5.9 correspond to the array using one matching step. At $b = 0.91\lambda$ (Figure 5.10), the array aperture has good natural match, while the array with $b = 1.1\lambda$ (Figure 5.11) uses a matching transition section from the single-mode waveguide to the dual-mode radiation section.

Some examples of the characteristics corresponding to the array with partial filling of the horn sections with dielectric, as shown in Figure 5.5, may be found in [53–55]. If the upper (radiating) section supports only one propagating mode at the partial filling, the element pattern, as a rule, has resonant dips. However, in some cases, they may be avoided. An appropriate example of the array geometry and characteristics is given in Figure 5.12 for the dielectric element with relative permittivity $\varepsilon_t = \varepsilon_a = \varepsilon = 2$ and $\varepsilon_t = \varepsilon_a = \varepsilon = 4$. Note that the higher the element permittivity, the smaller the optimal width of the element.

5.4 Excitation of Array in TEM Modes (H-Polarization)

5.4.1 Statement of the Problem and Representation of the Fields

Here we again consider the structure shown in Figure 5.5 and described in Section 5.3.1. Let now the input waveguides be excited in the dominant TEM modes of unit amplitudes and progressive phases with the same increment $= kb \sin\theta$ as considered earlier. The purpose of this section is to develop a hybrid projective algorithm allowing calculation of the array characteristics at the indicated

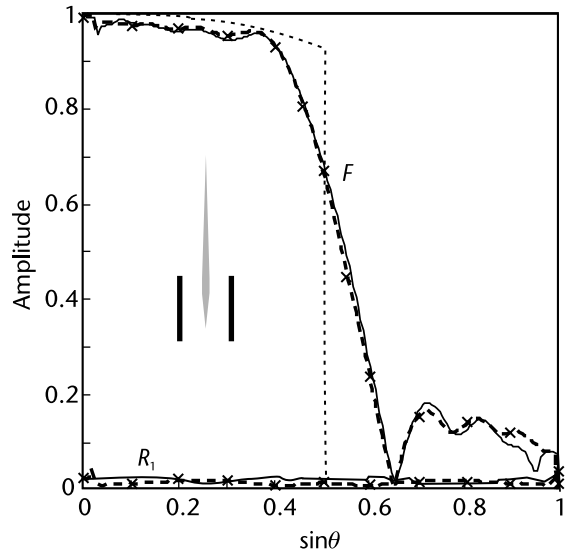

Figure 5.12 Reflection coefficient and element pattern of array with $b = 0.98\lambda$, $a_w = a_0 = a = 0.96\lambda$, $\varepsilon_w = 1$, $t_{00} = t_1 = 0$, $h_0 = \lambda$, $h_1 = 0.5\lambda$, $h = 7.9\lambda$, $M_w = \bar{M} = M = 10$, $M = 12$, $\bar{N} = 21$, $N = 11$, $N = 80$; (——) is $\varepsilon_t = \varepsilon_a = \varepsilon = 2$, $t_{01} = t_{10} = t_{11} = t_0 = 0.28\lambda$; (–×–) is $\varepsilon_t = \varepsilon_a = \varepsilon = 4$, $t_{01} = t_{10} = t_{11} = t_0 = 0.075\lambda$; (- - -) is the ideal element pattern.

excitation corresponding to the case of H-polarization for a two-dimensional problem where the electromagnetic field components not equal to zero identically are H_x, E_x, and E_z. So, the magnetic field strength in the input waveguide section of the central element is represented as a superposition of TM modes

$$H_y(x,z \quad z\ ) = \sum_{n=1} \left(\delta_{n1} e^{i\gamma_{wn}(z\ \ z\ )} + R_n e^{\ i\gamma_{wn}(z\ \ z\ )}\right) \cos\beta_{wn}(x + a_w/2) \tag{5.33}$$

where $\gamma_{wn} = \sqrt{k^2\varepsilon_w \quad \beta_{wn}^2}$ are propagation constants, $\beta_{wn} = (n \quad 1)\pi/a_w$, and R_n are unknown amplitudes of reflected modes. The transverse component of the electric field strength component, which will also be involved in the subsequent operations, is determined by using (5.33) and Maxwell's equation like (1.104)

$$E_x(x,z) = \frac{1}{\omega\varepsilon_0\varepsilon_w} \sum_{n=1} \left(\delta_{n1} e^{i\gamma_{wn}(z\ \ z\ )} \quad R_n e^{\ i\gamma_{wn}(z\ \ z\ )}\right) \gamma_{wn}\cos\beta_{wn}(x + a_w/2) \tag{5.34}$$

where ε_0 is the electric constant of free space.

The transverse electric and magnetic field strength components in the lower and upper horn sections as well as in the free space region containing the protruding elements are represented as expansions over complete systems of transverse functions for the indicated regions

$$H_y(x,z \quad z \quad z) = \sum_{q=1} \bar{H}_q(z)\cos\bar{\beta}_q(x + a_0/2) \tag{5.35}$$

$$E_x(x,z \quad z \quad z) = \sum_{q=1} \bar{E}_q(z)\cos\bar{\beta}_q(x + a_0/2) \tag{5.36}$$

$$H_y(x,z \quad z \quad 0) = \sum_{n=1} \tilde{H}_n(z)\cos\tilde{\beta}_n(x + a/2) \tag{5.37}$$

$$E_x(x,z \quad z \quad 0) = \sum_{n=1} \tilde{E}_n(z)\cos\tilde{\beta}_n(x + a/2) \tag{5.38}$$

$$H_y(x,0 \quad z \quad h) = \sum_{q=}^{+} H_q(z)e^{i\alpha_q x} \tag{5.39}$$

$$E_x(x,0 \quad z \quad h) = \sum_{q=}^{+} E_q(z)e^{i\alpha_q x} \tag{5.40}$$

where $\bar{\beta}_q = (q \quad 1)\pi/a_0$, $\tilde{\beta} = (n \quad 1)\pi/a$, and $\alpha_q = (\psi + 2\pi q)/b$ are transverse propagation constants, while the unknown expansion coefficients depend on the longitudinal coordinate.

The transverse electric and magnetic fields in the free space above the protrusions are superpositions of the Floquet modes

$$H_y(x,z \quad h) = \sum_{q=}^{+} T_q e^{i\alpha_q x + i\Gamma_q(z \quad h)} \tag{5.41}$$

$$E_x(x,z \quad h) = \frac{1}{\omega\varepsilon_0} \sum_{q=}^{+} \Gamma_q T_q e^{i\alpha_q x + i\Gamma_q(z \quad h)} \tag{5.42}$$

with unknown amplitudes T_q.

5.4.2 Relations Resulted from Conditions on the Boundaries

Magnetic field (5.33) must be equal to magnetic field (5.35) in the input waveguide aperture. Projection of this equality on the transverse functions of the input waveguide results in algebraic equations

$$\frac{R_m}{2 \quad \delta_{m1}} + \sum_{q=1} \bar{H}_q(z \quad)Q_{mq}^{(0)} = \delta_{m1} \tag{5.43}$$

where $m = 1, 2, \ldots$, and

$$Q_{mq}^{(0)} = \frac{1}{a_w} \int_{-a_w/2}^{a_w/2} \cos\beta_{wm}(x + a_w/2)\cos\bar{\beta}_q(x + a_0/2)dx$$

$$= \frac{1}{2}\cos\frac{(m \quad q)\pi}{2}\left[\frac{\sin\left(m \quad \frac{q\,a_w}{a_0} \div \frac{\pi}{2}\right)}{m \quad \frac{q\,a_w}{a_0} \div \frac{\pi}{2}} + (\quad 1)^q \frac{\sin\left(m \; + \frac{q\,a_w}{a_0} \div \frac{\pi}{2}\right)}{m \; + \frac{q\,a_w}{a_0} \div \frac{\pi}{2}}\right] \tag{5.44}$$

with $m \; = m \quad 1$ and $q \; = q \quad 1$.

Electric field (5.36) in the lower horn section must vanish on the input waveguide flange and be equal to electric field (5.34) in the input waveguide. Projecting this boundary condition on the transverse functions used in expansions (5.35) and (5.36) for the lower horn section, we obtain

$$\bar{E}_p(z \;) = \frac{(2 \quad \delta_{p1})a_w}{\omega\varepsilon_0\varepsilon_w a_0} \sum_{n=1} (\delta_{n1} \quad R_n)\gamma_{wn}Q_{np}^{(0)} \tag{5.45}$$

where $p = 1, 2, \ldots$.

The similar projective matching of the transverse magnetic and electric fields on the junction of the lower and upper horn sections at $z = z \; = \; h_1$ gives the following algebraic equations

$$\frac{\bar{H}_p(z \;)}{2 \quad \delta_{p1}} + \sum_{n=1} \tilde{H}_n(z \;)Q_{pn}^{(1)} = 0, \quad p = 1, 2, \ldots \tag{5.46}$$

$$\tilde{E}_m(z \;) = \frac{(2 \quad \delta_{m1})a_0}{a} \sum_{q=1} \bar{E}_q(z \;)Q_{qm}^{(1)}, \quad m = 1, 2, \ldots \tag{5.47}$$

with coefficients $Q_{qm}^{(1)}$ determined by formula (5.44) where m, q, a_w, a_0, β_{wm}, and $\bar{\beta}_q$ should be replaced by q, m, a_0, a, $\bar{\beta}_q$, and $\tilde{\beta}_m$, respectively.

Projective matching of magnetic fields (5.37) and (5.39) in the upper section aperture at $z = 0$, as well as projective matching of electric fields (5.40) and (5.38) in the same aperture with accounting for the fact that (5.40) must vanish on the flange, give two more groups of algebraic equations

$$\frac{\tilde{H}_m(0)}{2 \quad \delta_{m1}} + \sum_{q=} H_q(0)Q_{mq} = 0, \quad m = 1, 2, \ldots \tag{5.48}$$

$$E_p(0) = \frac{a}{b} \sum_{n=1} \tilde{E}_n(0)Q_{np}, \quad p = 0, \pm 1, \ldots \tag{5.49}$$

with coefficients

$$Q_{mq} = \frac{1}{a}\int_{-a/2}^{a/2} \cos\tilde{\beta}_m(x+a/2)e^{-i\alpha_q x}dx$$
$$= i\alpha_q a\frac{e^{i\alpha_q a/2} - (-1)^m e^{-i\alpha_q a/2}}{(m\pi)^2 - (\alpha_q a)^2} \tag{5.50}$$

$m = m - 1$, and the asterisk at Q_{mq} in (5.48) denotes a complex conjugation.

Finally, matching similarly magnetic fields (5.39) and (5.41) as well as electric fields (5.40) and (5.42) at $z = h$, we obtain the relations

$$T_p = H_p(h) \tag{5.51}$$

$$E_p(h) = \frac{1}{\omega\varepsilon_0}\Gamma_p T_p = \frac{1}{\omega\varepsilon_0}\Gamma_p H_p(h) \tag{5.52}$$

$p = 0, \pm 1$, which will be used later.

5.4.3 Finite Element Method for H-Polarized Waves

Let us consider the magnetic field (5.35) in the lower horn section. Unlike (5.16) written for E-polarized waves, field (5.35) must satisfy the equation

$$-\frac{\partial}{\partial x}\left(\frac{1}{\tilde{\varepsilon}}\frac{\partial H_y}{\partial x}\right) - \frac{\partial}{\partial z}\left(\frac{1}{\tilde{\varepsilon}}\frac{\partial H_y}{\partial z}\right) + k^2 H_y = 0 \tag{5.53}$$

resulting from Maxwell's equations where $\tilde{\varepsilon}(x,z) = \varepsilon_t$ in the area occupied by the dielectric element and $\tilde{\varepsilon}(x,z) = 1$ in the gaps. Let's multiply (5.53) by the transverse function $[(2 - \delta_{p1})/a_0]\cos\bar{\beta}_p(x + a_0/2)$ and integrate over x from $-a_0/2$ to $a_0/2$. After integration of the first term in (5.53) by parts, we obtain

$$\frac{2 - \delta_{p1}}{a_0}\int_{-a_0/2}^{a_0/2} \bar{\beta}_p\frac{1}{\tilde{\varepsilon}}\frac{\partial H_y}{\partial x}\sin\bar{\beta}_p(x + a_0/2)$$
$$+ \left[-\frac{\partial}{\partial z}\left(\frac{1}{\tilde{\varepsilon}}\frac{\partial H_y}{\partial z}\right) + k^2 H_y\right]\cos\bar{\beta}_p(x + a_0/2)\,dx = 0 \tag{5.54}$$

Following the one-dimensional finite element method applied to solve (5.54), we represent the variable coefficients standing in expansion (5.35) in the form of superposition

$$\bar{H}_q(z) = \sum_{s=1}^{\bar{N}} \bar{H}_{sq} f_s(z) \tag{5.55}$$

of triangular functions (5.20) with unknown constant coefficients $\bar{H}_{sq}$. The other notations concerning the number of the nodes, coordinates of the nodes, and

node spacing remain the same as those introduced in Section 5.3 in the case of E-polarization. Let's multiply (5.54) by $f_s(z)$ and integrate over z from z to z. Integrating the first term in square brackets in (5.54) by parts and taking into account that

$$\frac{1}{\tilde{\varepsilon}}\frac{H_y}{z} = i\omega\varepsilon_0 E_x$$

we obtain

$$\begin{aligned}
&{}^{z}_{z}\frac{2}{a_0}\delta_{p1}\Big|_{a_0/2}^{a_0/2}\bar{\beta}_p\frac{1}{\tilde{\varepsilon}}\frac{H_y}{x}f_s\sin\bar{\beta}_p(x+a_0/2)\\
&+k^2H_yf_s\quad\frac{1}{\tilde{\varepsilon}}\frac{H_y}{z}\frac{df_s}{dz}\cos\bar{\beta}_p(x+a_0/2)\;dxdz\\
&+i\omega\varepsilon_0\frac{2}{a_0}\delta_{p1}\Big|_{a_0/2}^{a_0/2}[E_x(x,z)\delta_{s\bar{N}}\quad E_x(x,z)\delta_{s1}]\\
&\cos\bar{\beta}_p(x+a_0/2)dx=0
\end{aligned}\tag{5.56}$$

Substituting now (5.35), (5.36), and (5.55) into (5.56) and accounting for (5.45), we reduce (5.56) to a subsystem of linear algebraic equations

$$\begin{aligned}
&\delta_{s1}\frac{(2\quad\delta_{p1})ia_w}{\varepsilon_w a_0}\sum_{n=1}\gamma_{wn}Q_{np}^{(0)}R_n+\sum_{s=1}^{\bar{N}}\sum_{q=1}\bar{A}_{pq}^{s\,s}\bar{H}_{sq}\\
&+\frac{ik}{\eta_0}\bar{E}_p(z)\delta_{s\bar{N}}=\delta_{s1}\frac{(2\quad\delta_{p1})ia_w}{\varepsilon_w a_0}\gamma_{w1}Q_{1p}^{(0)}
\end{aligned}\tag{5.57}$$

where $s = 1, 2, \ldots \bar{N}$; $p = 1, 2, \ldots$; $\eta_0 = (\mu_0/\varepsilon_0)^{1/2}$ is the wave resistance of free space,

$$\begin{aligned}
\bar{A}_{pq}^{s\,s}=&\;\bar{\gamma}_p^2\int_z^z f_s f_s dz\int_z^z\frac{df_s}{dz}\frac{df_s}{dz}dz\div\delta_{pq}\\
&+\frac{\varepsilon_t\quad 1}{\varepsilon_t}\int_z^z f_s f_s\bar{X}_{pq}dz+\int_z^z\frac{df_s}{dz}\frac{df_s}{dz}\bar{W}_{pq}dz\div
\end{aligned}\tag{5.58}$$

$$\begin{aligned}
\bar{X}_{pq}(z)&=\frac{2\bar{\beta}_p\bar{\beta}_q}{a_0}\Big|_{t/2}^{t/2}\sin\bar{\beta}_p\;\;x+\frac{a_0}{2}\div\sin\bar{\beta}_q\;\;x+\frac{a_0}{2}\div dx\\
&=\bar{\beta}_p\bar{\beta}_q\cos\frac{(p\quad q)\pi}{2}\;\;\frac{\sin\dfrac{(p\quad q)\pi t}{2a_0}}{\dfrac{(p\quad q)\pi}{2}}\quad(\;\;1)^{q\;\;1}\frac{\sin\dfrac{(p+q\quad 2)\pi t}{2a_0}}{\dfrac{(p+q\quad 2)\pi}{2}}
\end{aligned}\tag{5.59}$$

$$\overline{W}_{pq}(z) = \frac{2 - \delta_{p1}}{a_0} \int_{-t/2}^{t/2} \cos\overline{\beta}_p \left(x + \frac{a_0}{2}\right) \cos\overline{\beta}_q \left(x + \frac{a_0}{2}\right) dx$$

$$= \frac{2 - \delta_{p1}}{2} \cos\frac{(p-q)\pi}{2} \left[\frac{\sin\dfrac{(p-q)\pi t}{2a_0}}{\dfrac{(p-q)\pi}{2}} + (-1)^{q-1} \frac{\sin\dfrac{(p+q-2)\pi t}{2a_0}}{\dfrac{(p+q-2)\pi}{2}} \right] \tag{5.60}$$

$\overline{\gamma}_p = (k^2 - \overline{\beta}_p^2)^{1/2}$ and $t(z) = t_{00} - (t_{00} - t_{01})(z - z_-)/h_0$ is the dielectric element width.

5.4.4 Total Algebraic System

The magnetic field (5.37) in the upper horn section is considered similarly. Each unknown variable coefficient in expansion (5.37) is represented in the form of a superposition of N triangular functions; that is,

$$\tilde{H}_n(z) = \sum_{s=1}^{\tilde{N}} \tilde{H}_{sn} f_s(z) \tag{5.61}$$

with unknown constant coefficients H_{sn}. The application of the finite element method results in the linear algebraic equations

$$\delta_{s1} \frac{(2 - \delta_{m1})a_0}{a} \sum_{q=1} Q_{qm}^{(1)} \frac{ik}{\eta_0} \overline{E}_q(z_-) + \sum_{s=1}^{\tilde{N}} \sum_{n=1} \tilde{A}_{mn}^{s\,s} \tilde{H}_{sn} + \frac{ik}{\eta_0} \tilde{E}_m(0)\delta_{s\,\tilde{N}} = 0 \tag{5.62}$$

where $s = 1, 2, ..., \tilde{N}$ and $m = 1, 2, ...$ In the process of deriving (5.62), we have accounted for expressions (5.38) and (5.47). Matrix elements $\tilde{A}_{mn}^{s\,s}$ are determined by expression (5.58) where pq, z_-, z_+, $\overline{\gamma}_p$, ε_t, $\overline{X}_{pq}$, and $\overline{W}_{pq}$ should be replaced by mn, z_-, 0, $\tilde{\gamma}_m = (k^2 - \tilde{\beta}_m^2)^{1/2}$, ε_a, X_{mn}, and W_{mn}, respectively, while the two latter functions are determined by formulas (5.59) and (5.60) with the replacement of a_0 and $\overline{\beta}_{p(q)}$ by a and $\beta_{m(n)}$, respectively, and taking into account that the dielectric element width in the section in question is determined by $t(z) = t_{10} - (t_{10} - t_{11})(z - z_-)/h_1$.

Finally, applying the finite element method to the determination of magnetic field (5.39) in the region $0 - z - h$ containing the protrusions, and accounting for expressions (5.40), (5.49), (5.51), and (5.52), we obtain one more subsystem of algebraic equations

$$\delta_{s1} \frac{a}{b} \sum_{n=1} Q_{np} \frac{ik}{\eta_0} \tilde{E}_n(0) + \sum_{s=1}^{N} \sum_{q=} A_{pq}^{s\,s} H_{sq} + i\Gamma_p H_{Np}\delta_{s\,N} = 0 \tag{5.63}$$

where $s = 1, 2, \ldots, N$; $p = 0, \pm1, \ldots$; H_{sq} are unknown values of the variable coefficients in expansions (5.39) in points $z_s = (s \quad 1) \quad , \quad = h/(N \quad 1)$, $H_{Np} = H_p(h)$,

$$A_{pq}^{s\,s} = \Gamma_p^2 \int_0^h f_s f_s dz \quad \int_0^h \frac{df_s}{dz}\frac{df_s}{dz} dz \div \delta_{pq} + \alpha_p \alpha_q \int_0^h f_s f_s W_{pq} dz + \int_0^h \frac{df_s}{dz}\frac{df_s}{dz} W_{pq} dz \tag{5.64}$$

$$W_{pq}(z) = \frac{\varepsilon \quad 1}{\varepsilon} \frac{\sin[\pi(p \quad q)t/b]}{\pi(p \quad q)} \tag{5.65}$$

and $t(z) = t_0 \quad (t_0 \quad t_1)z/h$ is the width of the protruding part.

Subsystems (5.43), (5.57), (5.46), (5.62), (5.48), and (5.63) in the indicated succession form the total system of linear algebraic equations for unknowns R_m, $\bar{H}_{sq}$, $i\bar{E}_q(z\ )/\eta_0$, $\tilde{H}_{sn}$, $i\tilde{E}_n(0)/\eta_0$, and H_{sq}. Note that $\bar{H}_q(z\ )$ in (5.43), $\bar{H}_p(z\ )$ and $\tilde{H}_n(z\ )$ in (5.46), as well as $\tilde{H}_m(0)$ and $H_q(0)$ in (5.48) are equal to $\bar{H}_{1q}$, $\bar{H}_{\bar{N}p}$, $\tilde{H}_{1n}$, $\tilde{H}_{\tilde{N}m}$, and H_{1q}, respectively. Note also that unlike [31], where the algorithm involves independent expansions both for E_x and for H_y in all the nodes, we use here the values of E_x only on the boundaries between the sections. This approach makes the algebraic system order almost two times smaller.

5.4.5 Realization of the Algorithm and Discussion of the Array Characteristics

The infinite algebraic system obtained earlier is solved by the method of truncation. If we account for M_w waveguide modes in (5.33) and (5.34), $\bar{M}$ transverse functions in (5.35) and (5.36), M transverse functions in (5.37) and (5.38), as well as M transverse functions in (5.39), (5.40), (5.41), and (5.42), the order of the system, like in the case of E-polarization, will be equal to $M_w + (\bar{N}+1)\bar{M} + (\tilde{N}+1)\tilde{M} + NM$. Since $f_s f_s \quad 0$ in (5.58) and (5.64) for $|s \quad s| > 1$, the matrix of the system has a block-banded structure. An example of such a structure is given in Figure 5.13, where only nonshadowed blocks have nonzero elements, while the blocks with diagonal lines have nonzero elements on the diagonals only. Calculation of the matrix elements in (5.57), (5.62), and (5.63) has been carried out using piecewise-linear approximation of functions (5.59), (5.60), (5.65), and similar functions $\tilde{X}_{mn}$ and $\tilde{W}_{mn}$, via which the elements $\tilde{A}_{mn}^{s\,s}$ in (5.62) are calculated. After obtaining numerical solution of the system by the Gauss' elimination method, we have the array reflection coefficient R_1, as well the ability to calculate the normalized array element pattern [41]

$$F(\theta) = \sqrt{\frac{\varepsilon_w^{1/2} b}{a_w}} \, |T_0(kb\sin\theta)| \cos\theta \tag{5.66}$$

where $T_0 = H_{N0}$ is determined as a result of solution of the system.

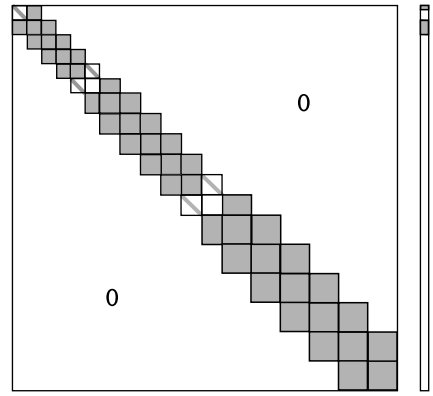

Figure 5.13 Structure of linear algebraic system corresponding to excitation of array in TEM modes.

The algorithm presented earlier has been realized in FORTRAN code tested in the same ways as those used for the case of E-polarization considered in Section 5.3. The power balance relation [41]

$$\sum_n \frac{\mathrm{Re}\{\gamma_{wn}\}}{(2-\delta_{n1})\gamma_{w1}} |R_n|^2 + \frac{\varepsilon_w b}{a_w} \sum_q \frac{\mathrm{Re}\{\Gamma_q\}}{\gamma_{w1}} |T_q|^2 = 1 \tag{5.67}$$

in all calculations is satisfied with accuracy of no less than six decimal digits. Some examples characterizing convergence of the array reflection coefficient corresponding to dielectric element permittivity $\varepsilon_w = \varepsilon_t = \varepsilon_a = \varepsilon = 6$, are presented in Figures 5.14 and 5.15. The other array parameters are indicated in the caption for Figure 5.14. The results shown in Figure 5.14 have been obtained at the number of Floquet modes $M = 31$, which is deliberately large enough to obtain accurate solutions for indicated element spacing $b = 0.6\lambda$ and at the number of waveguide modes $M_w = 15$. The solid curve corresponds to the number of nodes $N = 30$ for the protruding section. We can see that the curves obtained at smaller values of N quickly approach the solid curve as N increases. Similarly, the convergence of the results by increasing the number of transverse functions at sufficiently large number of the nodes N is demonstrated in Figure 5.15.

A comparison of the array element pattern calculated by the hybrid projective method described earlier with the results obtained in [20] by the mode matching method for array with parameters $b = 0.535\lambda$, $a_w = a_0 = a = t_{00} = t_{01} = t_{10} = t_{11} = t_0 = t_1 = 0.432b$, $h_0 = h_1 = h = 0.5\lambda$, $\varepsilon_w = \varepsilon_t = \varepsilon_a = \varepsilon = 2.56$ is shown in Figure 5.16. The results obtained by the former method shown by crosses have been obtained using $M_w = \bar{M} = \tilde{M} = 10$ waveguide modes, $M = 21$ Floquet modes, and $\bar{N} = \tilde{N} = N = 15$ nodes of the triangular functions. As we see, they practically coincide with the data given in [20]. The results of a similar comparison for the protrusion length two times larger ($h = \lambda$), also validating the code operation, may be found in [51].

Consider now some examples of shaping sector element patterns in the waveguide-dielectric array excited in TEM modes. The array characteristics corresponding to element spacing $b = 0.8\lambda$ and $b = 0.91\lambda$ for the case of uniform filling of the horn sections with dielectric considered in [51] are presented in Figures 5.17

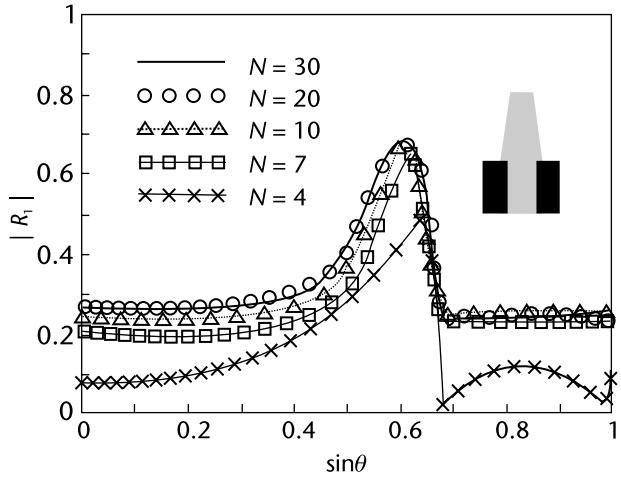

Figure 5.14 Reflection coefficient of array with $b = 0.6\lambda$, $a_w = a_0 = a = t_{00} = t_{00} = t_{10} = t_{11} = 0.3\lambda$, $t_0 = 0.4\lambda$, $t_1 = 0.2\lambda$, $h_0 = h_1 = 0.1\lambda$, $h = 0.6\lambda$, and $\varepsilon_w = \varepsilon_t = \varepsilon_a = \varepsilon = 6$, excited in TEM modes, calculated at $N = 4$, 7, 10, 20, and 30, and at constant $M = 31$, $M_w = \bar{M} = \tilde{M} = 15$, $\bar{N} = \tilde{N} = 5$.

and 5.18, respectively. The results have been obtained with the application of the one-dimensional finite element method only for the protruding part of the array element. The fields in the horn sections have been represented in the form of superpositions of forward and backward modes with subsequent matching of them on the boundaries of the sections. An optimization of the array geometry has been carried out in the same way as that for the case of E-polarization.

However, unlike the E-polarization, the input waveguide and lower horn section are not filled in with dielectric (i.e., $\varepsilon_w = \varepsilon_t = 1$), while the permittivity of filling in the upper section $\varepsilon_a = 1.5$ has been chosen to be smaller than that for the protrusion $\varepsilon = 2$. Such a choice has allowed us to obtain a smaller width of the protrusion at the base, thereby avoiding the resonance effects that would take place if the upper section was filled in with the same dielectric as that of the protrusion. A

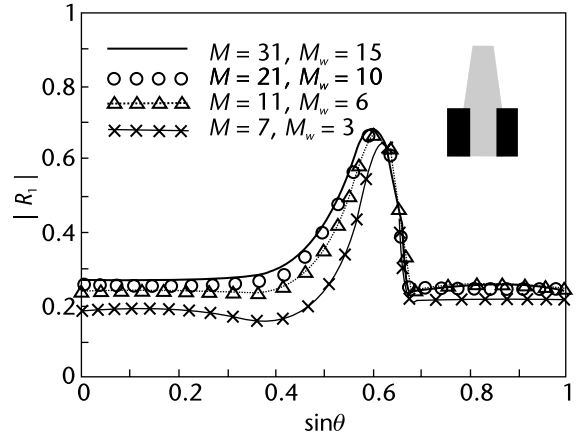

Figure 5.15 The same as in Figure 5.14 at $M = 7$, 11, 21, and 31, and at constant $\bar{N} = \tilde{N} = 5$, $N = 30$.

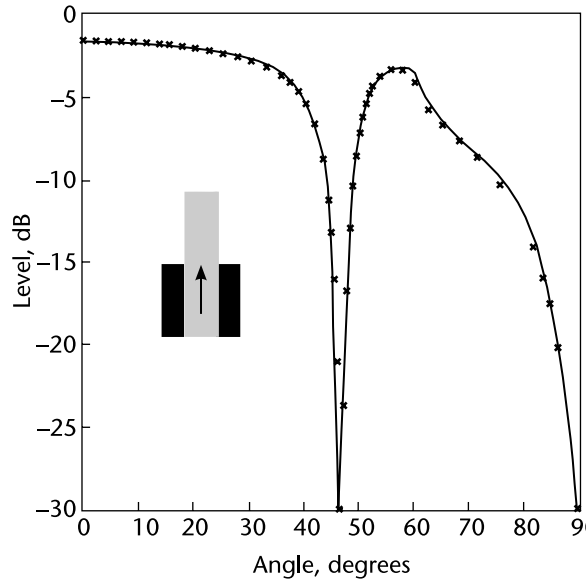

Figure 5.16 Array element pattern calculated by mode-matching method [20] (——) and hybrid projective method (×××).

comparison of the obtained sector element patterns with the ideal sector patterns and element patterns corresponding to optimized waveguide arrays without dielectric shows their relatively high quality. However, as we have already noted in the beginning of Section 5.3, the application of different dielectric materials for filling in the upper section and for the protrusion is not the best solution from the

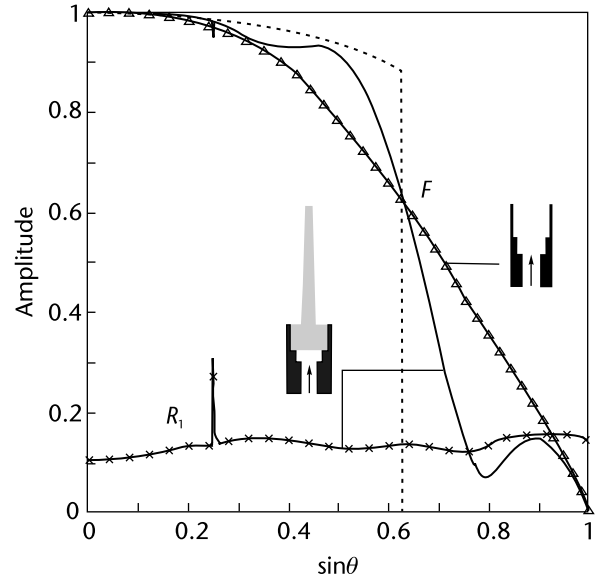

Figure 5.17 Reflection coefficient (×××) and element pattern (——) of array with $b = 0.8\lambda$, $a_w = 0.4\lambda$, $a_0 = 0.57\lambda$, $a = 0.78\lambda$, $h_0 = 0.17\lambda$, $h_1 = 0.35\lambda$, $t_0 = 0.32\lambda$, $t_1 = 0.21\lambda$, $h = 2.3\lambda$, $\varepsilon_w = \varepsilon_t = 1$, $\varepsilon_a = 1.5$, $\varepsilon = 2$, excited in TEM modes, calculated at $M_w = 8$, $M = 21$, and $N = 50$; (- - - -) is the ideal element pattern, and ( ) is the element pattern in array without dielectric at $a_w = 0.4\lambda$, $a_0 = 0.568\lambda$, $h_0 = 0.22\lambda$, and $h_1 = 0.4\lambda$.

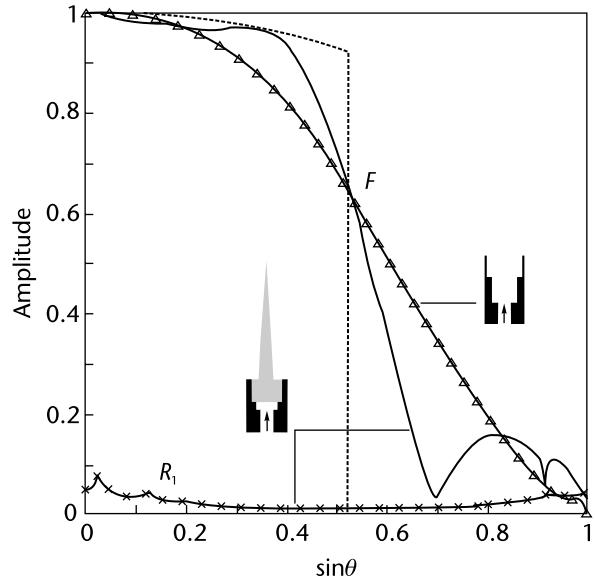

Figure 5.18 Reflection coefficient (×××) and element pattern (——) of array with $b = 0.96\lambda$, $a_w = 0.4\lambda$, $a_0 = 0.57\lambda$, $a = 0.78\lambda$, $h_0 = 0.17\lambda$, $h_1 = 0.53\lambda$, $t_0 = 0.45\lambda$, $t_1 = 0$, $h = 3.6\lambda$, $\varepsilon_w = \varepsilon_t = 1$, $\varepsilon_a = 1.5$, $\varepsilon = 2$, $M_w = 8$, $M = 21$, and $N = 73$; ( ) is the element pattern in array without dielectric at $a_w = 0.4\lambda$, $a_0 = 0.653\lambda$, $h_0 = 0.7\lambda$, $a = 0.94\lambda$, at $h_1 = 0.53\lambda$.

viewpoint of the practical array mechanical design. Some demonstrative results for a better array design with partial filling of the horn sections with dielectric (Figure 5.5) are presented and discussed later.

The study of how the geometric parameters of the structure influence on the quality of shaping the sector element patterns has shown that the best results are achieved when using long sharpened protruding elements. The modeling has been carried out as follows. We specify the element spacing b and the upper section width a, such that $b \quad a$ is equal to 0.01λ to 0.02λ, the protrusion length h of a few wavelengths, and the protrusion permittivity ε, and assume first that the input waveguide and the lower horn section have the same width as that of the upper section (i.e., $a_w = a_0 = a$). The input waveguide is assumed to be empty (i.e., $\varepsilon_w = 1$). The dielectric element with $\varepsilon_t = \varepsilon_a = \varepsilon$ passing through the horn sections is assumed to be sharpened at both ends ($t_{00} = t_1 = 0$), while its other transverse dimensions are identical ($t_{01} = t_{10} = t_{11} = t_0$). The height of the lower horn section is specified to be large enough (~2λ) to provide a natural good array match. An example of such an intermediate array version with an element spacing $b = 0.8\lambda$ is shown in Figure 5.19. The element pattern is shown for three values of the dielectric element width in its middle part, while the reflection coefficient is presented only for $t_{01} = t_{10} = t_{11} = t_0 = 0.4\lambda$ because its low level for two other values of the width almost coincides with the shown one. As we see, there exists an optimal dielectric element width at which the element pattern level in the scan region becomes closest to the ideal element pattern level also shown in Figure 5.19. The further optimization is carried out at the specified width and permittivity of the input waveguide. The natural choice here from the viewpoint of a mechanical design is $\varepsilon_w = \varepsilon$. The dielectric element width in the lower section is assumed to be equal to the width in the upper section (i.e., $t_{00} = t_{01} = t_{10} = t_{11}$), while

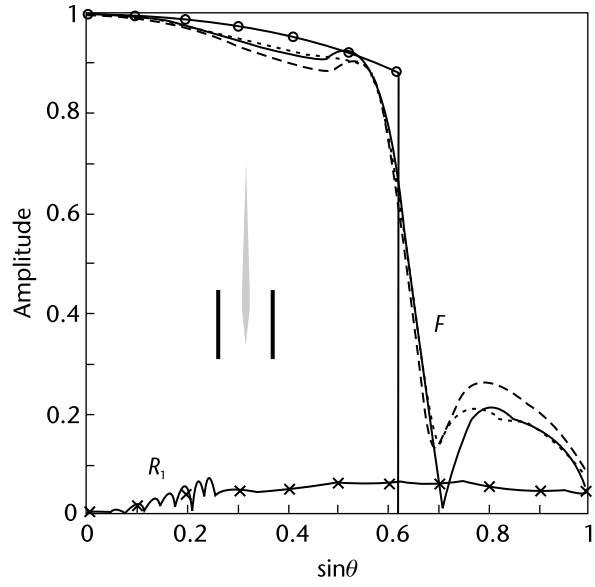

Figure 5.19 Characteristics of an array with $b = 0.8\lambda$, $a_w = a_0 = a = 0.78\lambda$, $h_0 = 1.8\lambda$, $h_1 = 0.5\lambda$, $h = 7.9\lambda$, $t_{00} = t_1 = 0$, $\varepsilon_w = 1$, and $\varepsilon_t = \varepsilon_a = \varepsilon = 2$, calculated at $M_w = \bar{M} = \tilde{M} = 11$, $M = 13$, $\bar{N} = 19$, $\tilde{N} = 11$ and $N = 81$; $t_{01} = t_{10} = t_{11} = t_0 = 0.33\lambda$ (– – –), 0.4λ (——), 0.47λ (- - -); (o o o o) is the ideal element pattern.

the height h_0 and width a_0 of the lower horn section are selected to provide passage of the dominant TEM mode from the input waveguide to the upper horn section without reflection. Then, we select the height of the upper section h_1 at which the element pattern shape becomes closest to the ideal one, and the resonance effects that are possible in the arrays in question are avoided or minimized. Some examples

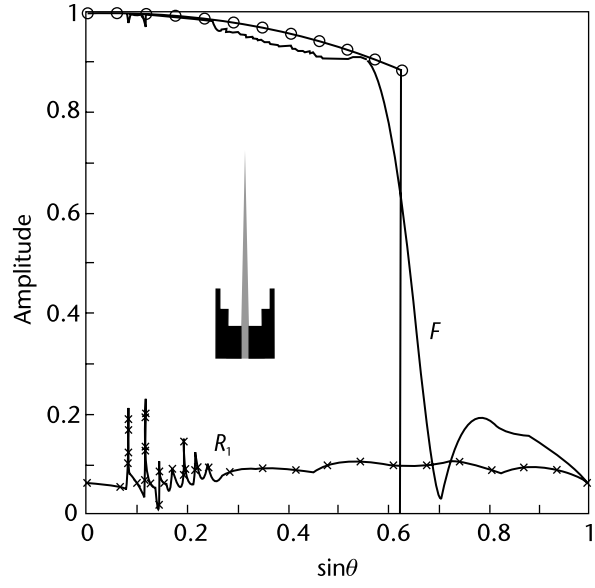

Figure 5.20 Characteristics of an array with $b = 0.8\lambda$, $a_w = 0.3\lambda$, $a_0 = 0.5\lambda$, $a = 0.78\lambda$, $h_0 = 0.55\lambda$, $h_1 = 0.5\lambda$, $h = 7.9\lambda$, $t_{00} = t_{01} = t_{10} = t_{11} = t_0 = 0.4\lambda$, $t_1 = 0$, $\varepsilon_w = \varepsilon_t = \varepsilon_a = \varepsilon = 2$, calculated at $M_w = 5$, $\bar{M} = 7$, $\tilde{M} = 11$, $M = 13$, $\bar{N} = 11$, $\tilde{N} = 7$, and $N = 81$.

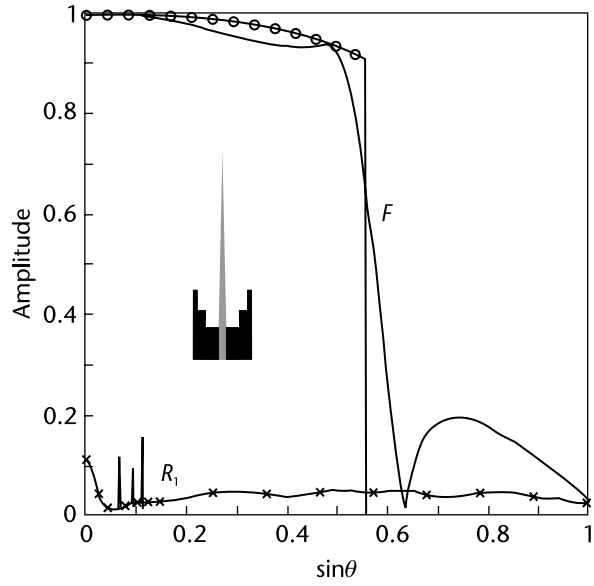

Figure 5.21 Characteristics of an array with $b = 0.9\lambda$, $a_w = 0.3\lambda$, $a_0 = 0.58\lambda$, $a = 0.88\lambda$, $h_0 = 0.18\lambda$, $h_1 = 0.52\lambda$, $h = 8\lambda$, $t_{00} = t_{01} = t_{11} = t_0 = 0.34\lambda$, $t_1 = 0$, $\varepsilon_w = \varepsilon_t = \varepsilon_a = \varepsilon = 2$, calculated at $M_w = 5$, $\bar{M} = 9$, $\tilde{M} = 15$, $M = 17$, $\bar{N} = 5$, $\tilde{N} = 11$, and $N = 81$.

of the array characteristics obtained as a result of the optimization described earlier are presented in Figure 5.20 for an array with $b = 0.8\lambda$ and in Figure 5.21 for an array with $b = 0.9\lambda$. The other array parameters are indicated in the captions to the figures.

The behavior of the array element pattern as the frequency deviates at ±3% is demonstrated in Figure 5.22 for an array without stepped transitions (like that in

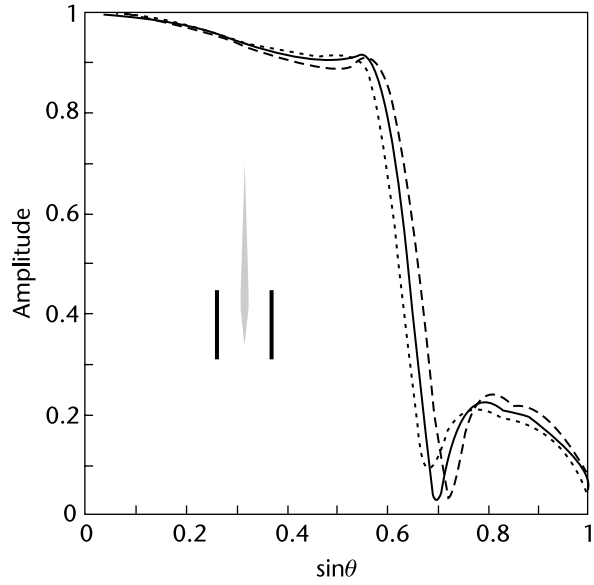

Figure 5.22 Element pattern in an array with parameters indicated in the caption for Figure 5.19 with $t_0 = 0.4\lambda$, at central frequency f_0 (——), as well as at $0.97f_0$ (– – –) and $1.03f_0$ (- - -).

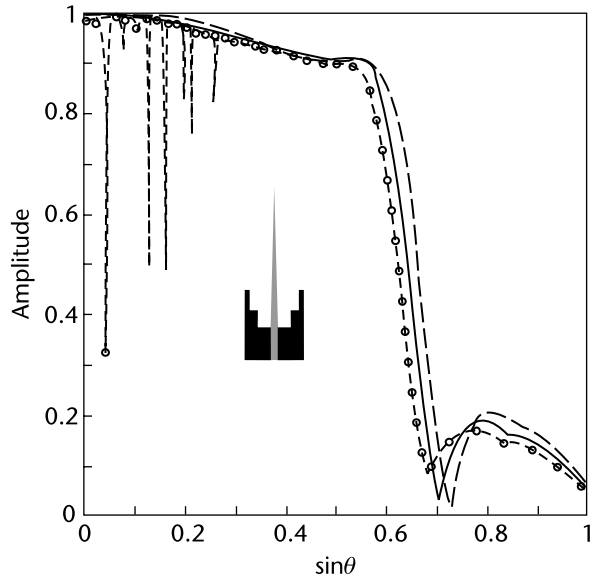

Figure 5.23 Element pattern in an array with parameters indicated in the caption for Figure 5.20 at the central frequency f_0 (——), as well as at $0.97f_0$ (– – –) and $1.03f_0$ (- - -).

Figure 5.19) and in Figure 5.23 for an element geometry similar to that shown in Figure 5.20. As we see, the element pattern shape remains a sector one with a change in the width in accordance with a change in the element spacing in wavelengths. No resonance effects are observed in the array without the stepped transitions. In the case of the array with the stepped transitions, the resonance effects that are minimized as a result of optimization at the central frequency (corresponding to λ), as shown in Figures 5.20 and 5.21, may occur to a greater degree with a change in the frequency as we see in Figure 5.23.

5.5 Three-Dimensional Problem

The hybrid projective method developed earlier for the solution of two-dimensional problems is generalized in the present section over a three-dimensional problem for an array of circular waveguides with protruding dielectric rods nonuniform in the longitudinal direction. Such a problem is of great interest for practice.

5.5.1 Statement of the Problem and Fields in the Structure

The array geometry in a rectangular Cartesian coordinate system $0xyz$ is shown in Figure 5.24. The elements of the array, which is considered here as an infinite periodic structure, are arranged in horizontal rows with spacing d_x, while the rows themselves are arranged with spacing d_y. The array lattice may be both rectangular and triangular, where, as shown in Figure 5.24(a), the adjacent rows are shifted along the x-axis at distance $d_x/2$ with respect to each other. The most important special case of the triangular lattice is a hexagonal one where $d_y = d_x\sqrt{3}/2$. The array element as a whole consists of an input semi-infinite circular waveguide of

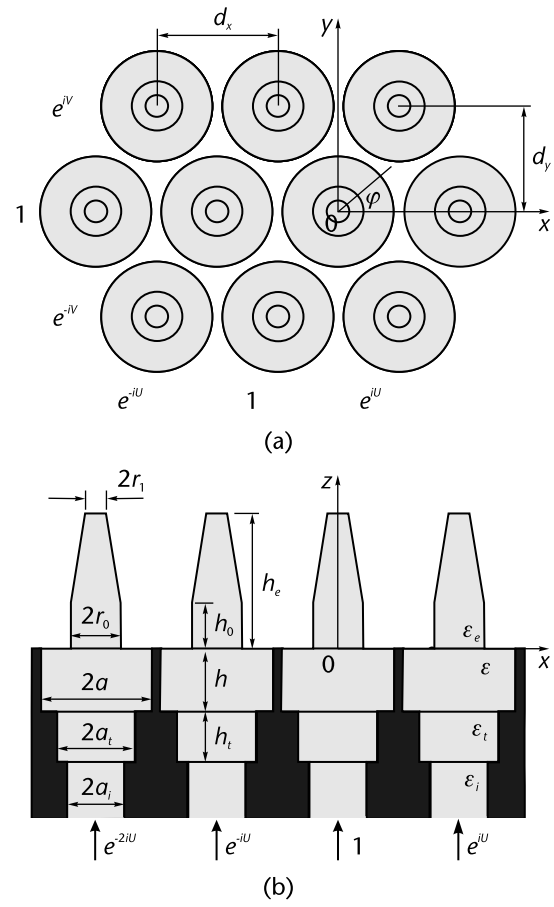

Figure 5.24 (a) Aperture and (b) longitudinal cut in plane 0*xz* of stepped circular waveguide array with protruding dielectric rods.

diameter $2a_i$, an intermediate section of diameter $2a_t$ and height h_t, and an upper section of diameter $2a$ and height h (the notations here are the same as those in [58]). The indicated waveguide sections are connected to each other by flanges and may be filled in with dielectric of relative permittivity ε_i, ε_t, and ε, respectively. The upper sections go to an infinite common flange arranged in the plane $z = 0$. Each array element has a dielectric rod of relative permittivity ε_e and height h_e protruding above the waveguide aperture. The rod at its base has a cylindrical part of diameter $2r_0$ and height h_0 changing for a conical part of diameter $2r_1$ at the end. The walls of all the waveguide sections and flanges are assumed to be perfectly conducting, while the sections and protruding rod have a common axis.

We also assume that the input waveguides are excited in their dominant modes TE_{11} of circular polarization. The amplitudes of the incident modes are equal to unity, while their phases change linearly with increment U between adjacent elements in each horizontal row and with increment V between adjacent rows, as shown in Figure 5.24. The indicated phase increments are related to the main array beam direction characterized by specified angles θ and φ measured from the z and x axes, respectively, by formulas [see also relation (1.22)]

$$U = kd_x u, \quad V = kd_y v + U\delta$$

where $u = \sin\theta\cos\varphi$ and $v = \sin\theta\sin\varphi$ are direction cosines, $\delta = 0$ for rectangular lattice, and $\delta = 1/2$ for triangular lattice.

To determine the field radiated by the array in free space and the field reflected back to the waveguides as well as the array reflection coefficient and element pattern, we represent the transverse components of the electric and magnetic field strength in the upper waveguide section in the form of expansions over eigenmodes of circular waveguide

$$\begin{aligned} \boldsymbol{E}_t(\rho,\varphi,0) = \eta_0 \sum_{m,n} & [(A_{1mn}\boldsymbol{e}_{1mn} + B_{1mn})k \quad _{mn} \\ & +(A_{2mn}\boldsymbol{e}_{2mn} \quad B_{2mn})\gamma_{2mn} \quad _{2mn}] \end{aligned} \tag{5.68}$$

$$\begin{aligned} \boldsymbol{H}(\rho,\varphi,0) \quad \boldsymbol{e}_z = \sum_{m,n} & [(A_{1mn}\boldsymbol{e}_{1mn} \quad B_{1mn})\gamma_{1mn} \quad _{1mn} \\ & +(A_{2mn}\boldsymbol{e}_{2mn} + B_{2mn})k\varepsilon \quad _{2mn}] \end{aligned} \tag{5.69}$$

where $\eta_0 = (\mu_0/\varepsilon_0)^{1/2}$ is the wave resistance for free space; A_{jmn} are unknown amplitudes of the TE ($j = 1$) and TM ($j = 2$) modes going from the beginning of the section toward the aperture; B_{jmn} are unknown amplitudes of the TE and TM modes going back from the aperture; $e_{jmn} = \exp(i\gamma_{jmn}h)$, $\gamma_{jmn} = (k^2\varepsilon \quad g_{jmn}^2)^{1/2}$, and $g_{jmn} = \mu_{jmn}/a$ are longitudinal and transverse propagation constants; μ_{1mn} and μ_{2mn} are nth roots of equations $J_m(\mu) = 0$ and $J_m(\mu) = 0$, respectively; $m = 0, \pm 1\ldots$, $n = 1$, $2, \ldots, J_m(\ldots)$, and $J_m(\ldots)$ are the Bessel function of the mth order and its derivative over the argument;

$$_{1mn}(\rho,\varphi) = \frac{im}{\rho} J_m(g_1\rho)\boldsymbol{e}_\rho \quad g_1 J_m(g_1\rho)\boldsymbol{e}_\varphi \quad \frac{e^{im\varphi}}{N_{1mn}} \tag{5.70}$$

$$_{2mn}(\rho,\varphi) = g_2 J_m(g_2\rho)\boldsymbol{e}_\rho + \frac{im}{\rho} J_m(g_2\rho)\boldsymbol{e}_\varphi \quad \frac{e^{im\varphi}}{N_{2mn}} \tag{5.71}$$

are orthonormalized vector wave functions for a circular waveguide, with normalizing coefficients

$$N_{1mn} = \pi^{1/2}(\mu_{1mn}^2 \quad m^2)^{1/2} J_m(\mu_{1mn}) \tag{5.72}$$

$$N_{2mn} = \pi^{1/2}\mu_{2mn} J_m(\mu_{2mn}) \tag{5.73}$$

$\boldsymbol{e}_z$ is the unit vector directed along the z-axis; and $\boldsymbol{e}_\rho$ and $\boldsymbol{e}_\varphi$ are unit vectors of cylindrical coordinates ρ and φ related to the Cartesian coordinates by formulas $x = \rho\cos\varphi$ and $y = \rho\sin\varphi$. The double index mn at the constants g_{1mn} and g_{2mn} in (5.70) and (5.71) is omitted for brevity. For simplification of the subsequent expres-

sions, we introduce a prevailing order numbering of the waveguide modes for each type and further replace the double index by a single-standing one.

The amplitudes A_{jmn} and B_{jmn} of the forward and backward modes in (5.68) and (5.69) relate to each other and to the incident mode amplitude in the input section by formula

$$A_{j\,n} \sum_{j=1}^{2} \sum_{n} S^{11}_{j\,n\,,jn} B_{jn} e_{jn} = S^{10}_{j\,n\,,1l} \tag{5.74}$$

where $j = 1, 2$; $n = 1, 2, \ldots$ and $n = 1, 2, \ldots$ are the ordinal numbers of the modes; l is the ordinal number of the incident mode; and $S^{\nu\ \nu}_{j\,n\,,jn}$ is an element of the scattering matrix of the transition between the input section ($\nu = 0$, $\nu = 0$,) and upper section ($\nu = 1$, $\nu = 1$). This element is a complex amplitude of a $j\ n$ th mode excited in the ν th section when a jnth mode of unit amplitude incidents to the transition from the νth section. The indicated matrix elements are calculated by the well-known mode-matching method [59–61] for a single-standing step in a waveguide in combination with the method of generalized matrices of scattering (see, for instance, [62]) for accounting for interaction between two steps.

The transverse electric and magnetic fields above the ends of the rods ($z \quad h_e$) are represented by expansions over the complete system of vector Floquet modes [18] [see also formulas (1.24) and (1.25)]

$$\boldsymbol{E}_t(x,y,z) = \eta_0 \sum_{p,q} (T_{1pq} k \boldsymbol{\psi}_{1pq} + T_{2pq} \Gamma_{pq} \boldsymbol{\psi}_{2pq}) e^{i\Gamma_{pq}(z\ \ h_e)} \tag{5.75}$$

$$\boldsymbol{H}(x,y,z) \quad \boldsymbol{e}_z = \sum_{p,q} (T_{1pq} \Gamma_{pq} \boldsymbol{\psi}_{1pq} + T_{2pq} k \boldsymbol{\psi}_{2pq}) e^{i\Gamma_{pq}(z\ \ h_e)} \tag{5.76}$$

with unknown amplitudes T_{jpq} (j = 1 and 2 for TE and TM modes, respectively), propagation constants determined by formula (1.21), and transverse wave functions determined by (1.20), (1.26), and (1.27). As with the waveguide modes, the double index pq used in (5.75) and (5.76) will be replaced in subsequent formulas by a single-standing index corresponding to an ordinal number of an appropriate Floquet mode.

As with the incomplete Galerkin method [26–30], we represent the transverse components of the fields in the free space region $0 \quad z \quad h_e$ containing the dielectric rods in the form of expansions over transverse vector functions (1.26) and (1.27)

$$\boldsymbol{E}_t(x,y,z) = \eta_0 k \sum_{q} [E_{1q}(z) \boldsymbol{\psi}_{1q} + E_{2q}(z) \boldsymbol{\psi}_{2q}] \tag{5.77}$$

$$\boldsymbol{H}_t(x,y,z) = k \sum_{q} [H_{1q}(z) \boldsymbol{\psi}_{1q} + H_{2q}(z) \boldsymbol{\psi}_{2q}] \tag{5.78}$$

with unknown coefficients depending on z. Then the longitudinal field components will be expressed by formulas

$$E_z(x,y,z) = \frac{\eta_0}{\tilde{\varepsilon}} \sum_q w_q H_{1q}(z)\psi_q \tag{5.79}$$

$$H_z(x,y,z) = \sum_q w_q E_{1q}(z)\psi_q \tag{5.80}$$

resulting from (5.77), (5.78), and Maxwell's equations

$$\boldsymbol{H} + \frac{ik\tilde{\varepsilon}}{\eta_0}\boldsymbol{E} = 0 \tag{5.81}$$

$$\boldsymbol{E} \quad ik\eta_0\boldsymbol{H} = 0 \tag{5.82}$$

where $\tilde{\varepsilon} = \varepsilon_e$ in the rods and $\tilde{\varepsilon} = 1$ outside the rods. The constants w_q in (5.79) and (5.80), where q is an ordinal number replacing the double index as indicated earlier, are determined in (1.21).

5.5.2 The Hybrid Projective Method

The electric field (5.77) at $z = 0$ must be equal to zero on the flange and to the field (5.68) in the waveguide aperture. Projecting this condition on the functions complex-conjugated to functions (1.26) and (1.27), we obtain algebraic equations

$$\sum_n (A_{1n}e_{1n} + B_{1n})Q_{1p}^{1n} \quad E_{1p}(0) = 0 \tag{5.83}$$

$$E_{2p}(0) = \sum_n [(A_{1n}e_{1n} + B_{1n})Q_{2p}^{1n} + (A_{2n}e_{2n} \quad B_{2n})Q_{2p}^{2n}\gamma_{2n}/k] \tag{5.84}$$

where p is an ordinal number and

$$Q_{j\,p}^{jn} = \int_0^a \int_0^{2\pi} {}_{jn}\times\psi_{j\,p}\rho d\rho d\varphi \tag{5.85}$$

The calculation of integrals (5.85) using the properties of the Bessel functions yields

$$Q_{1p}^{1n} = s\frac{(\ \ i)^m \mu_{1n}^2}{(\mu_{1n}^2 \quad m^2)^{1/2}} \frac{J_m(w_p a)}{\mu_{1n}^2 \quad (w_p a)^2} e^{im\phi_p} \tag{5.86}$$

$$Q_{2p}^{1n} = s\frac{(\ \ i)^m \ \ ^1 m}{(\mu_{1n}^2 \quad m^2)^{1/2}} \frac{J_m(w_p a)}{w_p a} e^{im\phi_p} \tag{5.87}$$

$$Q_{2p}^{2n} = s\frac{(\ \ i)^m w_p a J_m(w_p a)}{(w_p a)^2 \quad \mu_{2n}^2} e^{im\phi_p} \tag{5.88}$$

$s = 2ia[\pi/(d_x d_y)]^{1/2}$, $\phi_p = \text{arctg}(\beta_p/\alpha_p)$, $Q_{1p}^{2n} = 0$, and m is a number of an azimuthal variation in an nth waveguide mode.

Magnetic field (5.69) in the waveguide aperture must be equal to magnetic field (5.78) multiplied vectorially by $\boldsymbol{e}_z$. Projecting this condition on the functions complex-conjugated to functions (5.70) and (5.71) and taking into account that

$$\psi_{1q} \quad \boldsymbol{e}_z = \quad \psi_{2q}, \psi_{2q} \quad \boldsymbol{e}_z = \psi_{1q} \tag{5.89}$$

we obtain the algebraic equations

$$(A_{1m}e_{1m} \quad B_{1m})\gamma_{1m} \quad k \underset{q}{} [H_{2q}(0)Q_{1q}^{1m} \quad H_{1q}(0)Q_{2q}^{1m} \ ] = 0 \tag{5.90}$$

$$(A_{2m}e_{2m} + B_{2m})\varepsilon + \underset{q}{} H_{1q}(0)Q_{2q}^{2m} \ = 0 \tag{5.91}$$

where m is an ordinal number of a waveguide mode of appropriate type.

The projective matching of electric fields (5.75) and (5.77), as well as magnetic fields (5.76) and (5.78) (the latter must be multiplied vectorially by $\boldsymbol{e}_z$) at $z = h_e$ yields relations

$$\begin{aligned} &E_{1q}(h_e) = T_{1q}, \quad H_{1q}(h_e) = \quad T_{2q}, \\ &E_{2q}(h_e) = \frac{\Gamma_q}{k} T_{2q}, \quad H_{2q}(h_e) = \frac{\Gamma_q}{k} T_{1q} \end{aligned} \tag{5.92}$$

from which we obtain the equalities

$$E_{2q}(h_e) = \quad \frac{\Gamma_q}{k} H_{1q}(h_e) \tag{5.93}$$

$$H_{2q}(h_e) = \frac{\Gamma_q}{k} E_{1q}(h_e) \tag{5.94}$$

to be used for the derivation of subsequent formulas.

Let us consider now Maxwell's equation (5.81), which we multiply scalarly by ψ_{1p} and integrate over the cell area $S = d_x \quad d_y$. Doing that, we use the vector identity

$$\boldsymbol{F} \times(\quad \boldsymbol{G}) = \boldsymbol{G} \times(\quad \boldsymbol{F}) + \quad \times(\boldsymbol{G} \quad \boldsymbol{F})$$

which is valid for any vector functions $\boldsymbol{F}$ and $\boldsymbol{G}$, as well as the properties of the transverse wave functions (1.20), (1.26), and (1.27)

$$\boldsymbol{\psi_{1p}} = \quad i\omega_p \psi_p \boldsymbol{e}_z \tag{5.95}$$

$$\boldsymbol{F} \quad \boldsymbol{\psi_{1p}} = F_z \boldsymbol{\psi_{2p}} \quad (\boldsymbol{F} \times \boldsymbol{\psi_{2p}})\boldsymbol{e}_z \tag{5.96}$$

and as a result obtain projective relation

$$\underset{S}{} i\omega_p \psi_p H_z \quad \boldsymbol{\psi}_{2p}^* \times \frac{\boldsymbol{H}}{z} + \frac{ik\tilde{\varepsilon}}{\eta_0} \boldsymbol{\psi}_{1p}^* \times \boldsymbol{H} \div dxdy = 0 \tag{5.97}$$

Deriving (5.97), we have also taken into account that the part of the divergence associated with transverse coordinates gives no contribution to the integral because of the boundary conditions in the Floquet cell.

The second projective relation is obtained after carrying out a similar operation of projecting Maxwell's equation (5.82) on the same function ψ_{1p}

$$\int_S \left(iw_p \psi_p E_z \quad \psi_{2p} \times \frac{\boldsymbol{E}}{z} \quad ik\eta_0 \psi_{1p} \right) \boldsymbol{H} \div dxdy = 0 \tag{5.98}$$

Projecting of Maxwell's equations (5.81) and (5.82) on function ψ_{2p} with account for properties of functions (1.26) and (1.27)

$$\psi_{2p} = 0 \tag{5.99}$$

$$\boldsymbol{F} \quad \psi_{2p} = \quad F_z \psi_{1p} + (\boldsymbol{F} \times \psi_{1p}) \boldsymbol{e}_z \tag{5.100}$$

yields us two more relations

$$\int_S \psi_{1p} \times \frac{\boldsymbol{H}}{z} + \frac{ik\tilde{\varepsilon}}{\eta_0} \psi_{2p} \boldsymbol{E} \div dxdy = 0 \tag{5.101}$$

$$\int_S \psi_{1p} \times \frac{\boldsymbol{E}}{z} \quad ik\eta_0 \psi_{2p} \boldsymbol{H} \div dxdy = 0 \tag{5.102}$$

Substituting expansions (5.77) through (5.80) in relations (5.97), (5.98), (5.101), and (5.102), we reduce them to a system of ordinary differential equations

$$\Gamma_p^2 H_{1p} + \frac{w_p}{\varepsilon_e} \sum_q w_q W_{pq} H_{1q} \quad ik \frac{dE_{2p}}{dz} = 0 \tag{5.103}$$

$$ik \frac{dH_{2p}}{dz} + \Gamma_p^2 E_{1p} + k^2 \sum_q (Z_{pq} E_{1q} \quad Y_{pq} E_{2q}) = 0 \tag{5.104}$$

$$ik \frac{dH_{1p}}{dz} + k^2 \sum_q (Y_{pq} E_{1q} + Z_{pq} E_{2q}) + k^2 E_{2p} = 0 \tag{5.105}$$

$$H_{2p} = \frac{1}{ik} \frac{dE_{1p}}{dz} \tag{5.106}$$

with coefficients (see also [29])

$$Z_{pq}(z) = \frac{\alpha_p \alpha_q + \beta_p \beta_q}{w_p w_q} W_{pq} \tag{5.107}$$

$$Y_{pq}(z) = \frac{\alpha_p \beta_q \quad \alpha_q \beta_p}{w_p w_q} W_{pq} \tag{5.108}$$

$$W_{pq}(z) = (\varepsilon_e \quad 1)\frac{2\pi r^2}{d_x d_y}\frac{J_1(\ _{pq}r)}{\ _{pq}r} \tag{5.109}$$

where $_{pq} = [(\alpha_p \quad \alpha_q)^2 + (\beta_p \quad \beta_q)^2]^{1/2}$ and

$$r(z) = \begin{array}{l} r_0, \ 0 \quad z \quad h_0, \\ r_0 \quad \dfrac{r_0 \quad r_1}{h_e \quad h_0}(z \quad h_0), \ z > h_0 \end{array} \tag{5.110}$$

is the rod radius depending on the longitudinal coordinate in accordance with Figure 5.24(b).

Note that relation (5.106) first provides the necessary condition $\times \boldsymbol{H} = 0$ for the magnetic field with components (5.78) and (5.80) and second eliminates the redundancy of the number of the unknown coefficients standing in expansions (5.77) and (5.78).

To solve the differential equations (5.103) through (5.105), we represent the unknown variable coefficients standing in (5.77) and (5.78) in the form of expansions

$$H_{1q}(z) = \sum_{n=1}^{N} H_{1nq} f_n(z) \tag{5.111}$$

$$E_{jq}(z) = \sum_{n=1}^{N} E_{jnq} f_n(z), \quad j = 1, 2 \tag{5.112}$$

over triangle functions similar to those in (5.20) with tops in N nodes arranged uniformly on interval $0 \quad z \quad h_e$ including its edges. Further, we apply the finite element method to differential equations (5.103), (5.104), and (5.105). The process involves the following operations. The indicated equations are multiplied by $f_m(z)$ and are integrated from 0 to h_e. Expressions (5.84) and (5.93) are substituted into the nonintegral terms arising as a result of integration by parts of the derivative of variable coefficient E_{2p} in (5.103). Expression (5.94) is substituted into the nonintegral term arising after integration by parts of the derivative of variable coefficient H_{2p} in (5.104), and (5.106) replaces coefficient H_{2p} appearing under the integral sign. When using (5.93) and (5.94), we take into account that $H_{1p}(h_e) = H_{1Np}$ and $E_{1p}(h_e) = E_{1Np}$. Finally, we substitute expansions (5.111) and (5.112) into the integrals, and, as a result, obtain algebraic equations

$$\begin{aligned} & i\delta_{m1} \sum_n [(A_{1n}e_{1n} + B_{1n})Q_{2p}^{1n} + (A_{2n}e_{2n} \quad B_{2n})Q_{2p}^{2n}\gamma_{2n}/k] \\ & + i\delta_{mN}H_{1Np}\,\Gamma_p/k + \sum_{n=1}^{N}\sum_q \tilde{W}_{pq}^{mn}H_{1nq} + i\bar{K}^{mn}E_{2np} \quad = 0 \end{aligned} \tag{5.113}$$

$$i\delta_{m1}H_{2p}(0) + i\delta_{mN}E_{1Np}\Gamma_p/k + \sum_{n=1}^{N}\sum_{q}(\bar{Z}_{pq}^{mn}E_{1nq} \quad Y_{pq}^{mn}E_{2np}) = 0 \tag{5.114}$$

$$\sum_{n=1}^{N}[\ iK^{mn}H_{1np} + \sum_{q}(Y_{pq}^{mn}E_{1np} + \tilde{Z}_{pq}^{mn}E_{2nq})] = 0 \tag{5.115}$$

with the matrix elements

$$\tilde{W}_{pq}^{mn} = \frac{\Gamma_p^2}{k^2}I^{mn}\delta_{pq} + \frac{w_p w_q}{k^2\varepsilon_e}W_{pq}^{mn} \tag{5.116}$$

$$\bar{Z}_{pq}^{mn} = \frac{\Gamma_p^2}{k^2}I^{mn} \quad \bar{I}^{mn} \div \delta_{pq} + Z_{pq}^{mn} \tag{5.117}$$

$$\tilde{Z}_{pq}^{mn} = I^{mn}\delta_{pq} + Z_{pq}^{mn} \tag{5.118}$$

where

$$I^{mn} = k\int_0^{h_e} f_m f_n dz,\ \bar{I}^{mn} = \frac{1}{k}\int_0^{h_e}\frac{df_m}{dz}\frac{df_n}{dz}dz \tag{5.119}$$

$$K^{mn} = \int_0^{h_e} f_m\frac{df_n}{dz}dz,\ \bar{K}^{mn} = \int_0^{h_e}\frac{df_m}{dz}f_n dz \tag{5.120}$$

$$W_{pq}^{mn} = k\int_0^{h_e} f_m W_{pq} f_n dz \tag{5.121}$$

The integrals (5.119) and (5.121) are similar to those in (5.22), (5.23), and (5.24), the explicit expressions for which are presented in Appendix 5A. The values of integrals (5.120) are written in Appendix 5B. Coefficients Z_{pq}^{mn} and Y_{pq}^{mn} are calculated by formula (5.121), where function (5.109) should be replaced by functions (5.107) and (5.108), respectively.

Equations (5.74), (5.90), (5.91), and (5.92) (equalities $H_{1p}(0) = H_{11p}$ and $E_{1p}(0) = E_{11p}$ should be taken into account in the last three ones), as well as (5.113) through (5.115), form a complete infinite algebraic system. We solve this system by the method of truncation down to the order $4M+(3N+1)P$, where M is the number of the kept waveguide modes (for each of the sets of A_{jn} and B_{jn}, $j = 1, 2$) and P is the number of the kept transverse functions for each of the sets of $H_{2p}(0)$, H_{1nq}, E_{1nq}, and E_{2nq}, $n = 1, \ldots, N$. Since each triangular function partially overlaps only the adjacent functions, the integrals (5.119) through (5.121) are equal to zero for $|m–n|>1$, and, due to that fact, the matrix has a block-banded structure. Such a

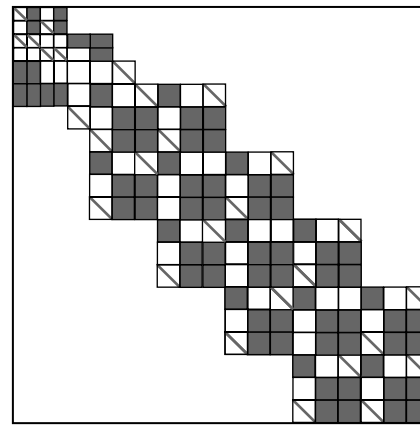

Figure 5.25 Structure of algebraic system matrix.

structure corresponding to $N = 5$ is shown in Figure 5.25 as an example, where the blocks containing nonzero elements are shown in gray, while the blocks containing nonzero elements only on its diagonals are marked by diagonal lines.

5.5.3 Array Characteristics

The amplitudes of the modes in the upper waveguide section obtained as a result of the solution of the algebraic system derived earlier are used for calculation of amplitudes of the modes reflected in the input waveguide section, including those of the copolar and cross-polar TE_{11} modes. The calculation is performed using the scattering matrix of the intermediate waveguide section applied in (5.74) by formula

$$R_{jn} = S^{00}_{jn,1l}\delta_{j1}\delta_{nl} + \sum_{j=1}^{2}\sum_{n} S^{01}_{jn,jn}B_{jn}e_{jn} \tag{5.122}$$

The amplitudes (5.122), together with the amplitudes of the Floquet modes above the rods standing in (5.75) and (5.76) and determined by formula (5.92), are used in the power balance relation

$$\begin{aligned}&\sum_{n}[|R_{1n}|^2\ \mathrm{Re}\{\gamma^{(i)}_{1n}\} + \varepsilon_i\,|R_{2n}|^2\ \mathrm{Re}\{\gamma^{(i)}_{2n}\}]\\ &+\sum_{q}[|T_{1q}|^2 + |T_{2q}|^2]\mathrm{Re}\{\Gamma_q\} = \gamma^{(i)}_{1l}\end{aligned} \tag{5.123}$$

where $\gamma^{(i)}_{jn} = [k^2\varepsilon_i \quad (\mu_{jn}/a_i)^2]^{1/2}$ are propagation constants of the modes in the input section.

The array element pattern components in spherical coordinates are determined via the amplitudes of the Floquet modes of zero order (see formulas (1.43) and (1.44) or [18]) corresponding to ordinal number 1 accepted in this section) by formulas

$$F_\theta(\theta,\varphi) = \sqrt{\frac{k}{\gamma_{1l}^{(i)}}} T_{21}(\theta,\varphi)\cos\theta \tag{5.124}$$

$$F_\varphi(\theta,\varphi) = \sqrt{\frac{k}{\gamma_{1l}^{(i)}}} T_{11}(\theta,\varphi)\cos\theta \tag{5.125}$$

where the normalization corresponds to the transmission coefficient of the input power in the main array beam.

Using (5.124) and (5.125), we can calculate the copolar and cross-polar array element patterns [18]

$$\begin{aligned} F^{++} &= \frac{F_\varphi^+ \quad iF_\theta^+}{\sqrt{2}} \\ F^{\ +} &= \frac{F_\varphi^+ + iF_\theta^+}{\sqrt{2}} \end{aligned} \tag{5.126}$$

respectively, where F_θ^+ and F_φ^+ are element pattern components (5.124) and (5.125) corresponding to the circular polarization of the incident mode with azimuthal index $m = +1$. The element pattern corresponding to excitation with circular polarization of the opposite rotation ($m = \ \ 1$) is calculated similarly. Using the appropriate linear combinations of the solutions obtained for the two cases of circular polarization, we can also calculate the characteristics of the array at its excitation in the TE_{11} modes of linear horizontal and vertical polarization.

5.5.4 Results and Discussion

Calculation of the multimode scattering matrix for the transition used in (5.74) and (5.122) has been carried out by taking into account the recommendations given in [60–62]. The results available in [60, 61] for the partial case of the first azimuthal variation have been used for testing the operation of the appropriate subroutine. The system of linear algebraic equations is solved by the Gauss elimination method with selection of the leading matrix element in a column. Minimization of the computation time is achieved by excluding the blocks filled in with only zero elements (Figure 5.25) from the processing.

The code operation has been validated in a few ways [18], including satisfaction of the necessary condition associated with the symmetry of the array geometry and with the power conservation law (the power balance relation is satisfied with accuracy of at least six decimal digits), as well as convergence of the results and their comparison to theoretical and measured data available in the literature for some special cases of the array geometry. Dependence of the reflected power (multiplied by 10) on the length of the cylindrical rods in the array considered in [23] is presented in Figure 5.26. The array elements are arranged in a square lattice with element spacing $d_x = d_y = 0.68\lambda$. The values for the other array parameters are indicated in the figure caption. The study of the convergence at the rod permittivity $\varepsilon_e = 2$ by increasing the number of nodes N has shown that high accuracy is already

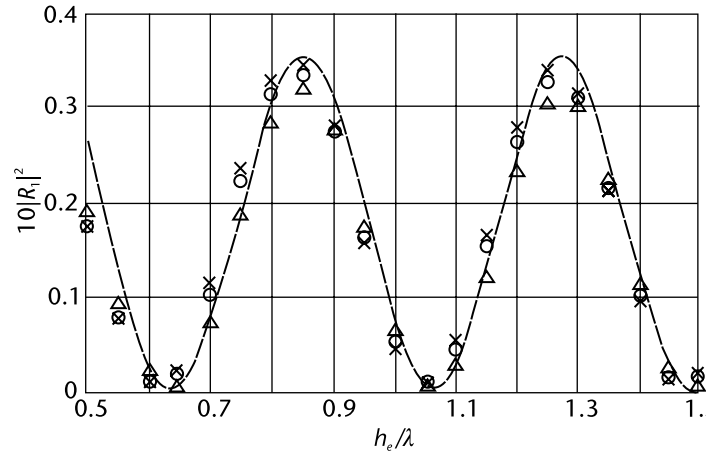

Figure 5.26 Reflected power versus rod length in equiphase array with square lattice at $d_x = d_y = 0.68\lambda$, $a_i = a_t = a = r_0 = r_1 = 0.24\lambda$, $\varepsilon_i = \varepsilon_t = \varepsilon = \varepsilon_e = 2$, $N = 1+20h_e/\lambda$, $M = 16$, $P = 25$ ( ), 49 ( ), and 81 (o o o); (– – –) is the curve from [23].

achieved at node spacing $= 0.05\lambda$ (i.e., at $N = 21$ nodes per one wavelength). We see in Figure 5.26 that the difference between the results obtained at $P = 81$ and 49 Floquet modes as a whole is smaller than the difference between the results obtained at $P = 49$ and 25 (i.e., the results converge). Besides, the results obtained by the proposed method are close to the results presented in [23] and shown in Figure 5.26 by the dashed line.

The next example relates to the array described in [10–14]. The sector element pattern in both main planes of this multi-element waveguide-rod array with hexagonal lattice is shaped by means of optimization of the rod parameters in the small breadboard shown in Figure 5.1(b). The breadboard radiation patterns measured in two main planes at excitation of the central element at circular polarization are shown by solid lines in Figure 5.27. The array parameters corresponding to the operating frequency are indicated in the figure caption. The element patterns calculated at $M = 16$, $P = 37$, and $N = 71$ are represented by the curves with crosses. As a whole, we see good correspondence between the measured and calculated results. The differences taking place in some parts of the patterns are explained by the resonance effects revealed by the theoretical model. However, such sharp resonances cannot be observed using the breadboard with such a small number of elements. A similar feature has been noted earlier in [20] as well. Moreover, the edge effect, which is not taken into account in the theoretical model, seems to be the reason for the difference between the results in the sidelobe region. This difference takes place for the angles at which the edge rods are seen from the central element aperture in the breadboard.

Characteristics of the array with element spacing $d_x = 0.91\lambda$ in the hexagonal lattice (i.e., smaller than that in the previous example) are presented in Figure 5.28. The waveguides of the array are excited in the TE_{11} modes of circular polarization with azimuthal index $m = +1$. The array parameters indicated in the caption for Figure 5.28 have been selected to shape a sector element pattern in the main planes. This pattern is compared to the element pattern of the array without rods shown by the lines with

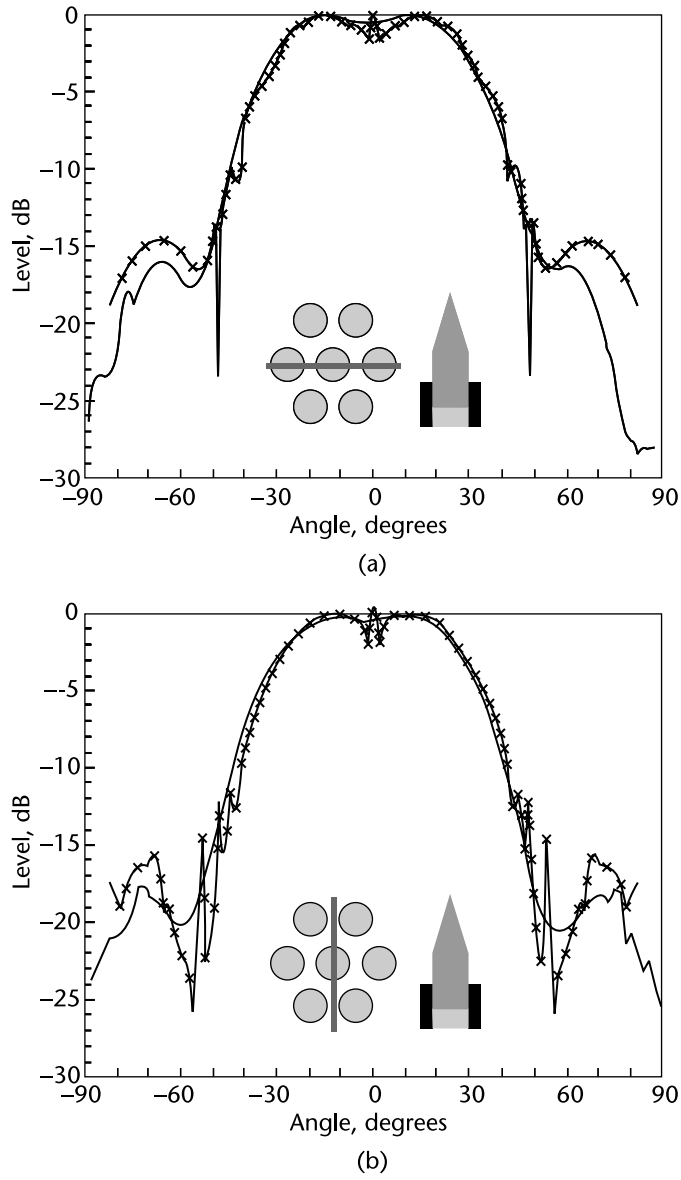

Figure 5.27 Element pattern in (a) horizontal and (b) vertical planes of hexagonal array with $d_x = 1.1347\lambda$, $a_i = a_t = a = r_0 = 0.4085\lambda$, $\varepsilon_i = 1$, $\varepsilon_t = 1.385$, $h_t = 0.268\lambda$, $\varepsilon = \varepsilon_e = 2.08$, $h = 1.1347\lambda$, $h_0 = 0.851\lambda$, $h_e = 1.9857\lambda$, $r_1 = 0$; ( ) is the calculation at $M = 16$, $P = 37$, $N = 71$, and (——) is the measurement.

crosses. Parameters of this array also indicated in the caption provide the absence of the blindness effects. As we see, the rods improve the element pattern shape. However they may cause the appearance of the dips in the region of single-beam scanning at the operating polarization. The indicated dips are accompanied by resonant increases of the cross-polar radiation as well as of reflections both at the operating polarization and at the cross-polarization. Removal of these undesirable effects so far is an important problem for the arrays with protruding dielectric elements.

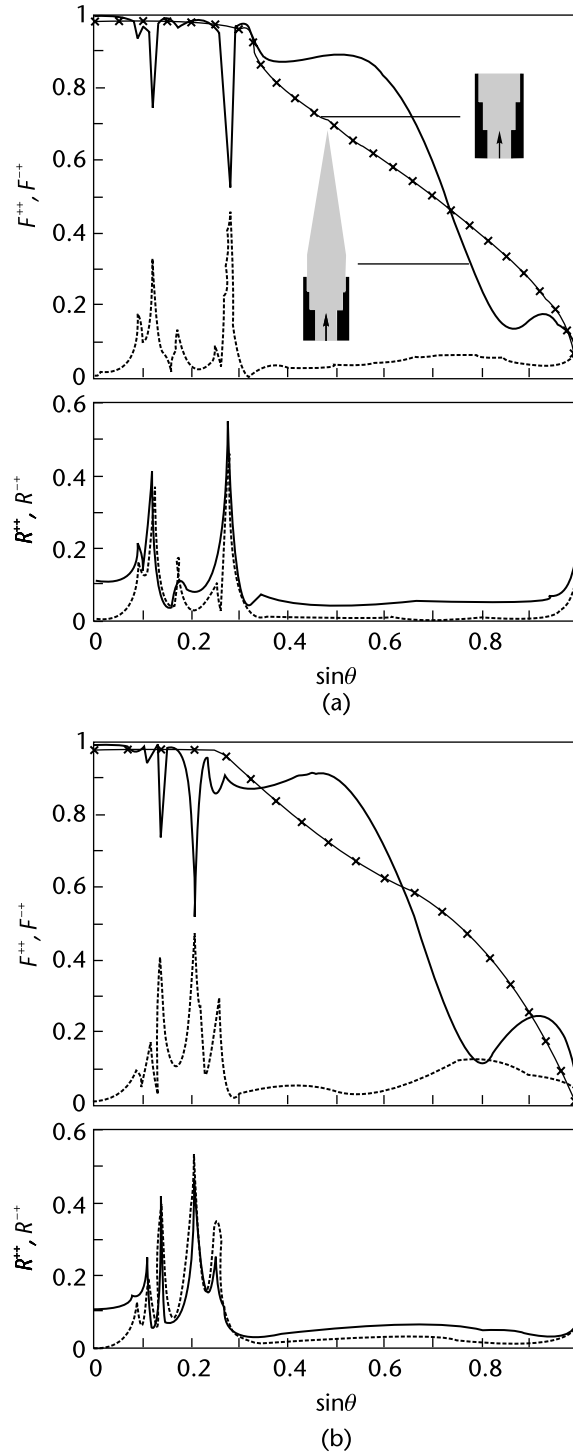

Figure 5.28 Element pattern and reflection coefficient in (a) horizontal and (b) vertical planes of hexagonal array at $d_x = 0.91\lambda$, $a_i = 0.24\lambda$, $a_t = 0.371\lambda$, $h_t = 0.315\lambda$, $a = 0.42\lambda$, $h = 0.3\lambda$, $r_0 = 0.4\lambda$, $h_0 = 0.5\lambda$, $h_e = 3\lambda$, $r_1 = 0$; $\varepsilon_i = \varepsilon_t = \varepsilon = \varepsilon_e = 2$, $M = 16$, $P = 37$, $N = 101$; (——) is the operating polarization; (- - - -) is the cross-polarization; ( ) is the element pattern of array without rods at $d_x = 0.91\lambda$, $a_i = 0.28\lambda$, $a_t = 0.3265\lambda$, $h_t = 0.57\lambda$, $a = 0.44\lambda$, $h = 0.56\lambda$, $\varepsilon_i = \varepsilon_t = \varepsilon = 1.5$.

References

[1] Vendik, O. G., and Y. V. Yegorov, "The First Phased-Array Antennas in Russia: 1955–1960," *IEEE Antennas and Propagation Magazine*, Vol. 42, No. 4, 2000, pp. 46–52.

[2] King, D. D., and H. J. Peters, "Element Interaction in Steerable Arrays," *Microwave Journal*, Vol. 6, No. 2, February 1963, pp. 73–77.

[3] Vendik, O. G., *Antennas with Non-Mechanical Movement of Beam*, Moscow: Sovetskoye Radio, 1965 (in Russian).

[4] Hannan, P. W., "Discovery of an Array Surface Wave in a Simulator," *IEEE Trans. on Antennas and Propagation*, Vol. 15, No. 4, 1967, pp. 574–575.

[5] Tanaka, S., et al., "Ceramic Rod Array Scanned with Ferrite Phase Shifters," *IEEE Proc.*, Vol. 56, No. 11, November 1968, pp. 2000–2010.

[6] Baklanov, E. V., et al., "Radiation Pattern of a Longitudinal Element in an Infinite Periodic Array," *Radiotekhnika i Electronika*, Vol. 17, No. 1, 1972, pp. 30–36 (in Russian).

[7] Andreyev, V. F., "Analysis of the Periodic Systems of Longitudinal Elements," *Radiotekhnika i Electronika*, Vol. 18, No. 1, 1973, pp. 40–48 (in Russian).

[8] Andreyev, V. F., "On Configuration of Partial Radiation Patterns in Antenna Arrays Formed by Radiators of Longitudinal Type," *Voprocy Radioelektroniki—Obschetekhnicheskaya Seriya*, No. 12, 1980, pp. 3–11 (in Russian).

[9] Corey, L. E., "A Survey of Russian Low Cost Phased Array Technology," *Proc. 1996 IEEE Intl. Symp. on Phased Array Systems and Technology*, Boston, MA, October 15–18, 1996, pp. 255–259.

[10] Tolkachev, A. A., et al., "High Gain Antenna Systems for Millimeter Wave Radars with Combined Electronical and Mechanical Beam Steering," *Proc. 1996 IEEE Intl. Symp. on Phased Array Systems and Technology*, Boston, MA, October 15–18, 1996, pp. 266–271.

[11] Tolkachev, A. A., et al., "Industrial Sample of a Millimeter-Wave-Band Phased Array Antenna Module," *Proc. 27th Scientific Conf. on Antenna Theory and Techniques*, Moscow, August 23–25, 1994, pp. 69–72 (in Russian).

[12] Tolkachev, A. A., et al., "Phase Shifters for Millimeter-Wave Band Multi-Element Phased Arrays," *Proc. 4th Intl. Symp. on Antennas and EM Theory*, Xi'an, China, August 1997, pp. 583–586.

[13] Korotkov, V. D., and S. P. Skobelev, "Dielectric Radiators for Array Antennas," *Proc. 26th Scientific Conf. on Antenna Theory and Techniques*, Part II, Moscow, November 27–29, 1990, p. 10 (in Russian).

[14] Denisenko, V. V., et al., "A Multi-Element Phased Antenna Array of the Ka Band," *Antenny*, No. 1, 2005, pp. 7–14 (in Russian).

[15] Ku, B. J., et al., "The Problem of Creating a Multi-Panel Multiple-Beam Antenna for a Stratospheric Communication System: Phases of Development," *Antenny*, No. 1, 2005, pp. 22–29 (in Russian).

[16] Korotkov, V. D., and S. P. Skobelev, "An Antenna Array of Dielectric Radiators," SU Author's Certificate No. 1769270, Int. Cl. H 01 Q 13/00, 1992 (in Russian).

[17] McGrath, D. T., "Accelerated Periodic Hybrid Finite Element Method Analysis for Integrated Array Element and Radome Design," *Proc. 2000 IEEE Intl. Conf. on Phased Array Systems and Technology*, Dana-Point, CA, May 21–25, 2000, pp. 319–322.

[18] Amitay, N., V. Galindo, and C. P. Wu, *Theory and Analysis of Phased Array Antennas*, New York: Wiley-Interscience, 1972.

[19] Vinichenko, Y. P., et al., "Plane Wave Diffraction on a Parallel-Plate Waveguide Array with Protruding Dielectric Plates," *Radiotekhnika i Electronika*, Vol. 17, No. 7, 1972, pp. 1382–1386 (in Russian).

[20] Lewis, R. L., A. Hessel, and G. H. Knittel, "Performance of a Protruding-Dielectric Waveguide Element in a Phased Array," *IEEE Trans. on Antennas and Propagation*, Vol. AP-20, No. 6, November 1972, pp. 712–722.

[21] Vinichenko, Y. P., et al., "Eigenmodes and Propagation Constants of an Array of Dielectric Rods," *Radiotekhnika i Electronika*, Vol. 19, No. 8, 1974, pp. 1583–1589 (in Russian).

[22] Krekhtunov, V. M., and V. A. Tyulin, "Eigenmodes of an Array of Dielectric Rods with Non-Orthogonal Lattice of Element Arrangement," *Radiotekhnika i Electronika*, Vol. 25, No. 1, 1980, pp. 44–50 (in Russian).

[23] Vinichenko, Y. P., et al., "Properties of a Phased Array of Circular Waveguides Loaded with Dielectric Rods," *Radiotekhnika i Electronika*, Vol. 20, No. 9, 1975, pp. 1804–1809 (in Russian).

[24] Krekhtunov, V. M., and V. A. Tyulin, "Electromagnetic Wave Diffraction on a Doubly Periodic Waveguide-Dielectric Array," *Radiotekhnika i Electronika*, Vol. 28, No. 2, 1983, pp. 209–216 (in Russian).

[25] Batov, P. L., and O. L. Dobrozhanskaya, "Results of Designing of Multimode Dielectric-Rod Radiators for Phased Antenna Arrays," *Antenny*, No. 5, 2008, pp. 58–63 (in Russian).

[26] Ilyinsky, A. S., and N. B. Kosich, "Plane Wave Diffraction on a Doubly Periodic Structure," *Radiotekhnika i Electronika*, Vol. 9, No. 6, 1974, pp. 1171–1177 (in Russian).

[27] Ilyinsky, A. S., and A. G. Sveshnikov, "Numerical Methods in the Problems of Diffraction on Nonuniform Periodic Structures," *Collective Volume of Scientific-Methodical Papers on Applied Electrodynamics*, No. 1, 1977, pp. 51–93 (in Russian).

[28] Ilyinsky, A. S., and S. V. Trubnikov, "Calculation of a Waveguide-Rod Phased Antenna Array by a Direct Projective Method," *Numerical Methods in Electrodynamics*, Moscow: Moscow State University Press, 1980, pp. 26–54 (in Russian).

[29] Trubnikov, S. V., "Projective Methods for Studying of Electrodynamical Problems for Waveguide and Waveguide-Rod Radiating Systems," Ph.D. Thesis, Moscow State University, 1980.

[30] Trubnikov, S. V., *Creation and Use of Mathematical Models for Study of Electrodynamical Characteristics of Waveguide Periodic Radiating Systems*, Research Report No. 0097831, Bryansk Pedagogic Institute, Bryansk, Russia, 1988 (in Russian).

[31] Davidovitz, M., "An Approach to Analysis of Waveguide Arrays with Shaped Dielectric Insets and Protrusions," *IEEE Trans. on Microwave Theory and Techniques*, Vol. 49, No. 2, February 2001, pp. 355–361.

[32] Kovalenko, A. N., "Application of a Projection Method to Calculation of Periodic Phased Arrays of Dielectric Radiators," *Proceedings of the Moscow Institute of Radio-Engineering, Electronics, and Automation—Electrodynamics, Antennas, and Microwave Engineering*, No. 70, 1974, pp. 60–72 (in Russian).

[33] Kishk, A. A., "Dielectric Resonator Antenna Elements for Array Applications," *Proc. 2003 IEEE Intl. Symp. on Phased Array Systems and Technology*, Boston, MA, October 14–17, 2003, pp. 300–305.

[34] Eshrah, I. A., et al., "Theory and Implementation of Dielectric Resonator Antenna Excited by a Waveguide Slot," *IEEE Trans. on Antennas and Propagation*, Vol. 53, No. 1, Pt. II, 2005, pp. 483–494.

[35] Skobelev, S. P., and L. L. Mukhamedov, "Analysis of Waveguide Antenna Arrays with Protruding Dielectric Elements," *IEEE Trans. on Antennas and Propagation*, Vol. 41, No. 5, May 1993, pp. 574–581.

[36] Kaklamani, D. I., and H. T. Anastassiu, "Aspects of the Method of Auxiliary Sources (MAS) in Computational Electromagnetics," *IEEE Antennas and Propagation Magazine*, Vol. 44, No. 3, June 2002, pp. 48–64.

[37] Eremin, Y. A., and A. G. Sveshnikov, "Method of Discrete Sources in the Problems of Electromagnetic Wave Scattering," *Uspekhi Sovremennoj Radioelektroniki*, No. 10, 2003, pp. 3–40 (in Russian).

[38] Malakshinov, N. P., and A. S. Smagin, "Application of the Method of Equivalent Sources for Solution of a Problem of Radiation from a Parallel-Plate Waveguide Array in the Presence of a Scattering Structure in Front of the Aperture," *Inter-Institutional Collective Volume of Papers "Computer-Aided Design of Microwave Devices,"* Moscow: Moscow Institute of Radio-Engineering, Electronics, and Automation, 1987, pp. 58–66 (in Russian).

[39] Skobelev, S. P., and L. L. Mukhamedov, "Algorithms of the Method of Auxiliary Sources for Analysis of Waveguide-Dielectric Periodic Structures," *Izvestiya Vuzov—Radiofizika*, Vol. 34, No. 4, 1991, pp. 392–402 (in Russian).

[40] Skobelev, S. P., and L. L. Mukhamedov, "Calculation of Characteristics of a Waveguide-Dielectric Array Excited by TM Waves," *Radiotekhnika i Elektronika*, Vol. 37, No. 7, 1992, pp. 1212–1219 (in Russian).

[41] Skobelev, S. P., "Algorithm of the Method of Auxiliary Sources for Analysis of Arrays of Circular Waveguides with Protruding Dielectric Rods," *Proc. 2003 IEEE Intl. Symp. on Phased Array Systems and Technology*, Boston, MA, October 14–17, 2003, pp. 333–338.

[42] Nikitin, K. V., and S. P. Skobelev, "An Algorithm of the Method of Volume Integral Equations for Analysis of Waveguide Arrays with Protruding Dielectric Elements," *Proc. 1998 Intl. Conf. on Mathematical Methods in Electromagnetic Theory*, Vol. 2, Kharkov, Ukraine, June 2–5, 1998, pp. 632–634.

[43] Nikitin, K. V., "Analysis of Antenna Arrays with Periodic Dielectric Covers by the Method of Volume Integral Equations," M.S. Thesis, Moscow Institute of Physics and Technology, 1998 (in Russian).

[44] Skobelev, S. P., "Analysis of Waveguide Arrays with Protruding-Dielectric Elements by Using the Method of Volume Integral Equations," *Proc. 2004 URSI Intl. Symp. on Electromagnetic Theory*, Vol. II, Pisa, Italy, May 23–27, 2004, pp. 679–681.

[45] Skobelev, S. P., et al., "Analysis of a Waveguide Array with Protruding Dielectric Elements by the Method of Integral Equation for Electric Field in the Protrusion," *Elektromagnitnye Volny i Elektronnye Sistemy*, Vol. 10, No. 3, 2005, pp. 31–35 (in Russian).

[46] Skobelev, S. P., et al., "Application of Integral Equations for Polarization Currents to the Analysis of Waveguide Arrays with Protruding Dielectric Elements," *Antenny*, No. 1, 2005, pp. 39–45 (in Russian).

[47] Mailloux, R. J., *Phased Array Antenna Handbook*, 2nd ed., Norwood, MA: Artech House, 2005.

[48] Yang, C.-F., W. D. Burnside, and R. C. Rudduck, "A Doubly Periodic Moment Method Solution for the Analysis and Design of an Absorber Covered Wall," *IEEE Trans. on Antennas and Propagation*, Vol. 41, No. 5, May 1993, pp. 600–609.

[49] Volakis, J. L., A. Chatterjee, and L. C. Kempel, *Finite Element Method for Electromagnetics*, New York: IEEE Press, 1998.

[50] Herd, J., and J. D'Angelo, "Efficient Modeling of Complex Three Dimensional Antenna Elements in Finite Arrays," *1998 IEEE AP-S Intl. Symp. Digest*, Atlanta, GA, 1988, pp. 768–771.

[51] Skobelev, S. P., and A. A. Yaparova, "A Hybrid Projection Method for Analysis of Waveguide Arrays with Protruding Dielectric Elements: 2D Problems," *Journal of Communications Technology and Electronics*, Vol. 52, No. 3, 2007, pp. 293–303.

[52] Pinello, W. P., R. Lee, and A. C. Cangellaris, "Finite Element Modeling of Electromagnetic Wave Interactions with Periodic Dielectric Structures," *IEEE Trans. on Microwave Theory and Techniques*, Vol. 42, No. 12, December 1994, pp. 2294–2301.

[53] Skobelev, S. P., and A. A. Yaparova, "Modeling of Horn Array Antennas with Protruding Dielectric Elements," *Proc. 6th Intl. Conf. on Antenna Theory and Techniques (ICATT'07)*, Sevastopol, Ukraine, September 17–21, 2007, pp. 409–411.

[54] Skobelev, S. P., and A. A. Yaparova, "Modeling of Horn Phased Antenna Arrays with Protruding Dielectric Elements," *Radiotekhnika*, No. 4, 2008, pp. 41–44 (in Russian).

[55] Skobelev, S. P., and A. A. Yaparova, "Analysis of Phased Antenna Arrays of Stepped Horns with Protruding Dielectric Elements Excited by TEM Waves," *Antenny*, No. 12, 2008, pp. 37–45 (in Russian).

[56] Ilyinsky, A. S., and G. Y. Slepyan, *Oscillations and Waves in Electrodynamical Systems with Losses*, Moscow: Moscow State University Press, 1983 (in Russian).

[57] Memelova (Yaparova), A. A., "Algorithms of the One-Dimensional Finite Element Method for Analysis of Waveguide-Dielectric Arrays," B.S. Diploma Work, Moscow Institute of Physics and Technology, 2006 (in Russian).

[58] Skobelev, S. P., "A Hybrid Projection Method for Analysis of Waveguide Arrays with Protruding Dielectric Elements: A 3D Problem," *Journal of Communications Technology and Electronics*, Vol. 52, No. 3, 2007, pp. 304–312.

[59] Clarricoats, P. J. B., and K. R. Slinn, "Numerical Solution of Waveguide-Discontinuity Problems," *IEE Proc.*, Vol. 114, No. 7, 1967, pp. 878–886.

[60] English, W. J., "The Circular Waveguide Step-Discontinuity Mode Transducer," *IEEE Trans. on Microwave Theory and Techniques*, Vol. MTT-21, No. 10, October 1973, pp. 633–636.

[61] Mittra, R., (ed.), *Computer Techniques for Electromagnetics*, New York: Pergamon Press, 1973.

[62] James, G. L., "Analysis and Design of TE_{11}-to-HE_{11} Corrugated Cylindrical Waveguide Mode Converters," *IEEE Trans. on Microwave Theory and Techniques*, Vol. MTT-29, No. 10, October 1981, pp. 1059–1066.

[63] Amitay, N., and V. Galindo, "On the Scalar Product of Certain Circular and Cartesian Wave Functions," *IEEE Trans. on Microwave Theory and Techniques*, Vol. MTT-16, No. 4, 1968, pp. 265–266.

Appendix 5A Explicit Expressions for Integrals (5.22), (5.23), and (5.24)

$$\bar{I}^{(0)}_{s's} = k\int_z^z f_{s'} f_s dz \qquad \bar{I}^{(1)}_{s's} = \frac{1}{k}\int_z^z f_{s'} f_s dz \qquad \bar{J}^{pq}_{s's} = k\int_z^z f_{s'} \bar{W}_{pq} f_s dz$$

$$\bar{I}^{(0)}_{11} = \frac{k}{3} \qquad \bar{I}^{(1)}_{11} = \frac{1}{k} \qquad \bar{J}^{pq}_{11} = \frac{k}{12}(3\bar{W}^1_{pq} + \bar{W}^2_{pq})$$

$$\bar{I}^{(0)}_{12} = \frac{k}{6} \qquad \bar{I}^{(1)}_{12} = \frac{1}{k} \qquad \bar{J}^{pq}_{12} = \frac{k}{12}(\bar{W}^1_{pq} + \bar{W}^2_{pq})$$

$$\bar{I}^{(0)}_{s,s-1} = \frac{k}{6} \qquad \bar{I}^{(1)}_{s,s-1} = \frac{1}{k} \qquad \bar{J}^{pq}_{s,s-1} = \frac{k}{12}(\bar{W}^{s-1}_{pq} + \bar{W}^s_{pq})$$

$$\bar{I}^{(0)}_{ss} = \frac{2k}{3} \qquad \bar{I}^{(1)}_{ss} = \frac{2}{k} \qquad \bar{J}^{pq}_{ss} = \frac{k}{12}(\bar{W}^{s-1}_{pq} + 6\bar{W}^s_{pq} + \bar{W}^{s+1}_{pq})$$

$$\bar{I}^{(0)}_{s,s+1} = \frac{k}{6} \qquad \bar{I}^{(1)}_{s,s+1} = \frac{1}{k} \qquad \bar{J}^{pq}_{s,s+1} = \frac{k}{12}(\bar{W}^s_{pq} + \bar{W}^{s+1}_{pq})$$

$$\bar{I}^{(0)}_{\bar{N},\bar{N}-1} = \frac{k}{6} \qquad \bar{I}^{(1)}_{\bar{N},\bar{N}-1} = \frac{1}{k} \qquad \bar{J}^{pq}_{\bar{N},\bar{N}-1} = \frac{k}{12}(\bar{W}^{\bar{N}-1}_{pq} + \bar{W}^{\bar{N}}_{pq})$$

$$\bar{I}^{(0)}_{\bar{N},\bar{N}} = \frac{k}{3} \qquad \bar{I}^{(1)}_{\bar{N},\bar{N}} = \frac{1}{k} \qquad \bar{J}^{pq}_{\bar{N},\bar{N}} = \frac{k}{12}(\bar{W}^{\bar{N}-1}_{pq} + 3\bar{W}^{\bar{N}}_{pq})$$

Appendix 5B Values of Integrals (5.119)

m,n	1, 1	1, 2	$m, m-1$	m, m	$m, m+1$	$N, N-1$	N, N
$K^{mn} = \int_0^{h_e} f_m \frac{df_n}{dz} dz$	$\frac{1}{2}$	$\frac{1}{2}$	$\frac{1}{2}$	0	$\frac{1}{2}$	$\frac{1}{2}$	$\frac{1}{2}$
$\bar{K}^{mn} = \int_0^{h_e} \frac{df_m}{dz} f_n dz$	$\frac{1}{2}$	$\frac{1}{2}$	$\frac{1}{2}$	0	$\frac{1}{2}$	$\frac{1}{2}$	$\frac{1}{2}$

CHAPTER 6

Arrays with Strip, Disk, and Wire Structures

The dielectric rods considered in Chapter 5 are one of the simplest and effective types of the phased array antenna elements used for shaping sector partial radiation patterns of width ±(20 to 30)°. However, their use in large arrays designed for operation in the S and L frequency bands is not justified because it would require too much dielectric material, which itself may be rather expensive, and moreover the radiating structure would bee too heavy. A more convenient slowing-down structure—an alternative to dielectric rod in the indicated frequency bands—is a metallic corrugated rod or a set of thin metallic disks arranged on a thin but strong dielectric rod. Moreover, the rods can be excluded from the array design if the disks of different elements but of the same level are arranged on thin dielectric films or on foam layers. Such multilayer disk structures may turn out to be a promising alternative to dielectric rod structures for operating in higher frequency bands.

The use of corrugated rods in the antenna engineering is well known (see, for instance, [1–3]). However, the possibility of shaping the sector partial patterns using such elements became a topic for study and discussion in the literature not so long ago [4, 5]. The studies started from purely experimental breadboarding. Then, a simplified theory for numerical modeling of one-dimensional waveguide arrays with strip slowing-down structures was developed [5–7]. Generalizations on the three-dimensional case, which is of primary interest for practice, was done in [8–10]. The effectiveness of the approach proposed for numerical analysis and optimization of the waveguide arrays with the disk slowing-down structures was confirmed by measurements of the array characteristics in the appropriate radiating structure breadboards [11].

Along with the strip and disk structures, array elements in the form of wire Yagi-Uda antennas have also been considered [12–14]. Finally, other wire structures have recently been proposed and considered in [15–18] for forming semitransparent waveguide walls allowing us to shape the sector element patterns in one-dimensional periodic arrays.

The methods developed for study of all the structures listed here and the array characteristics obtained as a result of such a study are described later.

6.1 Experimental Breadboard of Array with Multidisk Radiators

6.1.1 Breadboard Design

The purpose of the work has been creation of an S-band radiating element in an array designed for scanning in sector of ±(20 to 25)° in both principal planes. The

radiating element selected to provide the specified requirements contains a disk slowing-down structure excited by a pair of printed microstrip dipoles crossed at right angles. Similar dipoles were also applied in other subsequent projects—in particular, in a multibeam antenna designed for a stratospheric communication system. A fragment of such an antenna is shown in [19]. The work in the present case consists of a selection of such element parameters as the length of the struc-

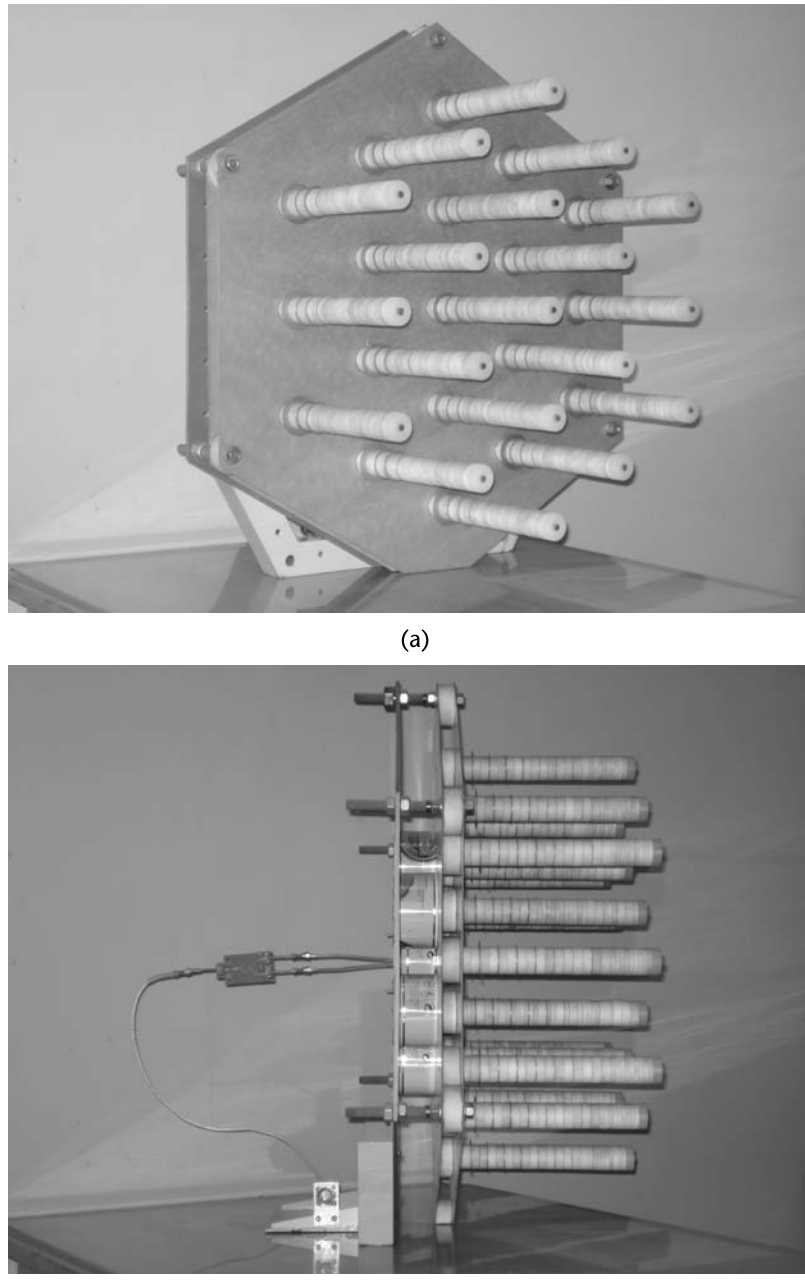

(a)

(b)

Figure 6.1 (a) General view and (b) side view of an array breadboard with multidisk radiators.

ture, number of the disks, diameters of the disks, and distance from the dipoles to the first disk. The indicated work was performed using a developed and fabricated breadboard shown in Figure 6.1.

The base of the breadboard is a bearing aluminum plate in the form of an equilateral hexagon. The pairs of the crossed dipoles enclosed in circular waveguide sections are installed on the plate in the nodes of a hexagonal lattice with element spacing $a = 1.12\lambda$, where λ is the wavelength corresponding to the central (reference) frequency f. The dipoles of the central element have inputs/outputs for connection to the measurement equipment via a technological hybrid microstrip divider/combiner designed for providing different types of excitation. The dipoles of peripheral elements are terminated with matching loads, as it is required for determining the array element pattern.

The disk structures are arranged on a common board, as shown in Figure 6.1. The board is made of two thin textolite sheets divided by foam spacers. The spacer thickness has been selected to provide minimum reflection at normal illumination of the board by a plane wave. The board has holes performed along the axes of the spacers. The holes are used for installing textolite rods of small diameter. The rod height exceeds two wavelengths in the operating frequency band. The rods are designed for arrangement of thin brass disks divided from each other by foam spacers. A few sets of the disks of various diameter and a few sets of spacers of various thickness were fabricated. The board with the disk structures is installed on the bearing board using six posts arranged in the hexagon corners. The indicated posts allow us to vary the distance from the board to the bearing plate.

6.1.2 Results of Measurement

Adjustment and testing of the assembled breadboard included two stages. At the first stage, carried out in laboratory conditions, the dipoles were adjusted to minimize VSWR and then measurements of isolation between the dipoles in the same element as well as the measurements of coefficients of coupling between dipoles of different elements were carried out. As a result of the dipole adjustment using matching devices, the VSWR does not exceed 1.5 in a ±4% frequency band. The isolation measured between the crossed dipoles in each radiating element was no less than 35 dB. The results of measurement of the coupling coefficients between the dipoles of different elements had shown that the coupling between the dipoles of the central element and the dipoles of the nearest elements did not exceed –30 dB. These results confirm the fact that the interaction between traveling wave elements takes place mainly in the direction of wave propagation.

The second stage of the breadboard adjustment and test was performed in an anechoic chamber using the conventional method of radiation pattern measurement in far zone. The previous experience of working with the dielectric rod elements had allowed us to suggest that the second (outer) ring of the passive elements surrounding the central element should not practically influence on the central element performance. So, to make the work easier, the adjustment of the breadboard was performed using only one (inner) ring of the passive elements. As a result of numerous measurements, it had turned out that the best results were obtained using 7 or 8 disks of diameter from 0.2λ to 0.4λ arranged with spacing of about 0.2λ.

Verification of the suggestion indicated earlier was carried out after the adjustment had shown that the central element patterns measured for one and two rings of passive elements coincided down to the levels of –18 dB. The results presented next correspond to the case of using all nineteen elements with identical disk structures, as shown in Figure 6.1.

The results of the element pattern measurements in two principal planes at the central and two edge frequencies f, $0.965f$, and $1.036f$ of the operating band, and at two linear orthogonal polarizations are shown in Figures 6.2 and 6.3. If the array under consideration is uniformly excited to scan the beam in the horizontal plane, the array grating lobes are arranged in the horizontal plane as well. The positions of two nearest grating lobes corresponding to steering of the main beam at 20° for

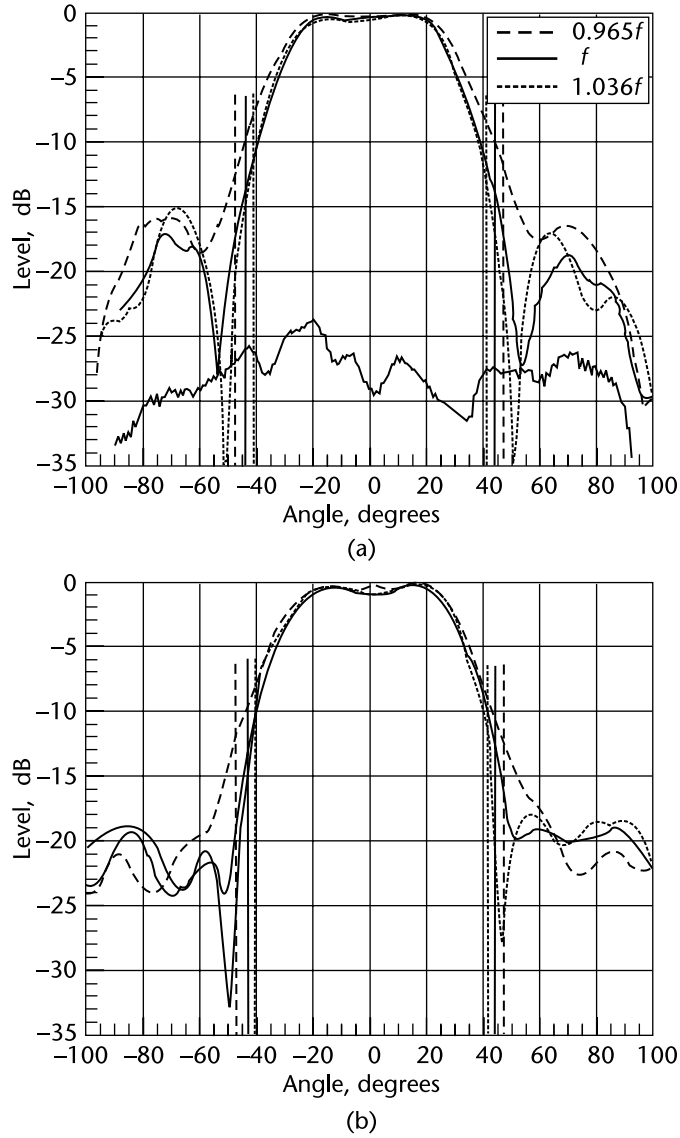

Figure 6.2 Radiation pattern of the central array element in horizontal plane at (a) vertical and (b) horizontal polarizations.

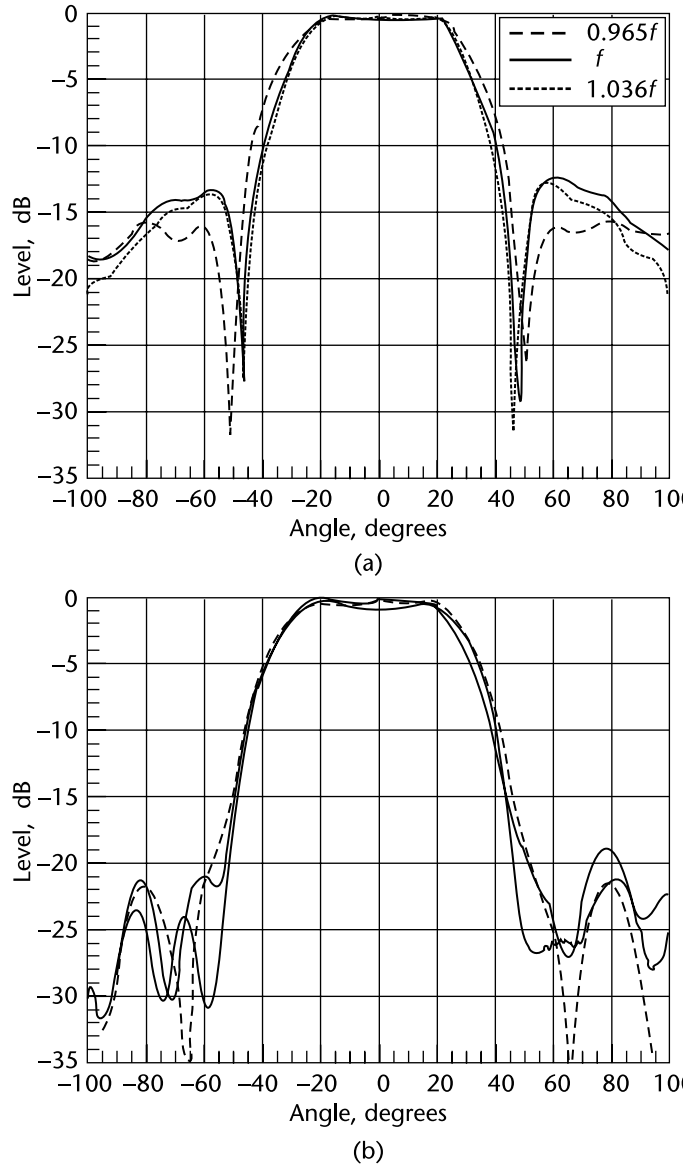

Figure 6.3 Radiation pattern of the central array element in vertical plane at (a) vertical and (b) horizontal polarizations.

the central and two edge frequencies are shown in Figure 6.2 by vertical straight lines. The grating lobes in these positions come to the element pattern slope where their level is –14 through –12 dB and has smaller values at smaller angles of the beam deflection from the broadside. The element pattern in the vertical plane [Figure 6.3(a)] has somewhat higher sidelobe level compared to that in the horizontal plane. However, the grating lobes do not come to the vertical plane when the main beam scans in the specified region. The patterns in both planes have a good flat top, so that the array gain variation in the specified scan region does not exceed 1.3 dB. An example of the cross-polar element pattern in the horizontal plane at the central frequency is shown in Figure 6.2(a) by the lower solid curve.

The measured radiation patterns were used to approximate an evaluation of the element directivity. This was done by means of appropriate integration of the radiation pattern obtained by averaging the measured patterns. The result obtained for the central frequency is equal to 10.7 dB. The appropriate theoretical maximum of the element directivity determined by formula $D_{\max} = 10\lg(4\pi A/\lambda^2)$, where $A = \sqrt{3}a^2/2$ is the geometrical area allotted to one array element and is equal to 11.35 dB, demonstrating a sufficiently good concentration of the radiated power in the specified scan region.

Note also that the element spacing selected according to the conventional approach corresponding to keeping the grating lobes outside the visible space for the specified scan region of the main lobe would be equal to 0.86λ. Therefore, the reduction of the controlled element number using the array element developed in this work would be $(1.12/0.86)^2 = 1.7$ times.

The result of the work described was a new multidisk radiating element designed for limited-scan phased array antennas. Improvement of the array element performance is possible if more accurate selection of its geometric parameters can be obtained. To do that with maximum effectiveness, it is of interest to develop appropriate algorithms for computer modeling the array type in question. The next sections are devoted to the development of such algorithms. We will first consider a simplified two-dimensional model of a waveguide array where shaping of the sector element pattern is performed with using multilayer strip structures. After that, the developed approach will be generalized to a more practical three-dimensional model.

6.2 Waveguide Arrays with Strip Structures

The purpose of the present section is the creation and investigation of a two-dimensional model of the corrugated-rod array where the disk structures are replaced by strip structures. The latter also possess the capability of supporting slow waves at a definite polarization of excitation [20]. The strip structures are excited by open ends of parallel-plate waveguides. The choice of the waveguide excitation was made on the basis of experience acquired from [4], which has shown that the best sector shape of the array element pattern is achieved when the dipoles of the feed system are arranged in the waveguide sections. In spite of the simplification, the model to be considered later reveals some important features and capabilities of the structures in question. The results obtained in the process of such modeling may be used in practice if the shaping of the sector element pattern is required in only one plane.

6.2.1 Statement of the Problem and Method of Solution

Consider an infinite array, the cross-section of which in the $0xz$ plane of the rectangular coordinate system $0xyz$ is shown in Figure 6.4. The array, assumed to be periodic with period (element spacing) b along the x-axis and uniform along the y-axis, consists of strip structures arranged symmetrically along the axis of the semi-infinite parallel-plate waveguides of width a. Each of the indicated structures comprises L

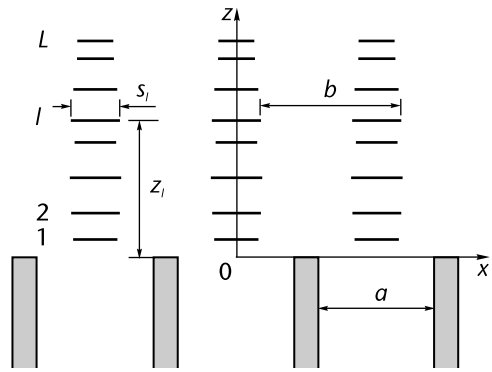

Figure 6.4 Geometry of a waveguide array with strip structures.

infinitely thin strips characterized by widths s_l, and distances z_l from the waveguide aperture (l = 1, 2, …, L). The strips, waveguide flanges, and waveguide walls are assumed to be perfectly conducting.

The array parameter of principal interest here is the array element pattern. This pattern corresponds to the case when only one waveguide of the array is excited, while all the other waveguides are terminated with matching loads. However, as done in the previous sections, we first consider the case of quasi-periodic excitation of the array, since the zero-order Floquet mode amplitude of the radiated field corresponding to such excitation can be used for determining the element pattern according to [21] or formulas (1.112) and (1.114).

The strip structures described earlier are able to support slow waves only at excitation of them by the TM waves with field components H_y, E_x, and E_z not equal to zero identically. Let each waveguide be excited by a superposition of TM modes coming to the apertures. The amplitudes of these waves in different waveguides are assumed to be identical, while the phases for adjacent waveguides are different by a value $U = kb\sin\theta$ determined by a specified angle θ of deflection of the main array beam from the array broadside. Then, omitting the time dependence assumed to be given by factor $e^{\,i\omega t}$, we write the total magnetic field in the central waveguide ($|x| < a/2$) in the form

$$H_y(x,z \quad 0) = \sum_{m=1} \left(A_m e^{i\gamma_m z} + R_m e^{\,i\gamma_m z}\right) \quad {}_m(x) \tag{6.1}$$

where A_m are amplitudes of the incident modes, which will be specified later; R_m are amplitudes of the reflected modes; γ_m are propagation constants determined by formula (3.17); and

$${}_m(x) = \sqrt{\frac{2 \quad \delta_{1m}}{a}} \cos\frac{(m \quad 1)\pi(x + a/2)}{a} \tag{6.2}$$

are the orthonormalized transverse functions of the waveguide modes.

The total magnetic field above the waveguide apertures is represented as an expansion in terms of the Floquet modes

$$H_y(x,z \quad 0) = \quad T_{0q} \quad _q(x)e^{i\Gamma_q z} + \sum_{l=1}^{L} \text{sign}(z \quad z_l) \quad T_{lq} \quad _q(x)e^{i\Gamma_q|z \quad z_l|} \tag{6.3}$$

where T_{0q} are amplitudes of the modes going up from the waveguide apertures, T_{lq} are amplitudes going up and down from the lth strips,

$$_q(x) = \frac{1}{\sqrt{b}} e^{i\alpha_q x} \tag{6.4}$$

are transverse wave functions orthonormalized on the period of the structure, and α_q and Γ_q are transverse and longitudinal propagation constants (4.7).

The field radiated into the region above the strips, which is of interest for the subsequent calculation of the array element pattern, is determined from (6.3) by the sum of Floquet modes

$$H_y(x,z > z_L) = \quad T_q \quad _q(x)e^{i\Gamma_q z} \tag{6.5}$$

with amplitudes

$$T_q = T_{0q} + \sum_{l=1}^{L} T_{lq} e^{\ i\Gamma_q z_l} \tag{6.6}$$

To determine the unknown amplitudes in the expansions (6.1) and (6.3), we use the mode-matching method [22]. The total magnetic field must be continuous in the waveguide aperture. Therefore, equating (6.1) and (6.3) and using the orthogonality of functions (6.2), we obtain the following relation between the waveguide and Floquet modes

$$A_m \ + R_m \ = \quad T_{0q} Q_{m\,q} \quad \sum_{l=1}^{L} \quad T_{lq} Q_{m\,q} e^{i \ \ q z_l} \tag{6.7}$$

where m = 1, 2, …, and

$$\begin{aligned} Q_{mq} &= \int_{a/2}^{a/2} \quad _m(x) \quad _q(x)dx \\ &= \sqrt{\frac{(2 \quad \delta_{1m})a}{b}} i\alpha_q a \frac{e^{\ i\alpha_q a/2} \quad (\ 1)^m \ 1 e^{i\alpha_q a/2}}{(\alpha_q a)^2 \quad [(m \quad 1)\pi]^2} \end{aligned} \tag{6.8}$$

The transverse component of the total electric field determined by the magnetic fields (6.1) and (6.3) from the Maxwell equation

$$E_x(x,z) = \frac{1}{i\omega\varepsilon_0}\frac{H_y(x,z)}{z} \tag{6.9}$$

must be continuous in the waveguide aperture and equal to zero on the waveguide flanges. This condition and the orthogonality of functions (6.4) lead to the second relation

$$\Gamma_q T_{0q} + \sum_{l=1}^{L} \Gamma_q T_{lq} e^{i\Gamma_q z_l} = \sum_{m=1} \gamma_m (A_m \quad R_m) Q_{mq} \tag{6.10}$$

where $q = 0, \pm1, \pm2, \ldots$, and the asterisk denotes complex conjugation.

Now consider the boundary conditions for the electromagnetic field in the region of the strips. The magnetic field (6.3) must be continuous in the gaps between the strips and must suffer jumps, equal to the current density, when going over the strips; that is,

$$H_y(x, z_l + 0) \quad H_y(x, z_l \quad 0) = 2 \sum_{q=} T_{lq} \quad _q(x)$$

$$= \begin{array}{ll} J_{xl}(x), & |x| \quad s_l/2, \\ 0, & s_l/2 < |x| \quad b/2, \quad l = 1, 2, \ldots, L \end{array} \tag{6.11}$$

The only nonzero x-component of the current density on each strip, $J_{xl}(x)$, must go to zero at the strip edges. So, we expand this function into the following series:

$$J_{xl}(x) = 2 \sum_{n=1} C_{ln} \tilde{} _{ln}(x) \tag{6.12}$$

where factor 2 is introduced for convenience of the subsequent calculations, C_{ln} are unknown coefficients, and

$$\tilde{} _{ln}(x) = \sqrt{\frac{2}{s_l}} \sin \frac{n\pi(x + s_l/2)}{s_l} \tag{6.13}$$

are functions orthonormalized on the lth strip, and equal to zero at the edges of the latter.

Using the orthogonality of functions (6.4), and taking into account (6.12), we express amplitudes T_{lq} from (6.11) via C_{ln} by formula

$$T_{lq} = \sum_{n=1} C_{ln} \tilde{Q}_{lnq} \tag{6.14}$$

where

$$\tilde{Q}_{lnq} = \int_{-s_l/2}^{s_l/2} \tilde{}_{ln}(x) \quad _q(x)dx = \sqrt{\frac{2s_l}{b}} n\pi \frac{(\ \ 1)^n e^{i\alpha_q s_l/2} \quad e^{\ \ i\alpha_q s_l/2}}{(\alpha_q s_l)^2 \quad (n\pi)^2} \tag{6.15}$$

The tangential component of the total electric field must be equal to zero on the strips. Therefore, equating (6.9) to zero on the l th strip, taking into account (6.14), and projecting the obtained functional equation on the n th function (6.13) for the indicated strip (i.e., applying the Galerkin method), we obtain the following algebraic equations

$$\sum_{q=} T_{0q}\Gamma_q\tilde{Q}_{l\ n\ q}e^{i\Gamma_q z_l} \quad \sum_{l=1}^{L}\sum_{n=1} C_{ln} \quad \sum_{q=} \Gamma_q\tilde{Q}_{l\ n\ q}\tilde{Q}_{lnq}e^{i\Gamma_q|z_l \quad z_l|} = 0 \tag{6.16}$$

where $l = 1, 2, \ldots, L$; and $n = 1, 2, \ldots$.

If we now substitute (6.14) into (6.7) and (6.10), the indicated equations together with (6.16) can constitute an infinite algebraic system for unknown amplitudes R_m, T_{0q}, and C_{ln}. However, such a system, which can be solved by the method of truncation, would have a rather high order, mainly because of the necessity of taking into account a large number of the Floquet modes. So, to obtain a system of a smaller order, we perform the following additional operations. Let be a set of numbers q of those Floquet modes for which, for instance, $\mathrm{Im}\{\Gamma_q\}<k$, and let be a set of numbers for all the rest of the modes of higher order. Then, substituting the amplitudes T_{0q}, expressed from (6.10) for q , into (6.7) and (6.16), and taking into account (6.14) in (6.7) and (6.10), we obtain the following final form of the algebraic system

$$\begin{aligned} &\sum_{m=1} [(R_m + A_m)\delta_{m\ m} + (R_m \quad A_m)\gamma_m \quad \Gamma_q{}^{1}Q_{m\ q}Q_{mq}] \\ &\sum_{q} T_{0q}Q_{m\ q} \quad \sum_{l=1}^{L}\sum_{n=1} C_{ln} \quad \sum_{q=} \eta_q Q_{m\ q}\tilde{Q}_{lnq}e^{i\Gamma_q z_l} = 0, \quad m = 1, 2, \ldots \end{aligned} \tag{6.17}$$

$$\sum_{m=1} (R_m \quad A_m)\gamma_m Q_{mq} + T_{0q}\ \Gamma_q \quad \sum_{l=1}^{L}\sum_{n=1} C_{ln}\tilde{Q}_{lnq}\, e^{i\Gamma_q\, z_l} = 0, \quad q \tag{6.18}$$

$$\begin{aligned} &\sum_{m=1} (R_m \quad A_m)\gamma_m \quad \sum_{q} \tilde{Q}_{l\ n\ q}Q_{mq}e^{i\Gamma_q z_l} \quad \sum_{q} T_{0q}\,\Gamma_q\tilde{Q}_{l\ n\ q}e^{i\Gamma_q z_l} \\ &+ \sum_{l=1}^{L}\sum_{n=1} C_{ln} \quad \sum_{q=} \Gamma_q\tilde{Q}_{l\ n\ q}\tilde{Q}_{lnq}(e^{i\ \ _q|z_l \quad z_l|} \quad \zeta_{l\ lq}) = 0 \end{aligned} \tag{6.19}$$

$$l = 1, 2, \ldots, L; \quad n = 1, 2, \ldots$$

where $\delta_{m\ m}$ is the Kronecker symbol, $\eta_q = 1$ and $\zeta_{l\ lq} = 0$ for q , and $\eta_q = 2$ and $\zeta_{l\ lq} = \exp[i\Gamma_q(z_l + z_l)]$ for q .

The infinite system of equations (6.17) through (6.19) is solved by the method of truncation. In this case, depending on the width of the waveguides and strips, high accuracy of calculations is achieved by taking into account 10 to 20 waveguide modes and 6 to 12 current harmonics for each strip. As follows from (6.8) and (6.15), the infinite series in (6.17) and (6.19) converge like q^{-3} as $|q|$, so their sums can be easily calculated with high accuracy.

After solving the truncated system (6.17) to (6.19), for instance, by the Gauss elimination method, the array element pattern corresponding to the coefficient of transmission of the incident power to the main beam is calculated by formula

$$F(\theta) = \sqrt{\frac{b}{a}}\,|T_0(kb\sin\theta)|\cos\theta \tag{6.20}$$

where $T_0(U)$ is the Floquet mode amplitude determined from (6.6).

6.2.2 Numerical Results and Discussion

The algorithm described earlier has been implemented in FORTRAN code whose operation has been tested via various ways indicated in [21] and in the previous chapters. Then code has also been used for studying the adopted array model. The study has shown that the sector element patterns can be shaped by the strip structures only if the latter support the slow waves (i.e., for $s_l<0.5\lambda$ and $z_{l+1}-z_l<0.5\lambda$ [20]). In this case, the better quality of the element pattern shape is achieved for the maximum waveguide width (i.e., for $a = b$). The quality of the pattern shape is also considerably influenced by the conditions of excitation of the strip structures. Some of the characteristic examples illustrating the indicated features are considered next.

Consider an array of dual-mode waveguides with parameters $a = b = 0.8\lambda$, excited by TE_1 modes (which are the TEM modes) of unit amplitudes [i.e., $A_1 = 1$ and $A_m = 0$ for $m > 1$ in (6.1) and (6.17) to (6.19)]. The element pattern (6.20) in the absence of the strips is a falling-off function shown by crosses in Figure 6.5. The use of the slow-wave structures, each of which consists of $L = 6$ strips with parameters $s_l = 0.2\lambda$ and $z_l = [0.2 + 0.14(l \quad 1)]\lambda$, $(l = 1, 2, \ldots, 6)$, obtained as a result of optimization, allows a considerable increase of the element pattern level in the region $\lambda/b \quad 1 < \sin\theta < \lambda/(2b)$, as shown in Figure 6.5 by the curve with major dashes. However, the fall-off of the element pattern level in the region $\sin\theta \quad \lambda/b \quad 1$ keeps the same as that for the array without the strips. Such behavior is associated with an increase of the reflected power at the quasi-periodic excitation reaching 11.5%, with almost all the reflected power (10.5% of the incident power) being transferred by the second propagating mode TM_2. This power can be used for improving the element pattern shape in the following way. Assume that the dual-mode waveguides in question are fed through single-mode waveguides and symmetric matching transitions, similar to those considered in Chapter 3. Then the TM_2 modes going down from the apertures will be completely reflected from the transitions, returned back to the apertures, and used for excitation of the strip structures. To simulate such a situation, we specify the amplitudes of the incident modes in (6.1) and (6.17) to (6.19) as follows: $A_1 = 1$, $A_2 = R_2 \exp(i\psi_2)$, where ψ_2 is the phase with which the

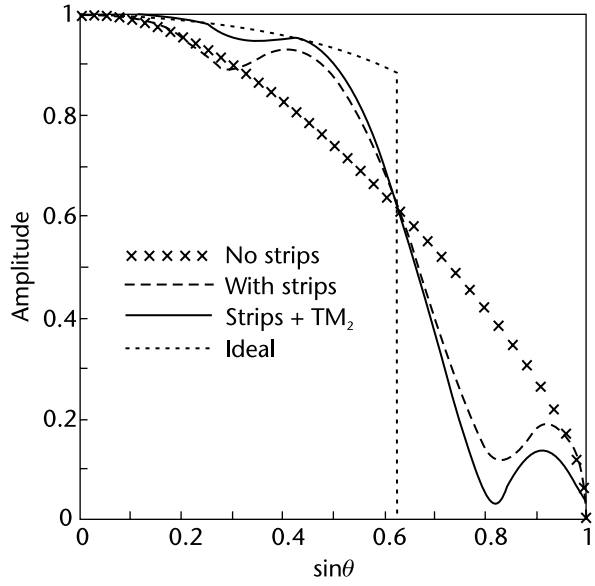

Figure 6.5 Element pattern of array with $b = a = 0.8\lambda$.

TM_2 modes return back to the apertures, and $A_m = 0$ for $m > 2$ (i.e., the interaction between the transitions and waveguide apertures over the evanescent modes is assumed to be negligibly small).

The calculations have shown that the performances of the accepted model for various values of ψ_2 are similar to those of the array of thick-walled waveguides with fences [23]. At $\psi_2 = 210°$, the element pattern of the array with the strip structures whose parameters were indicated earlier is shown in Figure 6.5 by a solid curve. Comparing this pattern to the sector element patterns presented in the previous chapters, as well as to the ideal sector element pattern shown in Figure 6.5 by small dashes, we can conclude that the obtained sector patterns is of relatively high quality.

The behavior of the element pattern shape when changing the frequency for the array in question is illustrated by the curves shown in Figure 6.6. The presented patterns have been calculated for the array with the linear dimensions multiplied by ratio f/f_0 , where f is an operating frequency and f_0 is a reference frequency to which all the dimensions indicated earlier in wavelengths correspond. The phase of the second mode in this case has been calculated by formula

$$\psi_2(f) = \frac{\psi_2(f_0)\gamma_2(f)}{\gamma_2(f_0)} \tag{6.21}$$

obtained in the assumption that the phase is mainly determined by the distance between the aperture and transition. The results show that the sector shape of the element pattern keeps well at least in a 10% frequency band, and the pattern width changes in a natural way in accordance with the change of the element spacing expressed in λ with frequency.

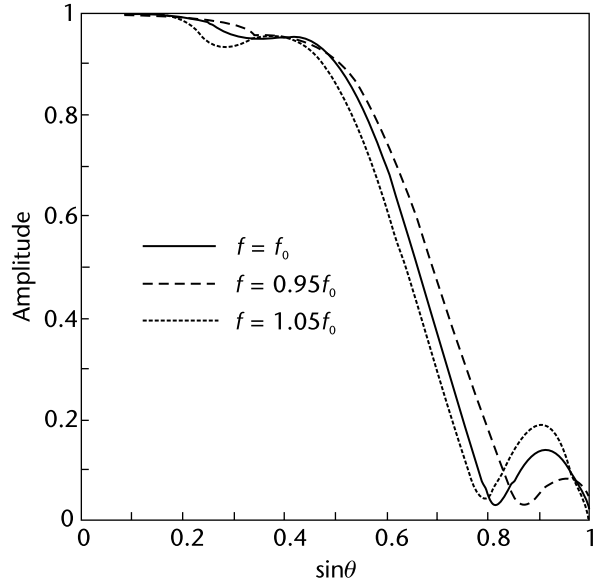

Figure 6.6 Element pattern of array with $b = a = 0.8\lambda$ in the presence of strip structures at frequencies f_0 (reference frequency), $0.95f_0$, and $1.05f_0$.

The next example is an array of waveguides of width $a = b = 1.2\lambda$, at which three waveguide modes (TEM, TM_2, and TM_3) are propagating. If the waveguides are only excited by the TEM modes, when $A_1 = 1$ and $A_m = 0$ for $m > 1$ in (6.1) and (6.17) to (6.19), the optimized structures consisting of $L = 6$ strips with parameters $s_l = 0.2\lambda$ and $z_l = [0.2 + 0.39(l \quad 1)]\lambda$, $(l = 1, 2, \ldots, L)$, allow us to obtain the element pattern shown by triangles in Figure 6.7, where the crosses correspond to the element pattern of the array without strips. The comparison shows that the strips improve the element pattern shape in the region of the grating lobe movement. However, the fall-off of the pattern level in the sector of scan remains considerable. The indicated fall-off is explained by the increase of the reflected power, which achieves about 19% at the edge of the scan sector, with up to 3% and 15% of the incident power being reflected in the TM_2 and TM_3 modes, respectively. If we assume that only reflected TM_2 modes return back to the apertures [i.e., $A_2 = R_2 \exp(i\psi_2)$ in (6.1) and (6.17) to (6.19)], we can slightly improve the element pattern shape, as shown in Figure 6.7 by a major-dashed curve calculated at $\psi_2 = 290°$. However, since the second modes transfer only a small part of the reflected power, the improvement achieved is not considerable. A significantly greater effect can be achieved by using both the second and the third modes. Assume that at some distance from the aperture, each triple-mode waveguide is divided by two symmetric dual-mode channels connected through symmetric matched transitions to single-mode waveguides. The latter, in turn, are connected to the arms of a symmetric matched two-channel power divider. In this case, both modes will be completely returned to the apertures, and, similarly to the second mode, for the third one we can write $A_3 = R_3 \exp(i\psi_3)$, where phase ψ_3 is determined independently from the phase ψ_2. The element pattern corresponding to the array in question with optimum value $\psi_3 = 300°$ is shown in Figure 6.7 by the solid curve, and the curve shown by small dashes represents the

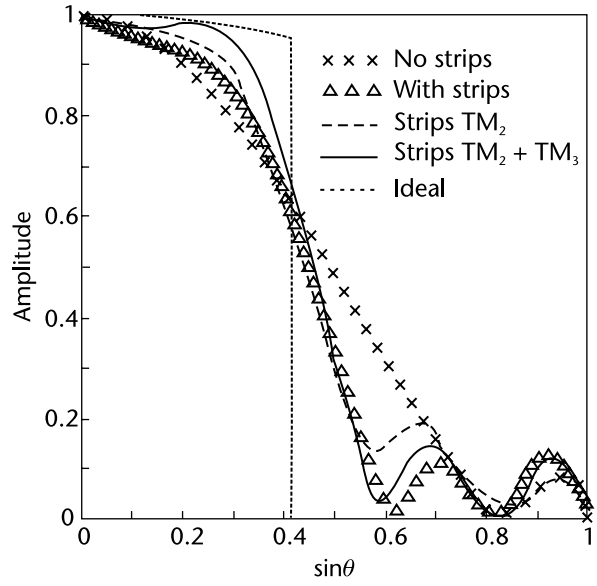

Figure 6.7 Element pattern of array with $b = a = 1.2\lambda$.

corresponding ideal sector element pattern. So, like in the case of the dual-mode waveguide array, the optimized strip structures at optimum excitation allow us to obtain the sector element patterns of high quality.

Variations of the element pattern shape in a 10% frequency band are shown in Figure 6.8. The frequency dependence of the phase for the third mode has been

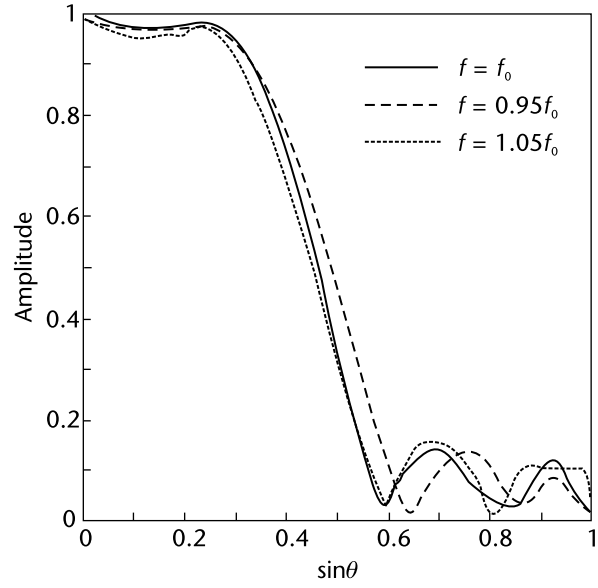

Figure 6.8 Element pattern of an array with $b = a = 1.2\lambda$ in the presence of strip structures at frequencies f_0 (reference frequency), $0.95f_0$, and $1.05f_0$.

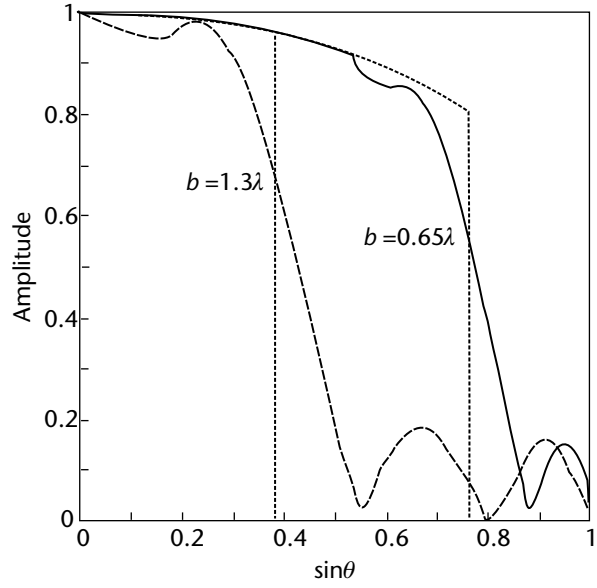

Figure 6.9 Element pattern of an array with $b = a = 0.65\lambda$ and $b = a = 1.3\lambda$ shaped by optimized strip structures.

calculated by formula (6.21) with replacement of the index 2 by index 3, while calculation of the phase for the second mode has been performed in the same way as in the previous example. Although the latter is a rather rough approximation in this case, it exerts no considerable influence on the results because the power in the second mode is much smaller than in the third one.

The range of the array element spacing, for which the strip structures allow shaping the sector element patterns of high quality, is characterized by the examples presented in Figure 6.9. The element patterns shown here correspond to the arrays with the following parameters $a = b = 0.65\lambda$, $s_l = 0.2\lambda$, $z_l = [0.2 + 0.0875(l \quad 1)]\lambda$, $l = 1, 2, \ldots, L$, $L = 9$, $\psi_2 = 230°$, and with $a = b = 1.3\lambda$, $s_l = 0.2\lambda$, $z_l = [0.2 + 0.39 (l \quad 1)]\lambda$, $l = 1, 2, \ldots, L$, $L = 6$, $\psi_2 = 300°$, $\psi_2 = 270°$. The quality of the achieved sector element patterns worsens with the further decrease of the element spacing due to increasing the reflected power in the dominant TEM mode. The further increase of the spacing from 1.3λ results in difficulties in suppressing the sidelobes.

6.3 Planar Array of Circular Waveguides with Disk Structures

6.3.1 Geometry, Excitation, and Field Representation

The technique developed for numerical analysis of the one-dimensional periodic array of parallel-plate waveguides exciting the strip slow-wave structures is generalized here for the case of a planar dually periodic array of circular waveguides exciting disk slow-wave structures. The geometry of the array accepted as a model for theoretical and numerical analysis is shown in Figure 6.10, together with a rectangular Cartesian system of coordinates x, y, and z. The array is an infinite dually periodic structure where the elements are arranged in rows with spacing d_x and the

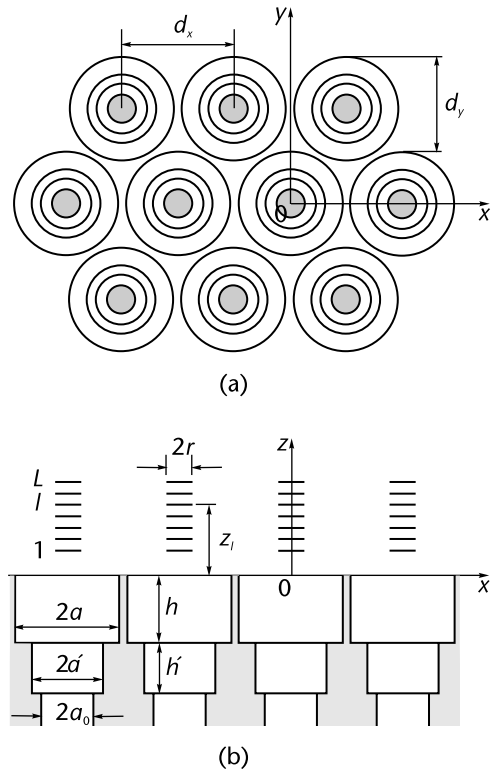

Figure 6.10 Geometry of planar periodic array of circular waveguides with multilayer disk structures: (a) top view and (b) cross-section on 0*xz* plane.

rows are arranged with spacing d_y. The array elements can form both a rectangular lattice and a triangular lattice, as shown in Figure 6.10, where the neighboring rows are shifted along the x-axis by $d_x/2$ with respect to each other. The array element consists of an input semi-infinite circular waveguide of diameter $2a_0$, a matching transition of diameter $2a$ and length h , and a radiation section of diameter $2a$ and length h. The indicated sections are connected by flanges, have a common axis, and may be filled with dielectric of relative permittivity $\varepsilon^{(0)}$, ε', and ε, respectively. The radiating sections have a common infinite flange. Along the axis of each waveguide, there are arranged L disks of diameter $2r$ and zero thickness. Their positions above the aperture are characterized by parameters z_l, where $1 \quad l \quad L$. All the waveguide sections, flanges, and disks are assumed to be perfectly conducting.

We also assume that the input waveguides are excited by their dominant TE_{11} modes of circular polarization. The incident modes have identical amplitudes, and their phases change linearly along the main axes corresponding to a specified direction of the main lobe in space in the same manner as described in Section 5.5.1. The radiated field calculated for such a quasi-periodic excitation will be subsequently used for calculation of the array element pattern, which is of primary interest in this study.

Comparing Figures 6.10 and 5.24, as well as their descriptions, we can note that the waveguide part of the array with dielectric elements is identical to the waveguide part of the array with disk structures up to notation of the parameters.

So, representing the electric and magnetic fields in the radiating section of the array in question, we will use formulas (5.68) and (5.69) together with the subsequent description of the parameters standing in them.

The disk structures differ from the protruding dielectric elements, and therefore the representation of the fields above the waveguide apertures will be different. Namely, the strengths of the total transverse electric and magnetic fields in the region $z \quad 0$ are represented as the following expansions in the terms of the complete system of the Floquet mode vector wave functions (1.26) and (1.27):

$$\begin{aligned} \boldsymbol{E}_t(x,y,z) = \eta_0 \sum_{l=0}^{L} \sum_{p,q} & [kT_{1pq}^{(l)} \psi_{1pq}(x,y) \\ & + \Gamma_{pq} T_{2pq}^{(l)} \psi_{2pq}(x,y)] e^{i\Gamma_{pq}|z \quad z_l|} \end{aligned} \tag{6.22}$$

$$\begin{aligned} \boldsymbol{H}(x,y,z) \quad \boldsymbol{e}_z = & \sum_{l=0}^{L} \operatorname{sign}(z \quad z_l) \\ & \sum_{p,q} [\Gamma_{pq} T_{1pq}^{(l)} \psi_{1pq}(x,y) + kT_{2pq}^{(l)} \psi_{2pq}(x,y)] e^{i\Gamma_{pq}|z \quad z_l|} \end{aligned} \tag{6.23}$$

where $T_{jpq}^{(l)}$ are unknown amplitudes of the TE ($j = 1$) and TM ($j = 2$) modes going from the planes $z = z_l$, with $z_0 = 0$. The transverse and longitudinal propagation constants involved in (6.22) and (6.23) are determined by formulas (1.21).

As with the case of the array with strip structures considered in the previous section, the amplitudes of the Floquet modes going from the planes of the disks are expressed via the surface current densities $\boldsymbol{j}_l(\rho,\varphi)$, $1 \quad l \quad L$, on the disks by formulas

$$T_{1pq}^{(l)} = \frac{1}{2\Gamma_{pq}} \int_0^r \int_0^{2\pi} \boldsymbol{j}_l(\rho,\varphi) \times \psi_{1pq}(x,y) \rho d\rho d\varphi \tag{6.24}$$

$$T_{2pq}^{(l)} = \frac{1}{2k} \int_0^r \int_0^{2\pi} \boldsymbol{j}_l(\rho,\varphi) \times \psi_{2pq}(x,y) \rho d\rho d\varphi \tag{6.25}$$

resulting from the more general expressions (1.29) through (1.32). The indicated current densities are represented by the expansions

$$\boldsymbol{j}_l(\rho,\varphi) = 2k \sum_{m,n} \sum_{j=1}^{2} C_{jmn}^{(l)} \boldsymbol{f}_{jmn}(\rho,\varphi) \tag{6.26}$$

in terms of a complete system of vector functions $\boldsymbol{f}_{1mn}(\rho,\varphi)$ and $\boldsymbol{f}_{2mn}(\rho,\varphi)$. Following the approach applied in [24] for analysis of a periodic structure with rectangular plates, we obtain the indicated functions from functions (5.70) and (5.71) by replacement of a by r, and subsequent vector multiplication of them by $\boldsymbol{e}_z$ and $\boldsymbol{e}_z$, respectively, to satisfy the zero condition for the radial component of the current density at the disk edge.

6.3.2 Algebraic System and Array Characteristics

The unknown coefficients in the expansions written earlier are determined using the boundary conditions for the fields in the waveguide aperture, on the flange, and on the surfaces of the disks. The electric field (6.22) at $z = 0$ must vanish on the flange and must be equal to the electric field (5.68) in the waveguide aperture. Using the orthogonality of functions (1.26) and (1.27), we obtain the relations

$$T_{1pq}^{(0)} = \sum_{m,n} Q_{1pq}^{1mn}(A_{1mn}e_{1mn} + B_{1mn}) \sum_{l=1}^{L} T_{1pq}^{(l)} e^{i\Gamma_{pq}z_l} \tag{6.27}$$

$$\Gamma_{p\,q} \sum_{l=0}^{L} T_{2p\,q}^{(l)} = \sum_{m,n} [kQ_{2p\,q}^{1mn}(A_{1mn}e_{1mn} + B_{1mn}) + \gamma_{2mn}Q_{2p\,q}^{2mn}(A_{2mn}e_{2mn} \quad B_{2mn})] \tag{6.28}$$

where coefficients $Q_{jpq}^{j\,mn}$ are determined by formulas (5.85) through (5.88).

Similarly, substituting (6.26), (1.26), and (1.27) into (6.24) and (6.25), we obtain

$$T_{1pq}^{(l)} = \frac{k}{\Gamma_{pq}} \sum_{m,n\,j=1}^{2} D_{1pq}^{jmn} C_{jmn}^{(l)} \tag{6.29}$$

$$T_{2pq}^{(l)} = \sum_{m,n} D_{2pq}^{1mn} C_{1mn}^{(l)} \tag{6.30}$$

where $l = 1, 2, \ldots, L$; $D_{1pq}^{1mn} = \quad Q_{2pq}^{1mn}$, $D_{1pq}^{2mn} = Q_{2pq}^{2mn}$, and $D_{2pq}^{1mn} = Q_{1pq}^{1mn}$ with replacement of a by r.

Now let us proceed directly to forming the final system of algebraic equations. The first part is formed by the relations between the amplitude of the incident mode in the input waveguide and the amplitudes of the forward and backward modes in the radiating section similar to (5.43):

$$A_{j\,mn} \sum_{n\;\;j=1}^{2} S_{j\,n\,,jn}^{m,11} e_{jmn} B_{jmn} = S_{j\,n\,,j\;n}^{m,10}\; A_{j\;mn}^{i} \tag{6.31}$$

where $j = 1, 2; m = 0, \pm 1, \pm 2, \ldots; n = 1, 2, \ldots; j = 1, 2; n = 1, 2, \ldots; A_{j\;mn}^{i} = \delta_{1j}\,\delta_{1m}\delta_{1n}$ or $A_{j\;mn}^{i} = \delta_{1j}\,\delta_{\;1m}\delta_{1n}$ are amplitudes of the incident modes; δ_{mn} is the Kronecker symbol; and $S_{j\,n\,,jn}^{m,\nu\;\nu}$ is the element of the scattering matrix for the transition between the input (index 0) and radiating (index 1) sections. This element is the amplitude of the $j\,mn$ th mode, excited in the ν section when the jmnth mode of unit amplitude incidents in the νth section.

The second part of the system is obtained from the continuity condition for the magnetic fields (5.69) and (6.23) in the waveguide aperture. Using the orthogonal-

ity of functions (5.70) and (5.71) here, as well as taking into account the relations (6.27), (6.29), and (6.30), we obtain

$$\begin{aligned}
&\sum_{m,n}(e_{1mn}A_{1mn}+B_{1mn})\sum_{p,q}\Gamma_{pq}Q_{1pq}^{1m\,n}\;Q_{1pq}^{1mn}\\
&\gamma_{1m\,n}(e_{1m\,n}A_{1m\,n}\quad B_{1m\,n})+\sum_{p,q}kQ_{2pq}^{1m\,n}\;T_{2pq}^{(0)}\\
&k\sum_{l=1}^{L}\sum_{m,n}[C_{1mn}^{(l)}\sum_{p,q}(2Q_{1pq}^{1m\,n}\;D_{1pq}^{1mn}+Q_{2pq}^{1m\,n}\;D_{2pq}^{1mn})e^{i\Gamma_{pq}z_l}\\
&+C_{2mn}^{(l)}\sum_{p,q}2Q_{1pq}^{1m\,n}\;D_{1pq}^{2mn}e^{i\Gamma_{pq}z_l}]=0
\end{aligned}\tag{6.32}$$

$$\begin{aligned}
&\varepsilon(e_{2m\,n}A_{2m\,n}+B_{2m\,n})+\sum_{p,q}Q_{2pq}^{2m\,n}\;T_{2pq}^{(0)}\\
&\sum_{l=1}^{L}\sum_{m,n}C_{1mn}^{(l)}\sum_{p,q}Q_{2pq}^{2m\,n}\;D_{2pq}^{1mn}e^{i\Gamma_{pq}z_l}=0
\end{aligned}\tag{6.33}$$

where $m=0,\pm1,\pm2,\ldots$ and $n=1,2,\ldots$.

The next part of the system is obtained from (6.28) and by taking (6.30) into account

$$\begin{aligned}
&\sum_{m,n}[kQ_{2p\,q}^{1mn}(A_{1mn}e_{1mn}+B_{1mn})+\gamma_{2mn}Q_{2p\,q}^{2mn}(A_{2mn}e_{2mn}\quad B_{2mn})]\\
&\Gamma_{p\,q}T_{2p\,q}^{(0)}\sum_{l=1}^{L}\sum_{m,n}C_{1mn}^{(l)}\;\Gamma_{p\,q}D_{2p\,q}^{1mn}e^{i\Gamma_{p\,q}z_l}=0
\end{aligned}\tag{6.34}$$

where $p,q=0,\pm1,\pm2\ldots$.

Finally, the fourth part of the system is obtained from the zero boundary condition for the electric field (6.22) on the surface of each disk. Projecting this equality on the weighting functions $f_{1m\,n}(\rho,\varphi)$ and $f_{2m\,n}(\rho,\varphi)$, as well as taking (6.27), (6.29), and (6.30) into account, we obtain

$$\begin{aligned}
&\sum_{m,n}(A_{1mn}e_{1mn}+B_{1mn})\sum_{p,q}kD_{1pq}^{j\,m\,n}\;Q_{1pq}^{1mn}e^{i\Gamma_{pq}z_l}\\
&+\delta_{j\,1}\sum_{p,q}T_{2pq}^{(0)}\Gamma_{pq}D_{2pq}^{1m\,n}\;e^{i\Gamma_{pq}z_l}+k\sum_{l=1}^{L}\sum_{m,n}\sum_{j=1}^{2}C_{jmn}^{(l)}\sigma_{ljmn}^{l\,j\,m\,n}=0
\end{aligned}\tag{6.35}$$

where

$$\begin{aligned}
\sigma_{ljmn}^{l\,j\,m\,n}=&\sum_{p,q}kD_{1pq}^{j\,m\,n}\;D_{1pq}^{jmn}\frac{e^{i\Gamma_{pq}|z_l\quad z_l|}\quad e^{i\,\Gamma_{pq}(z_l+z_l)}}{\Gamma_{pq}}\\
&+\delta_{j\,1}\delta_{j1}D_{2pq}^{1m\,n}\;D_{2pq}^{1mn}\frac{\Gamma_{pq}}{k}e^{i\Gamma_{pq}|z_l\quad z_l|}
\end{aligned}\tag{6.36}$$

$l=1,2,\ldots L$; $j=1,2$; $m=0,\pm1,\pm2,\ldots$ and $n=1,2,\ldots$.

After appropriate truncation (to be discussed in the next section), the system of equations (6.31) through (6.34) is solved numerically by the Gauss elimination method. The results of that solution are used for calculation of the array characteristics of practical interest. The amplitudes of the modes reflected in the input waveguide, including the copolar and cross-polar reflection coefficients for the dominant TE_{11} mode, are calculated using (5.122). The components of the array element pattern are determined by (5.124) and (5.125). The amplitudes of the Floquet modes above the disk structures used for calculation of the element pattern are determined by the expressions

$$T_{1pq} = \sum_{m,n} (A_{1mn} e_{jmn} + B_{1mn}) Q_{1pq}^{1mn} \\ 2ik \sum_{l=1}^{L} \frac{\sin(\Gamma_{pq} z_l)}{\Gamma_{pq}} \sum_{m,n} \left(C_{1mn}^{(l)} D_{1pq}^{1mn} + C_{2mn}^{(l)} D_{1pq}^{2mn} \right) \tag{6.37}$$

$$T_{2pq} = T_{2pq}^{(0)} + \sum_{l=1}^{L} e^{i\Gamma_{pq} z_l} \sum_{m,n} C_{1mn}^{(l)} D_{2pq}^{1mn} \tag{6.38}$$

resulted from (6.22) at $z = z_L$ and taking (6.27), (6.29), and (6.30) into account. Remember, the second index 1 in (5.124) and (5.125) corresponds to the zero values of indices p and q in this section. The amplitudes of the reflected modes (5.122) and the amplitudes Floquet modes (6.37) and (6.38) are used for checking satisfaction of the power balance relation (5.123).

6.3.3 Results of Numerical Modeling

The operation of the FORTRAN code developed according to the algorithm described earlier has been tested in different ways. In particular, the results of its operation obtained keeping 20 to 40 waveguide modes with $-4 \le m \le 4$ and 200 to 300 Floquet modes have been in complete agreement with the calculated and measured data available in [21] for a number of geometrical configuration of the array without the disks.

The calculations of the array with the disk structure have been performed with the same number of modes for each disk, as was used for the modes in the radiating sections. The number of the Floquet modes, N_f, has been determined from the condition $w_{pq} \le w_{\max}$, where $w_{\max}$ is a specified radius in the space of direction cosines. A typical example demonstrating the influence of N_f on the reflection coefficient for a hexagonal array with parameters $a_0 = 0.36\lambda$, $a = a' = 0.5\lambda$, $h' = 0$, $h = 2\lambda$, $\varepsilon^{(0)} = \varepsilon' = \varepsilon = 1$, $d_x = 1.14\lambda$, $r = 0.15\lambda$, $L = 8$, and $z_l = 0.3\lambda + 0.1(l - 1)\lambda$, chosen afterward in the breadboard design, is presented in Table 6.1.

As we can see, stabilization of the results takes place for a significantly greater number of the Floquet modes than that in the absence of the disks. This is explained by the accuracy required for the calculation of the matrix elements (6.36) converging as w_{pq}^{-3} for the disks of the same level when $l = l'$. The convergence of the matrix elements corresponding to the interactions between the disks of different levels in (6.36), as well as between the disks and waveguide apertures in (6.32) to (6.35), is

Table 6.1 Convergence of Reflection Coefficient with Increasing Number of Floquet Modes Kept for Array with Disks at Broadside Beam Position

N_f	w_{max}/k	$\mathrm{Re}\{R_{111}\}$	$\mathrm{Im}\{R_{111}\}$
169	7.3	–0.0196	–0.3188
235	8.3	–0.0816	–0.1683
295	9.3	–0.0858	–0.1363
361	10.3	–0.0842	–0.1363
433	11.3	–0.0738	–0.1087
511	12.3	–0.0596	–0.0926
595	13.3	–0.0521	–0.0839
703	14.3	–0.0537	–0.0854

exponential, and hence the necessary accuracy is achieved for a much smaller number of the Floquet modes.

After performing the tests indicated earlier, the developed code has been used for calculation and optimization of a hexagonal array designed for scanning within a cone with flare angles of ±20° in the horizontal and vertical planes (Figure 6.10). Taking into account of the experience of [4], the element spacing has been chosen as $d_x = 1.14\lambda$ at a specified reference frequency f_0. The numerical experiments have shown that the best results are achieved when the radiation section has maximum radius $a = d_x/2$ providing maximum element gain of the array element in the absence of the disks. However, to provide the necessary strength of the breadboard design, the chosen radiating section radius is slightly smaller: $a = 0.5\lambda$. The input waveguide radius $a_0 = 0.36\lambda$ is standard at the specified frequency. No dielectric filling has been used. The calculations have shown that the junction between the input and radiating sections is matched almost ideally itself so that the transition is not required, and the transition parameters in the subsequent calculations have been specified as $a = a$ and $h = 0$. The initial values for the radius and number of the disks in the element $r = 0.15\lambda$ and $L = 8$ have been chosen in accordance with the experience of the experimental work [4] and the simulations of the two-dimensional model [6, 7]. Finally, the radiation section length $h = 2\lambda$ and the equidistant arrangement of the disks with $z_1 = 0.3\lambda$ and $z_L = \lambda$ have been determined as a result of the numerical experiment taking into account the mechanical design of the breadboard. The calculations have been performed by taking into account 250 coefficients $T^{(0)}_{2pq}$ and up to N_f 700 terms in the series (6.36).

The calculated magnitudes of the copolar and cross-polar element patterns and reflection coefficients in horizontal and vertical planes of the array under consideration excited by the circularly polarized TE_{11} modes at reference frequency f_0 are presented in Figure 6.11. The copolar element patterns of the array without the disks are also given for comparison. The results show that when the main beam scans by 20° from the broadside (sin 20° 0.342) in the horizontal and vertical planes, the element gain of the array with the disks is higher than that in the absence of the disks by 1.6 and 1.5 dB, respectively. The use of the disks also results in a reduction of the maximum grating lobe level from –7.9 to –12 dB. The copolar reflection coefficient within the scan sector does not exceed 0.12 (VSWR 1.27) in the horizontal plane and 0.074 (VSWR 1.16) in the vertical plane. The total return loss in the indicated planes is less than –18.2 dB and –21 dB, respectively.

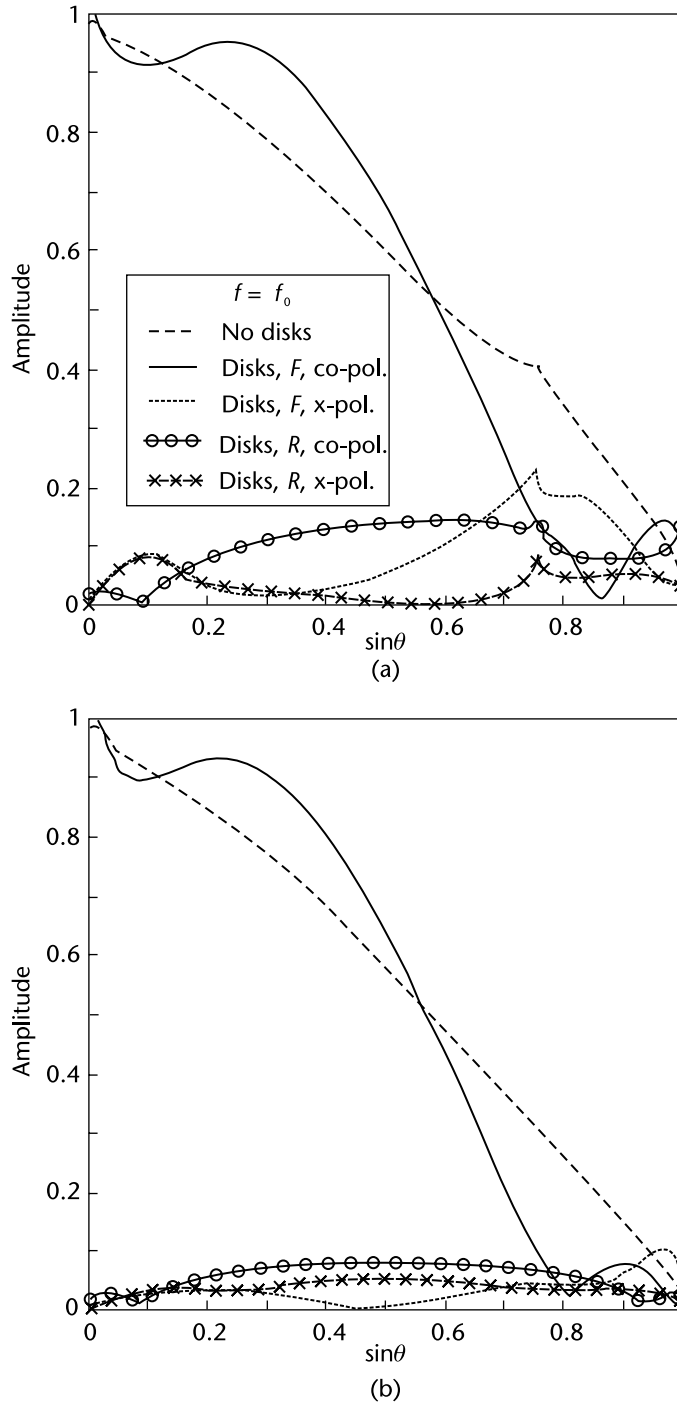

Figure 6.11 Element pattern and reflection coefficient at circular polarization in (a) horizontal and (b) vertical planes of a hexagonal array with $d_x = 1.14\lambda$, $a_0 = 0.36\lambda$, $a = a_0$, $h_1 = 0$, $a = 0.5\lambda$, $\varepsilon^{(0)} = \varepsilon = \varepsilon = 1$, $h = 2\lambda$, $r = 0.15\lambda$, $L = 8$, $z_1 = 0.3\lambda$, and $z_L = \lambda$ at central frequency f_0.

The modeling has also shown that the element pattern shape does not practically change as the parameters of the structure vary in the limits 6 L 9, 0.14λ r 0.16λ, and 0.1λ z_1 0.3λ.

As already noted in Chapter 1, one of the parameters characterizing the quality of limited-scan arrays is the element use efficiency [25] or its inverse parameter, the *element use factor* [26, 27]. The latter can be approximately evaluated as $\zeta = (d_{x,\max}/d_x)^2$, where $d_{x,\max}$ is the maximum element spacing corresponding to the ideal contour element pattern. This spacing is approximately equal to 1.688λ for the ideal element pattern of ±20° width. The indicated data as well as the value indicated earlier for the actual element spacing give ζ 2.19. However, since the average level of the actual array element pattern shown in Figure 6.11 is about 0.92 of the maximum level within the scan region, the "geometrical" value of the element use factor obtained earlier should additionally be multiplied by 0.92^{-2}. Then the element use factor will approximately equal 2.59. This value lies within the typical range for the arrays, where the efficient overlapping of the subarrays extends only to the closest neighbor array cells [27, 28].

The array element patterns calculated at frequencies $0.967f_0$ and $0.977f_0$, as well as at $1.017f_0$ and $1.033f_0$, are presented in Figures 6.12 and 6.13, respectively. The results show that the changes of the pattern shape within a 5.6% band from $0.977f_0$ to $1.033f_0$ are insignificant, and such behavior corresponds to the results presented in Section 6.1 and [4]. However, in Figure 6.12 we see that the element patterns of the array with disks at frequency $0.967f_0$ have sharp dips in the broadside, which are absent in the element pattern of the array without the disks. Therefore, the disk structure here is similar to a dielectric cover, the role of which in the surface wave excitation causing the similar dips is discussed in detail in [21].

The modeling shows that the dips also occur at the element pattern broadside in the array with a square lattice at $d_x = d_y$ 0.974λ and the disk structure parameters indicated earlier. Because of the high degree of the hexagonal and square lattice symmetry, as well as the circular symmetry of the array element, the effect in question is independent of the incident TE_{11} mode polarization. However, when the indicated lattice symmetry is broken, the effect can occur for only one linear polarization (e.g., at the vertical polarization in a rectangular lattice where d_x has a resonant value while d_y differs slightly). The calculations also show that the depth of the resonant pattern level reduction depends on the disk structure parameters—particularly on the height of its lower side above the waveguide apertures. This fact confirms the role of the higher order Floquet modes in the excitation of the surface waves in the structure.

The waveguide structure with hexagonal lattice period of 1.1 to 1.2λ and the radiating section diameter of about one wavelength without dielectric filling is characterized by good natural match to free space and by the absence of the resonance effects. The application of the disk structures allows shaping the sector element patterns in arrays designed for scanning within a sector of about ±20° in the principal planes. The shaping of wider sector element patterns requires the use of appropriately smaller element spacing and waveguides of smaller diameter. As shown in [9], this situation requires additional discussion. As an example, let us consider a hexagonal array with $d_x = 0.92\lambda$ and $a = 0.45\lambda$. The array element pattern at circular polarization in the absence of the dielectric filling and disk structures is shown

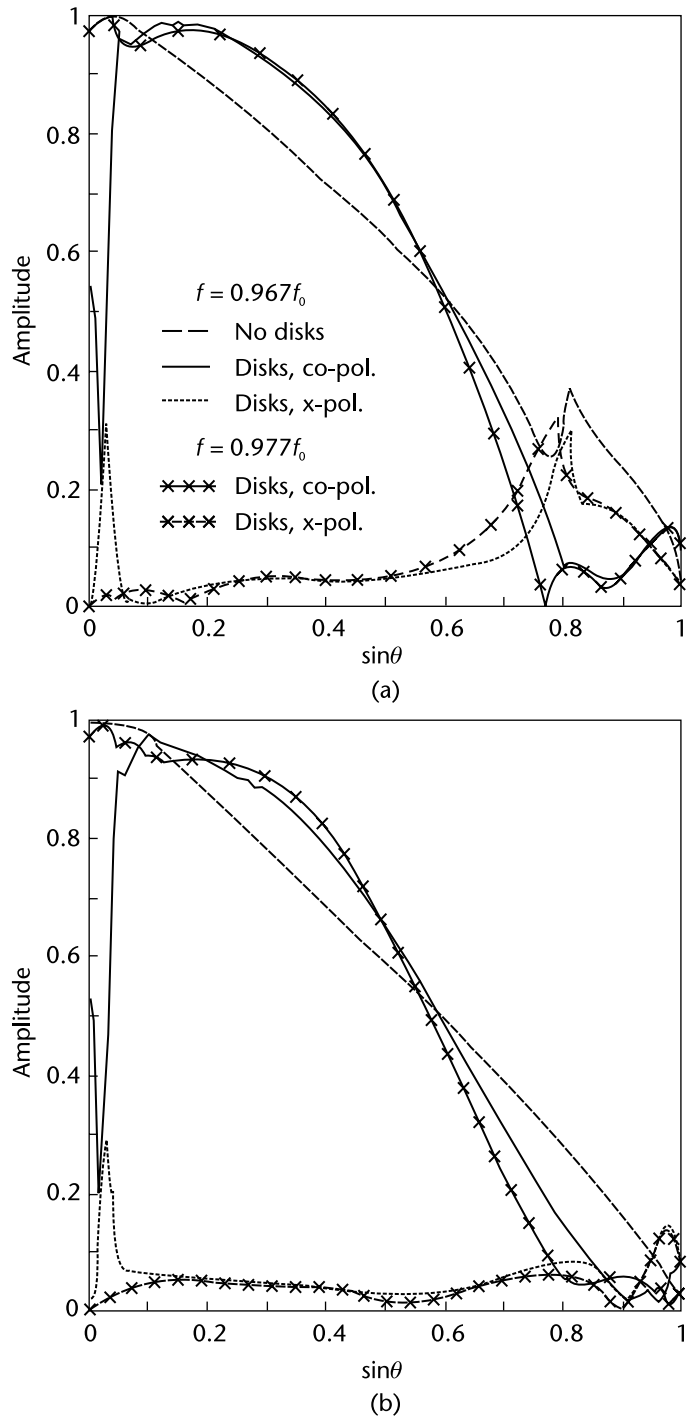

Figure 6.12 Element pattern at circular polarization in (a) horizontal and (b) vertical planes of hexagonal array with parameters indicated in the caption for Figure 6.11 at frequencies $f = 0.967f_0$ and $f = 0.977f_0$.

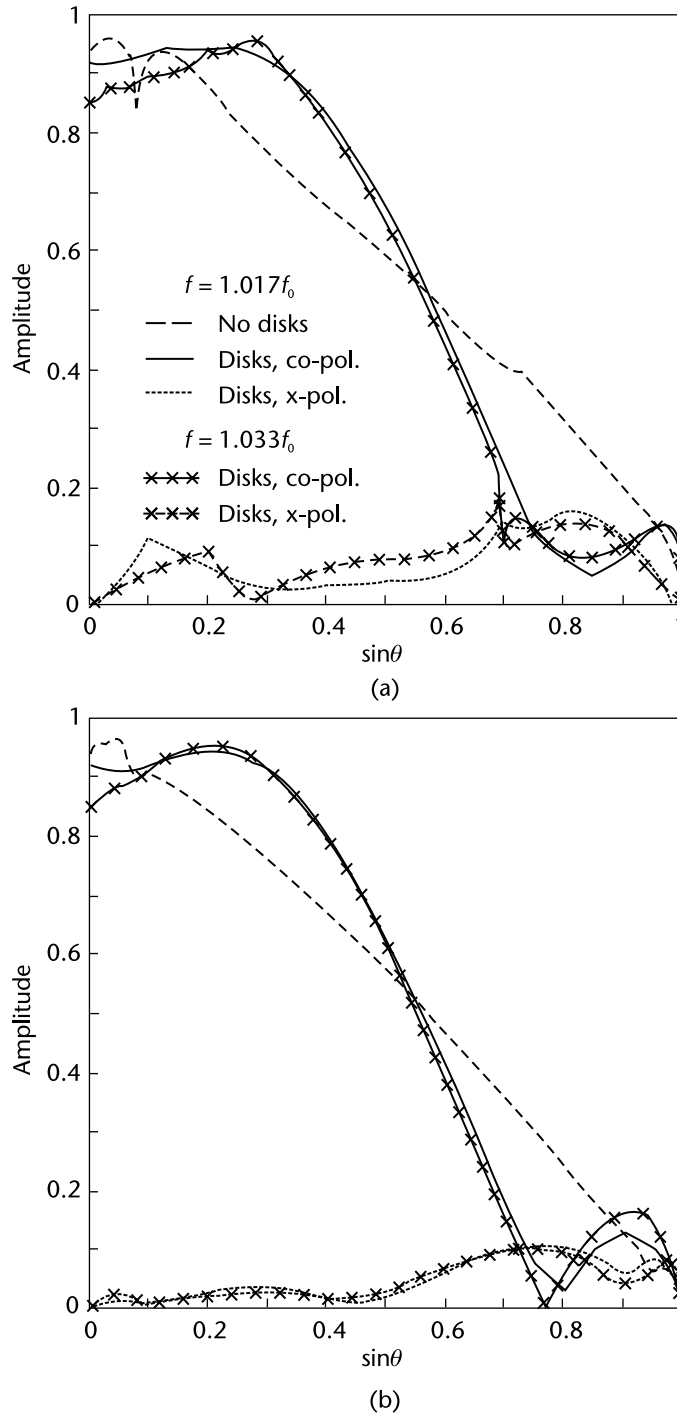

Figure 6.13 Element pattern at circular polarization in (a) horizontal and (b) vertical planes of hexagonal array with parameters indicated in the caption for Figure 6.11 at frequencies $f = 1.017f_0$ and $f = 1.033f_0$.

in Figure 6.14 by the curve with smaller dashes. This pattern has resonance dips in the single-beam scan region. These dips can be removed by application of dielectric plugs of definite height and permittivity [21]. The plug permittivity is chosen to make the mode TE_{21} propagate. The element pattern corresponding to parameters $\varepsilon = 1.5$, $h = 0.48\lambda$, $a_0 = a = 0.34\lambda$, $\varepsilon^{(0)} = \varepsilon = 1$, and $h = 0$ is shown in Figure 6.14 by the curve with major dashes. Application of the disk structures with $r = 0.15\lambda$, $L = 8$, and $z_l = 0.3\lambda + 0.093\lambda(l-1)$, $l = 1, 2, \ldots, L$, obtained as a result of numerical

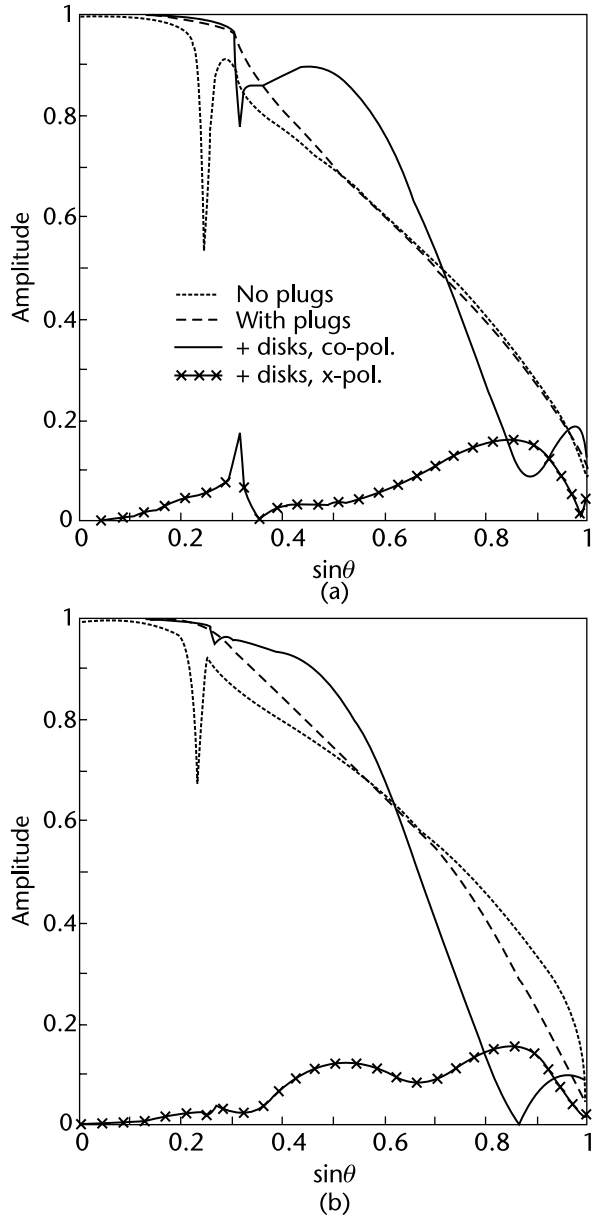

Figure 6.14 Element pattern at circular polarization in (a) horizontal and (b) vertical planes of hexagonal array with $d_x = 0.92\lambda$, $a_0 = a' = a = 0.45\lambda$, $h = 0$, $\varepsilon^{(0)} = \varepsilon = 1$, $\varepsilon = 1.5$, $h = 0.48\lambda$ in the absence of disks and of the same array with disks at $r = 0.15\lambda$, $L = 8$, and $z_l = 0.3\lambda + 0.093\lambda(l-1)$.

optimization, allows considerable improvement of the element pattern shape. This pattern, shown in Figure 6.14 by the solid curve, has a considerably higher level in the scan region of the main beam and a correspondingly reduced level in the regions of the grating lobes. Shaping of the sector element patterns of even greater width is also possible in principle, but already has a smaller effect [9].

6.3.4 Results of Breadboarding

The method of analysis and the results of calculations presented earlier for a hexagonal array with element spacing 1.14λ have been used for creating two breadboards of the array with disk structures designed for operation in the K_a- and X-bands of frequencies. The photographs of the K_a-band array breadboard are shown in Figure 6.15.

The antenna consists of two major parts, namely, an exciting structure and a disk structure. The former is a thick aluminum plate containing 19 holes of diameter $2a_0$ = 7.2 mm corresponding to the input waveguide sections shown in Figure 6.10(b).

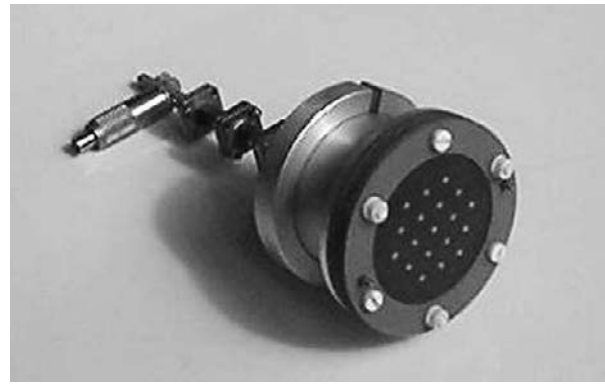

(a)

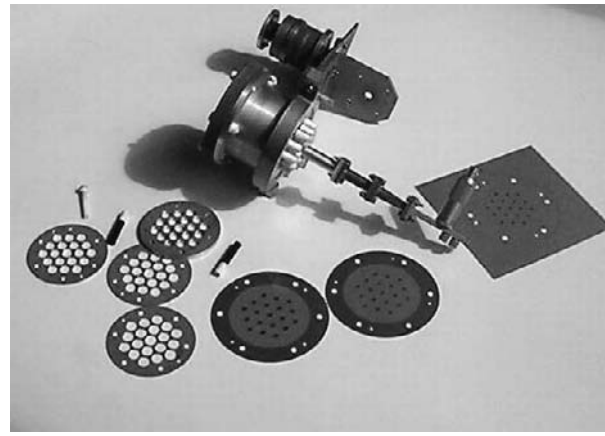

(b)

Figure 6.15 Nineteen-element breadboard of waveguide array with disk structures: (a) in assembled state and (b) separate components of design.

The axes of the holes are arranged in the nodes of a hexagonal lattice with period 11.4 mm. The upper radiating section is assembled using plates of different thickness, as shown in Figure 6.15(b), with holes of diameter $2a$ = 10 mm whose axes coincide with the axes of the input holes in the lower plate. The set of the indicated plates allows us to assemble the upper waveguide sections at different heights if necessary. The height of the radiating section in the final variant is equal to h = 20 mm.

The second major part of the breadboard contains the disk structures. The disks are arranged on eight dielectric films of thickness 0.05 mm. Formation of the disks on the films has been performed using the ion-beam method. The films are fixed on the ring frames with spacing between adjacent layers equal to 1 mm. The distance between the lower film and the apertures of the radiating sections is equal to 3 mm.

As we see in Figure 6.15(b), the central element of the array is excited through a coaxial-to-waveguide transition, a transition from the rectangular waveguide to a circular one, and a polarizer. After the polarizer, the TE_{11} mode of circular polarization comes to the input waveguide section with subsequent radiation through the disk structures. The matching loads also shown in Figure 6.15(b) are inserted in the input channels of all 18 peripheral elements.

The radiation patterns in the principal planes of the breadboard in the frequency band 29.0 to 30.5 GHz have been measured in an anechoic chamber of sufficient dimensions to provide the far zone condition for the breadboard aperture. The results of measurements are shown in Figure 6.16 for frequency 30 GHz corresponding to the central frequency f_0 mentioned in the theoretical model and in Figure 6.17 for frequency 29 GHz corresponding to $0.967f_0$. The measured patterns are compared to the calculated ones taken from Figures 6.11 and 6.12 and calculated into decibels.

The comparisons show that there is good agreement between the calculated and measured data regarding the width and shape of the sector beams. The differences observed in some other parts of the patterns are explained by the differences between the theoretical model in the form of an infinite array and the experimental breadboard of finite dimensions comprising only 19 elements. Moreover, the disk structures in the breadboard are surrounded by a dielectric cylinder formed by the dielectric rings supporting the films with the disks. This cylinder blocks the radiation at 60° to 90° angles from the broadside, where the most considerable differences in the radiation patterns are observed. One more reason for the differences is the resonance effects taking place in the infinite array at frequency $0.967f_0$ (corresponding to the measurements at 29 GHz) and revealing themselves by the narrow dips in the calculated array element patterns (Figure 6.17). The array fragment with a small number of elements does not reveal the indicated effects, as discussed in the earlier works on phased arrays (e.g., [21, 29]). Comparison of the measured and calculated array element patterns at 30.5 GHz gives a picture similar to that presented in Figure 6.16, and, for this reason, the results are not presented here.

The X-band array breadboard is described in [11]. Its exciting part is similar to the exciting part of the S-band array considered in Section 6.1. The array consists of 19 crossed microstrip dipoles arranged on longitudinal dielectric boards. Each dipole pair is arranged in a metallic cylinder. The central dipoles are fed through a

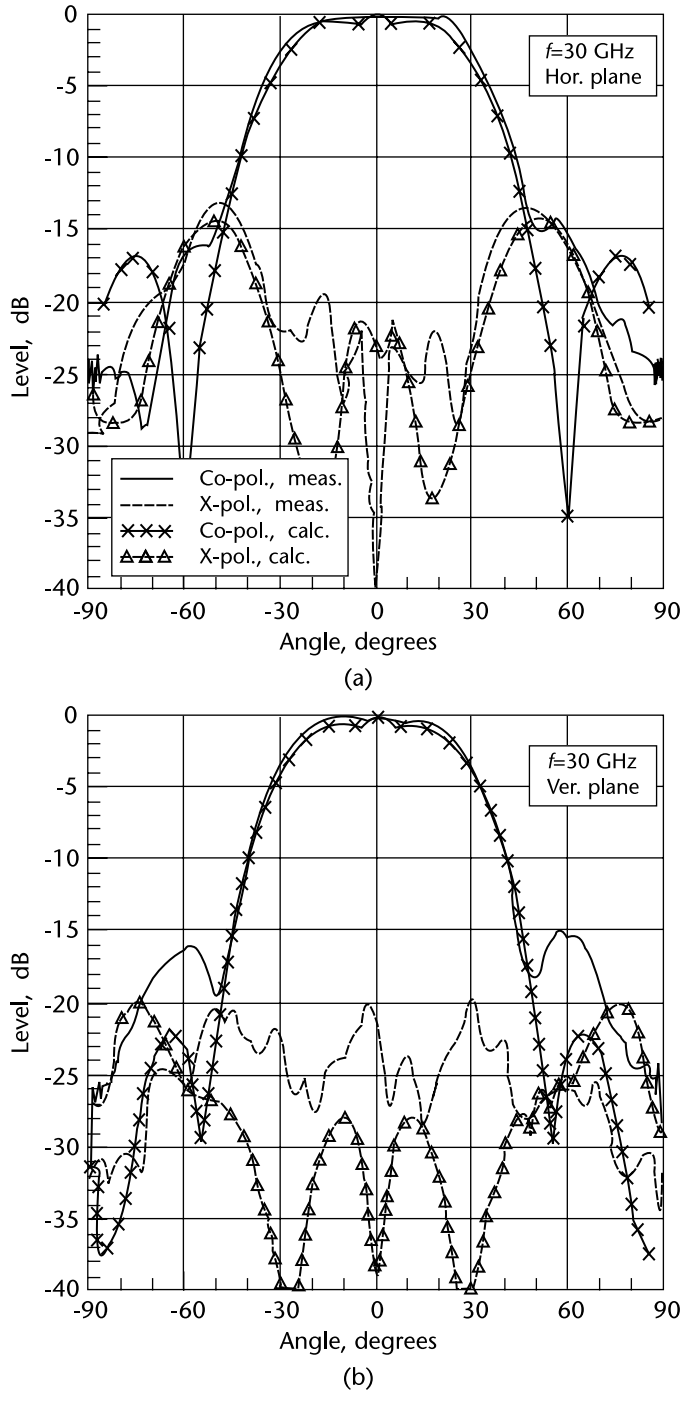

Figure 6.16 Measured and calculated array element patterns in (a) horizontal and (b) vertical planes at frequency 30 GHz.

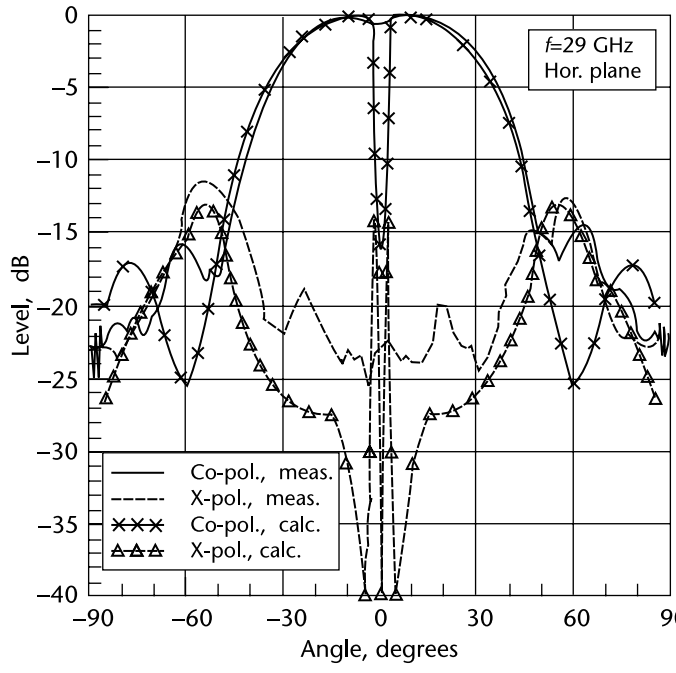

(a)

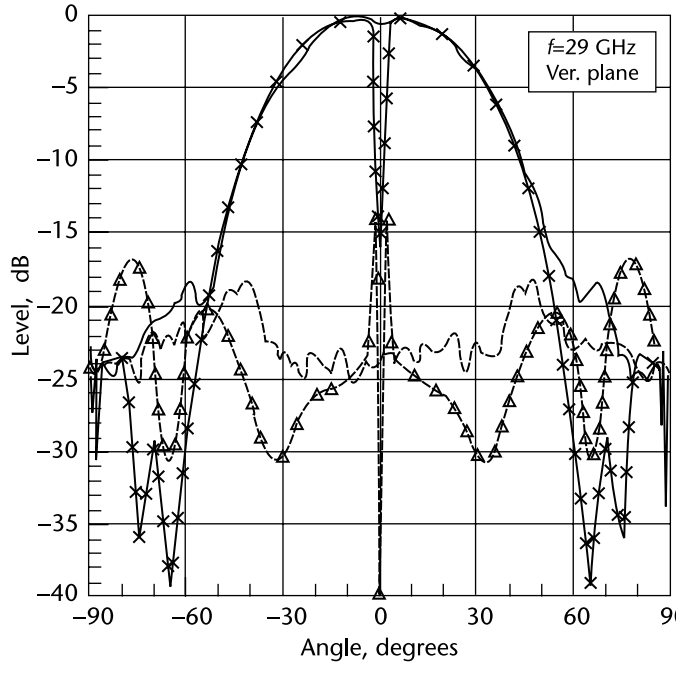

(b)

Figure 6.17 Measured and calculated array element patterns in (a) horizontal and (b) vertical planes at frequency 29 GHz.

hybrid device providing a circular polarization of radiation. The inputs of all the other dipoles are connected to matching loads. The disk structures forming the sector element patterns are performed in the same manner as in the K_a-band breadboard (i.e., on thin dielectric films fixed on dielectric ring frames). The difference consists of using 10 layers instead of 8 and using disks of nonidentical diameters. Other details are indicated in [11]. This work also compares the measured element patterns of the X-band array to the similar patterns of the K_a-band array at element spacing 1.12λ. The comparison shows that the results are very close to each other. Moreover, the element patterns of the array with the disk structures turn out to be very close to the element patterns of the array of the same element spacing with dielectric rods. This fact indicates that the arrays with disk and rod elements possess similar capabilities of shaping the sector element patterns.

6.4 Arrays of Yagi-Uda Antenna Elements

The corrugated rods excited by open-ended waveguides or dipoles, as well as the dielectric rods protruding from waveguides, are convenient radiating array elements for shaping sector radiation patterns in both principal planes. However, some array applications require scanning in a wide angular sector in one plane and in a narrow (limited) sector in another (orthogonal) plane (i.e., the appropriate element pattern must be sector-shaped only in one plane). In such cases, radiating elements in the form of Yagi-Uda dipole antennas are convenient. Their design allows arrangement of them with small element spacing in the plane of wide-angle scanning. At the same time, since they are capable of supporting traveling waves in the longitudinal direction similarly to the dielectric or corrugated rods, the interaction between such elements over free space in the limited scan plane can be used for shaping a sector element pattern in this plane. Some examples of that, though with sector patterns of not very high quality, are available in [30], where the Yagi elements are used for comparison with the elements in the form of dielectric plates, which have been the primary object of study there. A theoretical study of the director Yagi elements in planar arrays designed for wide-angle scanning in both planes has been carried out in [31]. A study of the possibilities of shaping the sector element patterns for providing effective beam scanning in a limited sector in one plane is carried out later.

6.4.1 Problem Formulation and Solution

The geometry of an infinite planar array chosen for study here is shown in Figure 6.18 together with a rectangular coordinate system $0xyz$. The Yagi elements can be arranged in the nodes of either a triangular lattice (as shown in Figure 6.18) or a rectangular one, with element spacing d_x in the horizontal rows and with spacing d_y between adjacent rows. The array element consists of M straight perfectly conducting cylinders (wires) arranged symmetrically in a plane parallel to the $0yz$ plane. Each wire is parallel to an infinite perfectly conducting screen and characterized by diameter $2a$, length $2d_m$, and height h_m above the screen, where $m = 1, 2, \ldots, M$. The first wire is considered to be a driven dipole, and all the others are passive directors. The dipoles are assumed to be fed in the infinitely narrow gaps in

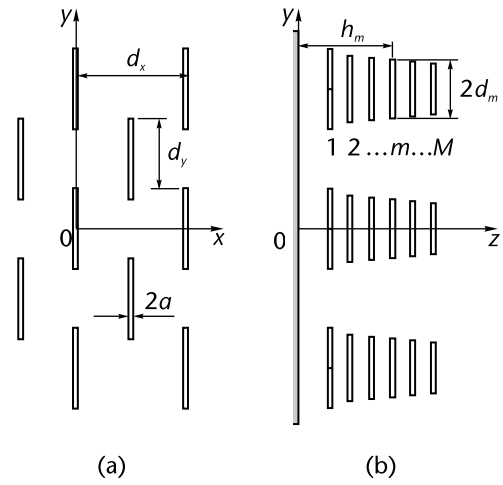

Figure 6.18 Geometry of planar array of Yagi (director) antenna elements: (a) top view and (b) side view in 0*yz* plane.

their centers via transmitting lines with wave resistance W_f. The amplitudes of the excitation are assumed to be identical, and the phases are linearly progressing in the principal planes.

To calculate the array characteristics, we assume that the wire diameter $2a$ is much smaller than the operating wavelength λ, element spacings, and distance between any two wires. This thin-wire approximation allows the surface currents on the wires to be replaced by the y-directed currents $I_m(y)$, $m = 1, 2, \ldots, M$, on the wire axes. The boundary condition on the wire surfaces and the subsequent standard procedure (e.g., [32]) aimed at determining the indicated currents give the following system of integral equations of Hallen type [1]:

$$\sum_{\mu=1}^{M} \int_{d_\mu}^{d_\mu} G_{m\mu}(y, y')I_\mu(y')dy' + C_m \cos ky + D_m \sin ky = \frac{iV\delta_{1m}}{2\eta_0} \sin k|y| \qquad (6.39)$$

where $|y| \quad d_m$, $m = 1, 2, \ldots, M$; C_m and D_m are constants to be determined; V is the voltage in the gap of the central dipole; δ_{1m} is the Kronecker symbol;

$$G_{m\mu}(y, y') = \frac{\delta_{m\mu}}{4\pi} \sum_{p=} \sum_{q=} \frac{e^{k R_{pq}} \cos k R_{pq}}{R_{pq}} e^{i \quad pq}$$
$$+ \frac{1}{2d_x d_y} \sum_{p=} \sum_{q=} \frac{e^{\Gamma_{pq}|h_m \quad h_\mu|} \quad e^{\Gamma_{pq}(h_m + h_\mu)}}{\Gamma_{pq}} \qquad (6.40)$$
$$\delta_{m\mu} \operatorname{Re} \frac{e^{\Gamma_{pq}|h_m \quad h_\mu|}}{\Gamma_{pq}} \quad e^{i\beta_{pq}(y \quad y')}$$

is the kernel; $_{pq} = k(x_{pq}u + y_q v)$ are the phases of the excitation of the dipoles, corresponding to the direction cosines $u = \sin\theta\cos\varphi$ and $v = \sin\theta\sin\varphi$ characteriz-

ing the main beam position; θ and φ are angles measured from the z- and x-axes, respectively,

$$R_{pq} = [x_{pq}^2 + (y \quad y \quad y_q)^2 + (h_m \quad h_\mu)^2 + a^2\delta_{0p}\delta_{m\mu}]^{1/2}$$
$$x_{pq} = \quad p + \frac{1 \quad (\ \ 1)^q}{4} \quad d_x, \quad y_q = qd_y \tag{6.41}$$

and

$$\Gamma_{pq} = (\alpha_p^2 + \beta_{pq}^2 \quad k^2)^{1/2}, \quad \Gamma_{pq} = (\Gamma_{pq}^2 + 2ik \ k \ \ )^{1/2}$$
$$\alpha_p = ku + \frac{2\pi p}{d_x}, \quad \beta_{pq} = kv + \frac{2\pi}{d_y} \ q + \frac{1 \quad (\ \ 1)^p}{4} \tag{6.42}$$

are the propagation constants for the Floquet modes. The parameters standing in (6.41) and (6.42) correspond to the triangular lattice shown in Figure 6.18. If the lattice is rectangular, the first one in (6.41) and the second one in (6.42) should be replaced by $x_p = pd_x$ and $\beta_q = kv + 2\pi q/d_y$, respectively. Note also that the expression for the longitudinal propagation constants (1.20) is taken here in an alternative form. However, if $\alpha_p^2 + \beta_{pq}^2 = w_{pq}^2 < k^2$, the propagation constants should be calculated by formula $\ _{pq} = \ i(k^2 \quad w_{pq}^2)^{1/2}$. Then, after substitution of the latter in (6.40), we obtain complete correspondence of (6.40) to the Green's function expressed by (1.19).

The kernel (6.40) has been obtained from (1.19) with the use of the generalization [14, 33] of the approach proposed in [34] for accelerating the convergence of the series representing the rectangular waveguide Green's function. As a result, the first (spatial) series in (6.40) converges exponentially. The second (spectral) difference series in (6.40) at $m \quad \mu$ converges exponentially as well. At $m = \mu$ and satisfaction of the key condition $k^{\ 2} \quad k^{\ 2} = k^2$ proposed in [34] for the components of the auxiliary wavenumber $k_a = k \ + ik \ $, this series converges as $1.5(k \ k \ \ )^2 \Gamma_{pq}^5$. This approach to accelerating calculation of the Green's function (1.19) for doubly periodic structures has been called in [35] Kummer's method of the second order. Modifications of Kummer's method of the fourth and sixth orders to provide convergence of the spectral difference series in as Γ_{pq}^9 and Γ_{pq}^{13}, respectively, have been proposed and considered in [36, 37; also private communication with M. M. Ivanishin, December 24, 2007]. The main results of that consideration are presented in Appendix 6A. The choice of the optimum proportion between k and k has been discussed in [36, 37].

The voltage V in the dipole gap standing in the right-hand side of (6.39) is determined by formula [38]

$$V = 2V^i \quad W_f I_1(0) \tag{6.43}$$

where V^i is the voltage of the incident wave in the feeding line and $I_1(0)$ is the value of the current in the gap. Breaking the wires of the radiating element into intervals by collocation points at $y_{mn} = (n \quad 1 \quad N_m)d_m/N_m$, $n = 1, 2, \ldots, 2N_m + 1$, using the

triangular basis functions for representing the currents, and satisfying (6.39) in the indicated collocation points, we reduce the integral equation (6.39) to the system of algebraic equations

$$C_m \cos ky_{mn} + \sum_{\mu=1}^{M} \sum_{\nu=2}^{2N_\mu} G_{m\mu,n\nu} I_{\mu\nu} + D_m \sin ky_{mn} = \frac{iV^i \delta_{1m}}{\eta_0} \sin k\,|y_{mn}| \tag{6.44}$$

where $m = 1, 2, \ldots, M$; $n = 1, 2, \ldots, 2N_m + 1$; $I_{\mu\nu}$ are is the value of the current at the νth collocation point on the μth wire;

$$\begin{aligned} G_{m\mu,n\nu} = {} & \frac{iW_f \delta_{1m} \delta_{\nu,N_1+1}}{2\eta_0} \sin k\,|y_{mn}| \\ & + \int_{y_{\mu,\nu-1}}^{y_{\mu,\nu+1}} (1 - |y - y_{\mu\nu}| / \Delta_\mu) G_{m\mu}(y_{mn}, y)\, dy \end{aligned} \tag{6.45}$$

$\Delta_\mu = d_\mu / N_\mu$, and it is taken into account that the currents at the wire ends are equal to zero, so that the number of unknowns turns to be exactly equal to the number of equations.

After solving the system (6.44), the array reflection coefficient is determined as

$$R(u,v) = 1 - \frac{W_f I_{1,N_1+1}(u,v)}{V^i} \tag{6.46}$$

and the components of the array element pattern normalized to the maximum of the ideal array element pattern (1.50) are calculated by formulas

$$F_\theta(\theta,\varphi) = F_y(\theta,\varphi) \cos\theta \sin\varphi \tag{6.47}$$

$$F_\varphi(\theta,\varphi) = F_y(\theta,\varphi) \cos\varphi \tag{6.48}$$

where

$$\begin{aligned} F_y(\theta,\varphi) = {} & \frac{1}{V^i} \sqrt{\frac{\eta_0 W_f}{d_x d_y}} \sum_{m=1}^{M} \Delta_m \left[\frac{\sin(k \Delta_m v/2)}{k \Delta_m v/2} \right]^2 \\ & \sin(kh_m \cos\theta) \sum_{n=2}^{2N_m} I_{mn}(u,v) e^{-iky_{mnv}} \end{aligned} \tag{6.49}$$

6.4.2 Results of Calculation and Discussion

The algorithm described earlier has been realized in a FORTRAN code tested in different ways, one of which has been compared against the results for the array

parameters available in [31]. All the calculations have been accompanied by verification of the power balance relation

$$|R|^2+\frac{\eta_0 W_f}{(V^i)^2}\sum_{p,q}(|T_{1pq}|^2+|T_{2pq}|^2)\,|\Gamma_{pq}|=1 \tag{6.50}$$

where the summation is performed only over the propagating Floquet modes for which $\alpha_p^2+\beta_{pq}^2=w_{pq}^2<k^2$. The amplitudes of the indicated modes are determined by formulas

$$T_{1pq}=\frac{i\alpha_p}{pq}F_{ypq},\quad T_{2pq}=\frac{\beta_{pq}}{k}F_{ypq} \tag{6.51}$$

where

$$F_{ypq}=\frac{1}{w_{pq}\sqrt{d_x d_y}}\sum_{m=1}^{M} m\left(\frac{\sin(\beta_{pq}\ m/2)}{\beta_{pq}\ m/2}\right)^2 \sum_{n=2}^{2N_m}\sh(\Gamma_{pq}h_m)\,I_{mn}e^{\,i\beta_{pq}y_{mn}} \tag{6.52}$$

and the reflection coefficient standing in (6.50) is determined by (6.46).

A number of calculations have been performed with optimization of the array element parameters to shape the sector element pattern in the E-plane (0yz plane) and wide-angle element pattern in the H-plane. The results to be discussed later correspond to the case when the directors have identical lengths different from the length of the dipoles, and the wires in the element are arranged with identical spacing $h=h_{m+1}\quad h_m$ from each other. In these cases, the parameters under optimization have been the number of directors $M-1$, the director length, and the spacing between the wires h. Some results of such optimization are presented in Figures 6.19 through 6.22. For all these results, the following values hold: $W_f=75\quad$, $2d_1=0.48\lambda$, $h_1=0.25\lambda$, $2a=0.014\lambda$, $2d_m=0.35\lambda$ for $2\quad m\quad M$, and $d_x=0.6\lambda$, where λ corresponds to some reference frequency f_0.

Figure 6.19 contains the element pattern components (6.47) and (6.48) in the E- and H-planes of the array with $d_y=0.8\lambda$. The elements, each of which has four directors (total number of wires is $M=5$) with spacing $h=0.12\lambda$, are arranged in a rectangular lattice. The similar element patterns for the array with $d_y=\lambda$ and six directors in the element ($M=7$) where $h=0.14\lambda$ are shown in Figure 6.20. The geometry of the elements that keep the proportions is shown in the insets of Figures 6.19(b) and 6.20(b). The solid curves with crosses presented for comparison correspond to the element with no directors. The comparison shows that the quality of the obtained sector element patterns in the E-plane in Figures 6.19(a) and 6.20(a) is rather high, and the magnitude of the reflection coefficient (6.46) does not exceed 0.1 in the area of the flat top. However, such quality has not been achieved if the E-plane spacing is greater than the wavelength. As for the H-plane, we see in Figures 6.19(b) and 6.20(b) that, as in [31], the patterns have narrow dips at the main lobe angles slightly smaller than those corresponding to the arising grating lobes

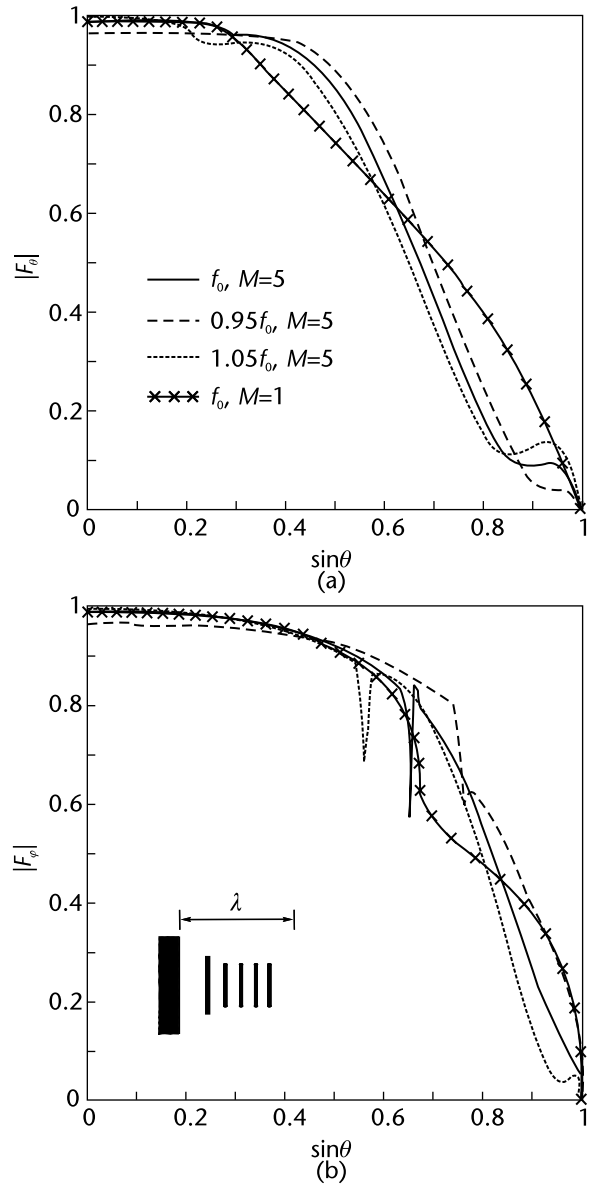

Figure 6.19 Element patterns in (a) E- and (b) H-planes of array with rectangular lattice for $d_x = 0.6\lambda$, $d_y = 0.8\lambda$, $h_1 = 0.25\lambda$, $h = 0.12\lambda$, $2a = 0.014\lambda$, $2d_1 = 0.48\lambda$, and $2d_m = 0.35\lambda$, 2 m M, $M = 5$, at frequencies f_0, $0.95f_0$, and $1.05f_0$.

in real space. The indicated dips are associated with the resonances of the surface waves excited in the director structure, forming a layer of artificial dielectric. It is seen that the resonance effects are stronger in the arrays with longer (in the z direction) director elements.

The results presented in Figures 6.19(a) and 6.20(a) show that the sector element pattern shape is kept well at least in a 10% frequency band, and the change of the pattern width corresponds to the natural change of the element spacing in wavelengths. The increase of frequency also leads to an increase of the electrical

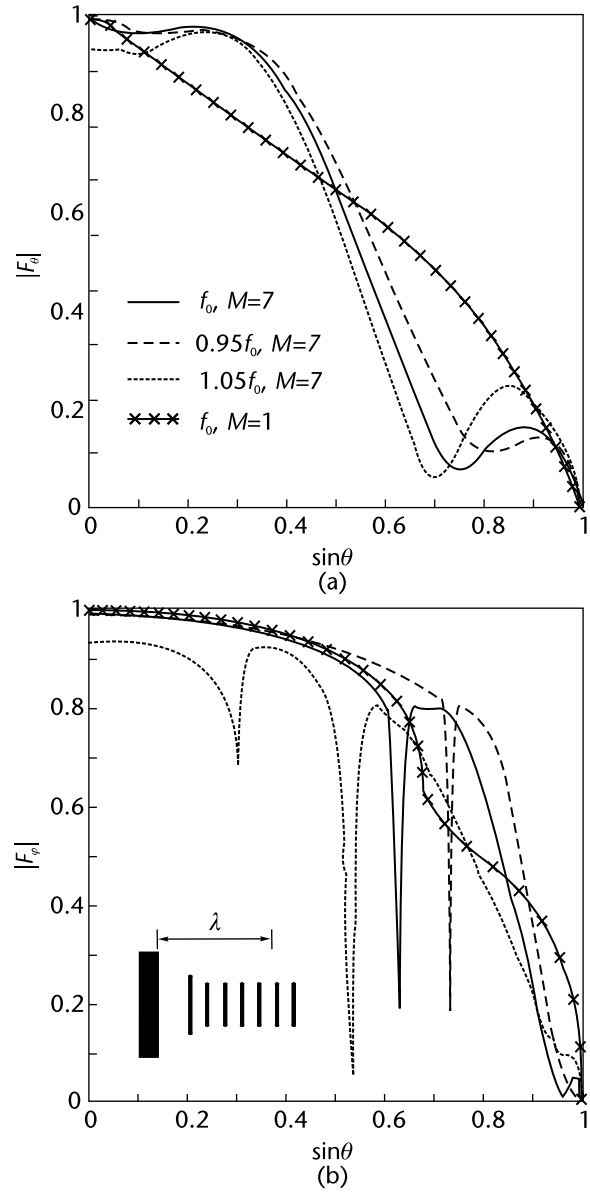

Figure 6.20 Element patterns in (a) E- and (b) H-planes of array with rectangular lattice for $d_x = 0.6\lambda$, $d_y = \lambda$, $h_1 = 0.25\lambda$, $h = 0.14\lambda$, $2a = 0.014\lambda$, $2d_1 = 0.48\lambda$, and $2d_m = 0.35\lambda$, 2 m M, $M = 7$, at frequencies f_0, $0.95f_0$, and $1.05f_0$.

element length, and therefore to the stronger resonance effects in the H-plane, and even to rising new dips in the element pattern. Moreover, as the H-plane electrical element spacing increases, the resonance dips move toward the array broadside.

The array with the same elements and the same element and row spacings, but with the triangular lattice as shown in Figure 6.18, has also been studied. As shown in [14], the element pattern shape in the E-plane for the triangular lattice is practically identical to the shape of the element patterns presented in Figures 6.19(a) and 6.20(a) for the rectangular lattice. So, the element pattern in the E-plane is

practically independent of the lattice type with the indicated parameters. A special test has shown that this conclusion remains valid for the corresponding arrays of rectangular or circular waveguides [21] as well. Such a generality is explained by the small element spacing in the H-plane. If the main beam scans in the E-plane, the nearest grating lobe columns in the space of direction cosines are rather far from the real space border, and hence the difference in the grating lobe arrangement in these side columns for the different lattice types weakly affects the scanning performance in the E-plane.

On the contrary, if the main beam scans in the H-plane, the nearest grating lobes come closer to the real space border, and the difference in the arrangement of the nearest grating lobes is manifested in the array characteristics to a greater degree. This feature is illustrated by comparing the H-plane element patterns shown in Figures 6.19(b) and 6.20(b) with the similar element patterns of the array with the triangular lattice presented in Figure 6.21 for $d_y = 0.8\lambda$ and in Figure 6.22 for $d_y = \lambda$. The nearest grating lobes for the triangular lattice are arranged at a greater distance from the main beam than takes place for the rectangular one, and hence the resonance effects occur at greater angles of the main beam direction. This confirms the known advantage of the triangular lattice for providing a better scan performance.

The results obtained here for a simplified array model show the director antenna elements' good potential for use in phased arrays designed for limited scanning in the E-plane and wide-angle scanning in the H-plane. They allow us to consider the arrays of Yagi's elements promising further studies in this area. One of the directions of them can be taking into account various possibilities for the realization of the Yagi's elements (e.g., printing such elements on longitudinal protruding dielectric boards, as has been considered in [39, p. 205], or in [40]). Another direction for future studies can be removal of the resonance effects that occur when scanning in

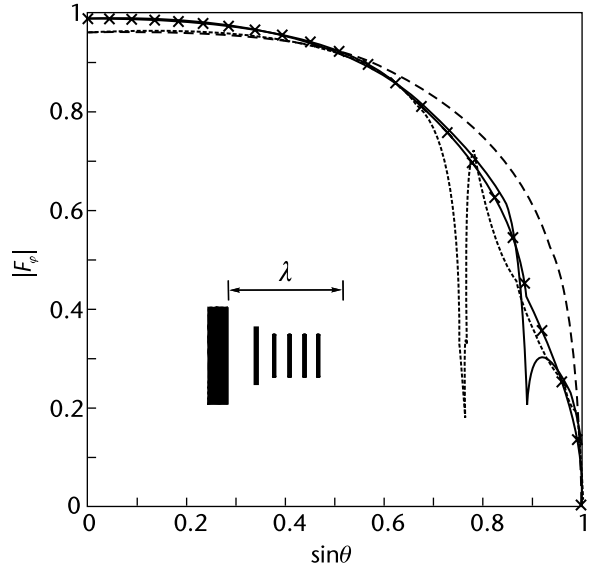

Figure 6.21 Element pattern in the H-plane of the array with triangular lattice for $d_x = 0.6\lambda$, $d_y = 0.8\lambda$, $h_1 = 0.25\lambda$, $h = 0.12\lambda$, $2a = 0.014\lambda$, $2d_1 = 0.48\lambda$, and $2d_m = 0.35\lambda$, 2 m M, $M = 5$, at frequencies f_0, $0.95f_0$, and $1.05f_0$.

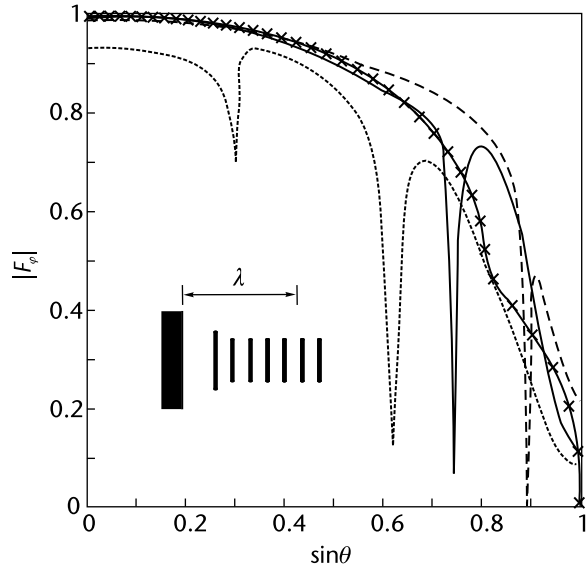

Figure 6.22 Element pattern in the H-plane of an array with a triangular lattice for $d_x = 0.6\lambda$, $d_y = \lambda$, $h_1 = 0.25\lambda$, $h = 0.14\lambda$, $2a = 0.014\lambda$, $2d_1 = 0.48\lambda$, and $2d_m = 0.35\lambda$, 2 m M, $M = 7$, at frequencies f_0, $0.95f_0$, and $1.05f_0$.

the H-plane. A possible solution for this problem is the breaking of the periodicity of the structure in the H-plane by means of arrangement of the array columns with random spacing.

6.5 Arrays of Waveguides with Semitransparent Wire-Grid Walls

One more approach to the shaping of sector array element patterns has been developed in [15–18] using single-mode waveguides with semitransparent walls. The latter are realized in the form of wire grids. The analysis of such arrays in [15–18], based on the theory of coupled waves applied first in [41], has some analogy with a phenomenological approach developed in [42] for analysis of arrays of traveling-wave elements. The phenomenological approach based on the theory of coupled waves applied to the waveguides of nonidentical width has been realized in a breadboard [15], where the semitransparent walls of the coupled waveguide sections are formed by rows of cylindrical conductors (wires). A technique for selection of the semitransparent wall parameters, including the diameter of the cylinders, their number, and the spacing between them, is described in [16]. The numerical simulation of the array by the finite element method aimed at determining the amplitudes of waves in the output waveguide sections without accounting for radiation is carried out in [15, 16]. The amplitudes determined as a result are then used for approximate calculation of the array element pattern according to the Kirchhoff method. The measured array element patterns confirming some conclusions drawn in [15, 16] have also been presented.

A full-wave two-dimensional mathematical model of a waveguide array containing semitransparent wire-grid walls is described later.

6.5.1 Statement and Solution of the Problem

The array geometry similar to that considered in [15, 16] is presented in Figure 6.23. The array is an infinite periodic structure of parallel-plate waveguides arranged with period (element spacing) b along the x-axis of a rectangular Cartesian coordinates $0xyz$. Each array cell contains two semi-infinite waveguides of width a_1 and a_2 ($a_1+a_2 \quad b$) with solid walls, as well as two waveguide sections of finite length (in the longitudinal direction) with semitransparent walls arranged symmetrically above the waveguides with solid walls. Each semitransparent wall is formed by L cylinders (wires) of a circular cross section of radius r arranged with spacing along the z-axis. The axes of the first row of the cylinders are arranged at distance h_1 above the waveguide apertures. The axes of the adjacent columns are arranged at distances a and $a = b - a$ from each other. The array geometry is assumed to be uniform along the y-axis, and the waveguide walls, flanges, and cylinders are assumed to be perfectly conducting.

The right-hand waveguides in each cell are considered passive and terminated with matching loads, while the left-hand ones are excited in their dominant TE modes with complex amplitudes $\exp(imU)$, where $m = 0, \pm1, \pm2, \ldots$ is the cell ordinal number, $U = kb\sin\theta$ is the phase difference between the fields in adjacent cells, $k = 2\pi/\lambda$ is the wavenumber, λ is the wavelength in free space, and θ is the angle between the z-axis and direction of the main lobe in the space.

To determine the array characteristics at the conditions specified earlier, we represent the total electric fields in the driven and passive waveguides of the central cell in the form of superpositions of their TE eigenmodes

$$E_{1y}(x,z) = \sum_{n=1} \delta_{n1} e^{i\gamma_{1n}z} + R_{1n} e^{\ i\gamma_{1n}z)} \ \sin\frac{n\pi(x + a_1/2)}{a_1} \tag{6.53}$$

$$E_{2y}(x\ ,z) = \sum_{n=1} R_{2n} e^{\ i\gamma_{2n}z)} \sin\frac{n\pi(x\ + a_2/2)}{a_2} \tag{6.54}$$

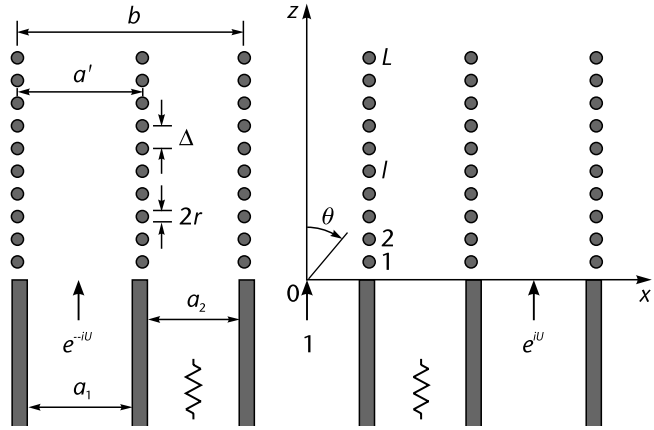

Figure 6.23 Geometry of an array of waveguides coupled via semitransparent wire-grid walls.

where

$$\gamma_{jn} = \sqrt{k^2 \quad (n\pi/a_j)^2} = i\sqrt{(n\pi/a_j)^2 \quad k^2} \tag{6.55}$$

are propagation constants of the modes in the driven ($j = 1$) and passive ($j = 2$) waveguides, R_{jn} are amplitudes of the reflected modes in the indicated waveguides to be determined, $_{mn}$ is the Kronecker symbol, and $x = x - b/2$. The harmonic time dependence omitted here is assumed to be taken in the form $e^{\ i\omega t}$.

The total electric field in the free space above the waveguide apertures ($z \quad 0$) is represented in the form of superposition of Floquet modes similar to those used for analysis of waveguide-dielectric arrays in [43] with application of the method of auxiliary sources

$$E_y(x,z) = \quad T_{0q} e^{i(\alpha_q x + \Gamma_q z)} + \sum_{l=1}^{L} \sum_{j=1}^{2} \sum_{s=1}^{S} I_{ljs} E_{ljs}(x,z) \tag{6.56}$$

The first sum in (6.56) represents Floquet modes with propagation constants (4.7) and unknown amplitudes T_{0q}, going to the free space directly from the waveguide apertures. The second summand in (6.56) where

$$E_{ljs}(x,z) = \quad k \frac{e^{i\Gamma_q |z \quad z_{ls}|} \quad e^{i\Gamma_q (z+z_{ls})}}{\Gamma_q} e^{i\alpha_q (x \quad x_{js})} \tag{6.57}$$

corresponds to the field of Floquet modes excited by the cylinders. This field is simulated by filamentary auxiliary electric currents of unknown amplitude I_{ljs} arranged inside the cylinders and passing through the points with coordinates

$$x_{js} = (j \quad 1.5)a + r \sin\varphi_s \tag{6.58}$$

$$z_{ls} = h_1 + (l \quad 1) \qquad r \cos\varphi_s \tag{6.59}$$

where $\varphi_s = 2\pi(s - 1)/S$, S is the number of the sources allotted to one cylinder, and $r < r$ is the radius of the circle on which the source points are located. Thus, the total number of the auxiliary sources in one cell containing two columns of the cylinders is equal to $S \quad L \quad 2$. As we see from (6.57), the sources are assumed to be arranged above a virtual perfectly conducting screen located in the plane $z = 0$.

The electric field (6.56) must be equal to electric fields (6.53) and (6.54) in the apertures of the driven and passive waveguides, respectively, and zero on the flanges. Projecting this functional equation on the functions complex-conjugated to the transverse functions of the Floquet modes, we obtain the relation between the amplitudes of the Floquet modes and the amplitudes of the waveguide modes

$$T_{0q} = \frac{a_1}{b} \sum_{n=1} (\delta_{1n} + R_{1n}) Q_{1nq} + \frac{a_2}{b} \sum_{n=1} R_{2n} Q_{2nq} \tag{6.60}$$

where

$$Q_{1nq} = \frac{1}{a_1} \int_{-a_1/2}^{a_1/2} \sin\frac{n\pi(x + a_1/2)}{a_1} e^{\ i\alpha_q x} dx \tag{6.61}$$

$$Q_{2nq} = \frac{e^{\ i\alpha_q b/2}}{a_2} \int_{-a_2/2}^{a_2/2} \sin\frac{n\pi(x\ + a_2/2)}{a_2} e^{\ i\alpha_q x}\, dx \tag{6.62}$$

The final expressions for coefficients (6.61) and (6.62) are similar to that in (5.13) and we omit them here for brevity.

The transverse component of the magnetic field strength H_x in the waveguides and above their apertures is determined by formula (1.101). The transverse magnetic field in the driven waveguide must be equal to the transverse magnetic field in the free space at $z = 0$. Projecting this equality on the transverse functions of the eigenmodes in the driven waveguide and accounting for (6.60), we obtain the following subsystem of linear algebraic equations

$$\begin{aligned} &\sum_n \left(\frac{\gamma_{1n}}{2}\delta_{mn} + \frac{a_1}{b} \sum_q \Gamma_q Q_{1mq} Q_{1nq} \dot{\div} R_{1n} + \sum_n \left(\frac{a_2}{b} \sum_q \Gamma_q Q_{1mq} Q_{2nq} \dot{\div} R_{2n} \right. \right. \\ &2 \sum_{ljs} I_{ljs} k \sum_q Q_{1mq} e^{\ i\alpha_q x_{js} + i\Gamma_q z_{ls}} = \frac{\gamma_{1n}}{2}\delta_{m1} \sum_q \frac{a_1}{b} \Gamma_q Q_{1mq} Q_{11q} \end{aligned} \tag{6.63}$$

where $m = 1, 2, \ldots$, and the asterisk at coefficients Q_{1mq} means complex conjugation.

The similar projective matching of the transverse magnetic fields in the aperture of the passive waveguide gives one more algebraic subsystem

$$\begin{aligned} &\sum_n \left(\frac{a_1}{b} \sum_q \Gamma_q Q_{2mq} Q_{1nq} \dot{\div} R_{1n} + \sum_n \left(\frac{\gamma_{2n}}{2}\delta_{mn} + \frac{a_2}{b} \sum_q \Gamma_q Q_{2mq} Q_{2nq} \dot{\div} R_{2n} \right. \right. \\ &2 \sum_{ljs} I_{ljs} k \sum_q Q_{2mq} e^{\ i\alpha_q x_{js} + i\Gamma_q z_{ls}} = \sum_q \frac{a_1}{b} \Gamma_q Q_{2mq} Q_{11q}, \quad m = 1, 2, \ldots \end{aligned} \tag{6.64}$$

The third algebraic subsystem is derived from the zero boundary condition for the total electric field (6.56) in the collocation points on the surfaces of the cylinders

$$\begin{aligned} &\sum_n \left(\frac{a_1}{b} \sum_q Q_{1nq} \eta_q(x_{j\,s}, z_{l\,s}) \dot{\div} R_{1n} + \sum_n \left(\frac{a_2}{b} \sum_q Q_{2nq} \eta_q(x_{j\,s}, z_{l\,s}) \dot{\div} R_{2n} \right. \right. \\ &+ \sum_{ljs} I_{ljs} E_{ljs}(x_{j\,s}, z_{l\,s}) = \sum_q \frac{a_1}{b} Q_{11q} \eta_q(x_{j\,s}, z_{l\,s}) \end{aligned} \tag{6.65}$$

where $\eta_q(x,z) = e^{i(\alpha_q x + \Gamma_q z)}$,

$$x_{js} = (j \quad 1.5)a + r\sin\varphi_s \tag{6.66}$$

$$z_{ls} = h_1 + (l \quad 1) \qquad r\cos\varphi_s \tag{6.67}$$

are coordinated of the collocation points, $l = 1, 2, \ldots, L$; $j = 1, 2$; and $s = 1, 2, \ldots, S$. Note that the subsystem (6.65) has been derived by accounting for (6.60).

The solution of the system of equations (6.63), (6.64), and (6.65) gives at once the values of the reflected mode amplitudes in the waveguides and therefore determines the reflected field. The total radiated field above the cylinders is determined from (6.56) by a sum of Floquet modes

$$E_y(x,z) = \sum_{q=} T_q e^{i(\alpha_q x + \Gamma_q z)} \tag{6.68}$$

with the amplitudes

$$T_q = T_{0q} \quad 2i \sum_{ljs} I_{ljs} \frac{k\sin(\Gamma_q z_{ls})}{\Gamma_q} e^{\ i\alpha_q x_{js}} \tag{6.69}$$

which are calculated by accounting for formula (6.60) for T_{0q} and using values for R_{1n}, R_{2n}, and I_{ljs} obtained as a result of solving the algebraic system. The amplitude of the zero-order Floquet mode determines the array element pattern

$$F(\theta) = \sqrt{\frac{2kb}{\gamma_{11}a_1}}\,|T_0(kb\sin\theta)|\cos\theta \tag{6.70}$$

which is of primary interest in the present study. The pattern (6.70) is normalized so that $F^2(0)$ corresponds to the coefficient of transmission of the input power to the main lobe of the array.

Finally, the amplitudes of the reflected and radiated modes must satisfy the power balance relation

$$|R_{11}|^2 + \frac{\gamma_{21}a_2}{\gamma_{11}a_1}|R_{21}|^2 + \frac{2b}{\gamma_{11}a_1}\sum_q |T_q|^2\ \mathrm{Re}\{\Gamma_q\} = 1 \tag{6.71}$$

written in the assumption that the driven and passive waveguides are single-mode ones.

Note that the algorithm developed earlier can also be used for calculation of a modified (simplified) structure [44] shown in Figure 6.24. This structure differs from the original structure [15, 16] shown in Figure 6.23 in the respect that the passive waveguides are absent and the remaining driven waveguides go to a common flange. Since the aperture of the passive waveguide in which the fields have been matched in the original array is now absent, the subsystem (6.64) should be excluded from the consideration, and all the sums containing R_{2n} should be

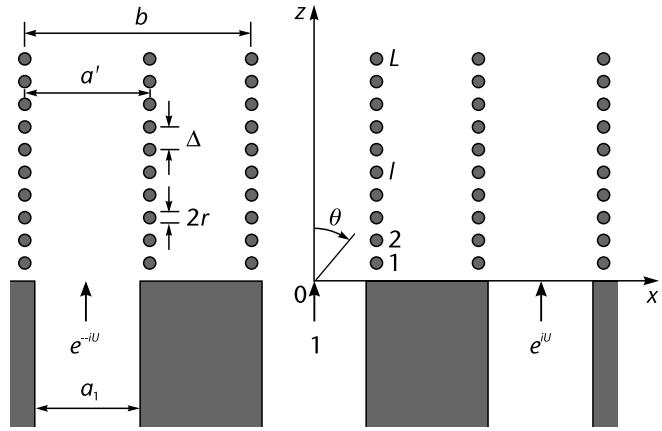

Figure 6.24 Geometry of a modified array of waveguides coupled via semitransparent wire-grid walls.

excluded from the expression (6.60), subsystems (6.63) and (6.65), as well as relation (6.71).

6.5.2 Realization and Validation of the Algorithm

The algorithm described earlier has been realized in two FORTRAN-90 codes for calculation of both the original structure (Figure 6.23) and the modified structure (Figure 6.24). The infinite system of algebraic equations (6.63), (6.64), and (6.65) has been truncated down to the order $M_1 + M_2 + 2 \quad L \quad S$, where M_1 and M_2 are numbers of the first waveguide modes kept in the driven and passive waveguides, respectively. The infinite series representing the matrix elements standing at the unknowns I_{ljs} in (6.63) and (6.64) as well as at the unknowns R_{1n} and R_{2n} in (6.65) converge exponentially, while the terms in the series standing at R_{1n} and R_{2n} in (6.63) and (6.64) decay as $|q|^{-3}$ so that the calculation of them does not meet any difficulties. The matrix elements (6.57) in (6.65) at $|z_{l\,s} - z_{ls}| \quad 0$ converge slowly. Acceleration of their convergence can be provided by several methods, particularly by using Kummer's method modification applied in [43]. As a result, the original series like (6.57) is represented by a spectral series converging as $\quad q^{5}$ and a spatial series of Hankel functions of zero order and complex argument converging exponentially. So, the convergence rate becomes much higher. However, the necessity of calculation of special functions (the Hankel functions in this case) requires additional time in comparison with calculation of elementary functions. For this reason, another modification of Kummer's method has been developed, described in Appendix 6B, providing a sufficiently high rate of convergence after transformation of (6.57) without involvement of any special functions. The truncated system of algebraic equations (6.63) to (6.65) is solved by the Gauss elimination method with selection of a leading matrix element in a column.

The correctness and accuracy of the solution of the problem has been validated using the power balance relation (6.71) as well as the equations (6.65) in the points arranged between the collocation points with coordinates (6.66) and (6.67). Fur-

thermore, the results obtained using the algorithm developed earlier have been compared to calculated and measured data available in [15]. To demonstrate the results of the indicated tests, let us consider the structure studied in [15]. This structure, using $L = 14$ cylinders in each semitransparent wall, is characterized by the following dimensions: $a_1 = a_2 = 0.61333\lambda$, $b = 1.33333\lambda$, $a = 0.68267\lambda$, $r = 0.06667\lambda$, $h_1 = 0.18667\lambda$, and $= 0.37333\lambda$, where λ is the wavelength corresponding to frequency of 8 GHz. The results have been obtained at $M_1 = M_2 = 11$, $r = 0.025\lambda$, and a few values for the number S of the auxiliary sources in each cylinder. The FORTRAN code used for the calculations mainly uses real and complex variables of ordinary precision (variables of double precision are used only in a subroutine designed for solving algebraic systems). The plots for the residual ΔE of satisfaction of equations (6.65) at $\theta = 0$ in the points situated on the surfaces of the cylinders between the collocation points for $S = 6$, 10, and 20 are presented in the logarithmic scale in Figure 6.25. The residual of satisfaction of the power balance relation (6.71) is 0.000057, 0.000017, and 0.000006, respectively. The results corresponding to other values of θ are similar. The element pattern (6.70) in decibels normalized to its maximum corresponding to $S = 6$ is presented in Figure 6.26, where it is compared to the corresponding calculated and measured patterns available in [15]. The patterns calculated with $S = 10$ and 20 coincide graphically with the pattern for $S = 6$. The results obtained in the tests characterized sufficient effectiveness of the developed mathematical model for its further use for numerical study of the array characteristics at various values of the array parameters.

6.5.3 Results of Analysis and Optimization

The characteristics of the original array (Figure 6.23) obtained as a result of numerical analysis and optimization of the array geometry for array period $b = 1.2\lambda$, 1.3λ,

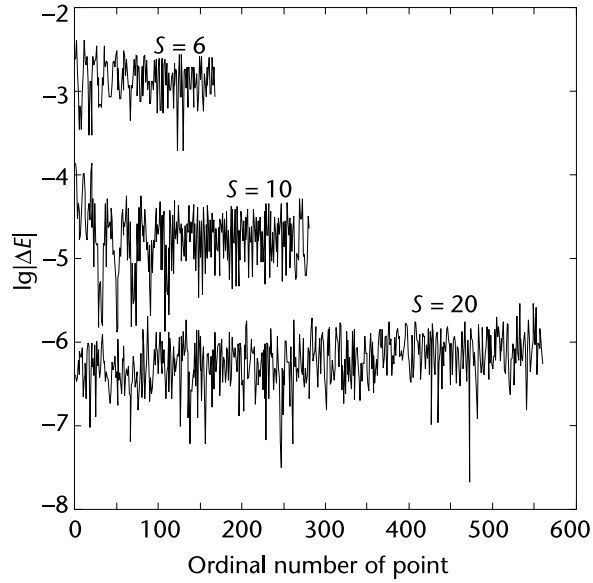

Figure 6.25 Residual of satisfaction of the boundary condition on the surfaces of the cylinders for different numbers of the auxiliary sources.

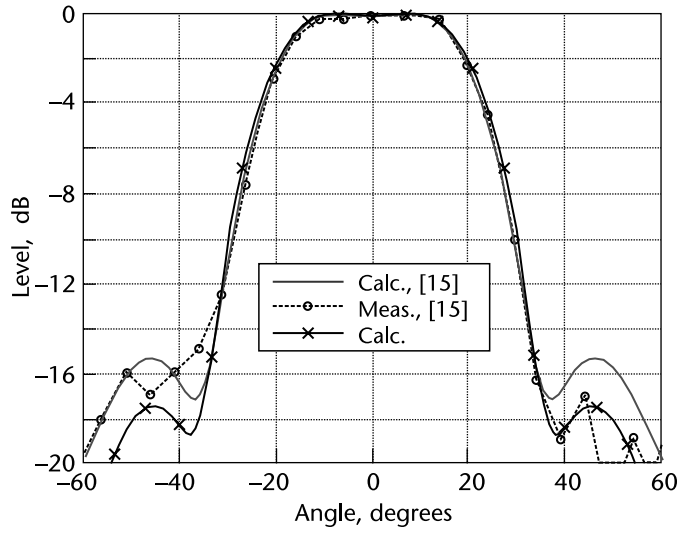

Figure 6.26 Comparison of the element pattern calculated by the present method with calculated and measured element patterns in [15].

and 1.4λ are presented in Figures 6.27 to 6.29. The geometric array parameters for $b = 1.3\lambda$ (Figure 6.28) are close to the parameters of the array considered in [15]. The sector element patterns for $b = 1.2\lambda$ (Figure 6.27) and $b = 1.4\lambda$ (Figure 6.29) are formed using respectively smaller and greater numbers of the cylinders in the semitransparent wall. The patterns obtained are compared to the normalized ideal sector element patterns. As we see, the level of the obtained patterns in the region of their flat top is considerably lower than the ideal pattern level. This difference

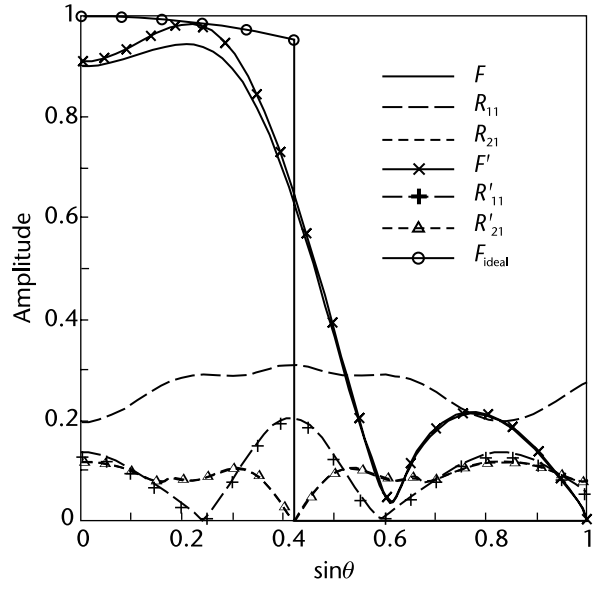

Figure 6.27 Characteristics of the array with parameters $b = 1.2\lambda$, $a_1 = a_2 = 0.55\lambda$, $a' = 0.62\lambda$, $r = 0.05\lambda$, $r' = 0.02\lambda$, $h_1 = 0.161\lambda$, $= 0.322\lambda$, $M_1 = M_2 = 11$, $L = 12$, and $S = 10$.

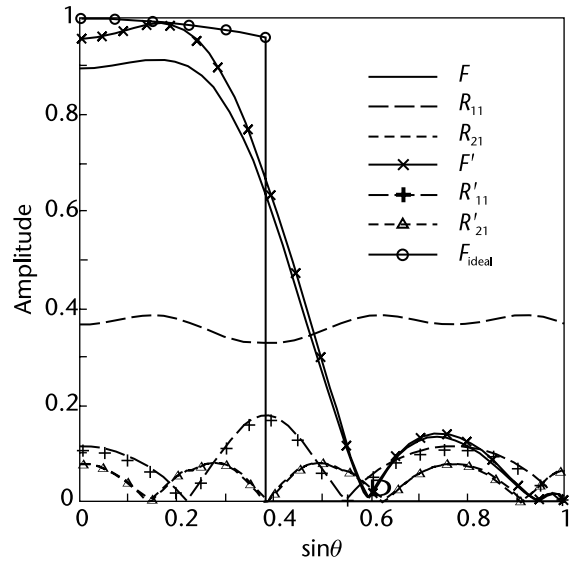

Figure 6.28 Characteristics of the array with parameters $b = 1.3\lambda$, $a_1 = a_2 = 0.6\lambda$, $a' = 0.668\lambda$, $r = 0.065\lambda$, $r' = 0.025\lambda$, $h_1 = 0.182\lambda$, $\quad = 0.364\lambda$, $M_1 = M_2 = 11$, $L = 14$, and $S = 10$.

is explained by the array mismatch. The magnitudes of the array reflection coefficients in the driven $|R_{11}|$ and passive $|R_{21}|$ waveguides characterizing the indicated mismatch are also shown in Figures 6.27 to 6.29. We see that the mismatch level of the driven waveguides, especially for smaller values of the period b, is rather high. The level of the dominant mode reflections in the passive waveguides is not so high when scanning, and it vanishes at all at the antiphase excitation (when $\sin\theta = \lambda/2b$), since the dominant modes in this case are not excited.

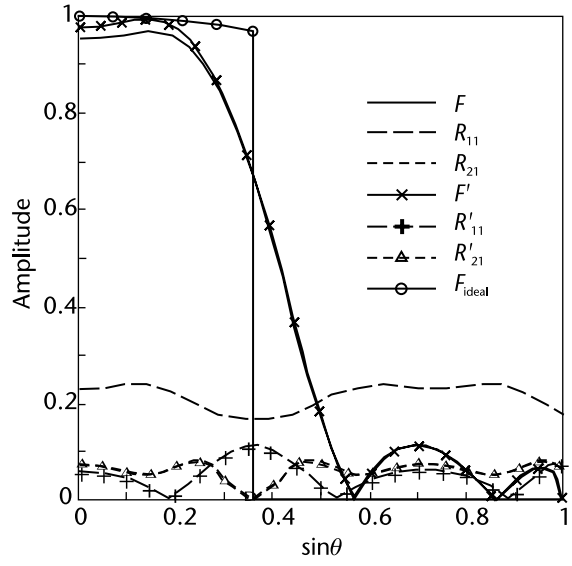

Figure 6.29 Characteristics of the array with parameters $b = 1.4\lambda$, $a_1 = a_2 = 0.65\lambda$, $a' = 0.724\lambda$, $r = 0.06\lambda$, $r' = 0.025\lambda$, $h_1 = 0.181\lambda$, $\quad = 0.362\lambda$, $M_1 = M_2 = 11$, $L = 17$, and $S = 10$.

Thus, the inputs of the original array [15] are not well matched. The matching of the array at a specified frequency and specified angle of scanning can be provided using matching discontinuities arranged in the driven waveguides at some distance from their apertures. Assuming that the scattering matrix of the matching discontinuity is unitary, and taking into account the interaction between the aperture and discontinuity over the dominant mode only, we can obtain the reflection coefficient in the driven waveguides in the form

$$R_{11}(\theta) = \frac{R \quad R_{11}(\theta)e^{2i\gamma_{11}h+i\psi}}{1 \quad RR_{11}(\theta)e^{2i\gamma_{11}h+i\psi}} e^{i\psi} \tag{6.72}$$

where R and ψ are magnitude and phase of the coefficient of reflection from the discontinuity, respectively, and h is the distance from the discontinuity to the aperture (the plane $z = 0$). If the indicated distance is selected according to the condition

$$2\gamma_{11}h + \psi_{11}(\theta_0) + \psi = 2\pi n \tag{6.73}$$

where $\psi_{11}(\theta_0)$ is the phase of the complex reflection coefficient $R_{11}(\theta_0)$ of the original array for some scan angle θ_0, and n is a natural number, the expression (6.72) takes the form

$$R_{11}(\theta) = \frac{R \quad R_{11}(\theta)e^{\ i\psi_{11}(\theta_0)}}{1 \quad RR_{11}(\theta)e^{\ i\psi_{11}(\theta_0)}} e^{i\psi} \tag{6.74}$$

which shows that if the discontinuity is selected so that $R = |R_{11}(\theta_0)|$, then the driven waveguides will be ideally matched for the specified angle of scanning.

The arrangement of the matching discontinuities in the driven waveguides changes the amplitudes of the modes coming to the apertures. It can be shown that instead of the unit amplitudes of the incident modes in (6.53), the amplitudes of the incident modes at the apertures after passing over the discontinuities will be determined by formula

$$A^i_{11}(\theta) = \frac{i\sqrt{1 \quad R^2}e^{i\psi}}{1 \quad RR_{11}(\theta)e^{\ i\psi_{11}(\theta_0)}} \tag{6.75}$$

and the element pattern and reflection coefficient in the passive waveguides will be determined by formulas $F(\theta) = F(\theta)|A^i_{11}(\theta)|$ and $R_{21}(\theta) = R_{21}(\theta)A^i_{11}(\theta)$, respectively.

The results of such matching for the array with geometric parameters indicated in the captions for Figures 6.27 to 6.29 are presented in the same figures by the curves marked by symbols " " for F, "+" for $|R_{11}|$, and " " for $|R_{21}|$. The angles θ_0 at which the matching of the driven waveguides is provided has been specified so that $\sin\theta_0 = 0.24$, 0.22, and 0.18 for $b = 1.2\lambda$, 1.3λ, and 1.4λ, respectively. As we observe, the discontinuities considerably improve the matching of the driven waveguides and result in pulling up the flat-top level of the array element patterns to the ideal level. The reflection coefficient level in the passive waveguides changes weakly because the low original reflection coefficient is mul-

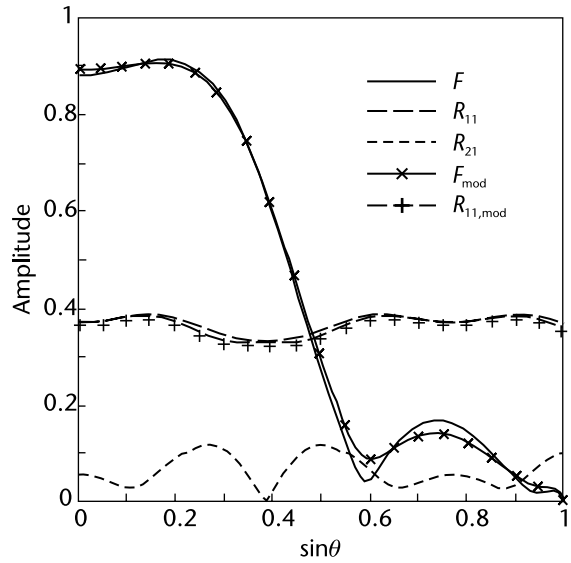

Figure 6.30 Comparison of the characteristics provided by the original and modified arrays with parameters $b = 1.3025\lambda$, $a_1 = a_2 = 0.59915\lambda$, $a' = 0.66688\lambda$, $r = 0.065125\lambda$, $r' = 0.025\lambda$, $h_1 = 0.18235\lambda$, $= 0.3647\lambda$, $M_1 = M_2 = 11$, $L = 14$, and $S = 10$.

tiplied by a value of about 1.02…1.04 in magnitude (i.e., not strongly different from unity).

Finally, Figure 6.30 compares the characteristics of the original and modified versions of the array with geometric parameters corresponding to the structure considered in [15]. The geometric parameters in wavelengths indicated in the figure caption correspond to frequency 7.815 GHz, mentioned in [15]. As we observe, the reflection coefficients in the active waveguides almost do not differ from each other. The sector element patterns as a whole are also close to each other. Small differences are observed mainly in the sidelobe region. These results show that the sector element patterns in the arrays of waveguides with semitransparent walls can be successfully obtained without using the passive waveguides with solid walls. This simplifies the structure to some extent. The matching of the modified array to free space can be carried out similarly to the original version.

References

[1] Markov, G. T., and D. M. Sazonov, *Antennas*, Moscow: Energiya, 1975 (in Russian).

[2] Brunstein, S. A., and R. F. Thomas, "Characteristics of a Cigar Antenna," *JPL Quarterly Technical Review*, Vol. 1, No. 2, July 1971, pp. 87–95.

[3] Wong, J. L., and H. E. King, "A Wide-Band Low-Sidelobe Disc-o-Cone Antenna," *IEEE Trans. on Antennas and Propagation*, Vol. AP-31, No. 1, January 1983, pp. 183–184.

[4] Skobelev, S. P., et al., "Optimized Phased Array Antenna Element Based on Multidisk Slowing Structure for Limited-Field-of-View Applications," *Proc. 28th Moscow Int. Conf. on Antenna Theory and Technology*, Moscow, Russia, September 22–24, 1998, pp. 266–269.

[5] Skobelev, S., "Some Features of Shaping the Flat-Topped Patterns by Disc and Strip Slow-Wave Antenna Elements in Arrays for Limited Field of View," *Proc. Millennium Conf. on Antennas & Propagation*, Davos, Switzerland, April 9–14, 2000.

[6] Skobelev, S. P., "Application of Strip Structures for Shaping Sector Element Patterns in a Waveguide Array," *Radiotekhnika*, No. 6, 2000, pp. 18–24 (in Russian).

[7] Skobelev, S. P., "Shaping of Flat-Topped Element Patterns in an Array of Slow-Wave Strip Structures Excited by Parallel-Plate Waveguides," *IEEE Trans. on Antennas and Propagation*, Vol. 49, No. 12, December 2001, pp. 1763–1768.

[8] Eom, S. -Y., et al., "Multi-Disk Radiating Structure with Flat-Topped Element Pattern for Planar Array Antenna," *Electronics Letters*, Vol. 38, No. 2, January 17, 2002, pp. 60–61.

[9] Skobelev, S. P., "Improvement of the Element Pattern in Circular-Waveguide Arrays Using Multilayered Disk Structures," *2002 AP-S Intl. Symp. Digest*, Vol. 3, San Antonio, TX, June 16–21, 2002, pp. 546–549.

[10] Skobelev, S. P., S. -Y. Eom, and H.-K. Park, "Shaping of Flat-Topped Element Patterns in a Planar Array of Circular Waveguides Using a Multilayered Disk Structure—Part I: Theory and Numerical Modeling," *IEEE Trans. on Antennas and Propagation*, Vol. 51, No. 5, May 2003, pp. 1040–1047.

[11] Eom, S.-Y., et al., "Shaping of Flat-Topped Element Patterns in a Planar Array of Circular Waveguides Using a Multilayered Disk Structure—Part II: Experimental Study and Comparison," *IEEE Trans. on Antennas and Propagation*, Vol. 51, No. 5, May 2003, pp. 1048–1053.

[12] Skobelev, S. P., and A. V. Shishlov, "On the Use of Director Elements in Antenna Arrays for Scanning in a Limited Sector," *Proc. LV Scientific Session Devoted to the Day of Radio*, Moscow, Russia, May 17–19, 2000, pp. 73–74 (in Russian).

[13] Skobelev, S. P. and A. V. Shishlov, "On the Use of Yagi-Uda Elements in Array Antennas for Limited Scan Applications," *Proc. 2000 IEEE Intl. Conf. on Phased Array Systems and Technology*, Dana Point, CA, May 21–25, 2000, pp. 299–302.

[14] Skobelev, S. P., "Performance of Yagi-Uda Elements in Planar Array Antennas for Limited-Scan Applications," *Microwave and Optical Technology Letters*, Vol. 34, No. 2, July 20, 2002, pp. 141–145.

[15] Bankov, S. E., V. A. Kaloshin, and E. V. Frolova, "Computer Design and Experimental Study of a Cluster Feed Based on an EBG Structure," *Journal of Radio Electronics*, No. 3, 2009 (http://jre.cplire.ru).

[16] Bankov, S. E., "Beamforming Network on the Basis of Unequal Coupled Waveguides," *Journal of Communication Technology and Electronics*, Vol. 54, No. 7, 2009, pp. 755–764.

[17] Bankov, S. E., "Two-Dimensional Beamforming Networks on the Basis of Coupled Waveguides," *Journal of Communication Technology and Electronics*, Vol. 54, No. 10, 2009, pp. 1097–1110.

[18] Bankov, S. E., V. A. Kaloshin, and E. V. Frolova, "Beam Forming Networks on the Base of Coupled Waveguides for Multi-Beam Hybrid Antennas," *Draft Proc. PIERS 2009*, Moscow, Russia, August 18–21, 2009, pp. 432–437.

[19] Ku, B. J., et al., "The Problem of Creating a Multi-Panel Multiple-Beam Antenna for a Stratospheric Communication System: Phases of Development," *Antenny*, No. 1, 2005, pp. 22–29 (in Russian).

[20] Weinshtein, L. A., *Electromagnetic Waves*, Moscow: Radio i Svyaz, 1988.

[21] Amitay, N., V. Galindo, and C. P. Wu, *Theory and Analysis of Phased Array Antennas*, New York: Wiley-Interscience, 1972.

[22] Diamond, B. L., "A Generalized Approach to the Analysis of Infinite Planar Array Antennas," *IEEE Proc.*, Vol. 56, No. 11, November 1968, pp. 1837–1851.

[23] Mailloux, R. J., "Surface Waves and Anomalous Wave Radiation Nulls in Phased Arrays of TEM Waveguides with Fences," *IEEE Trans. on Antennas and Propagation*, Vol. 16, No. 1, January 1972, pp. 160–166.

[24] Chen, C. C., "Scattering by a Two-Dimensional Periodic Array of Conducting Plates," *IEEE Trans. on Antennas and Propagation*, Vol. AP-18, No. 5, September 1970, pp. 660–665.

[25] Vendik, O. G., *Antennas with Non-Mechanical Movement of Beam*, Moscow: Sovetskoye Radio, 1965 (in Russian).

[26] Patton, W., "Limited Scan Arrays," in *Phased Array Antennas: Proc. 1970 Phased Array Symp*., A. A. Oliner and G. A. Knittel, (eds.), Dedham, MA, 1972, pp. 254–270.

[27] Mailloux, R. J., *Phased Array Antenna Handbook*, Norwood, MA: Artech House, 1994.

[28] Skobelev, S. P., "Methods of Constructing Optimum Phased-Array Antennas for Limited Field of View," *IEEE Antennas and Propagation Magazine*, Vol. 40, No. 2, April 1998, pp. 39–50.

[29] Lewis, R. L., A. Hessel, and G. H. Knittel, "Performance of a Protruding-Dielectric Waveguide Element in a Phased Array," *IEEE Trans. on Antennas Propagation*, Vol. AP-20, No. 6, November 1972, pp. 712–722.

[30] Baklanov, E. V., et al., "Radiation Pattern of a Longitudinal Element in an Infinite Periodic Rate," *Radiotekhnika i Electronika*, Vol. 17, No. 1, 1972, pp. 30–36 (in Russian).

[31] Indenbom, M. V., and V. S. Filippov, "Analysis and Optimization of Director Radiators in Planar Antenna Array," *Izvestiya Vuzov—Radioelektronika*, Vol. 22, No. 2, 1979, pp. 34–41 (in Russian).

[32] Chang, V. W. H., "Infinite Phased Dipole Array," *IEEE Proc.*, Vol. 56, No. 11, November 1968, pp. 1892–1900.

[33] Skobelev, S. P., "Comments on 'Comparative Analysis of Acceleration Techniques for 2-D and 3-D Green's Functions in Periodic Structures Along One and Two Directions,'" *IEEE Trans. on Antennas and Propagation*, Vol. 55, No. 12, December 2007, p. 3746.

[34] Ivanishin, M. M., "Use of Integral Equations in the Problem on a Cylinder Inside a Rectangular Waveguide," *Radio Eng. Electr. Phys.*, Vol. 29, No. 12, 1984, pp. 1–8.

[35] Valerio, G., et al., "Reply to Comments on 'Comparative Analysis of Acceleration Techniques for 2-D and 3-D Green's Functions in Periodic Structures Along One and Two Directions,'" *IEEE Trans. on Antennas and Propagation*, Vol. 55, No. 12, December 2007, p. 3747.

[36] Ivanishin, M. M., and S. P. Skobelev, "On the Efficient Computation of the Green's Function for Doubly Periodic Structures by Using the Kumme's Method of Higher Orders," *Proc. 12th Int. Conf. on Mathematical Methods in Electromagnetic Theory (MMET'08)*, Odessa, Ukraine, June 29–July 2, 2008, pp. 544–546.

[37] Ivanishin, M. M., and S. P. Skobelev, "A Modification of the Kummer's Method for Efficient Computation of the Green's Function for Doubly Periodic Structures," *IEEE Trans. on Antennas and Propagation*, Vol. 57, No. 9, September 2009, pp. 2794–2798.

[38] Bodrov, V. V., and G. T. Markov, "Excitation of Periodic Antenna Arrays," *Collective Volume of Scientific-Methodical Papers on Applied Electrodynamics*, No. 1, 1977, pp. 129–162 (in Russian).

[39] Voskresensky, D. I., (ed.), *Antennas and Microwave Devices (Design of Phases Antenna Arrays)*, Moscow: Radio i Svyaz, 1981 (in Russian).

[40] Bayard, J. -P. R., M. E. Cooley, and D. H. Shaubert, "Analysis of Infinite Arrays of Printed Dipoles on Dielectric Sheets Perpendicular to a Ground Plane," *IEEE Trans. on Antennas and Propagation*, Vol. 39, No. 12, December 1991, pp. 1722–1732.

[41] Bankov, S. E., and T. I. Bugrova, "Analysis of a Millimeter-Wave Integrated Beam-Forming Network for Quasioptical Multibeam Antennas," *Microwave and Optical Technology Letters*, Vol. 6, No. 13, October 1993, pp. 782–786.

[42] Andreyev, V. F., "Analysis of the Periodic Systems of Longitudinal Elements," *Radiotekhnika i Electronika*, Vol. 18, No. 1, 1973, pp. 40–48 (in Russian).

[43] Skobelev, S. P., and L. L. Mukhamedov, "Analysis of Waveguide Antenna Arrays with Protruding Dielectric Elements," *IEEE Trans. on Antennas and Propagation*, Vol. 41, No. 5, May 1993, pp. 574–581.

[44] Skobelev, S. P., "Analysis of an Array of Waveguides with Semitransparent Walls for Shaping Flat-Topped Element Patterns," *Proc. of the 4th European Conference on Antennas and Propagation: EuCAP'2010*, Barcelona, Spain, April 12–16, 2010.

[45] Korn, G. A., and T. M. Korn, *Mathematical Handbook*, 2nd ed., New York: McGraw-Hill, 1968.

[46] Ewald, P. P., "Die Berechnung Optischer und Elektrostatischer Gitter-Potentiale," *Ann. Phys.*, Vol. 64, 1921, pp. 253–287, translated by A. Cornell, Atomics International Library, 1964.

[47] Gradstein, I. S., and I. M. Ryzhik, *Tables of Integrals, Series, and Products*, New York: Academic Press, 1980.

[48] Fructos, A. L., et al., "An Efficient Approach for the Computation of 2-D Green's Functions with 1-D and 2-D Periodicities in Homogeneous Media," *IEEE Trans. on Antennas and Propagation*, Vol. 56, No. 12, December 2008, pp. 3733–3742.

Appendix 6A Calculation of the Green's Function for Doubly Periodic Structures by the Method of M. M. Ivanishin

Consider a doubly periodic structure arranged in free space and determined by a planar lattice parallel to the plane $z = 0$ of a rectangular Cartesian coordinate system $0xyz$. Let the lattice nodes be arranged in horizontal rows parallel to the x-axis with spacing d_x and let the adjacent rows arranged with spacing d_y along the y-axis be shifted at distance with respect to each other in the direction of the x-axis. So, the lattice is skew in a general case. In particular cases, = 0 corresponds to a rectangular lattice, while = $d_x/2$ corresponds to a triangular lattice. Further, we suppose that the time dependence omitted later is chosen in the form $e^{-i\omega t}$ and the coordinate system origin coincides with one of the point sources. Then the Green's function of such a structure phased in the direction characterized by angles θ and φ measured from the axes z and x, respectively, can be represented by a spatial series

$$G(\boldsymbol{r}) = \frac{1}{4\pi} \sum_{m=} \sum_{n=} \frac{e^{ikR_{mn}}}{R_{mn}} e^{i\psi_{mn}} \tag{6A.1}$$

where $\boldsymbol{r} = \{x, y, z\}$, $R_{mn} = [(x - x_{mn})^2 + (y - y_n)^2 + z^2]^{1/2}$, $x_{mn} = md_x + n$ and $y_n = nd_y$ are the coordinates of the nodes where the point sources are arranged, $k = 2\pi/\lambda$ is the wavenumber, $\psi_{mn} = k(x_{mn}u + y_n v)$ are phases, and $u = \sin\theta\cos\varphi$ and $v = \sin\theta\sin\varphi$ are direction cosines. Note that at = 0 and with appropriate choice of the phases, representation (6A.1) can be used as the Green's function for rectangular waveguide as considered in [34].

The series (6A.1) converges very slowly, and therefore it is not used in practical computations. To obtain another representation, we first perform a transformation consisting of adding and subtracting some auxiliary function under the sum sign in (6A.1). The auxiliary function is proposed to be taken in the form of a sum of standing spherical waves with attenuation; that is,

$$f_{mn} = e^{i\psi_{mn}} \alpha R_{mn} \sum_{s=1}^{S} a_s \frac{\cos k_s R_{mn}}{R_{mn}} \tag{6A.2}$$

where the choice of attenuation constant α, amplitudes a_s, and phase constants k_s for different S will be described later. Further, we apply the well-known Poisson

summation formula [45] to the difference series formed as a result of the transformation, and reduce (6A.1) to

$$G(\boldsymbol{r}) = \frac{1}{4\pi} \sum_{m=} \sum_{n=} f_{mn} + \frac{1}{2d_x d_y} \sum_{p=} \sum_{q=} F_{pq} \tag{6A.3}$$

where

$$F_{pq} = \frac{e^{\Gamma_{pq}|z|}}{\Gamma_{pq}} \sum_{s=1}^{S} a_s \operatorname{Re} \frac{e^{\tilde{\Gamma}_{spq}|z|}}{\tilde{\Gamma}_{spq}} e^{i\alpha_p x + i\beta_{pq} y} \tag{6A.4}$$

$\alpha_p = k(u + p\lambda/d_x)$ and $\beta_{pq} = k[v + (q \quad p /d_x)\lambda/d_y]$ are transverse propagation constants of the Floquet modes, while $\Gamma_{pq} = (\alpha_p^2 + \beta_{pq}^2 \quad k^2)^{1/2}$ and $\tilde{\Gamma}_{spq} = [\alpha_p^2 + \beta_{pq}^2 \quad (k_s + i\alpha)^2]^{1/2}$ are main and auxiliary longitudinal propagation constants.

The first (spatial) series of the auxiliary functions (6A.2) in representation (6A.3) converges exponentially, so that summation of this series is not a problem. Representation of the terms of the second series in (6A.3) as a difference constitutes the main point of the application of Kummer's method for accelerating the convergence of the spectral representation for the doubly periodic Green's function. The spectral difference series in (6A.3) at $z \quad 0$ also converges exponentially. If $z = 0$, the convergence is algebraic and its rate is determined by the degree of smoothing the singularity corresponding to $R_{00} \quad 0$ when subtracting (6A.2) from the terms of series (6A.1). Note that the imaginary part of $\exp(ikR_{00})/R_{00}$ corresponding to the central source is a smooth infinitely differentiable function. That function and similar functions corresponding to all the other sources of the structure give a finite number of propagating Floquet modes formed after application of the Poisson formula to series (6A.1), while the infinite number of evanescent Floquet modes in the spectral representation correspond to the superposition of the real parts of the Green's function (6A.1) including function $\cos(kR_{00})/R_{00}$ for the central source. Using the Taylor expansion for cosine, we can write

$$\frac{\cos kR_{00}}{R_{00}} = \sum_{n=0} (\quad k^2)^n \frac{R_{00}^{2n} \quad 1}{(2n)!} \tag{6A.5}$$

Removal of the singularity and smoothing of function (6A.5) can be provided by compensation of a few first terms of that series by similar terms in the expansion of function f_{00} determined from (6A.2). Expanding f_{00} over the powers of R_{00} and equating the first $2S$ coefficients of that expansion at odd powers of R_{00} to the corresponding coefficients in (6A.5), we obtain the system of algebraic equations

$$\sum_{s=1}^{S} a_s \operatorname{Re}\{(k_s + i\alpha)^{2n}\} = k^{2n} \tag{6A.6}$$

for amplitudes a_s and phase constants k_s with attenuation constant as a parameter and $n = 1, 2, \ldots, 2S - 1$.

Consider now some special cases of the general approach described earlier. At $S = 1$, the system (6A.6) consists of two equations. Its solution is $a_1 = 1$ and $k_1 = \sqrt{k^2 + \alpha^2}$. That solution corresponds to the technique proposed in [34] for rectangular waveguide. In this case, $\tilde{\Gamma}_{spq} = (\Gamma_{pq}^2 \quad 2ik_1\alpha)^{1/2}$, and coefficients (6A.4) for large Γ_{pq} and $z = 0$ behave as

$$F_{pq} \sim \frac{3(k^2 + \alpha^2)\alpha^2}{2\Gamma_{pq}^5} e^{i\alpha_p x + i\beta_{pq} y} \tag{6A.7}$$

The asymptotic (6A.7) corresponds to compensation of the first two terms of series (6A.5), and so the case $S = 1$ is naturally referred to as the second order Kummer's method, as has been suggested in [35].

The use of two waves in the auxiliary function (6A.2) (i.e., when $S = 2$) allows compensating the four first terms of the series (6A.5). This corresponds to Kummer's method of the fourth order. The system (6A.6) in this case contains four equations

$$a_1 + a_2 = 1 \tag{6A.8}$$

$$\sum_{s=1}^{2} (k_s^2 \quad \alpha^2) a_s = k^2 \tag{6A.9}$$

$$\sum_{s=1}^{2} (k_s^4 \quad 6k_s^2\alpha^2 + \alpha^4) a_s = k^4 \tag{6A.10}$$

$$\sum_{s=1}^{2} (k_s^6 \quad 15k_s^4\alpha^2 + 15k_s^2\alpha^4 \quad \alpha^6) a_s = k^6 \tag{6A.11}$$

Equations (6A.9) to (6A.11) can be rewritten in a more convenient form

$$k_1^2 a_1 + k_2^2 a_2 = k^2 + \alpha^2 \tag{6A.12}$$

$$k_1^4 a_1 + k_2^4 a_2 = k^4 + 6k^2\alpha^2 + 5\alpha^4 \tag{6A.13}$$

$$k_1^6 a_1 + k_2^6 a_2 = k^6 + 15k^4\alpha^2 + 75k^2\alpha^4 + 61\alpha^6 \tag{6A.14}$$

where (6A.12) has been obtained by using (6A.8), while (6A.13) has been derived by using (6A.8) and (6A.12). Equations (6A.8), (6A.12), and (6A.13) have been used for derivation of (6A.14).

Using (6A.8) and (6A.12), we obtain

$$a_1 = \frac{k_2^2 \quad k^2 \quad \alpha^2}{k_2^2 \quad k_1^2}, \quad a_2 = \frac{k^2 + \alpha^2 \quad k_1^2}{k_2^2 \quad k_1^2} \tag{6A.15}$$

Substituting (6A.15) in (6A.13) and (6A.14) and solving the latter [36, 37], we find

$$k_1 = \sqrt{k^2 + 7\alpha^2 \quad 2\alpha\sqrt{k^2 + 10\alpha^2}} \tag{6A.16}$$

$$k_2 = \sqrt{k^2 + 7\alpha^2 + 2\alpha\sqrt{k^2 + 10\alpha^2}} \tag{6A.17}$$

Substituting (6A.15) to (6A.17) in (6A.4) and noting that

$$\tilde{\Gamma}_{spq} = \sqrt{\Gamma_{pq}^2 + k^2 \quad (k_s + i\alpha)^2}$$

we can show that the first term in the asymptotic of (6A.4) for large Γ_{pq} and $z = 0$ is determined by formula

$$F_{pq} \sim \frac{35(k^2 + \alpha^2)(k^2 + 9\alpha^2)\alpha^4}{2\Gamma_{pq}^9} e^{i\alpha_p x + i\beta_{pq} y} \tag{6A.18}$$

As shown in [36, 37], the convergence rate of the spectral series characterized by (6A.18) is already sufficient for the fourth-order Kummer's method to compete successfully with Ewald's method [46], which has been believed to be the most efficient. However, if an even higher rate is required, it can be achieved using the sixth-order Kummer's method corresponding to $S = 3$. Omitting the intermediate operations including solution of a cubic equation in the process of solving system (6A.6) containing six equations, we give final formulas obtained for the phase constants of the auxiliary waves

$$k_1 = \sqrt{k^2 + 23\alpha^2 \quad 2\alpha\sqrt{5k^2 + 126\alpha^2}} \tag{6A.19}$$

$$k_2 = \sqrt{k^2 + 9\alpha^2} \tag{6A.20}$$

$$k_3 = \sqrt{k^2 + 23\alpha^2 + 2\alpha\sqrt{5k^2 + 126\alpha^2}} \tag{6A.21}$$

and their amplitudes

$$a_1 = \frac{1}{2(5k^2 + 77\alpha^2)} \quad k^2 + 73\alpha^2 + \frac{9\alpha(3k^2 + 91\alpha^2)}{\sqrt{5k^2 + 126\alpha^2}} \div \tag{6A.22}$$

$$a_2 = \frac{4(k^2 + \alpha^2)}{5k^2 + 77\alpha^2} \tag{6A.23}$$

$$a_3 = \frac{1}{2(5k^2 + 77\alpha^2)} \quad k^2 + 73\alpha^2 \quad \frac{9\alpha(3k^2 + 91\alpha^2)}{\sqrt{5k^2 + 126\alpha^2}} \div \tag{6A.24}$$

The spectral difference series in this case converges as Γ_{pq}^{13}.

Appendix 6B Accelerating the Convergence of Series (6.57)

The series (6.57) represents the field of phased filaments of electric current and of their images with respect to the plane $z = 0$. Since $z_{l's} + z_{ls} > 0$, the part of the series corresponding to the contribution of the images converges exponentially, and therefore it is not necessary to apply any additional means for improvement of its convergence. The part of the series corresponding to the field of the sources themselves can be written in the form

$$S = \frac{k \exp(i\alpha_0 \xi + i\Gamma_0 \zeta)}{\Gamma_0} + S^+ + S \tag{6B.1}$$

where $\xi = x_{j\,s} \quad x_{js}$, $\zeta = |z_{l\,s} \quad z_{ls}|$, and

$$S^{\pm} = \sum_{q=1} \frac{k \exp(i\alpha_{\pm q} \xi + i\Gamma_{\pm q} \zeta)}{\Gamma_{\pm q}} \tag{6B.2}$$

To accelerate the slow convergence of (6B.2) when $\zeta \quad 0$, we again apply Kummer's method. Taking into account that

$$\frac{k e^{i\Gamma_{\pm q}\zeta}}{\Gamma_{\pm q}} = \frac{ib}{q\lambda}\left(1 + \frac{k\zeta}{2} \mp \sin\theta \div \frac{b}{q\lambda}\right) e^{\mp \alpha_{\pm q}\zeta} + O\left(\frac{1}{q^3} \div\right)$$

for $q >> 1$, as well as that

$$\frac{1}{q^2} = \frac{1}{q(q+1)} + O\left(\frac{1}{q^3} \div\right) = \frac{1}{q}\left(\frac{1}{q+1} + O\left(\frac{1}{q^3} \div\right)\right.$$

for $q >> 1$, we represent the series (6B.2) in the form

$$S^{\pm} = S_a^{\pm} + \sum_{q=1} e^{i\alpha_{\pm q}\xi} \frac{k e^{i\Gamma_{\pm q}\zeta}}{\Gamma_{\pm q}}$$

$$+ \frac{ib}{q\lambda}\left(1 + \frac{k\zeta}{2} \mp \sin\theta \div \frac{b}{(q+1)\,\lambda}\right) e^{\mp \alpha_{\pm q}\zeta} \tag{6B.3}$$

where

$$S_a^{\pm} = \frac{ib}{\lambda} e^{(i\xi \mp \zeta)k\sin\theta} \sum_{q=1} \frac{u^{\pm}}{q}\left(\frac{v^{\pm}}{q+1} \div p^q e^{\pm iq\psi}\right. \tag{6B.4}$$

is the series of asymptotic terms with $p = \exp(\ 2\pi\zeta/b)$, $\psi = 2\pi\xi/b$, and

$$u^{\pm} = 1 + v^{\pm}, \quad v^{\pm} = \frac{k\zeta}{2} \mp \sin\theta \div \frac{b}{\lambda}$$

Using the tabulated sums 1.448.1 and 1.448.2 in [47], we can express the sums in (6B.4) as follows

$$\sigma_1 = \sum_{q=1} \frac{p^q e^{iq\psi}}{q} = \ln\sqrt{1 \quad 2p\cos\psi + p^2} + i\,\mathrm{arctg}\frac{p\sin\psi}{1 \quad \cos\psi} \tag{6B.5}$$

$$\sigma_2 = \sum_{q=1} \frac{p^q e^{iq\psi}}{q+1} = \sum_{q=2} \frac{p^{q \ 1} e^{i(q \ 1)\psi}}{q}$$

$$= \frac{e^{\ i\psi}}{p} \sum_{q=1} \frac{p^q e^{iq\psi}}{q} \quad pe^{i\psi} \div = \frac{e^{\ i\psi}}{p}\sigma_1 \quad 1 \tag{6B.6}$$

Formulas (6B.5) and (6B.6) allow us to rewrite the expressions (6B.4) in the closed form

$$S_a^+ = \frac{ib}{\lambda} e^{(i\xi \ \zeta)k\sin\theta}(u^+\sigma_1 \quad v^+\sigma_2) \tag{6B.7}$$

$$S_a = \frac{ib}{\lambda} e^{(i\xi+\zeta)k\sin\theta}(u \ \sigma_1 \quad v \ \sigma_2) \tag{6B.8}$$

Thus, the slowly converging series (6B.2) at $\zeta \quad 0$ is transformed into the sums (6B.3) containing the closed-form expressions (6B.7) and (6B.8), as well as sufficiently fast converging series with terms decaying like q^{-3} as q . Some modifications of Kummer's method providing even more fast convergences of series like (6B.2) are considered in [48].

About the Author

Sergei P. Skobelev received an M.S. in radio electronics and a Ph.D. in antennas and microwave engineering from the Moscow Institute of Physics and Technology (MIPT), Russia, in 1977 and 1984, respectively.

Since 1977, he has been working at the Research Institute of Radio Physics (now Joint-Stock Company "Radiophyzika"), Moscow, Russia, with a break from 1981 to 1984 for studying a Ph.D. course and writing his Ph.D. thesis. He is currently the leading research associate at the Antenna Department of Radiophyzika. He also teaches a course called "Applied Electrodynamics and Optics" at MIPT and was a scientific advisor of several M.S. and Ph.D. students at the MIPT.

From 2002 to 2004, he was a visiting researcher in the Antenna Group at Chalmers University of Technology, Gothenburg, Sweden, where he developed various numerical models of hard horn antennas. During 2007 and 2008, he was a Visiting Research Fellow at Northumbria University, Newcastle-upon-Tyne, United Kingdom, working in the area of microwave imaging and its antenna applications.

His main area of scientific interests includes antenna theory and technology, in particular, phased array antennas, as well as analytical and numerical methods in electromagnetics. He has published more than 130 journal articles and conference papers in the indicated area and has received seven SU (Soviet Union) Author's Certificates for inventions in the phased array antennas.

Dr. Skobelev was one of the organizers of the 10th International School Seminar on Wave Diffraction and Propagation, Moscow, 1993, and the 28th International Conference on Antenna Theory and Technology, Moscow, 1998. He was a cochairman of the Phased Array Sessions at ICEAA99, Torino, Italy, 1999, and at ISPAST2000, Dana Point, California, 2000. He serves as a cochairman of the monthly Moscow Joint Feld's seminar on electrodynamics and antennas.

Dr. Skobelev is a senior member of the IEEE and was the secretary and vice-chairman of the Moscow AP-S Chapter of the IEEE Russian Section.

Index